UAB
Universitat Autònoma de Barcelona

Expanding the Computational Toolkit for Studying Cell-Penetrating Peptides via Molecular Dynamics Simulations

Eric Catalina Hernandez

DOCTORAL THESIS

Expanding the Computational Toolkit for Studying Cell-Penetrating Peptides via Molecular Dynamics Simulations

Author

Eric Catalina Hernandez

PhD in Bioinformatics

Biophysics Unit. Department of Biochemistry & Molecular Biology

Barcelona, 2025

Co-Directors

Alex Peralvarez Marin

Mario Lopez Martin

Tutor

Alex Peralvarez Marin

Preface

ABBREVIATIONS

ΔQ	Transmembrane potential
ACPs	Anticancer peptides
AI	Artificial intelligence
AFPs	Antifungal peptides
AMPs	Antimicrobial peptides
Arg9	Nona-arginine
aSMD	Adaptive steered molecular dynamics
AVPs	Antiviral peptides
BigDyn	Big dynorphin
BPs	Bioactive peptides
CCVs	Clathrin-coated vesicles
CG-MD	Coarse-grained molecular dynamics
CHOL	Cholesterol
CME	Clathrin-mediated endocytosis
CompEL	Computational electrophysiology
CPPs	Cell-penetrating peptides
CvME	Caveolae-mediated endocytosis
CVs	Collective variables
DLS	Dynamic light scattering
DOPC	1,2-dioleoyl-sn-glycero-3-phosphocholine
DOPS	1,2-dioleoyl-sn-glycero-3-phospho-L-serine
DPPC	1,2-dipalmitoyl-sn-glycero-3-phosphocholine
DPPS	1,2-dipalmitoyl-sn-glycero-3-phospho-L-serine
DynA	Dynorphin A
DynB	Dynorphin B

DPX	p-Xylene-bis-pyridinium bromide
FME	Flotillin-mediated endocytosis
HIV	Human immunodeficiency virus
HPTS	8-hydroxypyrene-1,3,6-trisulfonic acid
HT-MD	High temperature molecular dynamics
IMM	Implicit membrane models
K-FGF	Kaposi fibroblast growth factor
KOR	κ-opioid receptor
L5S	Leucine to serine mutation in position 5
Leu9	Nona-leucine
MAP	Model amphipathic peptide
MAPs	Membrane active peptides
MD	Molecular dynamics
MFI	Median fluorescence intensity
MOR	μ-opioid receptor
MT-MD	Membrane tensioned molecular dynamics
PC	Phosphatidylcholine
PDYN	Prodynorphin
PE	Phosphatidylethanolamine
PFTs	Pore-forming toxin peptides
P:L	Peptide-to-lipid
PMF	Potential of mean force
POPC	1-palmitoyl-2-oleoyl-sn-glycero-3-phosphocholine
POPE	1-palmitoyl-2-oleoyl-sn-glycero-3-phosphoethanolamine
POPG	1-palmitoyl-2-oleoyl-sn-glycero-3-phospho-(1'-rac-glycerol)
POPS	1-palmitoyl-2-oleoyl-sn-glycero-3-phospho-L-serine
PPII	Polyproline helix

PS	Phosphatidylserine
R6W	Arginine to tryptophan mutation in position 6
R9C	Arginine to cysteine mutation in position 9
RE+US	Replica exchange molecular dynamics combined with umbrella sampling
REMD	Replica exchange molecular dynamics
SCA23	Spinocerebellar ataxia
SEC	Size-exclusion chromatography
SMD	Steered molecular dynamics
TAT	Trans-activator of transcription
TP2	Translocating peptide 2
TP10	Transportan 10
US	Umbrella sampling
WE	Weighted ensemble
WT	Wild type

TABLE OF CONTENTS

LIST OF FIGURES

LIST OF TABLES

Introduction

1. INTRODUCTION

1.1. Membranes

Biological membranes represent the fundamental biochemical structure that delineate cells and subcellular organelles, forming the basis of compartmentalization and regulatory control over molecular transport and signal transduction[1]. Particularly, the cell membrane separates the cellular internal environment from the extracellular space, thus keeping cellular components inside and foreign substances outside.

Membranes are primarily composed of lipid bilayers arranged in a dynamic and fluid mosaic[2–4]. This classical fluid mosaic model proposed by Singer and Nicolson in 1972 revolutionized the understanding of biological membranes by describing them as dynamic bilayers of lipids with embedded proteins capable of lateral mobility. Although visionary for its time, the original model provided a simplified view that underestimated both the density and the organizational complexity of membrane proteins. Subsequent refinements have highlighted that membranes are not uniform two-dimensional fluids but rather protein-crowded, heterogeneous, and dynamic environments with transient nanodomains and cytoskeleton-associated compartments[3,5–7]. Modern interpretations of the fluid mosaic model thus describe membranes as highly organized, multifunctional assemblies where protein–lipid and lipid–lipid interactions define local structure and function.

Lipid bilayers are constructed from a diverse array of lipid species (Figure 1), predominantly glycerophospholipids (e.g., phosphatidylcholine –PC–, phosphatidylethanolamine –PE–, phosphatidylserine –PS–), sphingolipids (e.g., sphingomyelin), and sterols (e.g., cholesterol)[1]. Amphipathic phospholipids, with hydrophilic head groups and hydrophobic acyl chains, self-assemble into two-dimensional structures that provide structural integrity and selective permeability to the membrane.

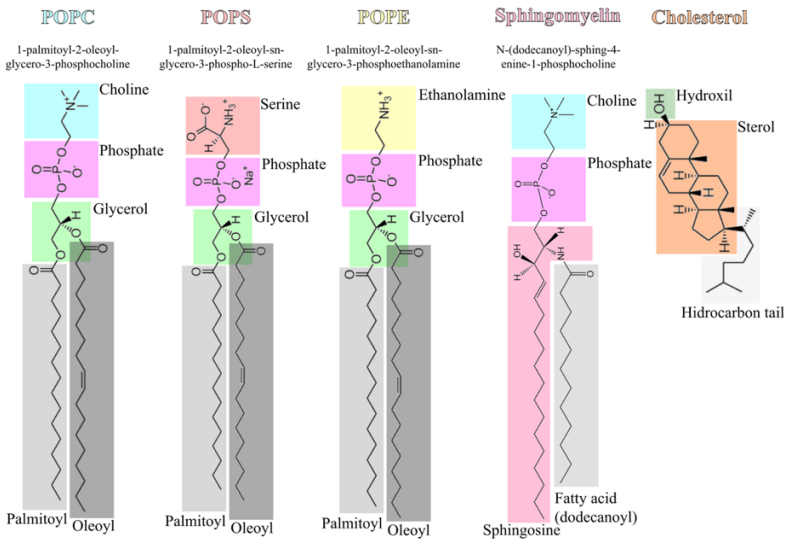

Figure 1. *Molecular 2D schemes of representative lipid components of the cell membrane, indicating their main parts.*

At the molecular level, the arrangement of such lipids is driven by the hydrophobic effect, that leads the non-polar acyl chains to congregate away from the aqueous environment, thus forming the hydrophobic core. On the contrary, polar heads groups interface with water, consequently delimiting the lipid–water interface, and generating two leaflets in the bilayer, namely the upper or extracellular and the lower or intracellular leaflets (Figure 2)[8].

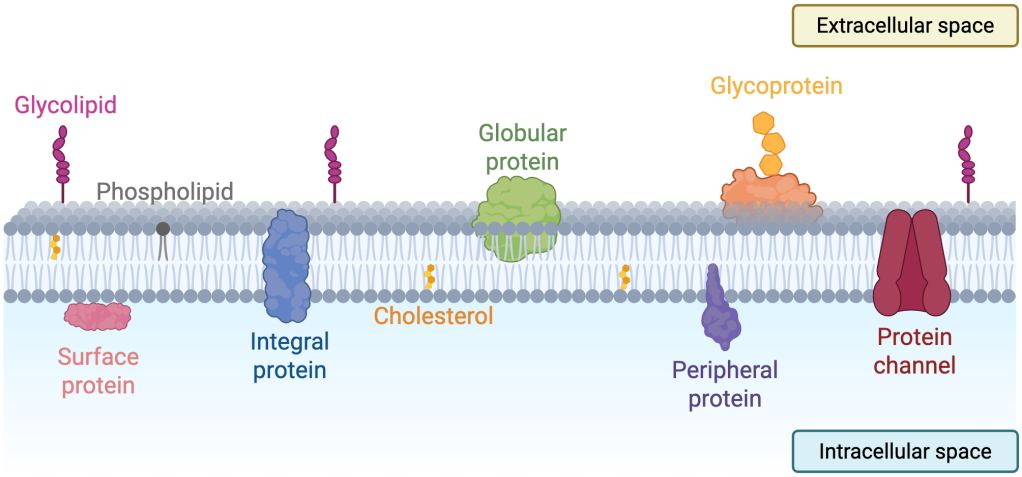

Figure 2. *Molecular representation of the cell membrane structure, which separates the extracellular and intracellular spaces. The membrane consists of a phospholipid bilayer containing cholesterol and diverse types of proteins.*

The intrinsic fluidity, lateral mobility, and asymmetry of biological membranes are key determinants of their biochemical function, as they allow the dynamic redistribution of lipids and

proteins in response to physiological changes. Membranes are continuously remodelled during processes such as endocytosis, exocytosis, vesicle trafficking, lipid turnover, and domain reorganization, enabling cells to adapt their composition and structure to environmental and metabolic cues[9–11].

Cell membranes also act as protective barriers, regulating the passage of substances into and out of the cell. Small organic molecules with a proper hydrophobicity and hydrophilicity balance (for instance, small hydrophobic compounds) can cross the cell membrane passively. In contrast, charged or large molecules generally cannot, and typically require specific transport mechanisms[12]. Beyond their structural role, membranes are inherently interactive surfaces where a wide range of biochemical processes occur, acting as active platforms that coordinate cellular signalling, material exchange, and energy transduction[13].

Molecular interactions at membranes are governed by a complex interplay of forces, each contributing in distinct ways to the binding, insertion, and translocation of biomolecules[14,15]. Electrostatic interactions arise from the attraction between charged groups on biomolecules (e.g., positively charged residues in proteins) and oppositely charged regions of the membrane (e.g., negatively charged phosphate headgroups in phospholipids), which can drive the protein–membrane interaction[16]. Conversely, hydrophobic interactions promote the insertion of nonpolar regions of proteins or small molecules into the lipid bilayer's hydrophobic core, a key step in the integration of transmembrane helices during protein folding[17]. In addition, hydrogen bonding can form both between biomolecules and lipid headgroups, and within the molecules themselves, helping to stabilize defined orientations or docking arrangements[18,19]. This is exemplified by peripheral membrane proteins that recognize specifics headgroups. Last, van der Waals forces, even though are individually weak, can become significant when large surface areas are in close proximity, as occurs in the tight packing of lipid acyl chains around an inserted protein domain or drug molecule[20].

These forces are essential for normal cellular processes, including receptor-ligand recognition at the cell surface, signal transduction through conformational changes in membrane proteins, and enzyme activation in lipid-modifying pathways[21]. Importantly, the same principles are harnessed in therapeutic contexts. For instance, liposomal drug carriers rely on hydrophobic and electrostatic cues to merge with target cell membranes[22,23].

One process in which these interactions are especially relevant is membrane disruption[24], a phenomenon in which the integrity of the lipid bilayer is transiently or permanently altered. Such disruption can be caused by several mechanisms, including extreme environmental conditions (e.g., pH, heat, electric fields), exposure to detergents, the action of virulence factors produced by pathogenic organisms, or the action of peptides. Peptides, in particular, can possess a remarkable capacity to engage with membranes in diverse ways. In fact, the term *membrane active peptides* (MAPs) refers to short, typically cationic peptides that exert their biological activity primarily through interactions with the cell membrane[25]. MAPs belong to a broader group known as bioactive peptides (BPs)[26], which are short amino acid sequences that can modulate physiological processes such as immune regulation, antioxidant defence, blood pressure control, and appetite modulation[27]. Together with proteins, BPs play key roles in the metabolic functions of living organisms[28]. Within MAPs, two principal groups are recognized (Figure 3): antimicrobial peptides (AMPs) and cell-penetrating peptides (CPPs)[25].

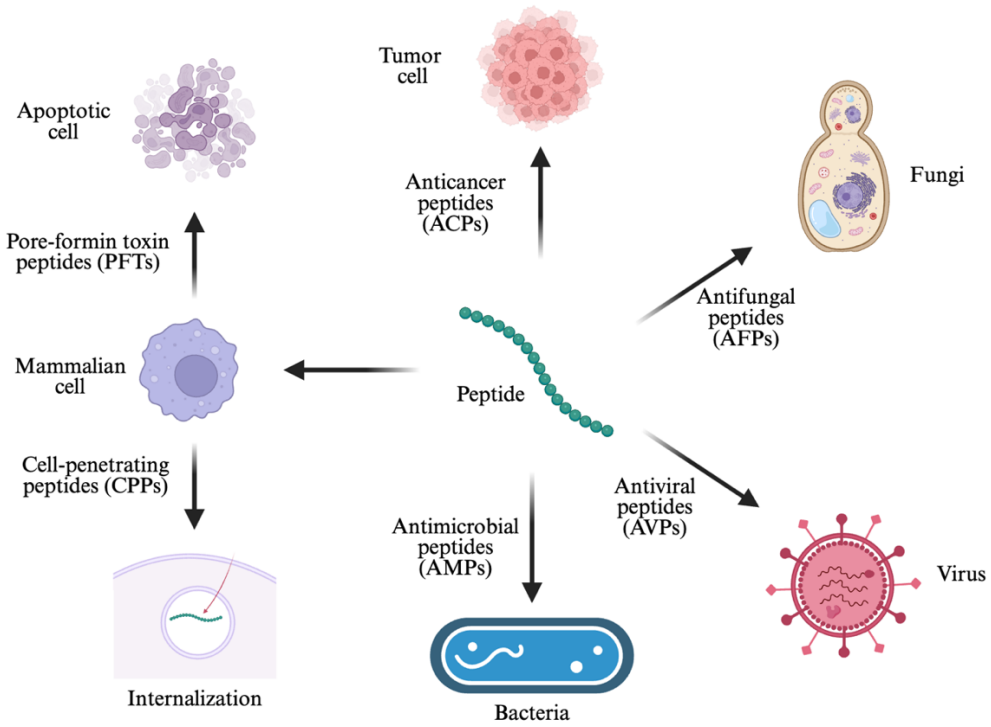

Figure 3. *Types of membrane actives peptides.*

AMPs are short, typically cationic peptides with broad spectrum activity against a wide range of pathogens, including bacteria, viruses, fungi, and protozoa[29]. Their mechanism of action often

involves electrostatic interactions with negatively charged components of microbial membranes, leading to membrane disruption, destabilization, pore formation, and rapid cell lysis. In contrast, CPPs are also short, cationic peptides but differ fundamentally in the way they interact with membranes. Rather than causing permanent disruption, CPPs facilitate their own internalization by inducing temporary, localized perturbations of the lipid bilayer, allowing translocation into the cell without inflicting lasting membrane damage nor compromising cellular viability[30]. Nevertheless, CPPs and AMPs also share similarities, as AMPs use a CPP-like mechanism at low concentrations, whereas at high concentrations will cause membrane leakage[31].

In addition, there are other groups of peptides which also interact with certain membranes and can also be considered as MAPs (Figure 3). First, anticancer peptides (ACPs) are also short BPs, typically ranging between 5 and 50 amino acids, that exhibit selective cytotoxicity toward cancer cells while sparing normal tissues[32,33]. Their cationic and amphipathic nature enables them to preferentially bind to the negatively charged membranes of tumour cells, leading to membrane destabilization and cell death. ACPs have the therapeutic potential to be used in next-generation cancer treatments[32,34].

Second, antiviral peptides (AVPs) are BPs that inhibit viral infections through a variety of mechanisms, such as binding to viral envelope proteins, host cell receptors or via disrupting viral membranes through pore formation[35,36]. Owing to these capabilities, AVPs are attractive candidates for broad-spectrum antiviral therapies[37].

Third, antifungal peptides (AFPs) are molecules that target fungal pathogens with high specificity and minimal toxicity to mammalian cells[38,39]. Primarily, AFPs exert their antifungal action by disrupting fungal cell membranes and interfering with cell wall biosynthesis, leveraging the unique composition of fungal membranes (rich in β-glucans, chitin, and mannoproteins) to achieve selectivity. AFPs provide a strong basis for alternatives to traditional antifungal agents, especially in the context of rising drug resistance[40].

In addition, pore-forming toxin peptides (PFTs) are peptides secreted predominantly by pathogenic bacteria that compromise host cell integrity by forming transmembrane pores[41,42]. The formation of such pores disrupts cellular ion gradients by permitting unregulated flux of ions and small molecules, ultimately leading to cell lysis or apoptosis. PFTs are important virulence factors and, thus, potential targets for therapeutic intervention[43].

1.2. CPPs

1.2.1. CPP history

Early studies on MAPs revealed that certain naturally occurring sequences possess intrinsic membrane-disrupting capabilities. Among the first described were melittin[44], the major component of bee venom, alamethicin, a voltage-gated pore-forming peptide[45], and magainin[46], an AMP isolated from amphibian skin, both capable of permeabilizing or destabilizing lipid bilayers through distinct mechanisms. These peptides, characterized during the 1980s, can permeabilize or destabilize lipid bilayers through distinct mechanisms, typically involving pore formation, rather than non-cytotoxic translocation across membranes. This distinction laid the conceptual groundwork for the later identification of CPPs.

The first observation of cell-penetrating behaviour is attributed to the trans-activator of transcription (TAT) protein of human immunodeficiency virus (HIV)-1 in 1988. TAT was shown capable of crossing cellular membranes without causing detectable damage to the lipid bilayer, enabling trans-activation of the HIV-1 promoter[47,48]. This unexpected ability was later attributed to a short, highly basic amino acid sequence within the TAT protein, which is particularly rich in lysine and arginine residues[49].

Shortly after, in 1991, a similar phenomenon was reported for the Antennapedia protein from *Drosophila melanogaster*, a transcription factor essential for regulating morphological differentiation[50]. Researchers determined that its membrane-translocating activity resided in the third α-helix of the protein, a segment later named penetratin[51]. Like TAT, penetratin is enriched in lysine and arginine residues, suggesting that electrostatic interactions with membrane phospholipids and glycosaminoglycans play a key role in facilitating cellular uptake.

These initial discoveries of TAT and penetratin established that CPPs can cross cell membranes either alone or carrying cargo. In the following years, new CPPs were identified in both natural and synthetic forms, many based on poly-arginine designs. The field has since grown rapidly (Figure 4), with current databases, such as CPPSite3.0[52], one of the most comprehensive CPP databases, containing thousands of entries with diverse sequences and delivery capabilities.

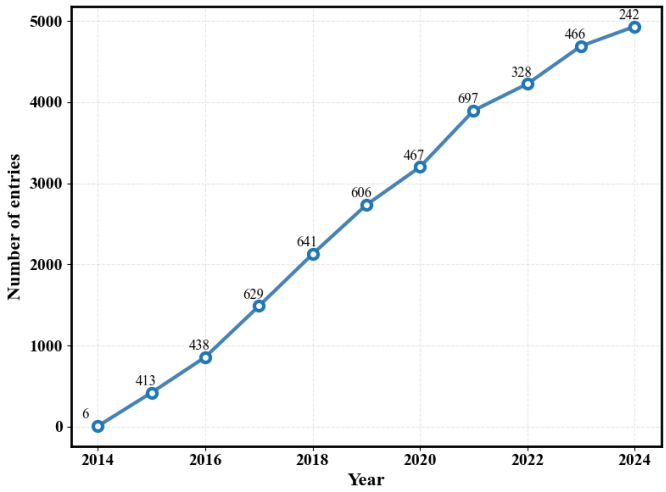

Figure 4. *Total number of entries each year in CPPSite3.0. The label indicates the number of new entries added to the database per year.*

1.2.2. Classification

Naturally occurring peptides and proteins have evolved mechanisms to interact with and sometimes cross biological membranes. Inspired by these processes, researchers have designed CPPs that exploit similar physicochemical principles. These peptides can be categorized based on their factors such as their nature, structure, or physicochemical properties (Figure 5). While some CPPs are derived directly from natural proteins, others are rationally designed to respond to environmental cues such as electric fields, temperatures, or pH, conditions that can drastically alter membrane organization and peptide behaviour.

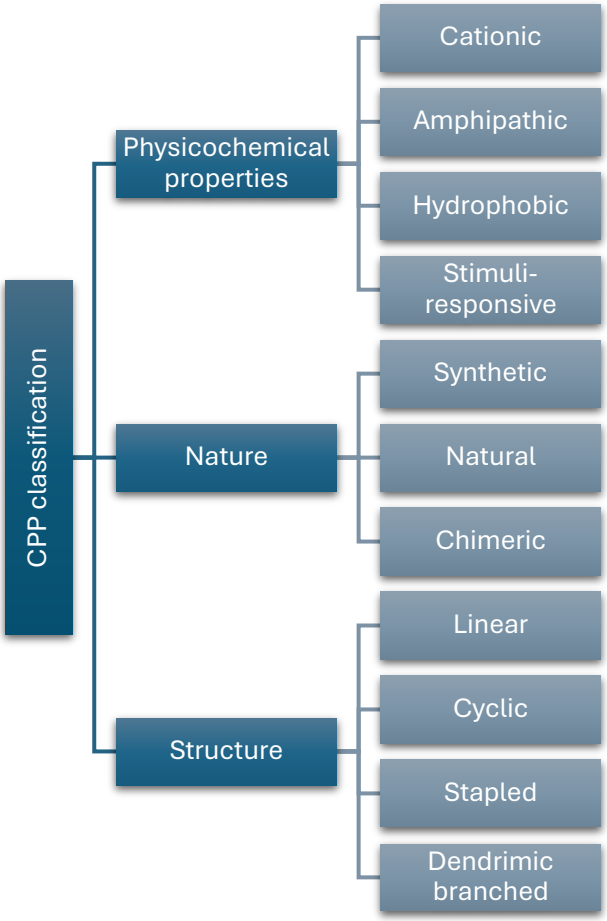

Figure 1. *Classification of CPPs according to their physicochemical properties, nature, and structural characteristics.*

Based on their physicochemical properties, CPPs are classified into four main groups: cationic, amphipathic, hydrophobic, and stimuli-responsive CPPs. Cationic CPPs (such as polyarginine–Arg9–[53], TAT, or penetratin) are characterized by a high content of positively charged amino acids, predominantly arginine and lysine, which facilitate electrostatic interactions with the negatively charged cell membranes. These peptides often utilize their positive charge density for cell entry[54], but other residues can be important too, as exemplified by penetratin, where a mutated tryptophan substantially diminishes cellular uptake[55].

Amphipathic CPPs, such as model amphipathic peptide–MAP–[56,57], transportan 10–TP10–[58], or Pep-1[59], possess both hydrophilic and hydrophobic regions, allowing them to interact with both the aqueous environment and the lipid bilayer of cell membranes.

These can be further divided into primary, secondary α-helical, secondary β-sheet, and proline-rich subclasses. Primary amphipathic CPPs possess an intrinsic distribution of hydrophobic and hydrophilic amino acids, whereas secondary CPPs are unstructured in solution but gain α-helix or β-sheet structure upon membrane interaction[60]. Last, proline-rich CPPs have a high content of proline residues in their sequence, which can lead to the formation of the left-handed polyproline helix (PPII), with 3.0 residues per turn, as opposed to the 3.6 of the right-handed conventional α-helix[61]. Further, PPII helices are particularly well-suited to protein-protein and protein-nucleic acid interactions, often acting as recognition motifs and facilitating peptide heterotypic interactions[62–64].

Hydrophobic CPPs are composed mainly of nonpolar amino acid residues and are less extensively studied than the other categories, relying on hydrophobic motifs for membrane traversal. Despite being the least studied group, they have notable examples such as Kaposi fibroblast growth factor (K-FGF)[65] or translocating peptide 2 (TP2)[54]. Hydrophobic peptide sequences were found to directly translocate the cell, which can be helpful because they are directly available in the cytosol and eliminate the risk of endosomal entrapment[66].

Stimuli-responsive CPPs become membrane-active only under acidic conditions, enabling activation within tumour regions. Examples include pH-(low)-insertion-peptide[67,68] and the histidine-rich designer peptide LAH4-L1[69]. Such pH-responsiveness enhances tumour selectivity and allows for targeted cargo release at the disease site[70].

CPPs can also be categorized by their nature. Here, three groups are differentiated: natural, those that are derived from natural proteins; chimeric, those created by combining sequences from different CPPs or proteins; and synthetic, CPPs that are designed from scratch. For instance, TAT and penetratin are examples of naturally derived CPPs, while transportan and Pep-1 are considered chimeric or synthetic.

Despite their many promising features, CPPs also face important limitations, such as poor stability under *in vivo* conditions, cytotoxicity, and restricted permeability across certain membrane systems. To overcome these drawbacks, researchers have developed structural modifications that not only enhance CPP stability and delivery efficiency but also minimize their adverse effects[71]. These modifications have, in turn, given rise to another mode of classification, in which CPPs are categorized according to their structural design.

Most CPPs are linear, but cyclic, stapled and dendrimeric have also been designed in order to improve resistance to protease activity[72,73]. Cyclic CPPs have been shown to enhance the penetrating properties compared to their linear counterparts, which, together with their reduced cytotoxicity and higher stability, make cyclic CPPs a promising new tool[74–76]. Stapled CPPs also increase proteolytic degradation and enhance cell permeability[77]. Similarly, branched dendritic peptides, with a branched, tree-like structure, enhance cellular uptake and improve stability[78].

The classification of CPPs is not always rigid, as some peptides can exhibit properties of more than one group, and their behaviour can be influenced by factors such as cargo, concentration, and experimental conditions. Understanding these classifications is crucial for predicting their interactions with cell membranes and their effectiveness in drug delivery applications.

1.2.3. Mechanism of entry

The mechanism by which CPPs breach the cellular barrier has been–and still is– the subject of intense investigation and debate[79], with multiple pathways proposed to account for their diverse behaviours. Mainly, CPPs utilize two primary mechanisms to enter cells: energy-independent direct translocation across the plasma membrane (Figure 6) and energy-dependent endocytosis (Figure 7)[80].

1.2.3.1.Energy-independent pathways

Direct penetration mechanisms are energy–independent processes, with proposed mechanisms involving inverted micelle formation, carpet model, membrane thinning and pore formation, such as the barrel-stave and toroidal pore models. The initial step in the internalization process is the establishment of electrostatic interactions between the peptide and the cellular membrane, thereby influencing the lipid supramolecular organization.

In the inverted micelles model, the electrostatic interactions may result in alterations in the membrane curvature, including invaginations[81]. These membrane curvatures or invaginations can facilitate the formation of inverted micelles that encapsulate the peptide[82–84]. Subsequently, the micelle undergoes destabilization, leading to the release of the peptide-cargo complex into the cytoplasm. Inverted micelle model has been proposed for TAT and oligoarginines into vesicles with an important negative charge component[85].

Similarly, the membrane perturbation caused by CPP interaction can also lead to translocation via pore formation, including the barrel-stave and the toroidal model. In the former, the peptides form bundles upon membrane interaction, which have channels in their centre, and these can be used by other CPPs to enter the cell[86]. In the latter, CPPs are able to form α-helices when interacting with the membrane, causing membrane bending and creating a pore through the interaction with the lipid polar heads[87,88]. Oligoarginines, TP10 and TAT are believed to be able to enter through these methods[89–91].

In the carpet model, peptides align parallel to the membrane surface, where their positively charged residues interact with the negatively charged phospholipid headgroups, while their hydrophobic regions make contact with the lipid bilayer's hydrophobic core. This arrangement, first proposed by Pouny and colleagues[92], resembles a 'carpet' covering the membrane. When a sufficient peptide density is reached, this carpet-like organization disrupts membrane packing, leading to local destabilization and facilitating CPP internalization.

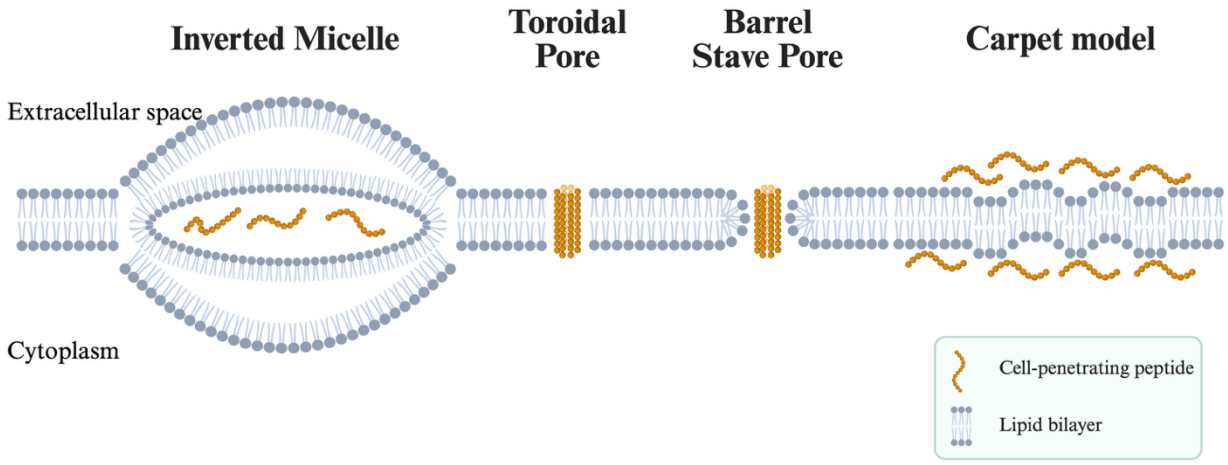

Figure 2. *Energy-independent mediating the direct entry of CPPs into the cell.*

1.2.3.2.Energy-dependent pathways

Endocytosis is an energy-dependent pathway that involves the formation of vesicles to internalize CPPs. In endocytosis, the positive charges on many CPPs play a central role in their initial interaction with the negatively charged molecules on the cell surface, resulting in a process that draws the peptide-cargo complex into the cell inside vesicular compartments. Several different mechanisms have been described as endocytic mechanisms involved in CPP entry:

macropinocytosis, clathrin-mediated endocytosis (CME), caveolae-mediated endocytosis (CvME) and clathrin- and caveolae-independent endocytosis[93].

First, macropinocytosis is a rapid, lipid raft-dependent and receptor-independent form of endocytosis [93]. It is triggered by growth factors or other stimuli that induce actin-driven membrane protrusions in many cell types. Unlike receptor-mediated uptake, macropinocytosis does not involve the engulfment of ligand-coated particles. Instead, it relies on large, actin-supported membrane protrusions that collapse back onto the cell surface, fusing with the plasma membrane to generate large vesicles known as macropinosomes. This leads to an increase in fluid-phase uptake and allows non-selective internalization of extracellular material, including CPPs. Arginine-rich peptides like TAT often exploit macropinocytosis, especially at higher concentrations.

Second, CME is one of the best-characterized and most common pathways for CPP internalization[80]. CME is a receptor-dependent, clathrin-mediated, and dynamin-required process that occurs virtually in all mammalian cells[94]. CME begins with the strong binding of a ligand—such as a CPP or a nutrient—to a specific cell surface receptor, which triggers the recruitment and assembly of clathrin into a polyhedral lattice on the cytosolic side of the plasma membrane. The recruitment of clathrin leads to the formation of shallow, clathrin-coated pits that progressively invaginate into dome-like structures. As invagination continues, the pits form spherical buds connected to the membrane. Dynamin, a GTPase, is then required to mediate the scission of the vesicle from the membrane. The resulting clathrin-coated vesicles (CCVs) are rapidly uncoated and delivered to early endosomes. These may mature into late endosomes and eventually fuse with lysosomes[95]. CME has been proposed as one of the mechanisms employed by arginine-rich CPPs for cellular entry.

Third, CvME[96] is a clathrin-independent, dynamin-dependent pathway that uses caveolae–small, flask-shaped membrane invaginations around 50-100 nm in diameter–for internalization. These structures are rich in cholesterol, sphingolipids, and the protein caveolin, and are especially abundant in endothelial and adipose cells. Often considered a type of lipid raft–dynamic assemblies of proteins and lipids that freely float within the liquid-disordered bilayer of cellular membranes–, caveolae serve as sites for signalling and endocytosis. In CPP uptake, CvME

provides a route that may bypass lysosomal degradation, facilitating more efficient intracellular delivery.

Last, clathrin- and caveolae-independent endocytosis refers to a group of endocytic mechanisms that are less understood and function independently of clathrin, caveolin, and can be dynamin-dependent or independent. There are several types, including the CLIC/GEEC mechanism[97], the Arf6-dependent pathway[98], and the flotillin-mediated endocytosis (FME)[99].

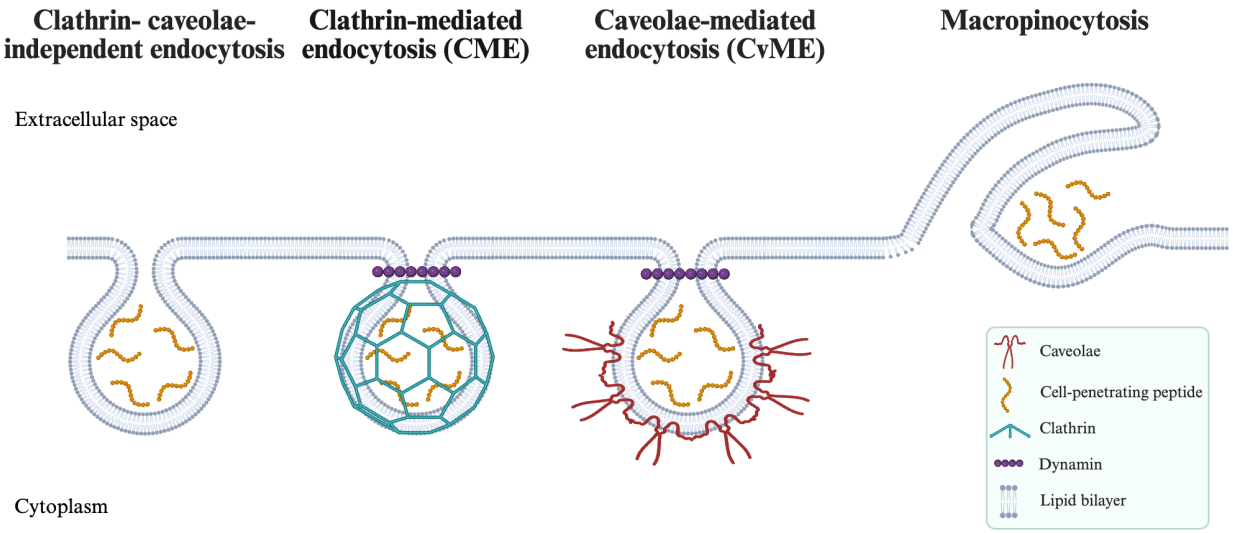

Figure 3. *Endocytic pathways involved in the internalization of CPPs into the cell.*

The specific mechanism employed can depend on three factors: the CPP (e.g., properties and/or concentration), the cargo characteristics, and the membrane composition. For instance, penetratin, TAT, and Arg9 use endocytic mechanisms, primarily including macropinocytosis, CME and CvME[100]. In fact, endocytosis may be responsible for the majority of CPP internalization, but direct penetration does also occur at high peptide concentration[101]. Nonetheless, penetratin is an exception to this rule, since it crosses the membrane in an energy-independent manner at low concentration but uses endocytosis at higher concentrations[102]. Therefore, the mechanism and even the extent to which they use each mechanism can also vary depending on the CPP involved[100], as amphipathic CPPs can occur preferentially through the more dynamic membrane regions, whereas arginine-rich CPP largely depend on proteins present in membrane surface[103–106].

1.2.4. Applications

CPPs have broad and versatile applications in biomedical research and therapy due to their unique ability to transport various cargoes across cell membranes. A primary use is in drug delivery, where CPPs facilitate the intracellular transport of small molecule drugs, peptides, proteins, and nucleic acids. Consequently, CPPs enhance the efficacy and increase the cellular uptake, which is especially useful for molecules that typically cannot cross membranes efficiently by themselves[79].

In gene therapy, CPPs offer a non-viral means of delivering genetic materials for the treatment of inherited disorders, and they are continually explored as safer alternatives to viral vectors due to reduced immunogenicity[107–109]. CPPs also have a prominent role in cancer therapy, enabling targeted delivery of chemotherapeutics and biologics, minimizing systemic toxicity, overcoming multidrug resistance, and even acting as tumour-targeted imaging agents[71].

Moreover, CPPs are being studied for vaccine development in order to improve cellular uptake, processing and presentation of exogenous antigens to induce more potent immune responses[110]. Additional applications involve treating inflammatory conditions (e.g., through transdermal delivery), antimicrobial therapy, and use in advanced nanocarrier systems, such as liposomes, nanoparticles, dendrimers, and exosomes, to further improve targeting and therapeutic outcomes[79].

Furthermore, several CPPs can be used as based therapeutics or diagnostic agents. For instance, CPP p28 can bind to a DNA binding domain, leading to inhibit cancer cell proliferation, or fluorescent-tagged CPPs to differentiate tumorous cells during surgery and resulting in improved precision of tumour resection[111,112].

1.2.5. Challenges

While CPPs offer great promise as delivery vehicles, they also have some significant drawbacks and limitations that hinder their clinical and research applications. A primary concern is their lack of target specificity, since most CPPs can penetrate almost any cell type without distinction. This non-selectivity can result in off-target effects and toxicity to healthy tissues, which is particularly problematic in applications such as cancer therapy where precise delivery is crucial. Efforts to enhance specificity, such as conjugation with targeting ligands, remain an active area of research but are not yet fully resolved[79].

Another major issue is cytotoxicity at high concentrations. CPPs, especially cationic and amphipathic varieties, may disrupt cell membrane integrity at higher concentrations, leading to dose-dependent cellular damage or immune responses. This issue can be related to the AMP mechanism, with CPP-like or membrane-leakage mechanisms at low or high concentrations, respectively, suggesting a tight relation between two types of MAPs. To overcome this limitation, CPPs can be administered subcutaneously, which reduces the immune response[113], or incorporate a compound to reduce the cytotoxicity[114].

Additionally, CPPs are susceptible to rapid enzymatic degradation by proteases present in serum and tissues, resulting in poor *in vivo* stability and short plasma half-life. Strategies mentioned above to enhance their properties, such as structural modifications, cyclization, and PEGylation can improve stability but may simultaneously reduce membrane penetration or introduce new immunogenicity concerns[115].

CPPs often face challenges related to intracellular trafficking. A substantial proportion of CPP-cargo complexes can become entrapped and subsequently degraded in endosomal or lysosomal compartments, limiting cytoplasmic delivery of therapeutic payloads. While modifications or adjuvants to enhance endosomal escape are being developed, these can increase overall toxicity[116].

Additional limitations include difficulties in large-scale production, high cost, and the need for extensive toxicological evaluation for each new CPP or CPP-cargo combination[117]. Besides, analytical detection of CPPs at low concentrations in biological samples is also technically challenging and can increase the cost of the process[115].

Despite decades of research on CPPs and MAPs, their translation into robust clinical or biotechnological applications remains limited. Early studies revealed their remarkable ability to traverse or disrupt biological membranes, highlighting their potential as antimicrobial agents, drug delivery vectors, and therapeutic modulators. However, practical implementation has been hindered by several challenges, including limited stability and specificity, cytotoxicity at elevated concentrations, and an incomplete mechanistic understanding of peptide-membrane interactions. These limitations emphasize the need for deeper molecular-level insight and rational design strategies. By elucidating the physicochemical determinants of these interactions, it becomes possible to identify sequence and structural features that enhance selectivity, efficacy, and stability, ultimately guiding the development of more effective CPPs and MAPs for biomedical applications.

Collectively, these issues underscore the necessity of sustained optimization and careful design in the development of CPP-based delivery systems. The objective is to engineer CPPs characterized by reduced cytotoxicity, enhanced delivery efficiency, and high target specificity. Beyond their direct biomedical applications, understanding CPPs is also crucial for elucidating fundamental physiological and pathophysiological processes, as cells naturally harbour numerous peptide sequences with CPP-like properties[118]. Gaining a comprehensive understanding of CPP internalization mechanisms therefore not only advances the fields of targeted therapies, precision medicine, and molecular diagnostics but also enriches our broader understanding of core cellular processes. Continued research in this area is essential to overcome current barriers and realize the full clinical and biological potential of CPPs.

1.3. Dynorphins

Another group of BPs are opioid peptides[28], such as dynorphins. Dynorphins are one of the most positively charged peptides in our body[119], and are an important family of endogenous opioid peptides. Dynorphins are derived from the larger prodynorphin (PDYN) precursor[120], which is cleaved at positively residues yielding Big Dynorphin (BigDyn, 32 residues). BigDyn is further processed by cutting the K-R hinge region, resulting in Dynorphin A (DynA, 1-17 residues), and Dynorphin B (DynB, 20-32) peptides[121,122]. Dynorphins serve as principal agonists for κ-opioid receptors (KOR) and μ-opioid receptor (MOR) (Figure 8), contributing to analgesia, stress responses, and addiction behaviours[123].

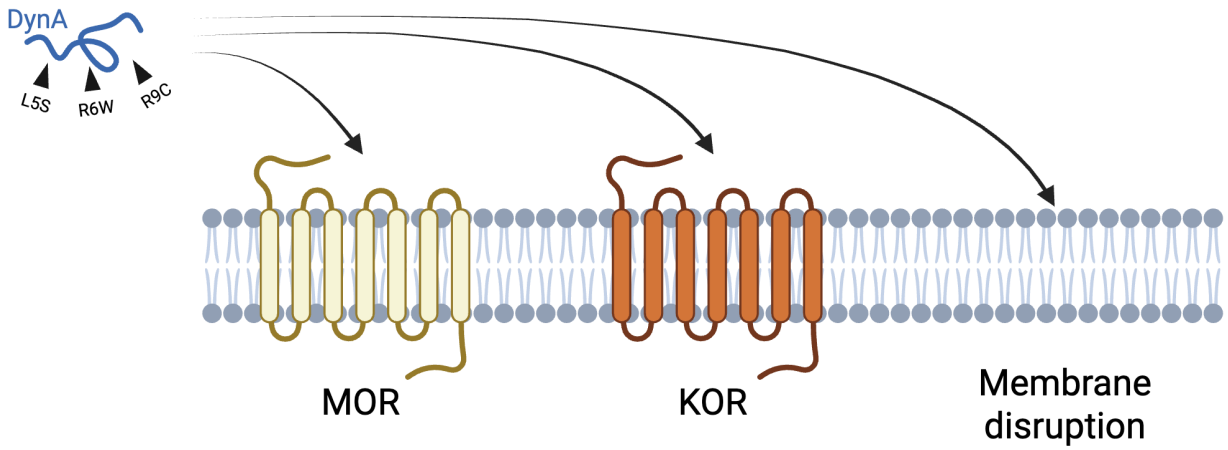

Figure 4. *Mechanisms for DynA interaction with the membrane.*

Besides, several studies have revealed that DynA possesses a second, less classical mode of activity: the disruption of lipid membranes through direct peptide–lipid interactions that occur independently of receptor activation[124–128]. These non-opioid effects have been implicated in the pathogenesis of neurological disorders such as spinocerebellar ataxia (SCA23)[129,130]. Importantly, mutations in the PDYN gene are directly associated with SCA23 and result in altered peptide properties[126,131,132]. Hence, DynA can suffer three coding mutations, which result in four clinically relevant DynA variants: the wild type (WT) peptide, L5S (serine-to-leucine substitution at position 5), R6W (arginine-to-tryptophan substitution at position 6), and R9C (arginine-to-cysteine substitution at position 9).

Research indicates that DynA and its clinical variants interact differently with membrane based on lipid composition, on peptide structure and function. DynA exhibits CPP-like behaviour, capable of translocating across plasma membranes[124,133]. In neutral membranes, DynA can form ion channel-like pores and exhibit direct translocation, distinct from its behaviour in charged membranes[128]. Specifically, DynA and BigDyn induce calcium leakage from negatively charged phospholipid vesicles, suggesting DynA–mediated membrane perturbation[125,126,134]. The R6W clinical variant is associated with increased neurotoxicity and resistance to degradation, shows a stronger tendency to insert into lipid bilayers and forms more stable pores in neutral and negatively charged membranes compared to WT[131,135]. Further, R6W and R9C demonstrate increased degradation resistance, potentially contributing to their heightened toxicity[132,135]. Experimentally, DynA L5S is the peptide that has been found to have the least membrane disruption and increased degradation, correlating with lower neurotoxicity[131,135].

In this thesis also focuses on the computational study of dynorphins, a subset of endogenous BPs with strong potential for redesign into CPPs or AMPs with therapeutical potential. We aim to investigate the interactions of dynorphins with lipid bilayers using the same techniques as presented for CPPs, characterizing the impact of membrane composition and single-point mutations on DynA's effect.

1.4. Computational techniques

Experimental techniques such as spectroscopy, microscopy, and biochemical assays provide valuable insights into the structure, behaviour, and membrane interactions of CPPs[136,137]. Yet, these methods can be limited in their ability to capture atomic-level details or fully resolve the dynamic processes underlying CPP–membrane interactions. Computational techniques address these challenges by enabling atomic-level resolution investigation of CPP structure, dynamics, and interactions with membranes. Through molecular simulations, researchers can rationally design CPPs with improved efficiency and selectivity, advancing the development of targeted drug delivery systems, particularly for intracellular applications. In this way, computational tools complement experimental studies, offering predictive insights and guiding hypothesis-driven research in CPP-based therapeutics.

Here, we focus on the use of molecular dynamics (MD) simulations[138,139] to explore how CPPs adopt specific conformations, interact with lipid bilayers, and respond to changes in environment or sequence modifications. MD simulations make use of Newton's equations of motion and the use of force fields (a set of equations and parameters) to calculate the movement of atoms and molecules over time. Thus, a trajectory that describes the movement of all the atoms in the system is generated.

In this field, MD simulations can be used to study the peptide interaction with the membrane. However, the process of translocation takes from seconds to minutes and is, therefore, unfeasible to observe in a conventional molecular dynamics (cMD) study, which is currently limited to the microsecond scale due to hardware constraints[140]. Therefore, different strategies including enhanced sampling techniques have been presented in order to study CPP interaction and translocation (Figure 9).

First, steered molecular dynamics (SMD) applies an external force (or *steering potential*) to a group of atoms to move them along a specified path. In this case, SMD is used to accelerate the movement of the peptide across the membrane, while allowing to compute the cost of translocation or potential of mean force (PMF)[140,141]. However, a long path can lead to large errors and several trajectories largely deviating from the original path. Therefore, adaptive steered molecular dynamics (aSMD)[142,143] was presented as a modification of SMD that offers greater efficiency for

systems in which the group of atoms is dragged through a long non-linear path. In aSMD, the steering path is divided in several steps, with multiple replicas run at each step. From these, the trajectory that remains closest to the predefined path is selected and used as the starting point for the next step. This iterative procedure ultimately enables PMF calculation[143]. This technique allows for the calculation of PMF in longer paths while reducing statistical error and noise through the use of replicas.

Second, metadynamics (MetD) enables the reconstruction of the free energy surface using a limited number of collective variables (CVs)[144,145]. This is achieved by guiding the system to avoid previously explored regions and to sample the unfavourable areas of the free energy landscape through a history-dependent bias potential along the CVs.

Third, umbrella sampling (US) divides the reaction coordinate (here, the peptide path to translocation) into overlapping windows, each restrained by a biasing potential to force the system to sample even high-energy regions [146]. US approach also yields accurate PMF calculations.

Fourth, replica exchange molecular dynamics (REMD) is a method that runs multiple replicas of the same system simultaneously, with occasional exchanges between replicas which allows to overcome high-energy barriers[147]. REMD is typically not used directly for PMF calculations but can be combined with US (RE+US) to increase sampling of a US simulation[148].

In addition, weighted ensemble (WE)[149,150] method partitions the configuration space into bins and runs many parallel simulations with assigned statistical weights to enhance sampling of rare events. WE method splits those steps that reach important regions (the ones where the peptide reaches deep within the membrane) and merges the others. This way, it efficiently explores the pathways and kinetics of rare but important transitions.

Other techniques explore the use of alternative options to facilitate peptide translocation. For instance, high-temperature MD (HT-MD) entails the simulation of systems at increased temperature, which speeds up the kinetics and allows larger membrane disruption[151]. Another possibility is to increase the membrane tension (hereafter referred to as MT-MD), which increases permeability and also leads to increased membrane disruption[31,152].

Furthermore, coarse-grained molecular dynamics (CG-MD) techniques have been used, for instance, to study linear and cyclic Arg9[153]. CG-MD simulations[154] reduce the system resolution

by grouping atoms into larger beads, sacrificing atomic detail for greatly enhanced computational efficiency and access to longer timescales and system sizes. Then, CG-MD can be run for longer timescales, although the observation of translocation is not guaranteed. Thus, CG-MD has been coupled with other techniques such as US or SMD to further increase sampling of the system[155,156].

An alternative approach is the utilization of an implicit membrane model (IMM), which strives to account for the influence of lipids and water through the solvation-free energy term in the energy function. This approach offers several advantages, including rapid speed, rapid equilibrium, and extensive exploration of configurational space. Lazaridis et al. developed IMM1, a method that can be used to determine the minimum energy pathway and the energy of the CPP transition states throughout the membrane[157]. In this method, the peptide is positioned at various depths within the membrane and oriented at different angles, after which short MD simulations are performed to enable PMF calculation.

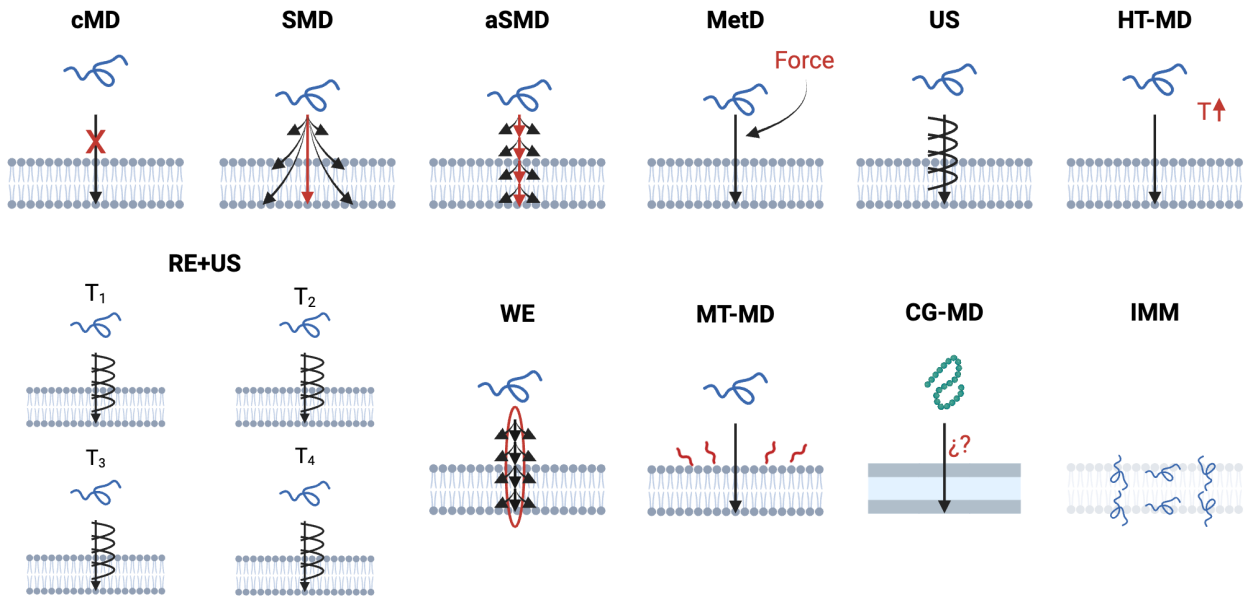

Figure 5. *Summary of the computational techniques used in CPP translocation study. Membrane in the IMM model is shown more transparent to indicate the use of an implicit membrane, while in the CG-MD model it is represented differently to indicate a coarse-grained membrane.*

However, all these techniques have inherent limitations (Table 1). For instance, in SMD or US, an external bias is applied to drive peptide translocation across the bilayer, making them primarily suited for PMF calculation. CG-MD approaches offer reduced resolution, and peptide insertion or translocation is not guaranteed, whereas IMM1 is restricted to α-helical secondary structure, and

peptide–membrane interactions cannot be explicitly observed. Moreover, HT-MD assumes that the force fields are still valid at high temperatures, and MT-MD applies non-physiological tension to the membrane. Last, the WE method strongly depends on the selection of reaction coordinates. Furthermore, most of these techniques are not ideal entry-level options, as they require prior expertise, particularly in defining reaction coordinates, and are computationally demanding.

Table 1. *Summary of the characteristics of the computational techniques used in CPP study.*

Technique	Resolution	PMF calculation[1]	Peptide translocation	Entry-level	Computational requirements
cMD	Atomic	No	No	Yes	Low
SMD	Atomic	Yes	Yes	No	Moderate
aSMD	Atomic	Yes	Yes	No	Intensive
MetD	Atomic	Yes	Yes	No	Moderate
US	Atomic	Yes	Yes	No	Intensive
HT-MD	Atomic	No	Yes	Yes	Moderate
RE + US	Atomic	Yes	Yes	No	Intensive
WE	Atomic	Yes	Yes	No	Intensive
MT-MD	Atomic	No	Yes	No	Moderate
CG	Beads	No	Yes/No	No	Low
IMM	Atomic, but without membrane and waters	Yes	No	No	Low

[1]Even though the technique does not allow for PMF calculation, they can be combined with techniques that do so.

Therefore, this thesis is intended to present new tools that can be used for the study of CPPs, and MAPs in general, while overcoming the limitations of the already available methods.

In the first chapter, a new method is presented, which combines aSMD with cMD. Here, we conduct the study with three canonical CPPs in three different membrane compositions.

In the second chapter, another method, computational electrophysiology (CompEL) is repurposed to be used in CPPs and MAPs field. In this case, the experiments are conducted with five peptides, four CPPs and one non-CPP, in one membrane composition.

In the third chapter, CompEL is expanded to different membrane compositions, and the study is limited to one peptide to reduce the computational time requirement.

In the fourth chapter, the technique presented in the first chapter, aSMD in combination with cMD, is used in the study of DynA and its clinical variants, to discuss the CPP-behaviour of each peptide.

Objectives

2. OBJECTIVES

The main objective of this thesis is to expand the range of computational tools available for studying peptide–membrane interactions, particularly for CPPs and MAPs. We intend to describe the principal interactions that dictate peptide partitioning, insertion, and translocation. Secondly, we apply the computational tools that we have presented in the case study of dynorphins, peptides that have presented potential for use as CPPs or AMPs.

We differentiate between the general and specific objectives.

The general objectives of this thesis are:

1. Expand the range of computational tools for studying peptide–membrane interactions, with a focus on CPP-mediated membrane disruption, using MD simulations to provide atomistic insights.
2. Elucidate the processes of peptide partitioning, insertion, and translocation across model membranes.
3. Establish a standardized, entry-level computational approach for investigating CPP–mediated membrane disruption that is broadly applicable to peptide–membrane interaction studies.
4. Extend computational methods to study dynorphin A and its clinical variants, characterizing their membrane interactions and comparing computational results with experimental data.

Besides, the specific objectives are:

1. Investigate the role of protein–lipid interactions in CPP internalization, including how specific amino acid residues affect partitioning, insertion, passage through the hydrophobic core, and inner leaflet interactions facilitating translocation.
2. Quantify peptide–membrane interactions using structural and dynamic descriptors such as peptide orientation, secondary structure, pore formation probability and extent, and rate of peptide–lipid contact events, to create a comparative framework for CPPs, dynorphins, and MAPs.

3. Assess how membrane composition (e.g., cholesterol-rich or negatively charged membranes) influences peptide internalization, free-energy cost of translocation (PMF), and likelihood of specific molecular interactions.
4. Examine how peptide-to-lipid (P:L) ratio affects membrane perturbation, aggregation behaviour, cooperative effects, and the free-energy profile of translocation.
5. Evaluate whether the computational methodologies can be generalized to other biologically relevant peptides, such as AMPs, to broaden applicability to MAPs and membrane–interacting biomolecules.

Results

3. RESULTS

3.1. Chapter I: computational insights into membrane disruption by cell penetrating peptides using adaptive steered molecular dynamics in combination with conventional molecular dynamics

In this chapter, we present aSMD in combination with cMD to study peptide-membrane interactions. Here, we use aSMD in combination with cMD to study general objectives 1, 2, 3, and specific objectives 1, 2, 3, 4.

3.1.1. Introduction

The lipid fraction of biological membranes is mostly composed of phospholipids, which accounts for selective permeation, such as the cell membrane, a highly selective and dynamic barrier that encloses the contents of all living cells, responsible for cellular structural integrity, and intra- and extracellular homeostasis. Cell-penetrating peptides (CPPs) are small peptides that can be found in nature and are capable of efficiently crossing the cell membrane. CPPs optimal and efficient design to transport cargo molecules into the cell is of paramount importance[30,158]. CPPs have emerged as powerful tools with promising outcomes in fields such as drug delivery[159], diagnosis of diseases [160], and therapeutics[161]. For instance, CPPs have been used as therapeutic agents targeting specific cell types[162], or coupled with anticancer molecules targeting tumour tissue, while healthy tissue remains unharmed[163–165].

CPPs translocate across cellular membranes via diverse mechanisms that can be classified into energy-independent and energy-dependent pathways[166]. Energy-dependent translocation involves three types of endocytosis, namely macropinocytosis, caveolae-mediated, and clathrin-mediated endocytosis[167]. Energy-independent penetration includes the pore formation[168], the carpet-like model (through membrane destabilization without pore formation)[92], the membrane thinning model[169], and inverted micelle formation[170]. However, direct validation of these energy-independent models has only been obtained for inverted micelles[171], and the other translocation methods have not yet been completely described.

Based on their physicochemical properties, CPPs have been classified[172] into cationic, such as nona-arginine (Arg9)[53]; hydrophobic, such as Kaposi fibroblast growth factor (K-FGF)[65] or Translocating peptide 2 (TP2)[54]; and amphipathic, such as Transportan 10 (TP10)[58] or model amphipathic peptides (MAP), a group of peptides derived from the α-helical amphipathic model peptide, designed in 1991, and here referred to as MAP[30,57]. Besides, amphipathic CPPs can be further divided as primary amphipathic (defined by their hydrophobic domains), secondary amphipathic (forming α-helices with one hydrophilic and one hydrophobic faces), β-sheet (that have a hydrophobic stretch and a hydrophilic stretch), proline-rich, and histidine-rich[54,173]. Therapeutic applications of these CPPs include its use in drug delivery, anticancer or anti-inflammatory treatments, among others[65,174–178]. Nonetheless, CPPs encounter limitations such as instability, since they are prone to proteolytic degradation; lack of selectivity, which could provoke

toxicity or side effects and limited efficacy, given that some CPPs only show powerful penetrating activity at high micromolar concentrations (> 10 μM)[179]. From the computational perspective, translocation of any CPP is a relatively slow process and computationally too demanding to be observed in a conventional molecular dynamics (cMD) simulation[180]. In this study, we examine the membrane disruption potential as an early step of the internalization process. We use adaptive steered molecular dynamics (aSMD) by applying an external potential followed by cMD to assess whether an equilibrium has been reached (i.e. the CPPs have overcome the bilayer energy barrier to cross) or not, as well as to analyse the bilayer-peptide interactions of CPPs. In order to represent the main three blocks, we decided to study a cationic CPP (Arg9), a hydrophobic CPP (TP2), and an amphipathic CPP (MAP).

3.1.2. Computational methods

3.1.2.1.Systems preparation

Peptides were initially modelled with ColabFold notebook[181], using AlphaFold[182] model for monomer prediction, and were relaxed in an explicit solvent system at 310.15 K. AMBER20 program was used to perform the simulations[183]. The AMBER ff14SB[184] force field and periodic boundary conditions were applied, and the SHAKE algorithm[185] was used to restrain the hydrogen atoms, allowing for a 2 fs timestep. Besides, the Monte Carlo method was used to add 150 mM KCl ions and water TIP3P molecules to solvate the system. A short minimization (5,000 cycles) and NVT equilibration (125 ps) were run with a restraint force of 1 $kcal \cdot mol^{-1} \cdot Å^{-2}$ on the peptide, before the unrestrained cMD simulation of 100 ns.

A peptide-bilayer system was built in CHARMM-GUI[186–192] for each relaxed peptide and membrane composition combination, amounting for a total of 12 systems (3 control membranes, without peptide, 1 for each bilayer, plus 9 peptide systems: 3 membrane compositions for 3 peptides). Here, a single peptide was placed at approximately 10 Å from the centre of mass (COM) of the upper leaflet bilayer membrane. The N-terminus or C-terminus of the peptides were not modified at any extent.

Three symmetric membrane compositions were defined. Firstly, one constituted of 1,2-Dipalmitoyl phosphatidylcholine (DPPC), a neutral, simple bilayer model commonly used in biophysical studies. Besides, it has been used in previous CPPs studies[142] and can be used to

compare the results obtained. Secondly, following the same study[142], we also used a more complex membrane, namely DPPC:DOPC:CHOL -where DOPC stands for Dioleoyl phosphatidylcholine and CHOL for cholesterol-, with the addition of cholesterol and a lipid with an unsaturated tail. Thirdly, we expanded the study of CPP behaviour by adding negatively-charged lipids, that is, DPPC:DOPC:DPPS:DOPS:CHOL membrane –where DPPS stands for Dipalmitoyl phosphatidylserine and DOPS for Dioleoyl phosphatidylserine–. To avoid bias, the molar ratio of lipids was kept balanced in the 2 heterogeneous bilayer systems. Moreover, to avoid membrane deformation artifacts in this pulling experiment, we used 150 lipids per leaflet which, according to Hub *et al.*[193–195], prevents such artifacts since the bilayers are large enough. The exact composition of each membrane is the following: DPPC (150 DPPC lipids); DPPC:DOPC:CHOL (50:50:50 lipids, respectively); DPPC:DOPC:DPPS:DOPS:CHOL (30:30:30:30:30 lipids, respectively). The same conditions as in the peptide relaxing simulations were used. For the membrane lipids, the Amber Lipid21[196] force field was selected.

Thereafter, the systems were energy minimized for 5,000 steps and equilibrated during 3.5 ns, starting in the NVT ensemble with positional restraints on the membrane atoms (restraint force of 2.5 kcal·mol^{-1}·Å^{-2}), and changing to the NPT ensemble after 500 ps while lowering the positional restraints on the membrane throughout the NPT equilibration procedure (1, 0.5, 0.2, and 0 kcal·mol^{-1}·Å^{-2}, respectively). Lastly, the membrane was relaxed for 100 ns of conventional molecular dynamics. During this step the peptide was kept restrained to avoid peptide-membrane interaction and allow for an unperturbed membrane relaxation (restraint force of 10 kcal·mol^{-1}·Å^{-2}).

3.1.2.2.Adaptive steered molecular dynamics (aSMD)

Peptide translocation is a procedure computationally too expensive to observe in a conventional molecular dynamics simulation, as it commonly occurs in the scale of seconds to minutes[180]. Consequently, we accelerated that process by using steered molecular dynamics (SMD)[197]. SMD is a molecular dynamics enhanced sampling method where an external potential is applied to accelerate the movement of a specific group of atoms -in this case, the peptide- along a defined set of coordinates. The *z* direction -the membrane normal direction- was defined as the pulling coordinate of the peptide. The reaction coordinate was defined as the distance between the COM of the carbon alpha (CA) residues of the peptide and the COM of the lipids' polar head in the lower

part of the bilayer, namely phosphate, nitrogen, oxygen, and the three main carbon atoms of this group.

In SMD simulations, many simulations must be run to achieve convergence of the potential of mean force (PMF). Adaptive steered molecular dynamics (aSMD)[143,198] was introduced to alleviate this problem. In aSMD, the reaction coordinate -here, the distance between the COM of peptide's CA atoms and membrane lower leaflets polar head's COM-, is divided in different steps. Then, separate SMD simulations are performed in each of these stages. In this case, the membrane length (ca. 40 Å) was divided in 8 stages of 5 Å and 25 replicas were run for each step (with a constant force of 10 kcal·mol^{-1}), thus using aSMD, as utilized in previous studies[142,199–201]. Briefly, after each step, the Jarzynski average[141,202,203] across all replicas was calculated, and the last frame of the closest replica was used as input for the following step. Each aSMD step was run at 1 Å per ns (5 ns per replica), discussed below. An aSMD step totalled 125 ns per step and 1,000 ns per aSMD simulation. Altogether, ~9 μs were run for the aSMD simulations of all 3 peptides.

To calibrate the system for aSMD and to determine that the membrane bilayer systems were comparable in terms of energy barrier, we performed a set of forward-backward simulations in all three bilayer systems using a single Arg residue (Arg1, Figure 10A).

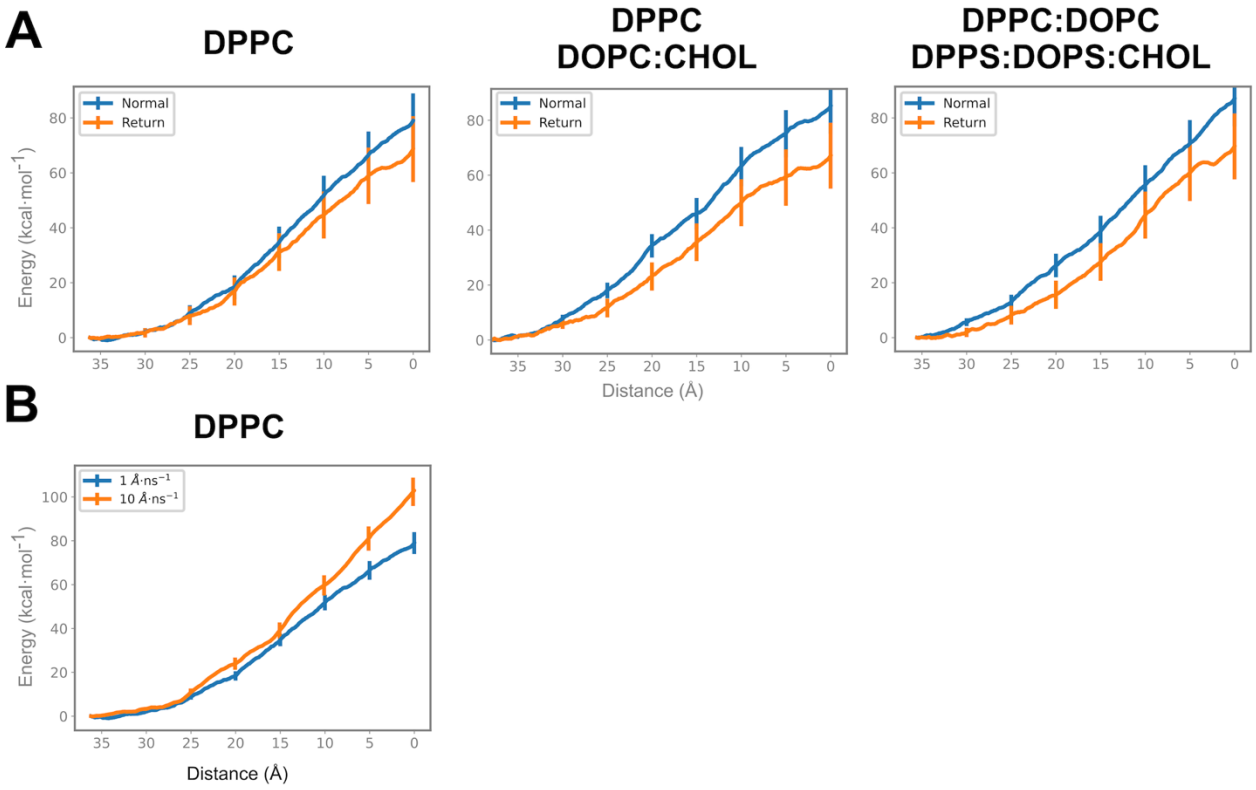

Figure 6. *PMF calculation in (A) forward and backward aSMD simulations and (B) different pulling speed simulations. (A) PMF has been calculated forwards (normal, blue) and backwards (return, orange) to calibrate the system and test that the bilayers' energy barriers were comparable. The effect of normal and return aSMD has been computed for the three membrane compositions. (B) To test the best pulling velocity, aSMD has been simulated at two different speeds: 10 Å/ns (orange) and 1 Å/ns (blue). The effect of pulling speed has been done in DPPC membrane.*

The reaction coordinate used was the same as in previously described aSMD simulations (distance between COM of the peptide's CA atom and COM of the lipids' polar head in the lower part of the bilayer). Forward and backward PMF values for Arg1 are within the same energy interval, thus the model membranes are valid to be used in this study. It is important to state that the higher heterogenicity in the bilayer composition, the higher the differences in the elastic/viscoelastic behaviour in the forward/backward pathways, as happens in real biological systems. In parallel, in order to choose the pulling velocity, the aSMD simulations were performed at different pulling speeds. Park and Schulten studied SMD with two pulling velocities: 100 Å/ns and 10 Å/ns. Since they concluded that the lower the pulling velocity, the more accurate the PMF calculation[141,204], we decided to use 10 Å/ns. Besides, we compared it to the velocity used in more recent studies[142,205], 1 Å/ns. Therefore, the pulling speeds chosen are 10 Å/ns and 1 Å/ns (Figure 10B). The results show that with a slower velocity, the lipids had more time to adjust, leading to a lower

and more accurate PMF[141,204]. Consequently, we decided to use the slowest pulling speed (1 Å/ns) for subsequent simulations.

3.1.2.3.PMF calculation

The Potential of the Mean Force is computed by employing the Jarzynski equality[203]. The Jarzynski equality is a powerful relationship that connects the non-equilibrium work performed during SMD simulations to the free energy difference between two states (A and B), as seen in Equation 1:

$$G_B = G_A - \frac{1}{\beta}\ln\langle e^{-\beta W_{A\to B}}\rangle_A$$

where β is the Boltzmann constant multiplied by the temperature ($k_B \cdot T$) and the tangled brackets indicate averaging over multiple trajectories.

In this study, after each aSMD step, the replica with the closest work value to the Jarzynski average was selected as the starting point for the next simulation step. This approach helps remove the trajectories that minimally contribute to the overall PMF and significantly reduces the number of simulations required for convergence[183].

3.1.2.4.Conventional molecular dynamics (cMD)

Lastly, starting from the last frame of the aSMD simulation last step (where the distance between peptide and lower leaflet COMs is 0 Å), a 100 ns of unbiased cMD (also referred to as *relaxation step*) was run with the purpose of allowing the system to relax after an external potential addition. The same simulating conditions were used as in the previous cases. A total of ~3 μs were run for the final relaxation part, accounting for 100 ns for each of the simulations (100 ns x 3 peptides x 3 membrane compositions x 3 replicas). Besides, the 3 control systems (without peptide) were run following the same equilibration and production protocol.

3.1.2.5.Data analysis

Trajectory visual analysis was performed with Visual Molecular Dynamics (VMD)[206], CPPTraj and PyTraj[207]. PyLipID[208] and LiPyPhilic[209–212] were used to analyse the simulations. An in-house script was used to analyse lipid order parameter. Lipid order parameter, typically denoted as S_{CD},

measures the orientation of the C-D bond in lipid acyl chains relative to the bilayer normal[213]. It is calculated using Equation 2:

$$S_{CD} = \langle \frac{3\cos^2\theta - 1}{2} \rangle$$

Where θ is the (time dependent) angle between the C-D bond and a reference axis. The angular brackets represent an ensemble average over time and lipid molecules. Lipid order parameter value of -0.5 indicates a perfectly ordered acyl chain[214]. Per convention, $-S_{CD}$ is plotted, so values closer to 0.5 indicate aligning respect to the bilayer normal[215]. An in-house Python script was implemented to compute the pore size distribution, calculating the minimum pore size in the z axis of the membrane. This script calculates the maximum distance of the water residues per each membrane z-stack and outputs the minimum distance of all the z-stacks per each simulation frame. Matplotlib[216] and Seaborn[217] were used for graphics plotting, and UCSF ChimeraX[218,219] for molecular graphics. For the membrane analyses, only the last 80 ns of the cMD simulation were taken into account.

For benchmarking purposes, all simulations and analysis have been performed in a single GPU-based (RTX-3080Ti) workstation, running at an average of 80 ns/day accounting for a total of 150 days of computation time.

3.1.3. Results

3.1.3.1. Bilayer resistance to steered peptide crossing

The simulation protocol includes two sets of simulations: aSMD for 40 ns divided in 8 steps and 25 replicas per step to move the peptide across the bilayer defining a non-equilibrium state, followed by 3 replicas of the relaxation step, consisting of 100 ns of cMD each. This experimental design was applied to investigate the behaviour of 3 canonical CPPs (Arg9, MAP, and TP2, see Table 2) in 3 different membranes (Figure 11A). GRAVY score is calculated using the Kite-Doolittle scale[220].

Table 2. *Characteristics of the peptides used in this study.*

Peptide	Length	Sequence	Type	Net charge	GRAVY score
Arg9	9	RRRRRRRRR	Cationic	+9	-4.5
MAP	18	KLALKLALKALKAALKLA	Amphipathic	+5	0.99
TP10	21	AGYLLGKINLKALAALAKKIL	Amphipathic	+4	0.93
TP2	13	PLIYLRLLRGQWC	Hydrophobic	+2	0.42
K-FGF	17	AAVALLPAVLLALLAP	Hydrophobic	0	2.42

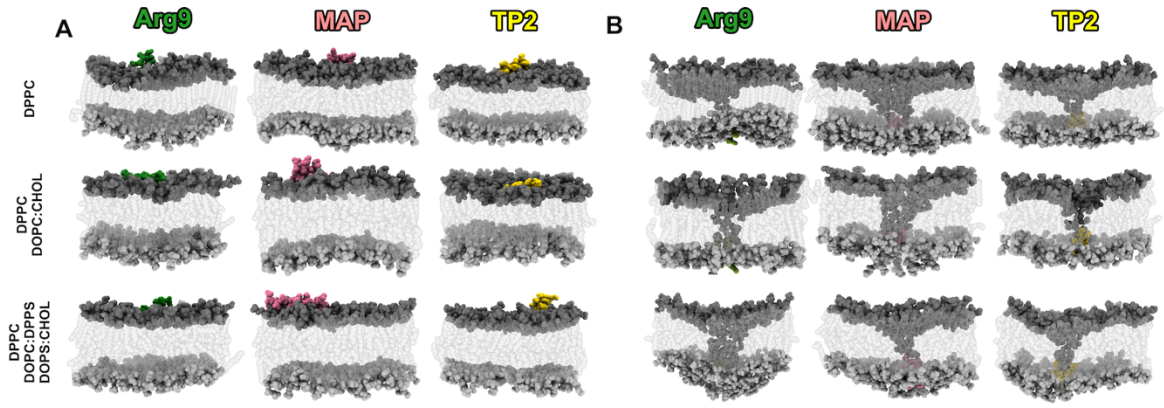

Figure 7. *Initial and final snapshots of the aSMD process. Starting (A) and final (B) snapshots of the aSMD for the three CPPs and the three membrane compositions.*

As a simplification of a complex cellular bilayer, a CPP, when internalizing into the cell, first encounters the extracellular leaflet, rich in neutral polar headgroups, which can be related to the DPPC system. Secondly, the CPP enters in contact with the hydrophobic core of the bilayer, with cholesterol and unsaturated lipid tails, as in the DPPC:DOPC:CHOL system. Thirdly, the CPP needs to break the interaction with the hydrophobic core and interact with the intracellular leaflet, richer in negatively charged polar headgroups, as in the DPPC:DOPC:DPPS:DOPS:CHOL system.

In short, we have modelled simplified systems for each bilayer phase, being DPPC system the equivalent to the extracellular leaflet, DPPC:DOPC:CHOL to the hydrophobic core, and DPPC:DOPC:DPPS:DOPS:CHOL to the intracellular leaflet, respectively.

After the aSMD simulation, the molecular distribution is similar for all cases (Figure 11B): the peptide has been steered into the lower part of the bilayer and is in contact with the polar heads of the lipids in the lower part of the bilayer. Some polar heads of the upper leaflet have been dragged along with the peptide during the steering process, in agreement with the previously described "Defect Assisted by Charge" (DAC) phenomenon[221], and the polar heads of the upper bilayer contact those of the lower bilayer. As seen in Figure 11B, on average, MAP causes the highest and TP2 the lowest membrane disturbance (DAC). This means that the DAC caused is related, but not directly proportional, to the peptide charge, as discussed by Elber[221]. The author stated that, when working with a CPP, there is a higher number of degrees of freedom, and charge plays a lesser role. Conversely, for small molecules, charge plays an important part in the DAC created. Besides, for CPPs, the peptide length seems to be an important aspect, since MAP (18 residues, net charge +5) produces more DAC than Arg9 (9 residues, net charge +9) even though it has smaller net charge.

PMF values are indicative of the resistance opposed by the bilayer during the peptide crossing, showing that bilayer complexity is, on average, positively correlated with higher PMF values (Figure 12). In the DPPC membrane, peptides exhibit, on average, the lowest energy requirement to traverse the bilayer, indicated by a mean PMF barrier of 181.52 ± 20.33 kcal·mol^{-1}. The introduction of cholesterol to the membrane results in an overall increase in the mean PMF barrier to 200.91 ± 13.87 kcal·mol^{-1}. Cholesterol has been associated with reduced efficiency in CPP translocation, a phenomenon previously discussed by Pae *et al.* [102]. Addition of unsaturated fatty acids (DOPC) should enhance the internalization of CPPs and lower the PMF[100], but this effect seems to be counterbalanced by the influence of cholesterol. Finally, in the DPPC:DOPC:DPPS:DOPS:CHOL membrane, we observe the highest resistance to bilayer crossing, with a mean PMF barrier of 225.65 ± 17.40 kcal·mol^{-1}. This PMF increase can be related to the effect of increased adsorption in the upper leaflet when negative lipids are present[222], requiring higher energy to break these lipid-peptide interactions.

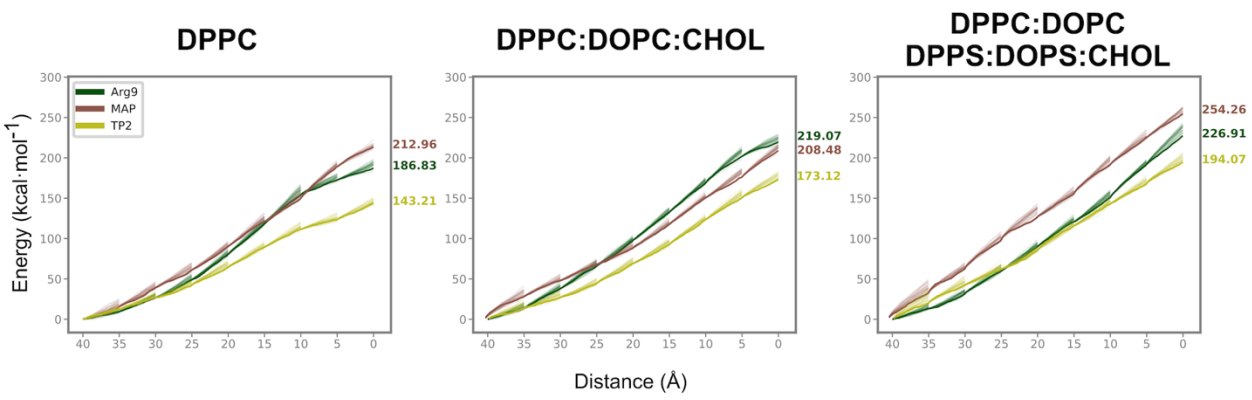

Figure 8. *PMF barrier of peptides with respect to the membrane composition. The values indicated correspond to the last value (highest energy) of the PMF analysis. PMF profiles of the three membrane compositions are shown. PMF profiles of all replicas are shown with a transparency of 10%.*

Arg9 in DPPC and in DPPC:DOPC:CHOL shows a similar PMF value (~190 kcal·mol^{-1}, and ~220 kcal·mol^{-1}, respectively, as seen in Figure 12) to previously published data[142]. Besides, the energy required to move Arg9 into the middle of the DPPC membrane (from 40 to 20 Å) is similar to the energy obtained in a previous study using neutral lipids [223]. Taking into consideration all three CPPs and the three bilayer systems (Figure 12), TP2 and Arg9 partition more efficiently in the upper leaflet (DPPC) compared to MAP. The transition energy from the water-bilayer interface to the hydrophobic core (DPPC to DPPC:DOPC:CHOL) is lower for MAP and TP2, and slightly higher for Arg9. Finally, from the hydrophobic core to the lower leaflet (DPPC:DOPC:DPPS:DOPS:CHOL) all peptides require higher energy for the transition, especially MAP.

aSMD has demonstrated PMF value accuracy calculation for peptides[143,198,199,224] and the relative trends shown for the peptides studied here are qualitatively coherent and considered as a measure to compare each peptide in the three bilayer compositions. This is of paramount importance in CPPs, where sequences differ significantly in amino acid composition, secondary structure propensities, length and physicochemical properties. Thus, quantitative assessment of PMF values should be interpreted with caution. For absolute quantitative output, computationally demanding methods with higher sampling such as, multi branched aSMD (MB-ASMD), full-relaxation aSMD (FR-ASMD)[199], or adaptively biasing MD (ABMD)[142], should be considered to obtain fully converging PMF profiles[140], although the different nature among peptides should still pose a limitation.

3.1.3.2.Peptide release after aSMD

At the end of the aSMD simulations, the peptide has been successfully transferred to the lower region of the lipid bilayer. It is important to determine whether this steered process has overcome the bilayer energy barrier reaching an equilibrium state (the energy of the process has been released) or not (the energy of the process is stored in the last step of the aSMD simulation). Thus, we performed three replicas (all with the same outcome) of cMD simulations relaxing the system to compare the peptides' behaviour in each bilayer system. At this stage we observed four possible behaviours for the peptides: (1) "Lower leaflet equilibrium state": after the aSMD simulation, the peptide has reached an energy minimum and stays at the lower part of the bilayer; (2) "Pore formation": the energy stored in the process results in the peptide bouncing back towards the upper leaflet remaining in the hydrophobic core and leading to formation of pores of different radius in the membrane -we define a pore as a large defect in the membrane that allows for a continuous water flow between the upper and lower leaflets; (3) "Insertion": the energy stored in the process results in the peptide bouncing back towards the upper leaflet remaining in the hydrophobic core of the bilayer without leading to pore formation; (4) "Return": the energy stored in the process results in the peptide bouncing back to the upper part of the bilayer. For sake of clarity, a summary of these behaviours, observed across all peptides and membrane compositions, is presented in Figure 13 and Table 3.

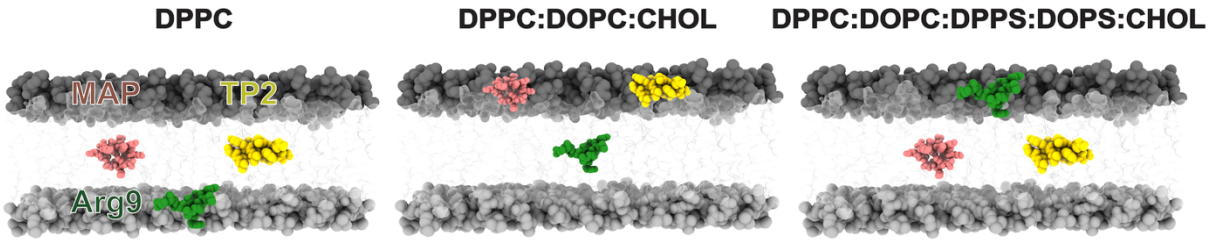

Figure 9. *Illustrative representation of the peptide location in the 3 membrane compositions after the 100 ns of conventional MD (relaxation). Peptides are coloured as: Arg9 in dark green, MAP in rose, TP2 in gold. The polar heads of phospholipids in both the upper and lower bilayers are illustrated in darker and lighter shades of grey, respectively, while the lipid tails are portrayed in transparent white. Peptide colours are maintained in the following figures. Waters are omitted for clarity.*

Table 3. *Simulation results for all CPPs in the 3 membrane compositions. All replicas show the same behaviour, and the ratios are thus omitted for clarity. See Table 4 for small or large pores details.*

Peptide	DPPC	DPPC DOPC:CHOL	DPPC:DOPC DPPS:DOPS:CHOL
Arg9	Lower leaflet equilibrium state	Large pore	Return
MAP	Small pore	Return	Insertion
TP2	Insertion	Return	Insertion

In the cMD simulation, Arg9 overcomes the imposed DPPC bilayer energy barrier since it stays in the lower leaflet for the 100 ns of simulation (equilibrium state), although the formation of a small transient pore is observed (Table 4 and Figure 14). The cMD simulation for Arg9 in DPPC:DOPC:CHOL shows a relaxation from a non-equilibrium state to a more stable state where Arg9 remains trapped in the bilayer hydrophobic core while forming a large-sized pore (Table 4 and Figure 14 for pore details). In the DPPC:DOPC:DPPS:DOPS:CHOL membrane, the energy stored at the end of the Arg9 aSMD simulation is sufficient to take the peptide back to the upper leaflet.

Table 4. *Mean radius size (Å) of the last 80 ns of the simulation.*

Peptide	DPPC	DPPC:DOPC:CHOL	DPPC:DOPC:DPPS:DOPS:CHOL
Arg9	0.19 ± 0.03	6.30 ± 0.04	0
MAP	0.71 ± 0.03	0	0
TP2	0	0	0

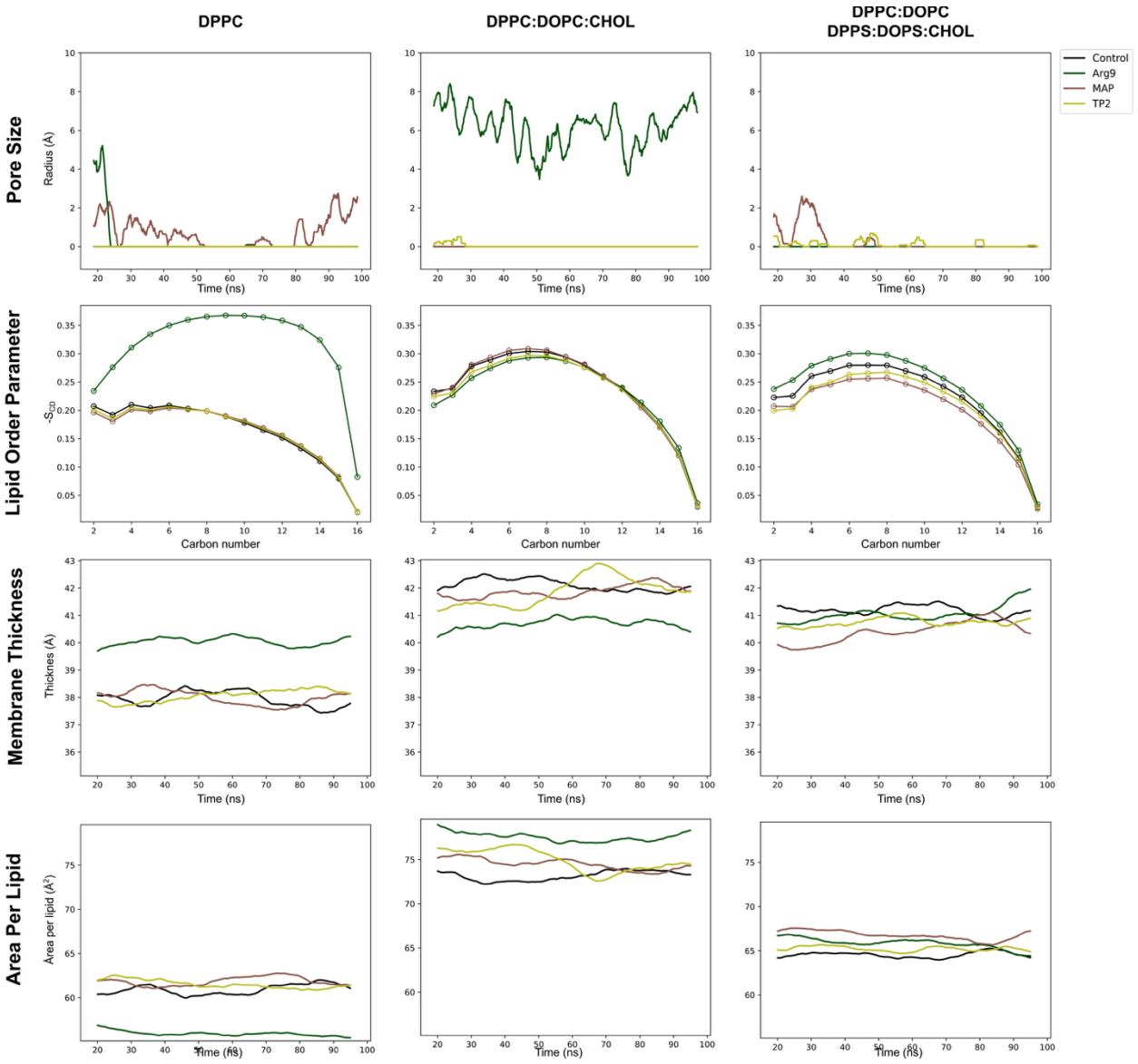

Figure 10. *Pore size, lipid order parameter, membrane thickness and area per lipid analyses. The analyses have been performed for the last 80 ns of the cMD part of the DPPC, DPPC:DOPC:CHOL and DPPC:DOPC:DPPS:DOPS:CHOL membrane simulations. Lipid Order Parameter has been computed for the lipid tails and results are shown for carbon number 2 to 16.*

The cMD simulation for MAP in DPPC shows the peptide bouncing back but remaining in the hydrophobic core of the bilayer forming a small pore. The cMD simulation for MAP in DPPC:DOPC:CHOL shows a relaxation of the peptide and an upper part reallocation. In the DPPC:DOPC:DPPS:DOPS:CHOL bilayer, the cMD simulation for MAP shows how the peptide returns to the upper bilayer but becomes inserted in the hydrophobic core. In average, MAP has the highest PMF values, indicating that an internalization process is not as favourable as in the other cases. This can be related to experiments where they observed that the internalization of

MAP requires, in a large amount, an energy-dependent pathway or vesicle transport event[56,57,225,226].

Similarly to MAP, TP2 has not reached an equilibrium in the lower part of the bilayer in any condition. In DPPC:DOPC:CHOL, TP2 releases all the stored energy and returns to the upper bilayer, indicating that cholesterol induced rigidity poses a high energy barrier for TP2 to remain in the bilayer. On the other hand, in DPPC and DPPC:DOPC:DPPS:DOPS:CHOL bilayers, we observe the insertion of TP2 in the hydrophobic core of the bilayer, but without leading to the formation of a pore. This behaviour can be related to the fact that TP2 in monomeric form enters the cell via spontaneous membrane translocation, rather than the pore formation mechanism[66,227].

Effects of the peptides on bilayer behaviour have been performed, namely lipid order parameter, membrane thickness and area per lipid (Figure 14). Membrane thickness and area per lipid fluctuate accordingly. DPPC membrane has the lowest area per lipid (~60.1 $Å^2$ is the average value for all peptides over the simulation) and membrane thickness (average value of ~38.5 Å along the simulation), indicating that DPPC is the most compact membrane. The addition of cholesterol has been documented to decrease area per lipid[228], but it seems that the addition of unsaturated lipids (DOPC) counterbalances cholesterol's effect due to the kinks in its structure, and makes the bilayer less compact, showcasing higher area per lipid (average of ~75 $Å^2$) and membrane thickness (~41.6 Å). Thirdly, the addition of negatively charged lipids compacts the membrane (thickness of ~40.8 Å), while lowering area per lipid (~65.6 $Å^2$). Area per lipid and membrane thickness analyses can also be related to the fluctuations in PMF among membranes. Firstly, DPPC has the lowest average PMF value. DPPC:DOPC:CHOL is less compact, which should lower PMF values, but this effect is counterbalanced by cholesterol, which does not favour peptide crossing, as previously discussed. In DPPC:DOPC:DPPS:DOPS:CHOL membrane, negatively charged lipids tighten the membrane and strengthen interactions between peptide and membrane[222], causing the highest increase in PMF values.

Lipid order parameter values are in line with previously reported values[214], showing that membranes are well organized, and thus indicating that the CPPs do not destabilize the membrane upon interaction and/or disruption. Furthermore, secondary structure analyses were conducted; however, the peptides do not exhibit any defined secondary structure (Figure 15).

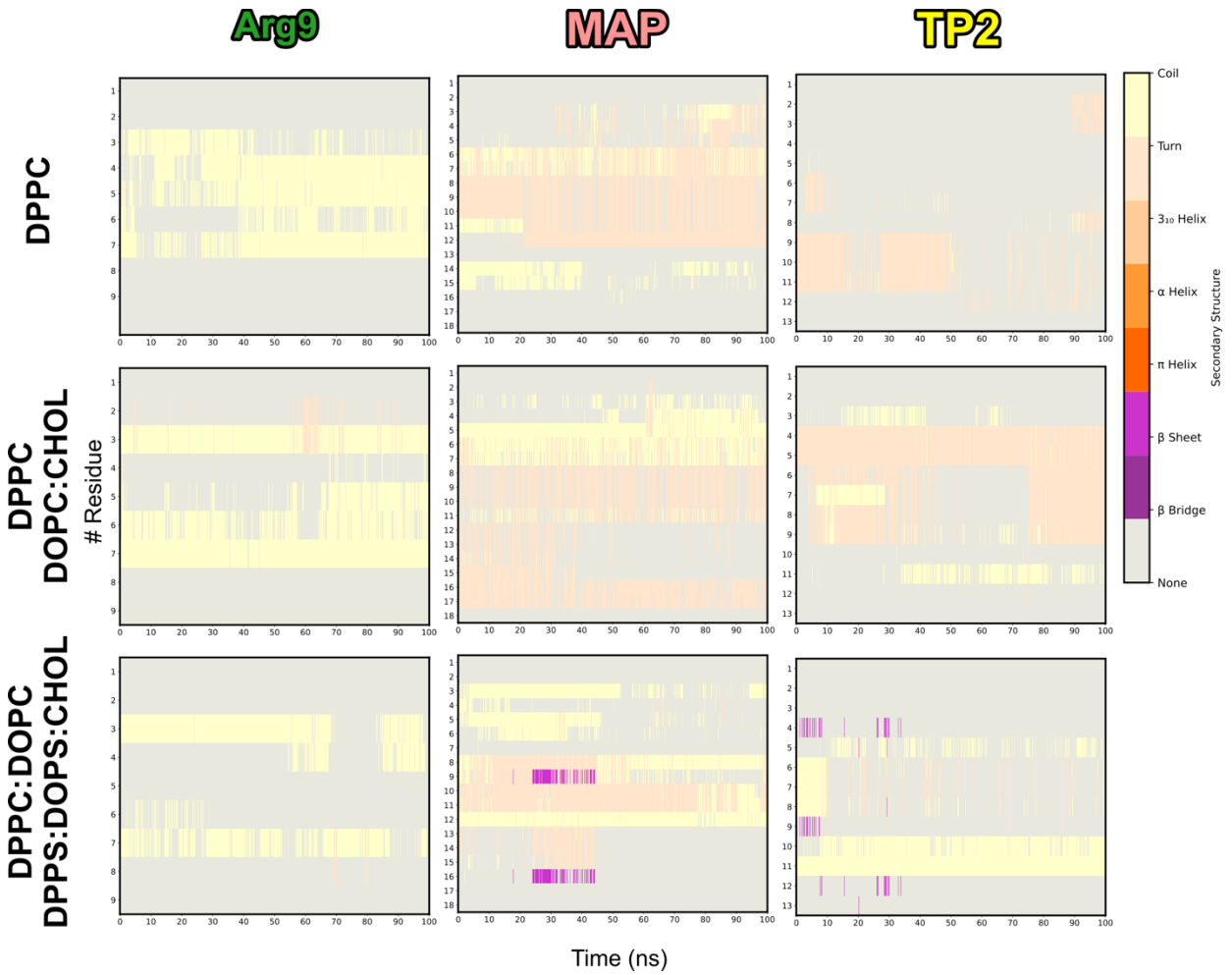

Figure 11. *Secondary structure. The secondary structure analysis has been performed for each peptide in the cMD part of the DPPC, DPPC:DOPC:CHOL and DPPC:DOPC:DPPS:DOPS:CHOL membrane simulations.*

Thus, we have focused on the occupancy of peptide residues by the polar heads of the phospholipids in upper and lower leaflets (Figure 16).

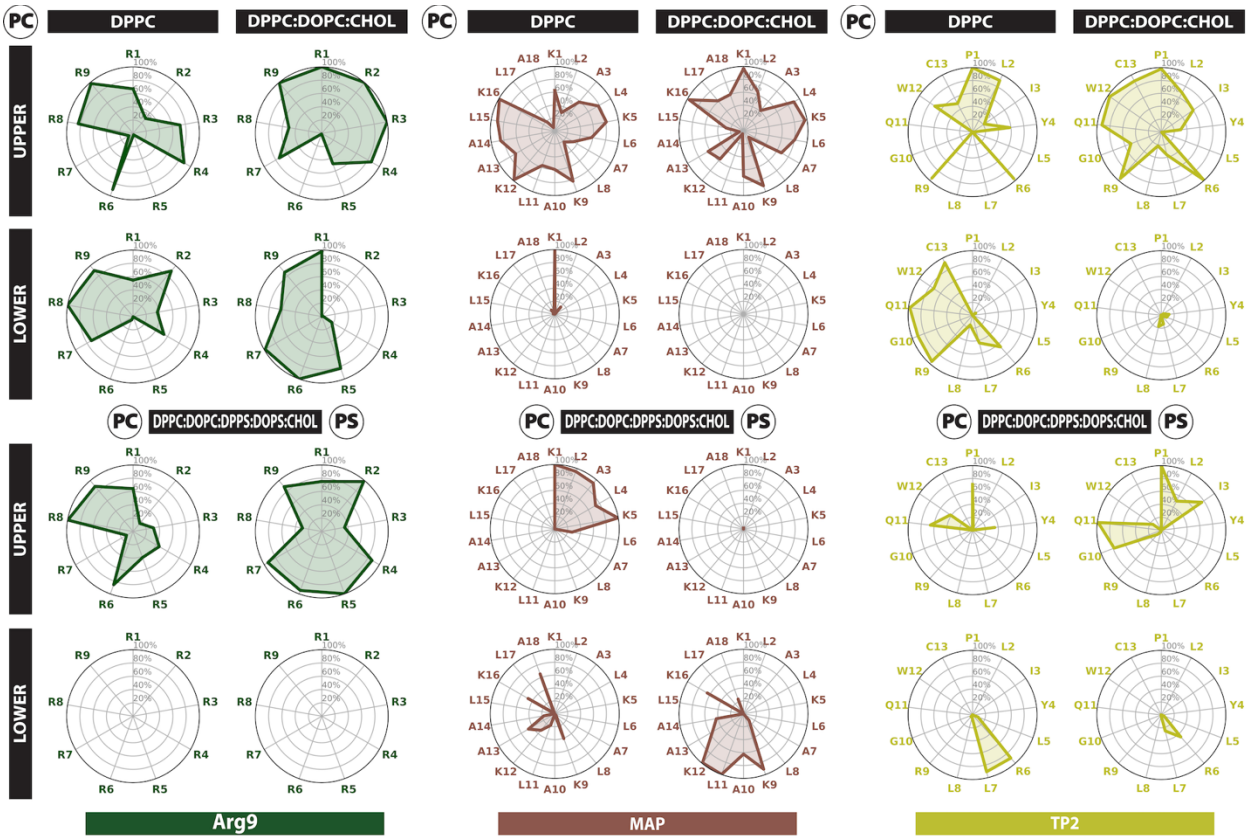

Figure 12. *Residue occupancy by the polar head of the phospholipids in the upper and lower leaflets. Polar heads corresponding to PC (phosphatidylcholine) occupancy is shown for DPPC, DPPC:DOPC:CHOL and DPPC:DOPC:DPPS:DOPSCHOL membranes. For the third membrane, PS (phosphatidylserine) occupancy is also shown. The occupancy analysis refers to the first replica.*

3.1.3.3.Peptide-bilayer interactions

Sequence composition, charge and the hydrophobicity index GRAVY score (Table 2) are key determinants driving peptide-bilayer interactions. The GRAVY score is a measure of peptide hydrophobicity based on the Kyte-Doolittle scale[220], where the more negative the value the higher peptide hydrophilicity, and the more positive the value the higher the hydrophobicity. In this regard, Arg9 has a highly negative GRAVY score, indicating how Arg9 is more likely to interact with water and, in this case, with lipids' polar heads. Thus, Arg9 shows 3 different modes: lower bilayer steady-state, upper part relocation or pore formation, but, in each of these, it stays in contact with the polar heads of the bilayer (in the two former cases) or with the waters (in the latter case). In the other two canonical CPPs, MAP and TP2, we see how they get inserted into the bilayer and stay in contact with the hydrophobic part of the membrane, which is related to the more hydrophobic nature indicated by the GRAVY score. The differences in GRAVY score explain why

MAP and TP2 can get inserted into the bilayer without pore formation, but Arg9 requires to be in contact with water and forces pore formation. In parallel, both MAP and TP2 have key positively charged residues (Table 2), which allows them to interact with the polar heads in the membrane.

In Figure 16 we present the occupancy analysis regarding the lipids' polar heads for every peptide in all membranes, such as, PC for phosphatidylcholine (in DPPC/DOPC) and PS for phosphatidylserine (in DPPS/DOPS). Occupancy is defined as the percentage of simulation time that a residue is in contact with a lipid. In Figure 17, we show the occupancy by the lipid tails and cholesterol.

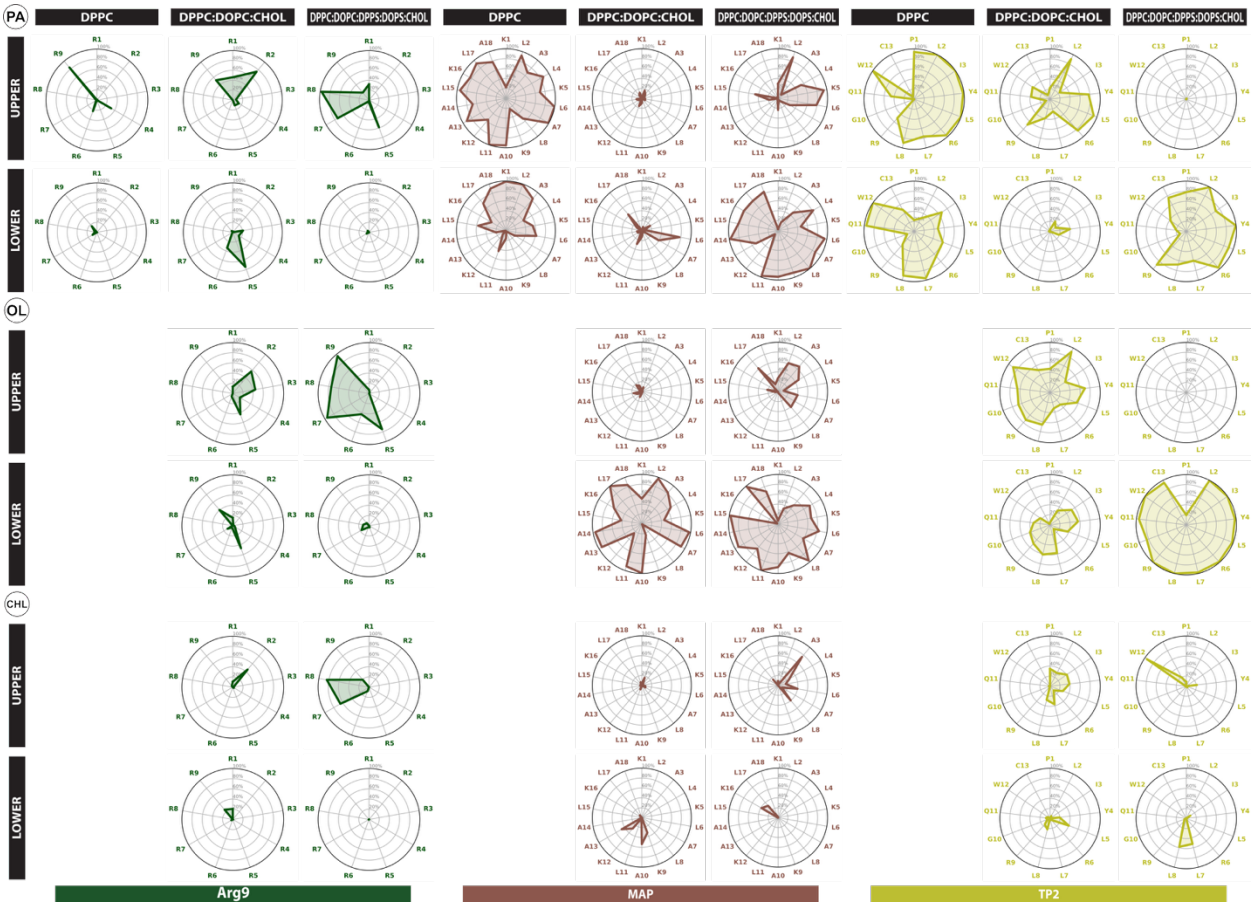

Figure 13. *Occupancy of the lipid tails and the cholesterols. PA refers to the lipid tail present in DPPC/DPPS lipids, namely palmitic acid. OL refers to the lipid tail in DOPC/DOPS, namely oleic acid. CHL refers to cholesterol. These are the lipid names provided by the AMBERFF14SB forcefield.*

Regarding peptide-polar head interactions (Figure 16), we observe a higher interaction ratio for Arg9 (several residues have close to 100% occupancy), which can be explained due to the polycationic nature of this CPP, strongly attracted to the negatively charged polar heads of the

lipids. K/R neighbouring residues also show high occupancy in all three CPPs. MAP, which has alternating positive (K) and hydrophobic (L, A) residues, preferably interacts with the polar heads through positive residues, that is, K1, K5, K9, K12, and K16. TP2 contains only two charged residues, R6 and R9, which are prone to interact with the polar heads of the lipids and show high occupancy across the three bilayers. However, the N- and C-terminal parts are also interacting with the polar heads in three and two bilayers, respectively. In DPPC, the peptide is inserted in the membrane and stretched, thus interacting with a leaflet in each end. In the DPPC:DOPC:CHOL bilayer, R9 favours the lipid interaction of TP2 C-terminal residues. Besides, the N-terminal residues (specially P1) show high occupancy, which can be explained by the positive charge in the N-terminal residue. On the other hand, regarding the occupancies by lipid tails, Arg9 shows, in average, low occupancy, again, explained by its polycationic nature, whereas MAP and TP2 show high occupancy by the lipid tails, mainly interacting with the hydrophobic residues (L, A in MAP, and L, I, Y, W in TP2).

In parallel, when comparing the occupancies across all three bilayers, there are noteworthy differences between: (1) the case where the peptide that has reached an equilibrium in the lower part of the bilayer, which has a higher occupancy in the lower leaflet (Arg9 in DPPC), (2) the peptides that form a pore and interact with the polar heads in upper and lower leaflets (MAP in DPPC, and Arg9 in DPPC:DOPC:CHOL), (3) the peptides that get inserted into the bilayer and also interact with both leaflets (TP2 in DPPC, MAP and TP2 in DPPC:DOPC:DPPS:DOPS:CHOL), and (4) the peptides that have been reallocated to the upper leaflet and are only interacting with the polar heads in the upper leaflet (MAP and TP2 in DPPC:DOPC:CHOL, Arg9 in DPPC:DOPC:DPPS:DOPS:CHOL). MAP in the first membrane composition generates a pore in the bilayer and only interacts with the lower leaflet with the first residue, indicating that it shows an extended conformation, perpendicular to the membrane[229,230], stabilized by the hydrophobic interactions with the lipid tails and the hydrophilic interactions with water, with a similar distribution to the three cases of insertion. Interestingly, Arg9 in DPPC:DOPC:DPPS:DOPS:CHOL interacts rather with the polar heads in PS lipids than PC lipids, likely by the strong attraction between the side chains and the negatively charged lipids, as seen in previous studies[231].

In short, specific phospholipid preferences can be extracted from this study. Arg9 has a preference for polar heads, and if both PC and PS heads are present, Arg9 favours the interaction with PS lipids. TP2 and MAP have a higher interaction with lipid tails, but they also interact strongly with PC heads, indicating that they have parts with a preference for heads and other parts that prefer to interact with lipid tails. No preference for cholesterol interaction has been seen, similar to the results seen for other CPPs [232].

The cationic Arg9 seems to require pore formation to cross the bilayer[233,234] as we observe for Arg9 by either forming transient (in the DPPC bilayer) or more stable (in DPPC:DOPC:CHOL) pores, likely a mechanism to overcome the bilayer energy barriers. For MAP, the energy barrier could be lowered by the formation of a pore[235], related to what we see in DPPC, but MAP also seems to require translocation through energy-dependent mechanisms[56]. TP2 may involve direct translocation (through a quick and transient pore or without pore formation as we observe here) of a monomeric peptide[66,227], leading to a minimum leakage.

There are other aspects, beyond the scope of this study, that could play a relevant role in the internalization process of CPPs and would require further investigation, such as secondary structure conversions, peptide organization, and/or peptide self-assembly[152,221,223,231,236].

3.1.4. Conclusions

In conclusion, we have analysed the effect of neutral, saturated, and unsaturated lipids, cholesterol, and negatively charged lipids on the membrane disturbing potential of representative CPPs. As a general conclusion, the presence of cholesterol adds more stability to the membrane and increased thickness, which entails higher deformation resistance. Negatively charged lipids are not directly correlated with the internalization efficiency of CPPs. CPPs interactions with the upper leaflet strongly influence the ability of the peptides to interact with the lower leaflet and, consequently, their ability to form pores or to reach the lower leaflet. In cationic CPPs, such as Arg9, the peptide-lipid and peptide-water interactions lead to larger disturbance of the bilayer and formation of large transient pores which would be key to overcome the energy barrier at the hydrophobic core layer. Hydrophobic CPPs, such as TP2, find a lower energy transition path across the bilayer, without requiring the formation of transient pores. Amphiphilic CPPs, such as MAP, find a limiting step in

the upper leaflet partitioning, requiring the formation of transient water pores to overcome energetic barriers opposed by the bilayer.

In this study, due to computing restraints, we have focused on a representative peptide of the three main CPP groups (cationic, amphipathic, and hydrophobic) and studied against three simplified model membranes, to understand CPPs membrane disruption capacity. Further studies should consider the plethora of CPPs available, their physicochemical properties, the translocation mechanisms, and the specific lipid-peptide interactions in biological membranes. Better characterization and understanding of the diverse CPP mechanism are of paramount importance, which will lead to more efficient design and development of CPPs and their cargoes. Enhancing the CPPs targeting and internalization potential will lead to better and more personalized drug delivery systems, anticancer, antimicrobial, and/or antiviral therapies[152,221,223,231,236]. Despite the significant strides made in the understanding of CPP internalization, translocation, and pore formation, certain aspects remain elusive, which underscores the need for future investigation, as well as the need for out-of-the-box ideas to study such processes.

3.2. Chapter II: understanding cell penetrating peptide mechanisms using computational electrophysiology simulations

In this chapter, we use computational electrophysiology (CompEL) technique to study peptide–membrane interactions. Here, we focus on objectives 1,2,3 and specific objectives 1,2,4.

3.2.1. Introduction

Cell-penetrating peptides (CPPs) represent a diverse class of molecules renowned for their ability to traverse biological membranes and facilitate the intracellular delivery of various cargoes without inducing cytotoxicity[30,86,237]. CPPs can internalize into cells coupled with various cargoes, such as proteins, DNA, RNA, nanoparticles or low molecular weight drugs[115,162,238–241]. Moreover, CPPs are currently being used for therapeutic purposes, such as cancer treatment, Alzheimer's disease, and immunotherapy[242–246]. Nevertheless, the molecular mechanism of CPP translocation and internalization requires further investigation[247], for controlled rational design of these biomedically relevant molecules.

Many molecular mechanisms have been proposed, which can be classified into energy-dependent and energy-independent methods[166]. Energetic mechanisms entail endocytosis[248,249], whereas energy-independent mechanisms include pore formation[168], the carpet-like model (through membrane destabilization)[92], the membrane thinning model[169], and inverted micelle[170]. More recently, CPPs have been discovered to translocate across both the endosomal and plasma membranes by a vesicle budding and collapse (VBC) mechanism[250,251]. In fact, the diverse possible translocation methods lead to talk about a *landscape* of different internalization mechanisms[252]. In addition to these mechanisms, other variables, such as peptide concentration, can also affect the internalization dynamics[253].

CPPs exhibit a wide range of structural and biochemical characteristics, often classified based on their predominant physicochemical properties. Among these classifications, peptides can be categorized as cationic, hydrophobic or amphipathic[54]. Cationic peptides, such as Arg9[53] are characterized by an abundance of positively charged residues, such as arginine or lysine, which promote electrostatic interactions with negatively charged cell membranes. Hydrophobic peptides, such as TP2[66], and K-FGF[254] possess a high proportion of hydrophobic residues, facilitating interactions with lipid bilayers. Amphipathic peptides, such as TP10[255] or MAP[30,57], can be further divided into primary amphipathic (featuring distinct hydrophobic and hydrophilic regions within their sequences), secondary amphipathic (which adopt amphipathic conformations upon interaction with lipid membranes), proline-rich, and histidine-rich[54,173]. Understanding the classification of CPPs based on these physicochemical properties is essential for elucidating their mechanisms of cell penetration and optimizing their utility in biomedical applications[172].

Molecular dynamics (MD) simulations have been extensively used to investigate the internalization mechanisms, since it can provide meaningful insights of peptide-membrane interaction at atomic level[256–258]. In this study, we seek to study the insertion or translocation abilities of CPPs. Nonetheless, the translocation process takes from seconds to minutes[140,259], and is too computationally demanding to be observed in a conventional Molecular Dynamics (cMD) simulation. In this regard, enhanced sampling techniques have been employed to explore a larger conformational space, such as Umbrella Sampling (US)[146,235], Replica Exchange (RE)[260,261], adaptive Steered Molecular Dynamics (aSMD)[142], and Weighted Ensemble (WE)[150]. Besides, coarse graining techniques, such as MARTINI, have also been used to study the thermodynamics of CPP translocation[153] (interested readers are redirected to the exhaustive review by Ouyang and colleagues [262]). However, these methods have inherent limitations. For instance, US is primarily used to calculate free energy of translocation, aSMD requires powerful computational resources, and they are strongly biased methods requiring reaction coordinates, whereas coarse-grained simulation have lower resolution. Therefore, we repurpose computational electrophysiology (CompEL)[259] to elucidate the key steps involved in CPP cell penetration. CompEL has been previously used to study membrane proteins, mainly ion channels (see the CompEL review in Ref.[263]), but, to the best of our knowledge, this is the first study to employ CompEL for the study of CPPs and their mechanism of action.

Simulations at high temperatures (up to 500 K) have been performed to study membrane disruption of small molecules[264], following the high kinetics rationale to enhance sampling [265]. Following a parallel reasoning, in CompEL, we generate a difference in potential through ion imbalance using a double membrane configuration[259], allowing for enhanced sampling and easier CPP-mediated membrane disruption. Through this approach, we seek to identify critical molecular events and kinetic barriers that dictate the efficiency of CPP internalization. We aim to provide a new possibility to unravel the interactions between CPPs and lipid membranes, shedding light on the processes governing their cellular uptake.

In this regard, we chose four representative CPPs (Arg9, MAP, TP10, and TP2, to compare them with our previous study) and a negative control (Leu9, non-CPP) to conduct the study. First, we ran simulations with one peptide at different potentials to decide the appropriate transmembrane potential for this system setup. Then, we analysed the simulations at the chosen transmembrane

potential. Last, we simulated the systems with eight peptides to study and analyse CPP cooperation and aggregation.

In this study, we aim to expand the computational toolkit for investigating membrane active peptides[25,266], with a particular emphasis on CPPs. To this end, we employ CompEL –an entry-level, rapid, and reproducible computational technique– to explore the molecular mechanisms underlying CPP internalization. Our objectives are to differentiate between CPP-like and non-CPP peptides, and to compare single- to multiple-peptide simulations. Our findings hold promise for guiding the rational design of CPP-based delivery systems and advancing targeted therapeutic interventions in biomedical research.

3.2.2. Computational methods

3.2.2.1.Systems preparation

Peptides were initially modelled with ColabFold notebook[181], which uses AlphaFold[182] monomer prediction to model the peptides.

3.2.2.2.Computational electrophysiology simulations

In CompEL, a transmembrane potential triggered by charge imbalance (ΔQ) is generated between one side and the other of the membrane. But, since PBC are applied, a double membrane configuration system must be designed to achieve the desired transmembrane potential. Simulations were run at 350 K. To prepare the system, we followed the methodology described in previous studies[259,263,267]. In this regard, we used GROMACS built-in *gmx* utilities: first, we duplicated the system, then, rotated the second system, doubled the box size, and concatenated both files into a single box with a double membrane configuration. After that, the desired transmembrane potential was achieved by ion imbalance between both membranes: a positive charge (K^+ ions) was added to the inner water compartment, and a negative charge (Cl^- ions) was added to the outer water compartment. Thus, water molecules were swapped with ions into the corresponding water compartment, done using *gmx insert-molecules*. In Table 5, we present the configurations for all the systems simulated in this study. When a peptide was added to the system –in the inner water compartment–, the corresponding counterions were inserted –in the same water compartment– following the same procedure as before.

Table 5. *System configurations in the computational electrophysiology (CompEL) method, indicating the number of positive ions (K^+), negative ions (Cl^-) and water molecules in the different compartments. The composition is shown for the system without peptides (membrane control). When a peptide is added to the system (in the outer water compartment), the corresponding counterions were added (in the same water compartment).*

Transmembrane potential (ΔQ)	K+ in outer water compartment	K+ in inner water compartment	Cl- in outer water compartment	Cl- in inner water compartment	Water residues
0	28	28	28	28	22850
8	30	26	26	30	22820
12	31	25	25	31	22831
16	32	24	24	32	22839
24	34	22	22	34	22832

Thereafter, the system was minimized for 5 000 steps and equilibrated for approximately 2 ns (the different steps were of 125, 125, 125, 500, 500, 500 ps) while gradually lowering the positional restraints (1 000, 400, 400, 200, 40, 0 $kJ \cdot mol^{-1} \cdot nm^{-2}$, respectively). Last, a 250 ns simulation was run for each system. The ion number was kept constant in each water compartment through the whole duration of the simulation using computational electrophysiology protocol in GROMACS, which controls ion/water position exchanges (production files can be found at the GitHub repository). A summary of the number of simulations run can be found at Table 6 (see next section for explanation of simulation number and/or difference in simulation length), accounting for 31.5 μs of simulation time (ca. 3μs for membrane only systems, ca. 14 μs for systems with one peptide, and 15 μs for systems with eight peptides). The simulations were run using a workstation with a GPU RTX3080Ti, at approximately 80 ns per day.

Table 6. *Summary of the simulations and replicas run in this study. The columns differentiate the transmembrane potential through ion imbalance (ΔQ), and the rows indicate the number of peptides. If not indicated otherwise, the simulations have been run for 250 ns.*

Number of peptides	0 ΔQ	8 ΔQ	12 ΔQ	16 ΔQ	20 ΔQ
1	2 replicas	2 replicas	2 replicas	3 replicas	2 replicas
8	2 replicas	2 replicas	2 replicas	3 replicas (500 ns)	-

3.2.2.3.Data analysis

MD simulation analysis was executed in a Jupyter Notebook IDE[268], used along with the MDAnalysis package in Python, and *gmx* utilities[210,211,269–272]. PyLipID was used to analyse lipid occupancy, which is a measure of the simulation time that a protein residue is in contact with the lipids[208]. Visual inspection and molecular graphics were performed in VMD[206]. Secondary structure was analysed in VMD using STRIDE program[273]. An in-house Python script was utilized to calculate the radius pore size, employing Scipy[274]. Basically, the script computes the maximum distance between water molecules in each membrane z-stack (2 Å thick) and outputs the minimum radius among all z-stacks, repeated for each simulation frame. S_{CD} computes the orientation of the lipids with respect to the membrane normal[213]. S_{CD} is calculated using Equation 1. Matplotlib[216] was used for plotting.

3.2.3. Results

3.2.3.1.ΔQ benchmarking

We decided to use 4 canonical CPPs: Arg9, MAP, TP10 and TP2 (Table 7). Besides, we chose Leu9 as a negative control, a peptide not expected to present CPP-like capacities due to its high hydrophobicity[275].

Table 7. *Sequence and characteristics of the peptides used in this study.*

Peptide	Length	Sequence	Type	Net charge	GRAVY score
Arg9	9	RRRRRRRRR	Cationic	+9	-4.5
MAP	18	KLALKLALKALKAALKLA	Amphipathic	+5	0.99
TP10	21	AGYLLGKINLKALAALAKKIL	Amphipathic	+4	0.93
Dynorphin A	17	YGGFLRRIRPKLKWDNQ	Amphipathic	4	-1.26
TP2	13	PLIYLRLLRGQWC	Hydrophobic	+2	0.42
Leu9	9	LLLLLLLLL	Hydrophobic	0	3.8
K-FGF	17	AAVALLPAVLLALLAP	Hydrophobic	0	2.42

In parallel, we ran a simulation without a peptide, as a membrane only control. We chose POPC as membrane lipid, since it is extensively used owing to its biological relevance, reliability and stability in MD simulations, and relevance in physiological systems[276]. The starting configuration of the peptides and the membranes are presented in Figure 18, where the total number of membrane lipids and water residues are also displayed. Besides, the electron density plot is included, indicating membrane, water, and ions densities.

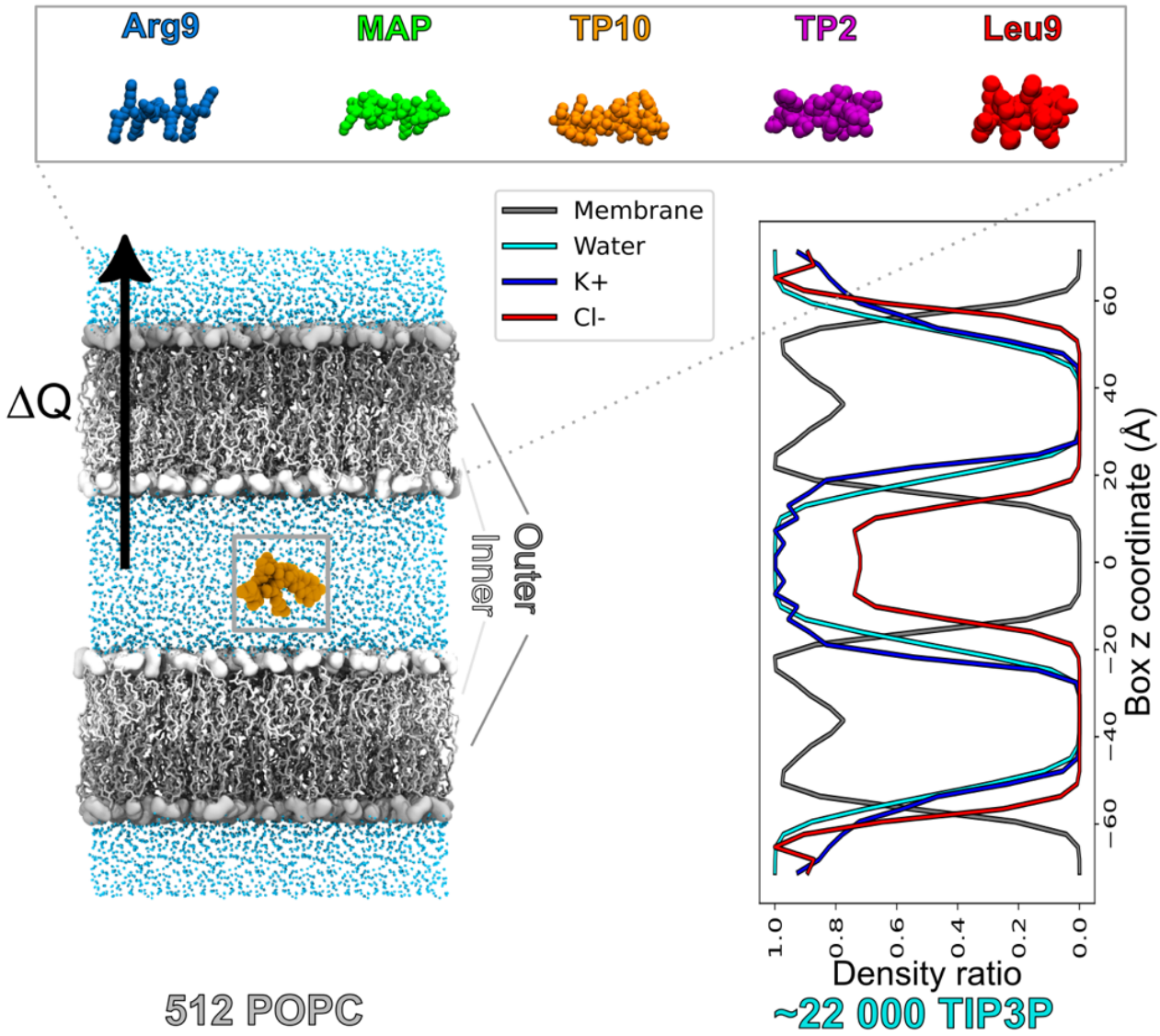

Figure 14. *Graphical representation of CompEL initial configuration. Initial structure of Arg9, MAP, TP10, TP2 and Leu9, as well as the membrane used are shown. The number of lipids and waters are indicated, and the electron density ratio plot of the system is shown. The circle and the peptide coloured in orange indicate the peptide starting position in the computational electrophysiology (CompEL) simulation. Peptides are represented as Van der Waals spheres, and coloured as: Arg9 in cornflower blue, MAP in green, TP10 in orange, TP2 in purple, Leu9 in red. The polar heads (phosphate and choline groups) of the phospholipids*

are represented as surface, and the lipid tails are represented as licorice. The inner and outer membrane are coloured in dark and light grey, respectively. Waters are coloured in cyan and represented as licorice. Hydrogens are hidden for clarity. These colours are maintained throughout the study.

In order to conduct the CompEL simulations, we created a series of systems with increasing ΔQ, starting from 0 (0 net charge in any of the two compartments) to 24, where the charge imbalance was obtained by placing ΔQ/2 K+ ions in the inner water compartment and the other half by placing ΔQ/2 Cl- ions in the outer water compartment. We initially ran 4 sets of 250 ns simulations: at ΔQ 0, 8, 16, and 24, with 2 replicas for each simulation. However, given the sudden change in simulation outcomes between ΔQ 8 and 16 (see below), we decided to add a new set of simulations, at ΔQ 12, to try to better describe the phenomena occurring.

In Figure 19, we show the number of occurrences of each behaviour in every transmembrane potential simulation (Figure 19A). In ΔQ 16 is where the most different behaviours can be seen and, moreover, a similar occurrence ratio of each behaviour is observed, allowing to differentiate between peptides. Thus, we decided to carry on the analysis mainly with the simulation of ΔQ 16 (Figure 19B).

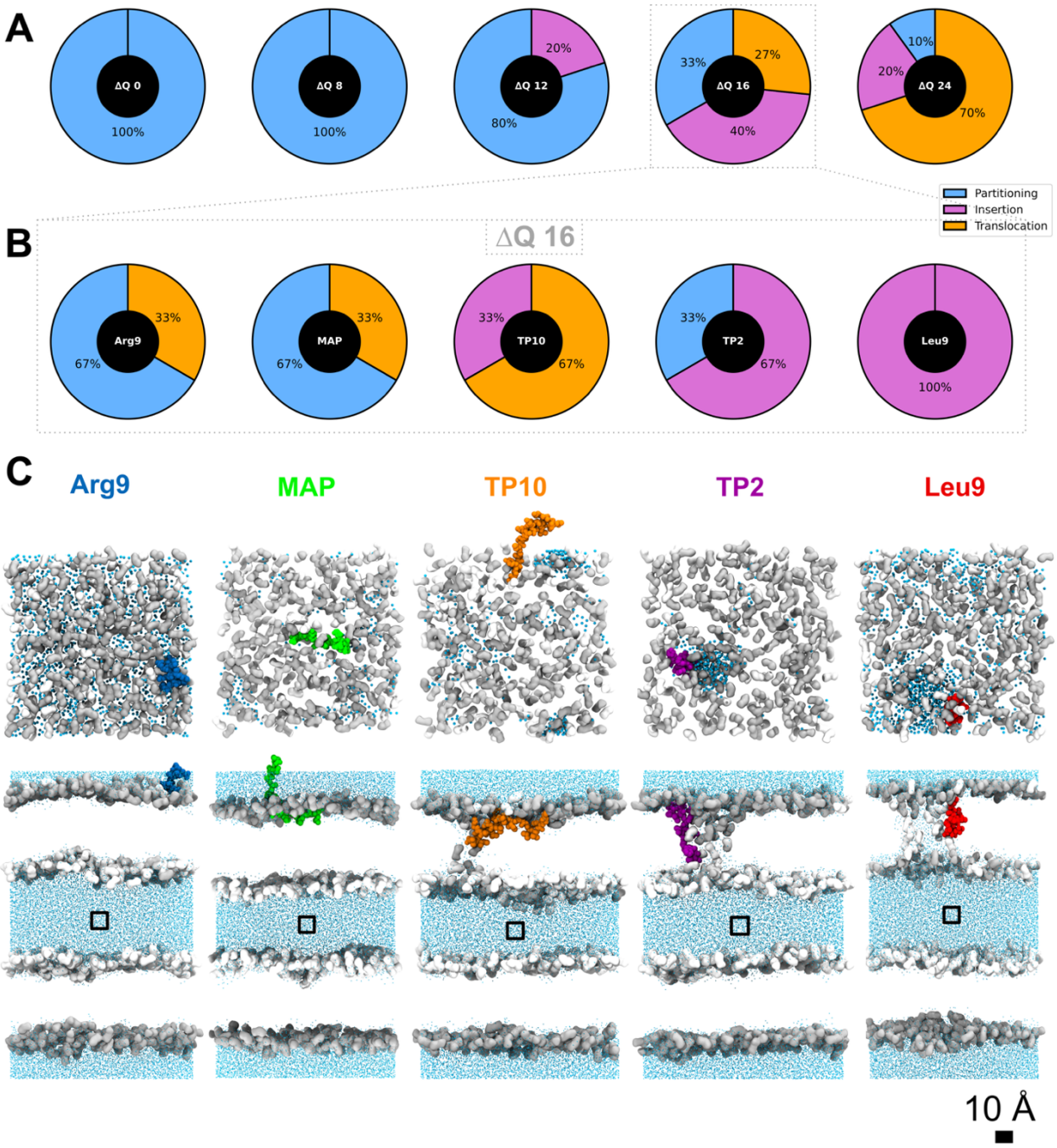

Figure 15. *Results in CompEL simulations with one peptide. (A) Illustrative summary of behaviours seen throughout the CompEL simulations in each transmembrane potential (ΔQ). We differentiate between peptide partitioning, insertion, and translocation. The results represent the ratio of behaviours in the two (ΔQ 0, 8, 12, 24) and three (ΔQ 16) replicas conducted. (B) Summary of the outcomes in the simulations of ΔQ 16 divided by peptide. (C) Molecular representation of the final snapshot in the ΔQ 16 CompEL simulations: top pose (upper image) and side pose (lower image). Two behaviours are observed: translocation of Arg9, MAP, and TP10, and insertion with pore formation of TP2 and Leu9. Peptides are coloured in its own colour, inner membrane in white, outer membrane in grey and waters in cyan. Peptides are depicted as spheres, membrane and waters as licorice. Only waters pertaining to the pore are shown in the top pose. Hydrogens are omitted for clarity. A scale bar is added for size clarity. The black box indicates the peptide starting position.*

Here, we differentiate between three possible behaviours. First, inner leaflet adsorption or partitioning: the peptide stays in the inner water compartment and interacts with the inner part of the membrane. Second, insertion and pore (Figure 19C: TP2, Leu9): the peptide gets in contact with the polar heads in the outer part of the membrane, but it is still in contact with the inner part of the membrane. Moreover, there is a flow of water molecules, defining a water pore, with a toroidal-like nature[277,278]. Third, outer leaflet stabilization or translocation (Figure 19C: Arg9, MAP, TP10): the peptide is able to cross the membrane and interact with the outer part of the membrane and the outer water compartment.

The potential and field distributions were calculated using GROMACS built-in *gmx potential* tool (Figure 20). We see how the potential and field grow as the transmembrane charge imbalance increases, reaching to a voltage of approximately 2 V in CompEL ΔQ 16 simulations (the ones chosen to be analysed). Besides, the calculated field in one membrane averages to ca. 0.3 V/nm (considering both membranes, the field adds up to 0). Therefore, potential and field values are both in the normal range used in other biological studies[279–281].

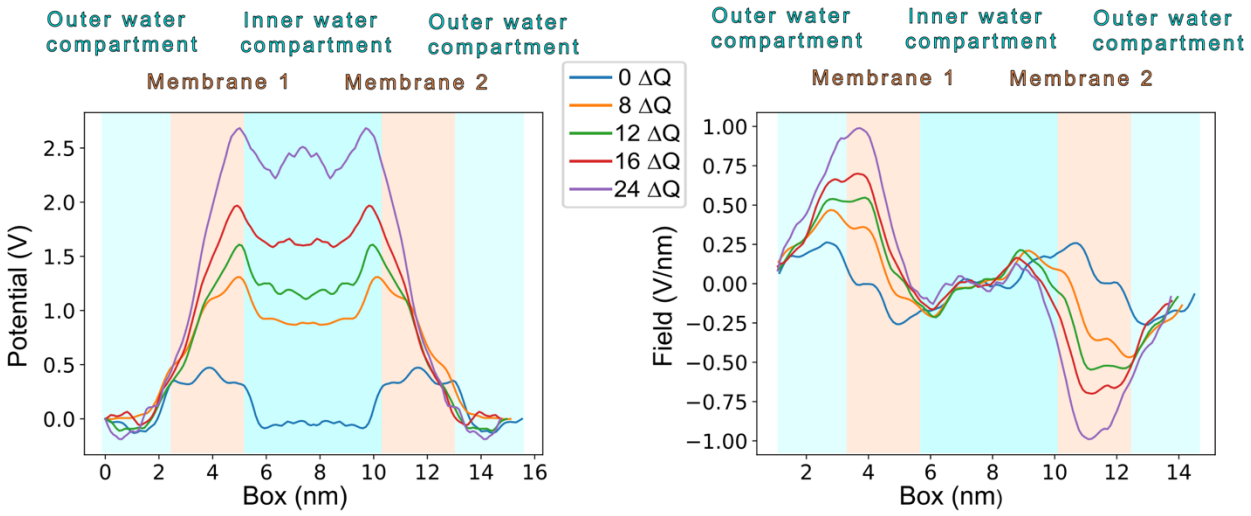

Figure 16. *Potential (left) and field (right) calculated throughout the simulation box in the control simulations (without peptides). Only the first 10 ns were used for the analysis. The analysis has been centred to the membranes. The transmembrane potentials shown are: ΔQ 0, 8, 12, 16, and 24.*

3.2.3.2.CompEL simulations at 16 ΔQ

3.2.3.2.1. Peptide analyses

To increase the simulation set and achieve better sampling of the phenomenon with greater certainty, we ran a third replica of simulations in ΔQ 16. The results of all the simulations, divided by peptide, can be seen in Figure 19B (and Table 8). We see how the translocation is the most common result for TP10, whereas Arg9 and MAP partition in most cases, but they also have the ability to translocate the membrane. On the other hand, TP2 and Leu9 are the only peptides that do not show translocation capabilities and get inserted in the membrane in most cases.

Table 8. *Results of the behaviours of each peptide in the 250 ns CompEL simulations with one peptide for every transmembrane potential. The ratio (in brackets) indicates the occurrence of each result.*

ΔQ	Control	Arg9	MAP	TP10	TP2	Leu9
0	-	Partitioning (2/2)	Partitioning (2/2)	Partitioning (2/2)	Partitioning (2/2)	Partitioning (2/2)
8	-	Partitioning (2/2)	Partitioning (2/2)	Partitioning (2/2)	Partitioning (2/2)	Partitioning (2/2)
12	-	Partitioning (2/2)	Partitioning (2/2)	Partitioning (2/2)	Partitioning (1/2) / Insertion with pore (1/2)	Partitioning (1/2) / Insertion without pore (1/2)
16	Pore	Partitioning (2/3) / Translocation (1/3)	Translocation (2/3) / Partitioning (1/3)	Translocation (2/3) / Insertion (1/3)	Insertion with pore (2/3) / Partitioning (1/3)	Insertion with pore (3/3)
24	Pore	Partitioning (1/2) / Translocation (1/2)	Translocation (2/2)	Translocation (2/2)	Translocation (2/2)	Insertion with pore (2/2)

These behaviours can be spotted in Figure 21, which shows the occupancy of the peptide residues by lipid molecules. Occupancy, analysed with PyLipID[208], measures the simulation time in which a residue is in contact with a lipid. In short, Figure 21 shows how do peptides interact with POPC membranes. We differentiate between the inner and the outer part of the membrane, and between the interaction with the polar head and the hydrophobic tail of the lipids.

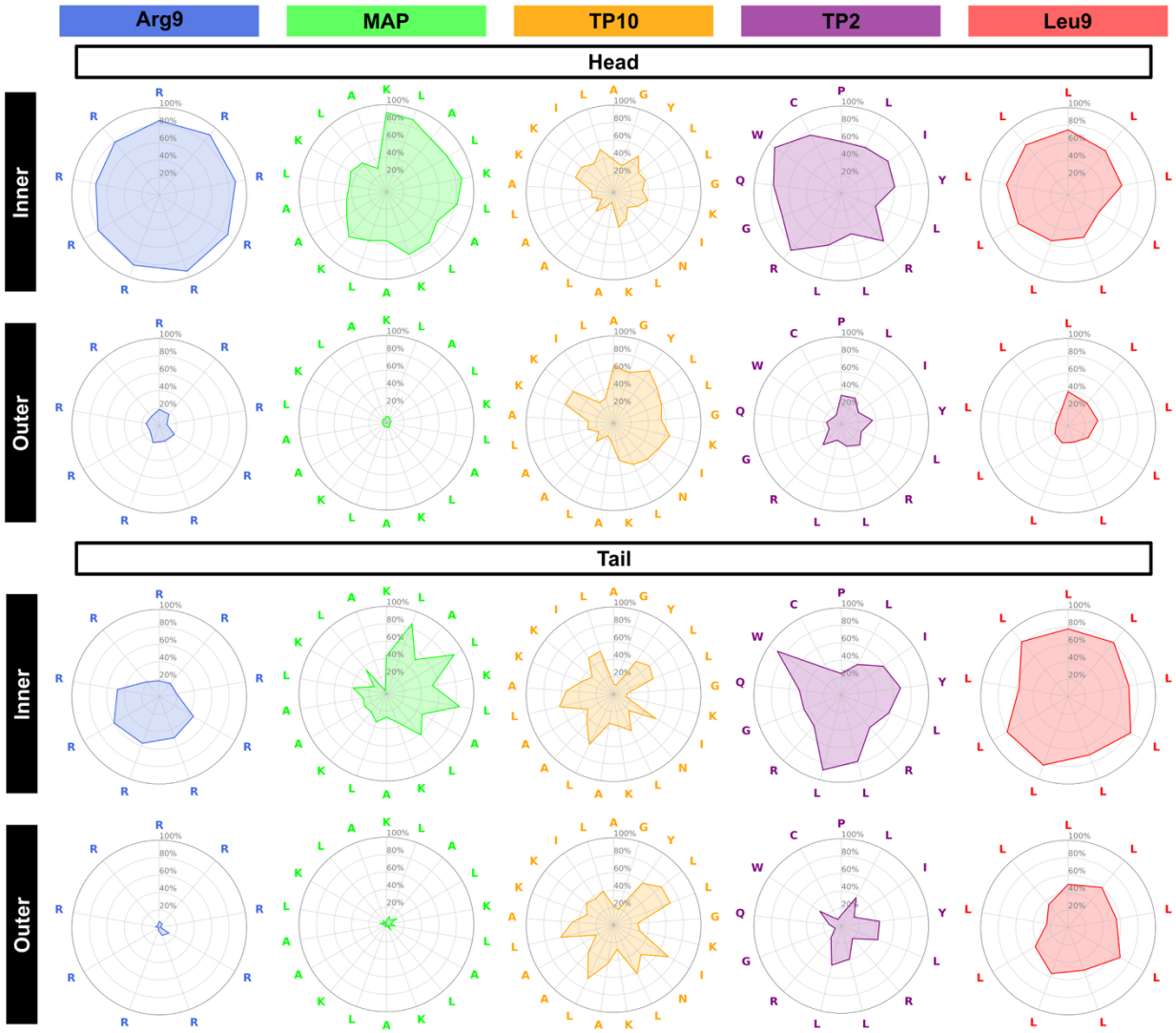

Figure 17. *Lipid occupancy. Occupancies are differentiated by each peptide residue, divided by inner and outer membrane contacts, and by interaction with the polar heads or lipid tails. Residue occupancy is defined as the ratio of simulation time that a residue is in contact with the lipid. The average values for the three replicas are represented.*

In this regard, TP10, the peptide that translocates in most cases, shows a higher occupancy in the outer part of the membrane, demonstrating the translocation behaviour. On the other hand, in the case of the other four peptides, we see a higher occupancy in the inner part of the membrane. Besides, TP2 and Leu9, the peptides that do not translocate in any replica, also show interaction with the outer leaflet, indicating that the insertion mechanism entails interaction with both leaflets. Observing the residues that show a higher occupancy, Arg9 and Leu9 show a homogeneous behaviour, with a similar occupancy for all residues, given that they are polychains of the same amino acid. Nonetheless, we see a clear difference in the occupancy of these two peptides: Arg9

preferably interacts with POPC polar heads, whereas Leu9 shows a higher interaction with the lipid tails. These behaviours are explained by the cationic polar nature of arginine, preferably interacting with the negative charge in the phosphate group, and the hydrophobicity of leucine, rather interacting with the hydrophobic lipid tails, respectively[282,283]. In parallel, in the cases of MAP, TP10 and TP2 we see how, in average, cationic (K, R) or -partly- polar (Y, N, Q) amino acids show a higher occupancy with the polar heads[282] and, conversely, hydrophobic amino acids (L, I, W) preferably interact with the lipid tails. Interestingly, we see how W12 has a high occupancy with the lipid tails in TP2, which proves that this residue, together with L7-L8, are stabilizing the peptide in the hydrophobic core of the membrane and, therefore, hampering its translocation. In fact, tryptophan was found to strongly interact with the hydrophobic part in the interfacial region of the membrane[284].

In parallel, peptide secondary structure was analysed (Figure 22). We observe that Arg9 and MAP are mostly unstructured during the simulations, as seen in previous studies[233,285], TP2 and TP10 remain at a stable structure, and Leu9 is the only peptide where we see a drastic change during the simulation, reaching more than a 50% of α-helix structure when it gets inserted in the membrane, phenomena previously described in other studies[286–288]. TP2 is highly structured in the N-terminal, whereas TP10 shows higher α-helix percentage in the C-terminal part[289].

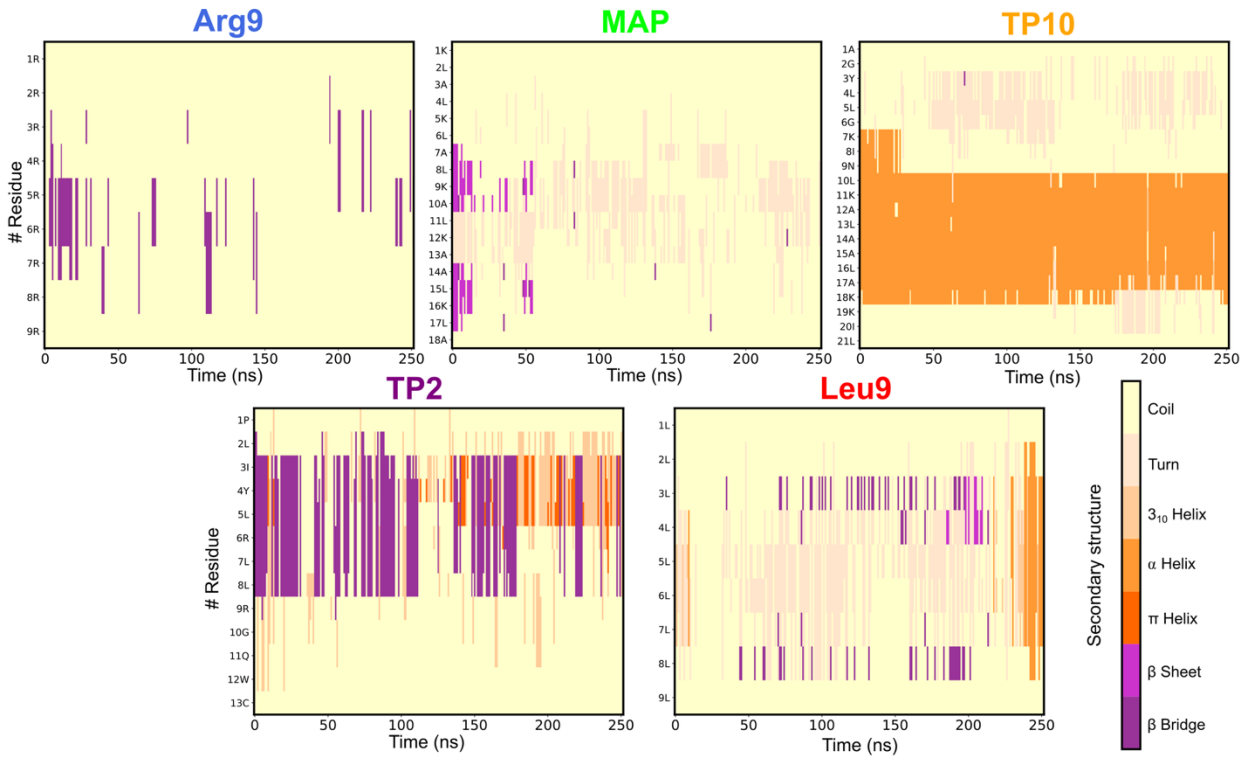

Figure 18. *Secondary structure analysis of the five peptides. The analysis has been done through a tcl script that employed VMD Secondary Structure tool. The arrow indicates the time in which the peptide got inserted in the membrane.*

Furthermore, the hydrogen bonds analysis (Figure 23) shows that Arg9 prefers to interact with lipids, predominantly polar heads as discussed before, which correlates with the lack of secondary structure. On the other hand, Leu9 or TP2 have the highest number of intrapeptide hydrogen bonds, owing to their higher hydrophobicity. Leu9 and TP2, together with TP10, show the highest percentage of secondary structure, again, correlated with higher number of intrapeptide H bonds[290].

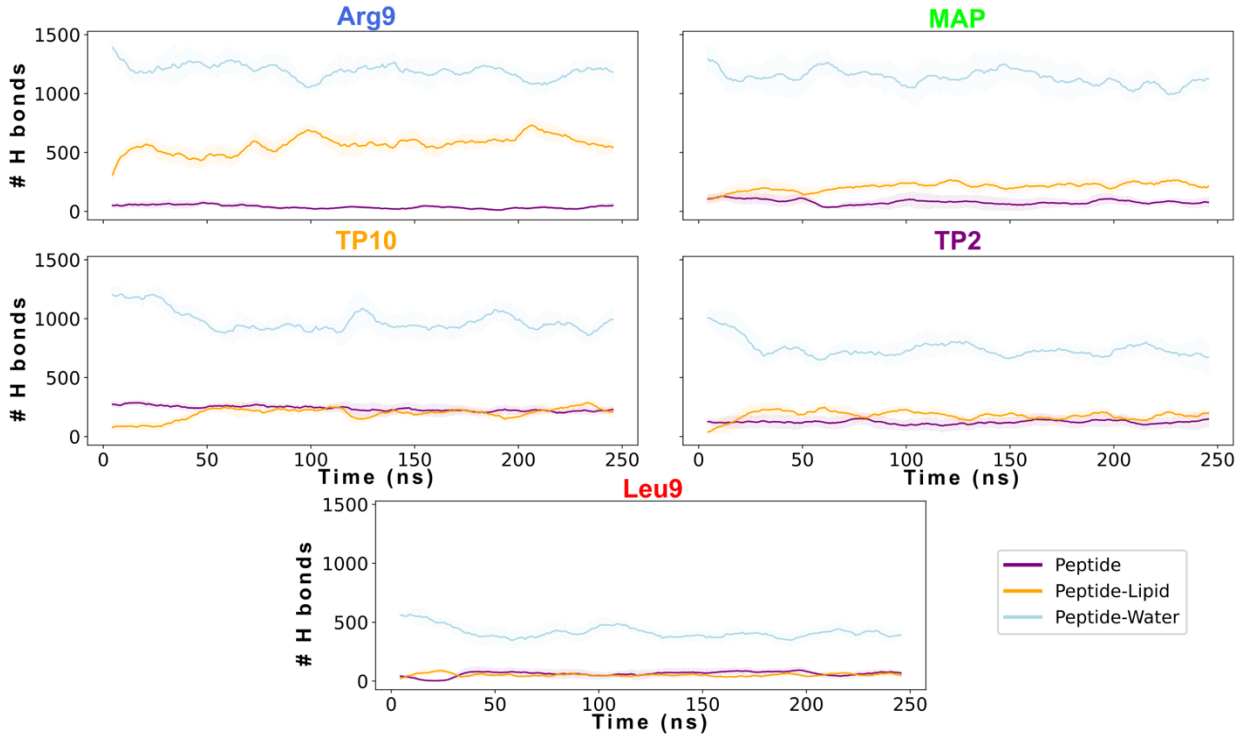

Figure 19. *Hydrogen bond analysis. The lines represent the average values across the three replicas, while the shaded areas indicate the standard deviation. Hydrogen bonds are shown as intrapeptide (purple), peptide–lipid (orange), and peptide–water (cyan) interactions.*

3.2.3.2.2. Membrane disruption analysis

An interesting comparison is the pore that is formed in the membranes during the simulations. Transient, small pores are spontaneously formed in biological membranes[291]. In CompEL, owing to membrane stress[292] caused by the ion imbalance, pores are also generated without the presence of a peptide (membrane control, Table 9)[293,294], highlighting that peptides are not responsible for pore formation. Still, some of these peptides are able to translocate using the pre-formed pores, as seen in previous studies[152,295–297].

Table 9. *Average pore radius (Å) during the 250 ns of CompEL ΔQ 16 simulation. Standard deviation (SD) values are shown. The pore radius is averaged over all frames in the simulation.*

# Replica	Control	Arg9	MAP	TP10	TP2
1	0	31.8 ± 6.7	0.6 ± 0.3	11.5 ± 2.8	4.7 ± 1.9
2	24.8 ± 5.5	6.3 ± 2.1	8.2 ± 2.8	3.7 ± 0.6	10.6 ± 2.6
3	21.2 ± 5.4	0	0.4 ± 0.2	9.3 ± 1.8	16.7 ± 3.4

S_{CD} analyses have been performed to test the organization and orientation of lipids in the membrane. S_{CD} calculates the angle between the carbon-hydrogen bond in the acyl chains of lipids. Here, we focused in the palmitoyl segment of POPC, the sn-1 tail (Figure 24). We see a similar results to the ones observed by Ferreira *et al.*[298], and thus conclude that the lipids are well-oriented in the membrane.

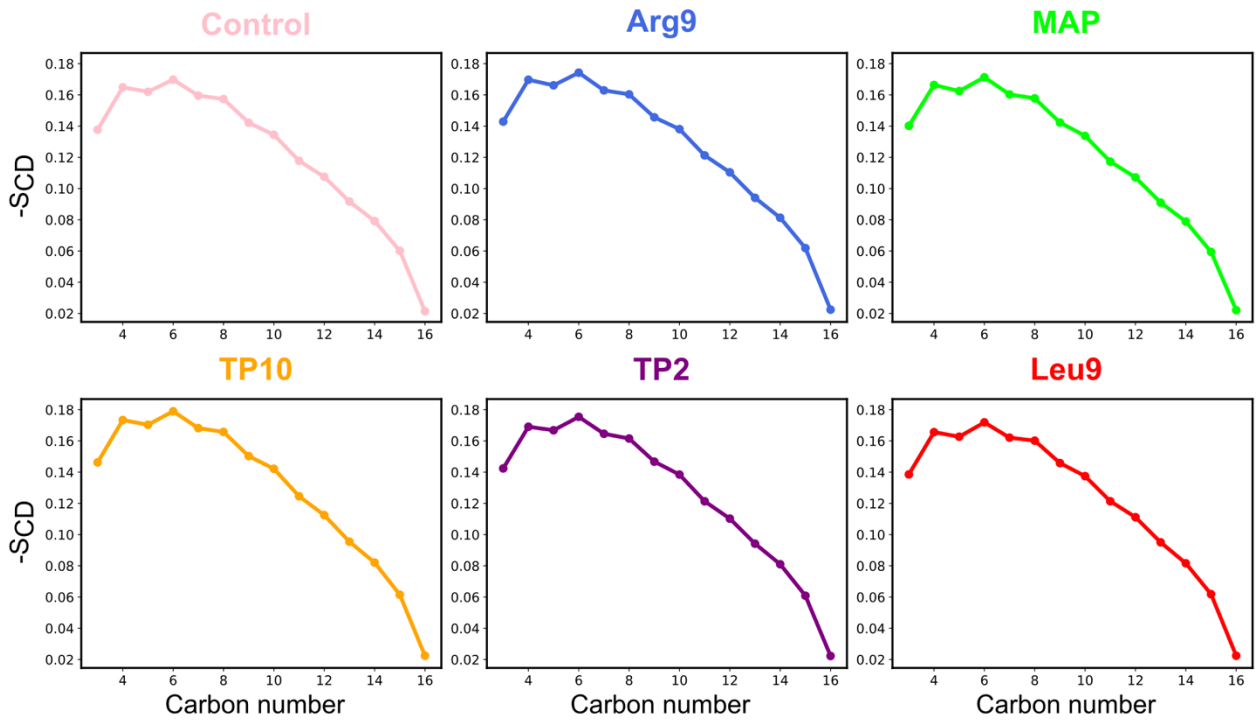

Figure 20. *Ordering of the sn-1 chain of POPC illustrated by the deuterium lipid order parameter (S_{CD}) analyses in CompEL ΔQ 16 simulations. Simulations without peptides are shown as a control.*

3.2.3.3.CompEL simulations at higher peptide:lipid ratio

3.2.3.3.1. Peptide analyses

Simulations with only one peptide are useful to test the method, but since CPPs do not cross a membrane as individual monomers[299,300], we simulated the same POPC CompEL system with 8 peptides, and 256 lipids (per bilayer), corresponding to a 1:32 protein:lipid (P:L) ratio, as in previous studies[301]. This P:L ratio showed full peptide binding in previous studies[253], it was shown enough to create stable pore channels for melittin [302], and is close to the ratio used by Herce and Garcia[231] in the study with TAT peptides (1:18). Besides, more peptides would require larger water compartments, and we wanted to keep the same system conditions as for one peptide.

Two replicas of CompEL 250 ns simulations were run for ΔQ 0, 8, 12, and 16. ΔQ 24 was discarded in order to reduce the electric field applied to the system. As in the CompEL simulations with one peptide, the ΔQ 16 simulations presented the possibility of observing peptide translocation and were, thus, used for simulation analysis (Figure 25).

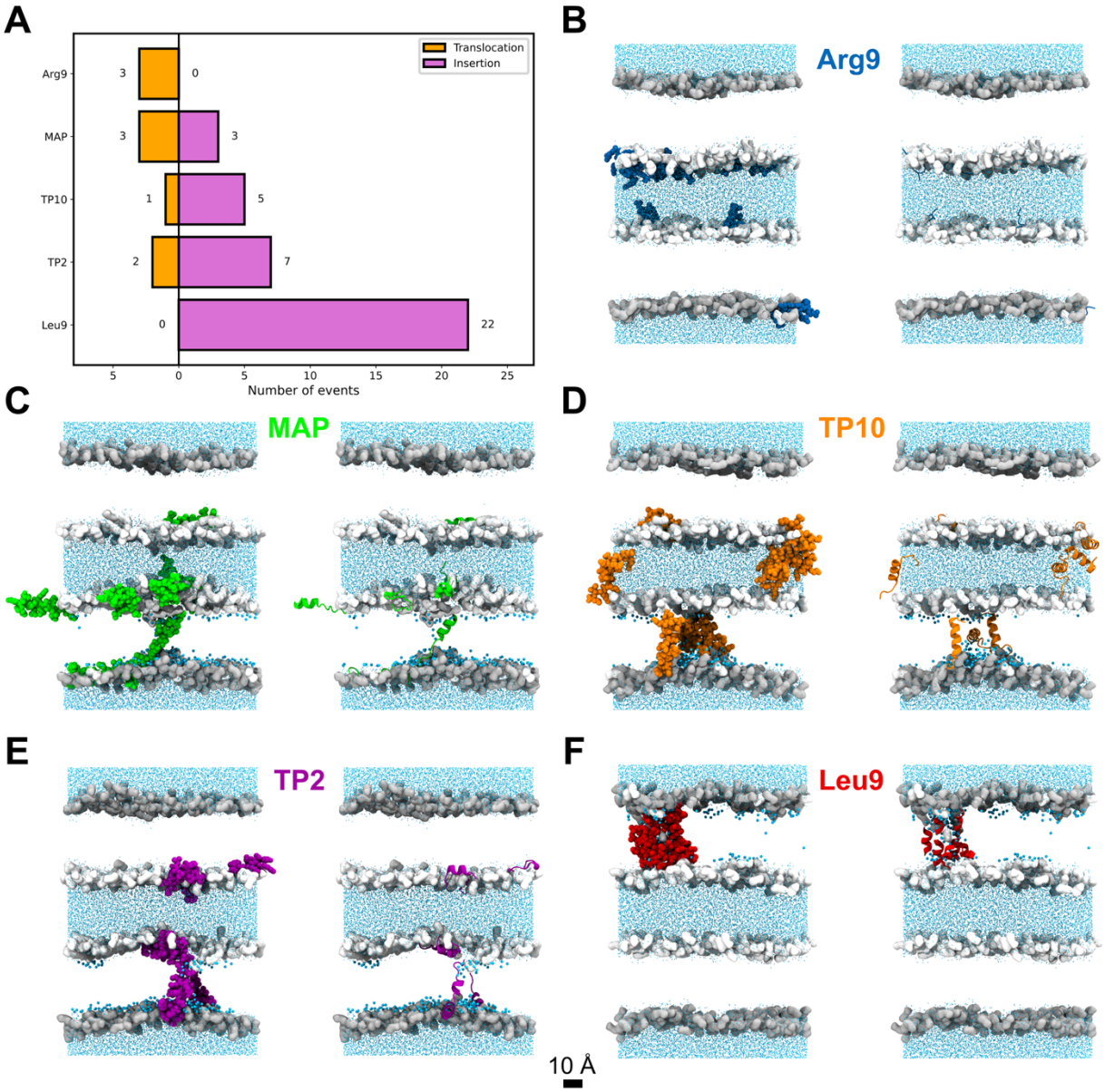

Figure 21. *Results of CompEL ΔQ 16 simulations with 8 peptides. (A) Number of behaviours observed. Only relevant (i.e., translocation and insertion) results are shown. A complete depiction of the results can be seen in Figure 26. The values include the results in the three replicas. (B, C, D, E, F) Molecular representation of the system at the end of the 500 ns of simulation. The peptides represented are Arg9, MAP, TP10, TP2, and Leu9, respectively. Peptides are shown as Van der Waals spheres (left) or cartoon (right). Surface of the polar heads is shown, differentiating between inner (white) and outer (grey) leaflets. Water molecules are shown*

as licorice, representing in bigger size the water residues in the pore. Hydrogens are omitted for clarity. A scale bar is added for size clarity.

The global results seen for ΔQ 0, 8, and 12 can be seen in Figure 26 and Table S2.

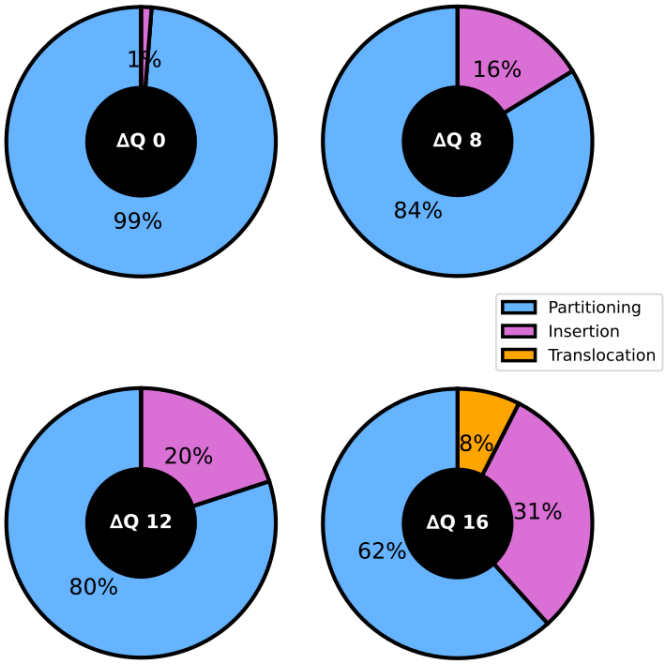

Figure 22. *Results in ΔQ 0, 8, 12, and 16 in CompEL simulations with 8 peptides.*

Table 10. *Behaviours observed for the 8 peptides in ΔQ 16 simulations.*

# Replica	Arg9	MAP	TP10	TP2	Leu9
1	Translocation 1 Partitioning 7	Translocation 1 Insertion 1 Partitioning 6	Insertion 3 Partitioning 5	Translocation 1 Insertion 2 Partitioning 5	Insertion 7 Partitioning 1
2	Translocation 1 Partitioning 7	Translocation 1 Insertion 1 Partitioning 6	Translocation 1 Partitioning 7	Insertion 3 Partitioning 5	Insertion 8
3	Translocation 1 Partitioning 7	Translocation 1 Insertion 1 Partitioning 6	Insertion 2 Partitioning 6	Translocation 1 Insertion 2 Partitioning 5	Insertion 7 Partitioning 1

System stabilization was not achieved with 250 ns (as shown by the RMSD analysis, Figure 27), thus the ΔQ 16 simulations were extended to 500 ns. Besides, a third replica was run to improve statistical power.

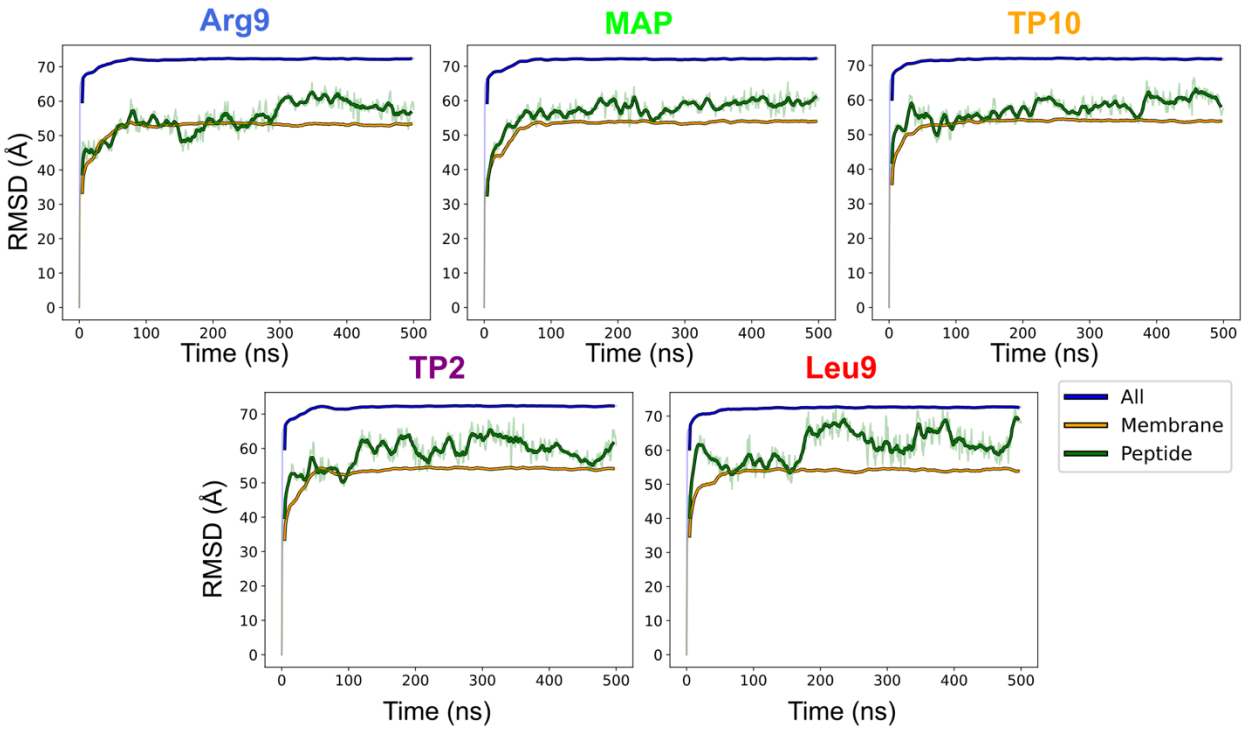

Figure 23. *RMSD analysis of the ΔQ 16 CompEL simulations with 8 peptides. RMSD of the system, the membrane and the peptides are shown.*

As shown in Figure 27A and Table 10, the results reveal different translocation and insertion behaviours among the peptides. From a total of 8 peptides, 1 Arg9 peptide is able to translocate in each replica, achieving a total of 3 translocation events in total in the 3 replicas. MAP shows 1 translocation and 1 insertion in each replica, with a total of 3 translocations and 3 insertions among the 3 replicas. Thus, Arg9 and MAP were the peptides with the highest translocation ratio. For TP10, only 1 TP10 translocates in one replica, whereas in the other two replicas, 2 and 3 TP10 peptides get inserted in the membrane. For TP2, which showed no translocation capacity in simulations with one peptide, 1 TP2 peptide is now able to translocate in 2 replicas, with a total of 2 translocation and 7 insertion events in the 3 replicas. Last, as in simulations with one peptide, Leu9 does not show translocation capacity, but it does show insertion behaviour, with 22 peptides getting inserted across the 3 replicas. In short, ΔQ 16 simulations demonstrate the CPP behaviour of the four CPPs used in the study, whereas Leu9, the negative control without CPP characteristics, can get inserted but has no translocation capacity.

At the molecular level (Figure 25 B-F), Arg9 peptides show two possible behaviours: partitioning, where they get adsorbed to the inner leaflet and interact with the polar heads, or translocation,

where they cross the membrane and interact with the polar heads in the outer leaflet. In both cases, Arg9 interacts with POPC polar heads, owing to the positive charges in Arg9 structure and negative charges in the polar heads, as discussed previously. The opposite behaviour is seen for Leu9 peptides, which mostly get inserted in the membrane, preferring the interaction with the hydrophobic lipid tails. The other 3 CPPs (MAP, TP10, TP2) have hydrophobic, polar, and charged amino acids in their structure and can, therefore, interact with the polar heads in the partition and translocation behaviours, or get inserted and interact with the aliphatic lipid chains.

Regarding the secondary structure (Figure 28), we see similar results to the ones discussed for simulations with one peptide (Figure 22), with Arg9 mainly unstructured, most MAP peptides unstructured, even though some showed β-sheet structure, TP10 with a stable α-helix structure in the C-terminal, and Leu9 gaining secondary structure owing to the membrane insertion. Only TP2 shows considerable differences, since it changes from β-sheet to α-helix, with most peptides unstructured during the simulation, which can be related to a higher partitioning or translocation behaviours and, therefore, lower insertion ratio, typically associated with α-helix formation, as seen for Leu9.

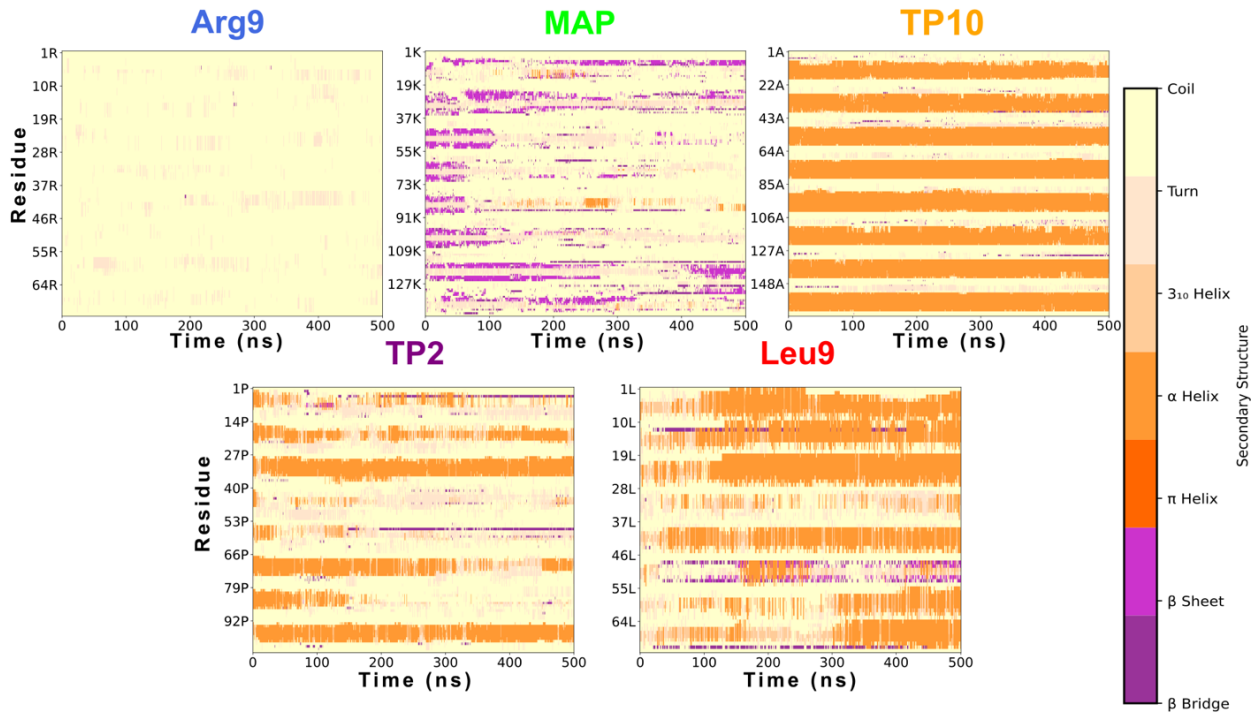

Figure 24. *Secondary structure of the 8 peptides in CompEL ΔQ 16 simulations with 8 peptides. The average of the 3 replicas is displayed.*

Comparing the results to the simulation with one peptide, we see now more translocation or insertion events, demonstrating that peptide-peptide interactions are relevant for translocation capacity[152,247,285]. However, the high numbers affect differently for each peptide. As seen in Figure 25B, Arg9 peptides do not show strong interaction among them[233,297,303,304] and, instead, Arg9 peptides primarily interact and form H bonds with lipids (Figure 29).

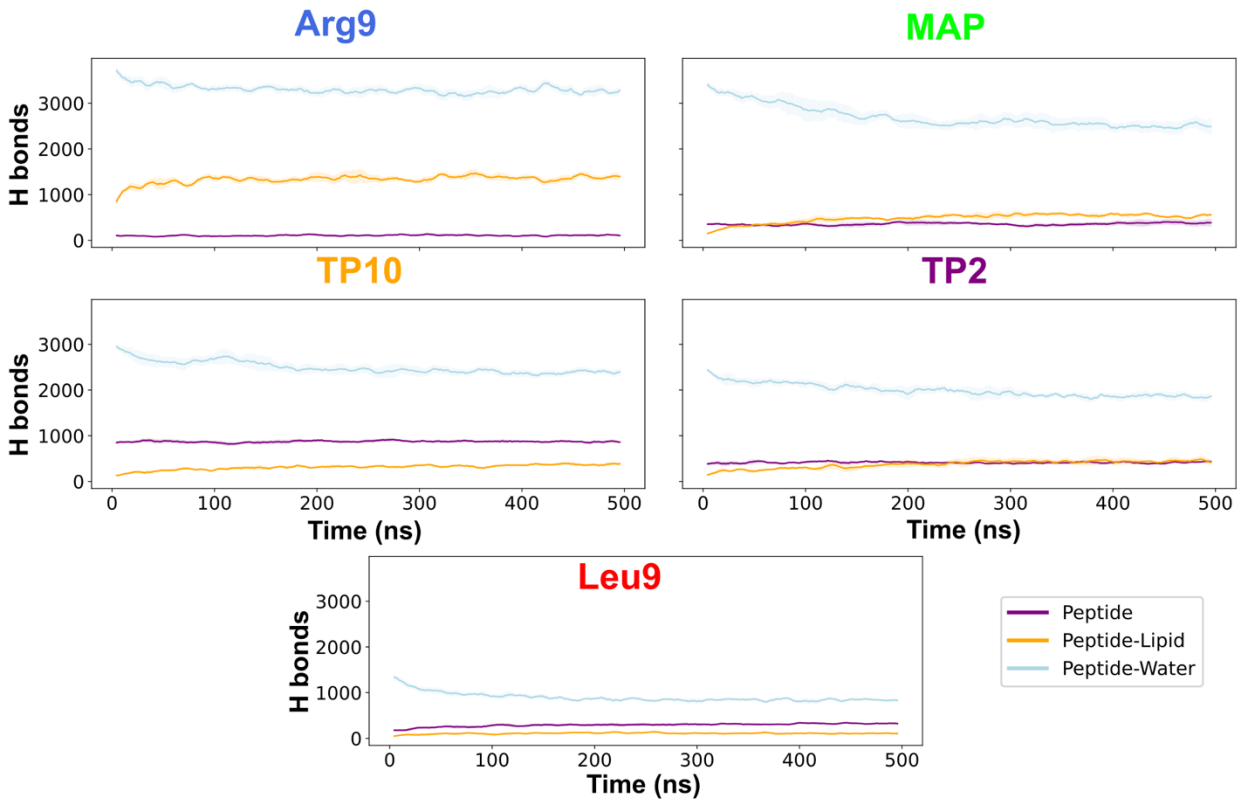

Figure 25. *Hydrogen bond analysis of the CompEL ΔQ 16 simulations with 8 peptides. The average H bond ratios between protein-protein (purple), protein-lipid (orange), and protein-water (cyan) are shown as lines. The shaded areas represent the standard deviation across replicas.*

Besides, Arg9 peptides form most of the protein-protein bonds within the same peptide (80 % intra-protein H bonds) (Table 11), indicating that Arg9 peptides are mostly present in the monomeric form. Conversely, the other four peptides do show cooperativity[289], supported by a higher inter-peptide H bond ratio (Table 11). Specially, Leu9 and TP2 show the highest self-assembly capacity to get inserted in the membrane[305]. Leu9 shows the highest self-assembly capacity, preferably interacting among them or with lipids tails.

Table 11. *Average ratio of intra-peptide H bonds formed during the 3 replicas of 500 ns of CompEL ΔQ 16 simulations with 8 peptides. Standard error of the mean (SEM) values are shown.*

H bonds	Arg9	MAP	TP10	TP2	Leu9
Average	82.5 ± 0.7	60.7 ± 3.5	57.8 ± 4.2	51.7 ± 4.9	51.8 ± 1.9

A closer look at the pore is seen in Figure 30, where we see how Leu9 peptides can stabilize the pore. In order to do so, Leu9 peptides present the polar atoms (N, O) oriented to the water molecules, whereas C atoms point to the aliphatic lipidic acyl chains.

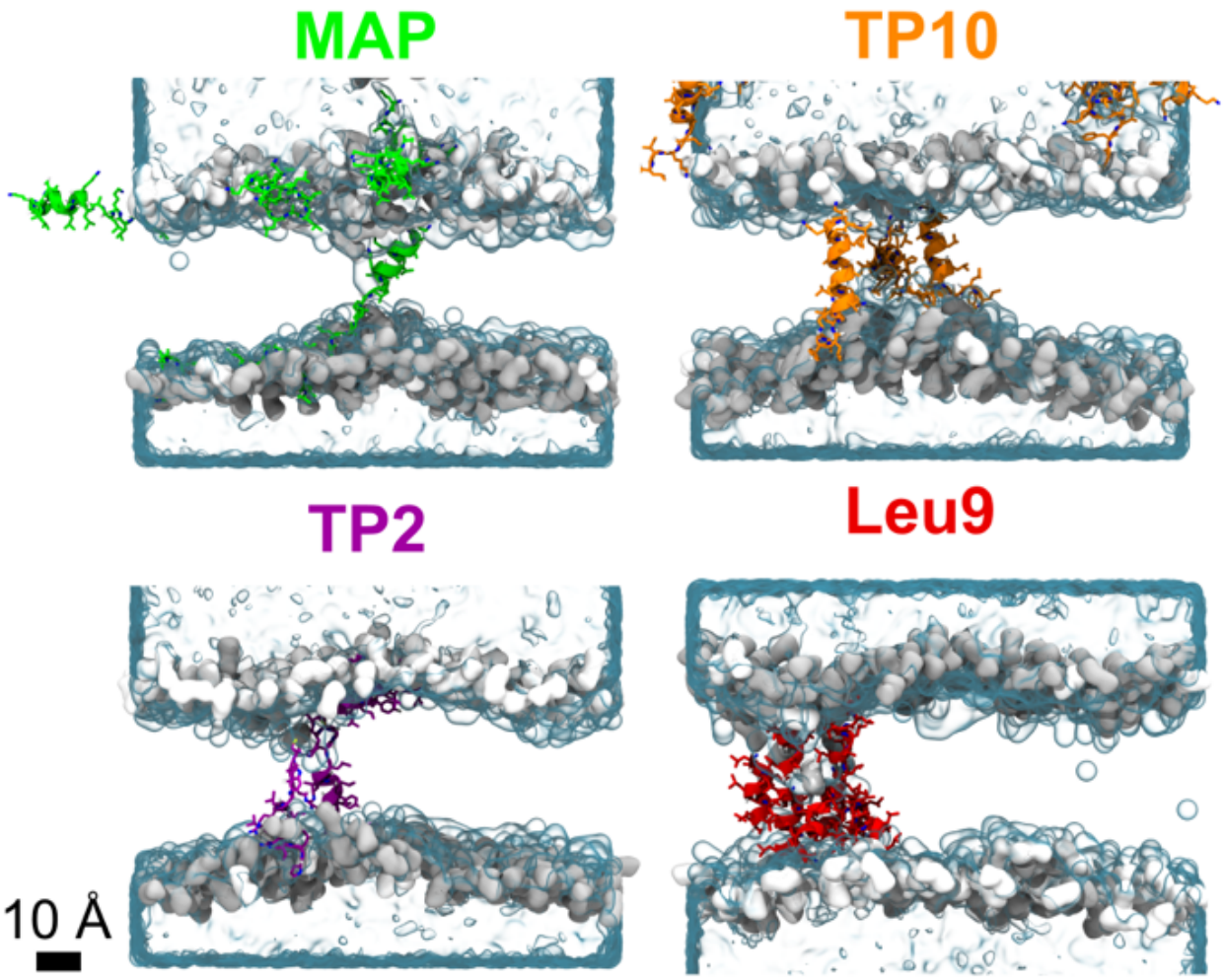

Figure 26. *Pore molecular representation. Only peptides that get stabilized inserted in the membrane or in pores are shown (Arg9 does not get stabilized in the membrane and is, thus, not shown). Peptides are shown as cartoon and the sidechain as licorice, with C atoms in the peptide colour, N atoms in blue and O in white. Polar heads and water residues are represented as surface, and coloured as white (inner), grey (outer), and cyan (waters). A scale bar is added for size clarity.*

3.2.3.3.2. Membrane disruption analysis

Table 12 shows the pore analyses conducted for ΔQ 16 simulations with 8 peptides. Arg9 and MAP do not contribute to the pore persistence, but TP10, TP2, and, specially, Leu9 are able to stabilize it.

Table 12. *Average pore radius (Å) during the 500 ns of CompEL ΔQ 16 simulation with 8 peptides. SD values are shown. The pore radius is averaged over all frames in the simulation. (B) The second part of the table indicates the number of peptides involved in pore formation in each replica. (A)*

# Replica	Arg9	MAP	TP10	TP2	Leu9
1	6.2 ± 1.5 1 peptide	6.2 ± 1.6 1 peptide	11.5 ± 2.2 3 peptides	4.7 ± 1.2 2 peptides	15.5 ± 2.3 7 peptides
2	5.3 ± 1.4 1 peptide	5.5 ± 1.4 1 peptide	5.7 ± 1.6 1 peptide	10.6 ± 2.1 3 peptides	20.1 ± 2.7 8 peptides
3	6.0 ± 1.5 1 peptide	5.7 ± 1.5 1 peptide	9.3 ± 1.8 2 peptides	16.7 ± 2.3 3 peptides	24.7 ± 3.8 7 peptides
Average	**5.3 ± 0.5**	**5.8 ± 0.5**	**8.8 ± 0.9**	**10.7 ± 0.8**	**20.1 ± 1.6**

This behaviour is depicted in Figure 30, where we see how one MAP peptide is inserted in the bilayer, but does not allow water flow, opposite to TP10, TP2, and Leu9, which cooperate and are able to stabilize the pore through the formation of a barrel-stave-like pore[278], with mostly peptides stabilizing the pore. The pore nature is different from the one seen for simulations with one peptide, where the polar heads played a higher part in pore formation.

These simulations have also allowed us to observe lipid flip flop from upper to lower leaflet (Figure 25B-F). Lipid flip-flop occurs at the same time as the peptide is translocating across the water channel[233,247,301,306,307], from the peptide-enriched to the peptide-free bilayers[301].

In Figure 31, snapshots of the translocation (A-G) and insertion (H-M) processes are shown. The phases of pore creation and annihilation are compared to those described by Levine & Vernier[293]. Taking the Arg9 simulations, we observe a 4-step process. First, pore formation starts with a water defect, resulting in the interaction of water molecules from both water compartments, defined as pore initiation (Figure 31B). As seen in the previous section, peptides are not responsible for this process. Second, pore construction (Figure 31C) takes place, where polar heads from both bilayers

enter in contact, which is followed by pore maturation (Figure 31D), characterized by a large number of waters and polar heads in the pore. In this step we can see how peptides get attracted to these pores. Third, one Arg9 peptide gets inserted into the membrane through the pore (Figure 31E). The peptide remains stable in the pore for approximately 300 ns, until it crosses to the lower leaflet and starts the process of pore annihilation (Figure 31F). Pore closure involves i) pore degradation, when water molecules and polar heads start to migrate out of the bilayer and the pore starts to thin, and ii) pore deconstruction, when there are no polar heads involved in the pore formation. Fourth and last, the Arg9 peptide has crossed the bilayer and stabilized in the lower leaflet, triggering pore dissolution (Figure 31G) and completing pore annihilation, when all water molecules are expulsed from the membrane.

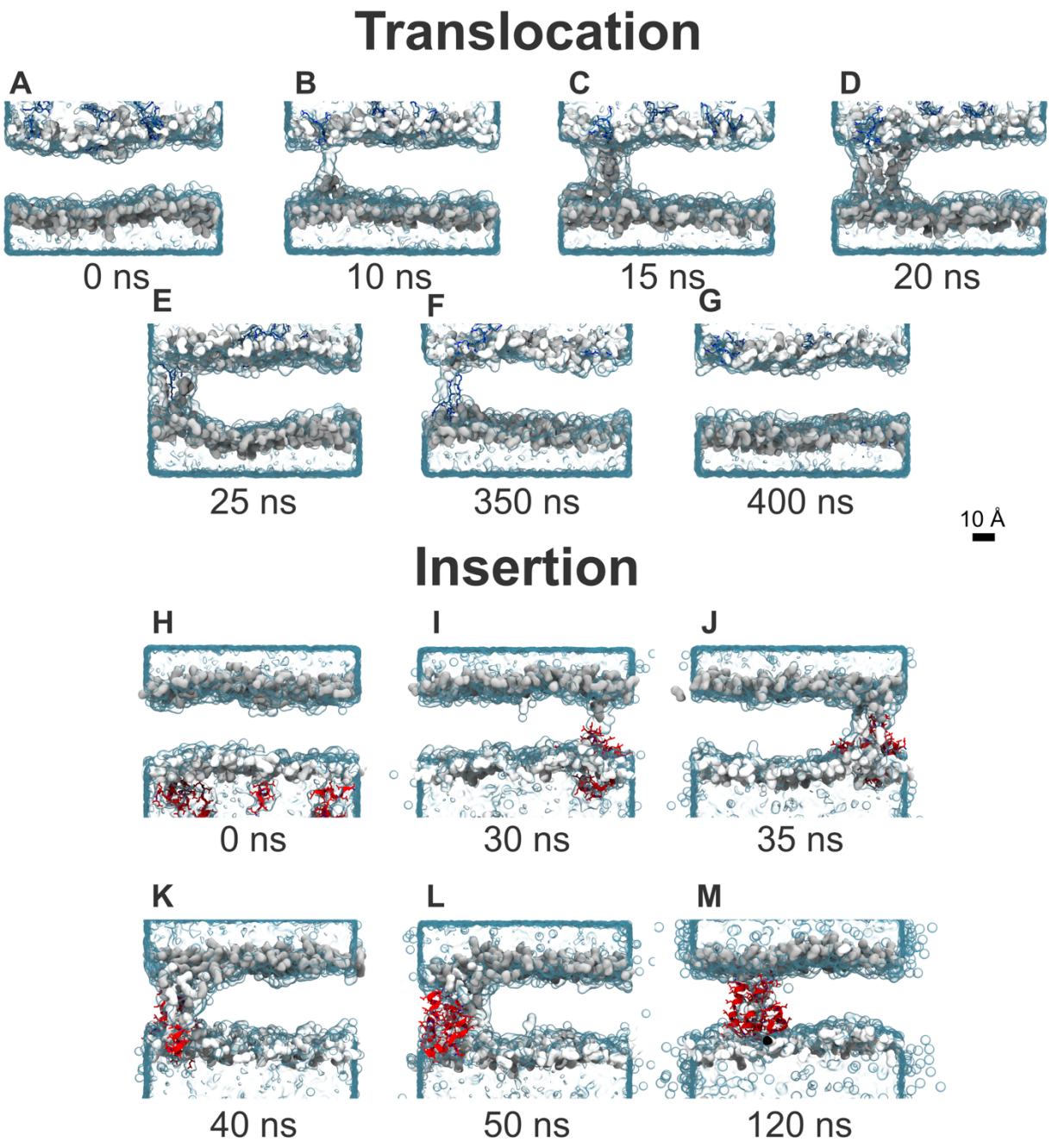

Figure 27. *1. Arg9 translocation procedure in CompEL ΔQ 16 simulation with 8 peptides. Representative snapshots illustrate the structural organization of the membrane during the translocation process, portraying the key steps: (A) simulation start, some peptides adsorb to the bilayer surface, (B) pore initiation, with water molecules entering in contact, (C) pore construction, the polar heads from both bilayers interact, (D) pore maturation, with polar heads connected, resulting in a larger pore; a peptide gets attracted to the pore and starts the insertion, (E) one peptide gets inserted into the pore, (F) the peptide reaches the lower leaflet, causing pore deconstruction, with no more interactions between polar heads, and (G) the peptide finalizes the translocation and stabilizes into the outer leaflet, leading to pore dissolution. 2. Leu9 insertion procedure in CompEL ΔQ 16 simulation with 8 peptides. (H) Start of the simulation, (I) Pore initiation, and peptide insertion, (J) Pore construction, (K) Pore maturation, (L) More peptides insertion, and (M) Eight peptides insertion. Arg9 and Leu9 peptides are coloured in cornflower blue and red respectively, and represented as*

Cartoon, while showing the sidechain atoms (C in cornflower blue or red, respectively, N in darker blue, O in white). The polar heads surface is shown and coloured based on the bilayer: inner in white, outer in grey. Water molecules are shown as transparent cyan surface. Lipid tails are omitted for clarity

A similar process is followed in the first steps of Leu9 peptides insertion. First, a water defect is created, and the pore initiation starts, with one Leu9 peptide already close to the formed pore (Figure 31I). Second, pore construction and peptide insertion happen concomitantly (Figure 31J), followed by pore maturation (Figure 31K). Third, more peptides get attracted to the pore and get inserted in the membrane (Figure 31L), until all peptides are stabilizing the pore (Figure 31M), structure stable during the rest of the 500 ns simulation. In Figure 31, we can also see how peptides are parallel to the membrane when they are partitioning, rotate and are perpendicularly oriented to the bilayer when they achieve insertion, and they finally adopt an orientation parallel to the bilayer when they complete the translocation[301].

3.2.3.4.CompEL analysis

In the CompEL simulations, we have seen how CPPs are able to use the pores formed due to ion imbalance to internalize[296,304]. Moreover, when a CPP translocates, it is able to trigger pore closure[152,235,304] (Figure 31D), with rapid water expulsion from the membrane[293], as seen for Arg9 and MAP, which have the least average pore sizes (still, this may be related to the underlying charge imbalance in CompEL, and further studies need to be conducted to confirm this statement). TP10 only translocates in the second replica (Table 10), precisely the one in which pore closure occurs (Table 12), confirming the relationship between these two events. TP2 also shows translocation in two of the replicas, but pore closure is not seen, which can be related to the TP2 lower net charge (+2), possibly not being enough to reduce the transmembrane potential under the pore-forming threshold. Still, we hypothesize that in longer timescales, more TP2 peptides are able to translocate, ultimately inducing pore closure (we extended the TP2 simulations to 1 μs, but no significative changes were observed, so larger timescales may be needed). In short, the four CPPs have demonstrated translocation capabilities, as opposed to our previous CPP study, where only Arg9 (TP10 was not studied) was able to achieve translocation. In this sense, we have seen how CPP translocation can occur through pore formation, leading to pore closure and potentially explaining the lack of cell toxicity of CPP translocation[308]. On the other hand, Leu9 causes larger pore sizes, marking the difference compared to peptides with CPP characteristics, since Leu9

peptides are not able to translocate and they are indeed able to stabilize the pore, a behaviour correlated with other bioactive peptides such as antimicrobial peptides (AMPs)[301].

Charge seems to be an important factor in deciding translocation, so simulations containing K-FGF[65], a neutral CPP, and Dynorphin A[121,309], a positively charged peptide that does not show internalization behaviour, as seen in Chapter IV (Table 7), have been run. Both systems containing 8 peptides and ΔQ 16, showed no translocation behaviours, with only insertion or partitioning in both cases (Figure 32). Therefore, we can conclude that the charge is not the sole determinant of the translocation process in CompEL.

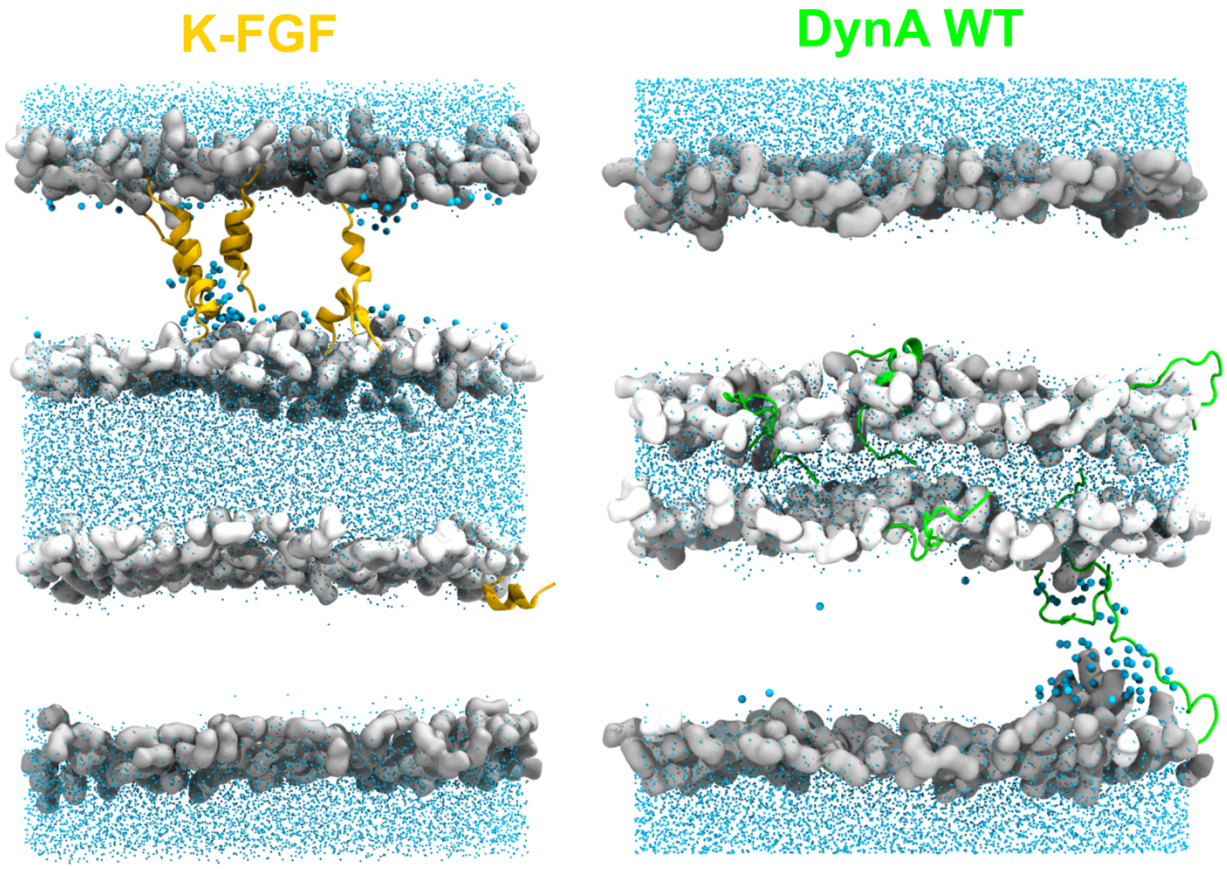

Figure 28. *Outcome of CompEL ΔQ 16 simulations with 8 peptides of K-FGF (left) and Dynorphin A wild type (WT, right). In average for the three replicas, 7 K-FGF and 2 DynA WT peptides get inserted in the membrane. K-FGF (yellow/orange) and Dynorphin A (green) peptides are shown as cartoon. Lipid polar heads residues are represented as surface and coloured as white (inner water compartment) or grey (outer water compartment). Waters are represented as licorice and coloured in cyan, with larger water molecules representing the waters present in the pore channel.*

In conclusion, CompEL simulations are valuable for enhancing the dynamics of the system by inducing pore generation thanks to the ion imbalance. According to the CPP translocation process[58,231], peptides adsorb or partition to the upper leaflet. They then destabilize the membrane while attempting to reach the polar heads in the lower leaflet, ultimately causing pore formation and allowing peptide translocation. However, it is challenging to observe pore formation in cMD, owing to the energetic cost of the process[291]. Precisely, CompEL allows for pore formation, thus enabling the observation of unbiased translocation of CPPs.

3.2.4. Conclusions

In this study, we have performed CompEL simulations to study CPP behaviour under applied potential in model lipid membranes. The first step in CPP translocation through pore formation is the peptide adsorption to the membrane, destabilizing the membrane and allowing pore formation, which the CPPs will use to translocate. However, to observe the complete translocation in cMD simulations is cumbersome, owing to the energetic cost of pore formation. Precisely, CompEL enhances pore formation via ion imbalance in the membrane, allowing the computational study of CPP translocation.

In short, in ΔQ 16 CompEL simulations with one peptide, TP10 showed the highest translocation capacity, followed by Arg9 and MAP, with TP2 and Leu9 not showing internalization behaviour. More translocation events were seen in ΔQ 16 CompEL simulations with eight peptides, where Arg9 and MAP showed the highest translocation capacity, followed by TP2 and TP10. Moreover, CompEL simulations have also revealed that once pores spontaneously form in the cell membrane under charge imbalance conditions, peptides can stabilize them (such as Leu9) or translocate through them (such as Arg9, MAP, TP10, or TP2).

We present CompEL, a method with significantly lower computational requirements compared to US, where up to 4 μs[235] are needed. Besides, CompEL is entry-level, easier to parallelize, and less GPU-intensive than aSMD. In this study, simulations at several ΔQ values were required to perform method calibration, but in subsequent studies, simulations at only one ΔQ (e.g. ΔQ16) need to be run, considerably decreasing the overall computational cost. Additionally, CompEL increases the feasibility of performing replicas and allows simulations with higher number of peptides, being able to analyse peptide cooperativity or aggregation. Moreover, CompEL is an

enhanced molecular dynamics technique, but contrary to aSMD or US, in CompEL the peptide is not forced to cross the membrane, rather it provides an unbiased exploration of the peptide-membrane interaction. Thus, CompEL can be used to describe at the molecular level the peptide interaction with the membrane, and with higher resolution than coarse-graining methods. Simulations using a potential difference and a single membrane can be conducted, but peptides may translocate to the opposite membrane via the PBC, which is prevented in CompEL, enabling the encapsulation of peptides between two membranes, which also simplifies analysis and enhances control over the system.

We believe that this study can be a first step in the use of CompEL for CPPs computational research. However, CompEL simulations only account for CPP translocation via pore formation, whereas CPPs can internalize through additional mechanisms, as discussed in the introduction. Besides, this study only conducted simulations with neutral, zwitterionic POPC bilayers; future work should explore negatively charged bilayers (e.g., containing POPS or POPG) and more physiologically relevant compositions (e.g., asymmetric containing POPE or cholesterol) in order to perfect this technique. Lastly, CompEL requires the application of a high voltage, which necessitates cautious interpretation of the results. Additional simulations may be needed to further increase the sampling of the systems, possibly combining CompEL with elevated temperatures to increase molecular mobility. Future studies should also investigate different P:L ratios to assess the influence of P:L ratio in CPP internalization.

In conclusion, we propose the use of CompEL to computationally study CPP insertion or translocation at a molecular level, which is challenging to achieve with other techniques. Furthermore, CompEL can be expanded to study the interaction of other types of membrane active peptides, such as AMPs, antiviral, or anticancer peptides.

3.3. Chapter III: membrane composition modulates peptide disruption mechanisms revealed by computational electrophysiology

In this chapter, we expand the use of CompEL technique to more complex and biologically relevant membranes. Here, we focus on objectives 1,2,3 and specific objectives 1,2,3,4,5.

3.3.1. Introduction

Cell-penetrating peptides (CPPs) are short, cationic peptides that are capable of interacting with membranes and translocating them without causing cytotoxicity[30,54,86]. Besides, they can be coupled with cargos in order to deliver them intracellularly[115,238]. Understanding the physicochemical features behind their translocation mechanisms, including lipid perturbation, pore formation, and direct penetration, is key to improve the design and efficiency of CPPs and membrane active peptides (those that engage with membranes to exert their action[25]) in general. However, the determination of factors affecting translocation is challenging experimentally due to the involved nanoscopic length and time scales. Therefore, computational methods have emerged as tools that can complement such studies by providing atomistic detail and controlling environmental parameters, such as membrane composition, temperature, ion concentration, and pH. Methods range from molecular dynamics (MD) simulations designed to capture atomistic details, to machine-learning (ML) models that predict CPP propensity based solely on sequence descriptors[310–313].

In the molecular study of CPP, MD simulations provide insights into conformational transitions, peptide–lipid binding events, and membrane perturbation. However, the translocation of a CPP is a process that takes from seconds to minutes[140], which is computationally too expensive to observe in a conventional MD (cMD). Therefore, enhanced sampling techniques are necessary tools in CPP study.

In this regard, various methods have been presented. For instance, Steered Molecular Dynamics (SMD)[141,204] can be used to force the movement of the CPP through the membrane, allowing for the calculation of translocation energy. Similarly, Umbrella Sampling (US)[146,314] allows computing the cost of translocation through the use of several windows throughout the process. In parallel, Weighted Ensemble (WE)[149,150] consists of partitioning the configuration space into bins along defined progress coordinates and systematically replicating or pruning simulation trajectories (walkers) within these bins. Furthermore, in a previous study, we presented the combination of adaptive Steered Molecular Dynamics (aSMD) in combination with cMD, which can be used to compute the translocation energy path, and to observe the molecular disruption of membranes caused by CPPs. However, such methods are biased and are, generally, computationally demanding or are not readily accessible. Therefore, we presented Computational

Electrophysiology (CompEL) for the study of CPPs. In this technique, a transmembrane potential through ion imbalance (ΔQ) is used to induce membrane disruption, allowing the peptides to get inserted or translocate without the need of reaction coordinates.

In our previous study, we explored the use of CompEL in POPC membranes, using 1 and 8 peptides, and different ΔQ potentials. We concluded that the best conditions to study peptide–mediated membrane disruption was to employ 8 peptides and a ΔQ of 16 (that is, 8 positive charges in the inner water compartment and 8 negative charges in the outer water compartment, see Figure 33 for clarification). However, our study was limited to POPC membranes, and we now expand its use to more complex membranes.

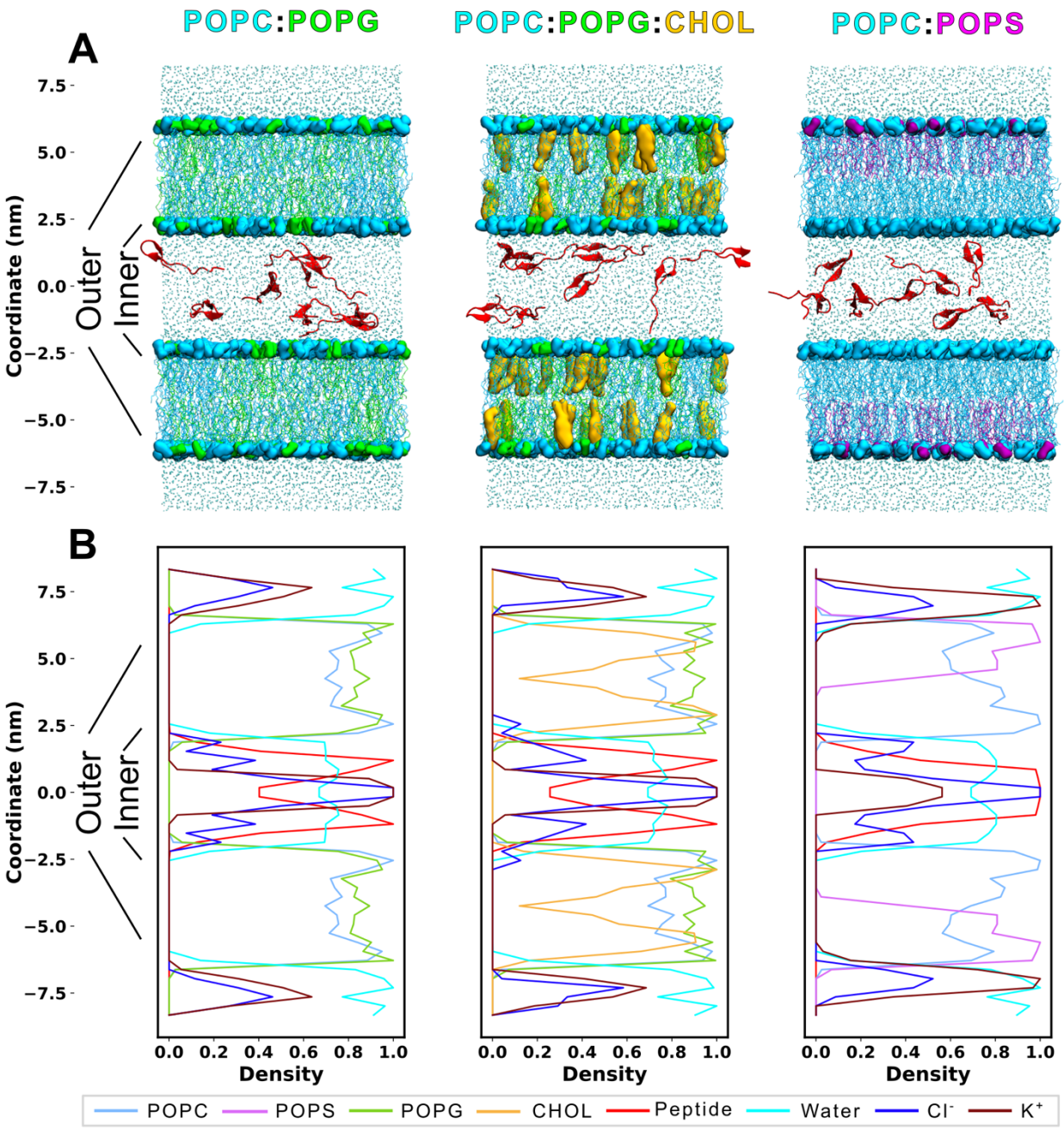

Figure 29. *System set-up. (A) Molecular representation of the starting point of the membranes. The polar heads for POPC (coloured in light blue), POPG (in green), and POPS (in purple) are shown as QuickSurf, whereas lipid tails are represented as lines. Cholesterol (yellow) is shown as QuickSurf, and the peptides (red) are represented as NewCartoon. Water residues are shown as licorice (cyan). Inner and outer leaflets for both membranes are indicated. Peptides starting point in all simulations is the inner water compartment. (B) Electron density analysis. The density values have been normalized for each individual species.*

Here, the objectives are to describe the membrane disrupting potential of a model CPP, such as the model amphipathic peptide (MAP–KLALKLALKALKAALKLA)[56], in membranes of different complexity, and to observe the unbiased translocation of MAP in more biologically relevant membranes. Moreover, we compare computational results with experimental studies. Hopefully, we aim to present a computational method able to discriminate peptides with translocating capacity, and to be able to establish an entry-level method for the computational study of peptide–membrane interactions.

3.3.2. Computational and experimental methods

3.3.2.1.Peptide simulation

The same MAP peptide model as in our previous study was used. Briefly, MAP was modelled using AlphaFold 3[315]. Then, the peptide was introduced in a box of 7.5x7.5x7.5 nm and solvated with TIP3P waters. The system was minimized during 5000 steps, equilibrated in the NVT ensemble during 125 000 steps, and a 250 ns production was run. CHARMM36m force field was selected. GROMACS[269–272,316–319] software was used, specifically employing GROMACS 2020.7 package. The temperature was kept at 350 K throughout the study with the aim of accelerating the system dynamics. Periodic boundary conditions (PBC) were applied.

Clustering analysis of the peptide 250 ns trajectory was performed using MDAnalysis package in Python[210,211]. Later, the obtained centroid structure was used as input for the CompEL simulations.

3.3.2.2.Membrane systems set-up

Three membrane compositions were used. First, a symmetric membrane composed of POPC, and POPG, using a 7:3 POPC:POPG ratio, namely POPC:POPG. Second, a symmetric cholesterol–containing membrane using a 6:3:1 POPC:POPG:CHOL ratio, namely POPC:POPG:CHOL. Third, an asymmetric membrane with POPC and POPS, with only POPC in the upper leaflet, and POPC:POPS with a 7:3 ratio in the lower leaflet, namely POPC:POPS membrane. Specific lipid compositions for all three membranes are displayed in Table 13. Systems without ions were built using CHARMM-GUI[187,188,192] web server, solvating with TIP3P water. Ions were added in the CompEL set-up part.

Table 13. *Membrane compositions.*

Membrane	Lipid ratio in upper leaflet	Lipid ratio in lower leaflet	Lipids in upper leaflet	Lipids in lower leaflet
POPC:POPG	7:3 POPC:POPG	7:3 POPC:POPG	90 POPC, 38 POPG	90 POPC, 38 POPG
POPC POPG:CHOL	6:3:1 POPC: POPG:CHOL	6:3:1 POPC: POPG:CHOL	77 POPC, 38 POPG, 13 CHOL	77 POPC, 38 POPG, 13 CHOL
POPC:POPS	1 POPC	7:3 POPC:POPS	128 POPC	92 POPC, 40 POPS

3.3.2.3.CompEL set-up

CompEL involves the generation of a transmembrane potential through ion imbalance, ΔQ, between both sides of the membrane. However, since PBC are applied, a double membrane configuration is required. To generate the desired transmembrane potential between one side and the other of the membrane, membrane systems without ions, obtained with CHARMM-GUI server, were used as input. The system was then duplicated, the second system was rotated, the box size was doubled, and both system files were concatenated into a single box with a double membrane configuration, as described in our previous study. Then, *gmx insert-molecules* utility was used to obtain a ΔQ 16. The number of ions required to generate such ΔQ are in Table 14. As can be seen, the goal is to obtain a total net charge of +8 in the inner water space, and -8 in the outer water compartment. After that, 8 peptides are inserted in the inner water compartment, along with the necessary counterions (5 per MAP peptide).

Table 14. *Ion composition in the different CompEL set-ups.*

Membrane	0 ΔQ				16 ΔQ			
	K+ inner space	**Cl- inner space**	**K+ outer space**	**Cl- inner space**	**K+ inner space**	**Cl- inner space***	**K+ outer space**	**Cl- inner space**
POPC:POPG	102	26	102	26	106	22	98	30
POPC POPG:CHOL	102	26	102	26	106	22	98	30
POPC:POPS	67	27	67	27	71	23	63	31

CompEL systems were minimized during 5 000 steps and equilibrated for ca. 2 ns. The equilibration procedure was run in six steps of 125, 125, 125, 500, 500, 500 ps, while lowering the positional restraints in each step: 1 000, 400, 400, 200, 40, 0 $kJ \cdot mol^{-1} \cdot nm^{-2}$, respectively. Finally, equilibrated systems were simulated during 500 ns, with 3 replicas for each system. Computational electrophysiology protocol[259,263] was used in order to control ion/water position exchanges (all production files have been uploaded to the GitHub repository). Thus, a total of 4.5 μs have been run for MAP simulations. Two replicas of control membranes(without peptides) have been also run, totalling 3 μs for control simulations, and 7.5 μs in total. Simulations have been run in a workstation with a GPU RTX3080Ti, at approximately 70 ns per day.

3.3.2.4.Simulation analysis

Simulation analysis was performed in a Jupyter Notebook integrated development environment (IDE)[268]. Matplotlib[216] was used for figure plotting. MDAnalysis[210,211] was used to analyse system compositions, RMSD, and membrane thickness. *gmx* utilities were used to calculate electron density, potentials, and H bonds. PyLipID[208] was employed to calculate occupancy. VMD[206] was used for visual plotting and to analyse secondary structure using STRIDE[273]. Peptide angle has been analysed using the method presented in[233]: i) calculate the centre of masses of the first three and the last three residues involved in the α-helix, ii) find the vector connecting these two centres of masses, and iii) compute the angle between this vector and a unit vector parallel to the normal of the membrane. Thus, this script calculates the angle of the peptide with regard to the membrane normal. Consequently, a value close to 90º indicates that the peptide is perpendicular to the membrane normal or, in other words, the peptide is parallel to the membrane plane. Conversely, values closer to 0º indicate a peptide parallel to the membrane normal and perpendicular to the membrane plane. An in-house Python script using Scipy[274] was developed to calculate the radius pore size. Briefly, the script calculates the maximum distance between water molecules through each membrane z-stack (2 Å thick) and run throughout all simulation frames. Lipid order parameter was calculated using Equation 1.

3.3.2.5.Liposome leakage experiments

POPC (Affymetrix, California, USA), POPG (Avanti, Alabama, USA), and CHOL (Sigma-Aldrich, Missouri, USA) were dissolved in a chloroform/methanol mixture (2:1, v/v) to prepare

lipid solutions with the following compositions: POPC alone, POPC:POPG (7:3 molar ratio), and POPC:POPG:CHOL (6:3:1 molar ratio). Liposomes were prepared as previously described[320]. Briefly, the organic lipid mixtures were evaporated under reduced pressure to form a thin film. This film was hydrated with 10 mM phosphate buffer (pH 7.2) containing 2 mM 8-hydroxypyrene-1,3,6-trisulfonic acid (HPTS), yielding multilamellar vesicles at a total lipid concentration of 10 mM. The vesicles were subsequently downsized by sequential extrusion through polycarbonate membranes with pore sizes of 800, 400, 200, and 100 nm. Dynamic light scattering (DLS, Nanotrac Wave, Microtrac, USA) revealed average radii of 120 nm for POPC liposomes and 90 nm for both POPC:POPG and POPC:POPG:CHOL liposomes. Non-encapsulated HPTS was removed by size-exclusion chromatography (SEC) using Sephadex G-25 PD-10 columns (Amersham Biosciences). Purified liposomes were then supplemented with p-xylene-bis-pyridinium bromide (DPX, Fisher Scientific) to final concentrations of 5 μM DPX and 100 μM total lipid. The HPTS-loaded, DPX-containing liposomes were transferred into black, clear-bottom 96-well plates. Fluorescence was recorded over time using excitation and emission wavelengths of 420 nm and 520 nm, respectively, on a FLUOstar Optima microplate reader (BMG LABTECH, Germany). The effect of peptides was assessed by adding them to the wells at a final concentration of 5 μM. After 4,000 s, complete fluorescence quenching was achieved by solubilizing liposomes with Triton X-100 (Sigma-Aldrich) at a final concentration of 5 μM. Data shown represent the average of three independent experiments.

3.3.2.6.Internalization and viability assay

HEK293, SH-SY5Y, and CaCO-2 human cell lines were seeded in 24-well plates at a density of 200,000 cells per well and incubated for 48 hours prior to treatment. Cells were then exposed in triplicate to TAMRA (5(6)-Carboxytetramethylrhodamine; Novabiochem®, Merck/Sigma-Aldrich, Cat. No. 851030) and TAMRA-labelled peptides at a final concentration of 1 μM for 1.5 hours. Following treatment, cells were harvested by trypsinization, washed and resuspended in flow cytometry buffer (PBS supplemented with 5% FBS). Cells were stained with 1ug/ml DAPI (ref: D9542(Merck)).

Flow cytometric analysis was performed using a CytoFLEX LX flow cytometer (Beckman Coulter), acquiring 10,000 events per sample. Doublets and aggregates were excluded by gating on forward scatter height versus area (FSC-H vs FSC-A) and side scatter width versus height (SSC-

W vs SSC-H), respectively. Cell viability was assessed using DAPI staining, detected with excitation at 405 nm and emission collected at 450/45 nm. TAMRA fluorescence was detected using excitation at 561 nm and emission collected at 610/42 nm. Data were analysed using CytExpert software (Beckman Coulter), and TAMRA signal was quantified as median fluorescence intensity (MFI) in viable, single-cell populations.

3.3.3. Results

In our previous study, we concluded that the computational study of membrane disruption by CPPs or bioactive peptides can be pursued with CompEL simulations. In this case, simulations with ΔQ 16 and 8 peptides was the most effective option to discriminate between peptides. However, our study was limited to symmetric POPC membranes. Here, we expand the use of CompEL to negatively charged, cholesterol–containing, and asymmetric membranes in order to discuss the effect of such lipids in peptide–mediated membrane disruption potential.

Hence, we run 3 replicas of 500 ns of CompEL ΔQ 16 simulations in POPC:POPG (7:3) and POPC:POPG:CHOL (6:3:1) symmetric membranes, and POPC:POPS asymmetric membrane (with POPS only in the outer membrane, at 7:3 POPC:POPS ratio). Further, we perform liposome leakage experiments with POPC:POPG and POPC:POPG:CHOL at the same ratios to compare them with computational simulations, as well as internalization assays in HEK293 cells to relate them to the asymmetric membrane simulations, a simplified cell membrane model containing negative lipids in the intracellular leaflet (Figure 33).

In this study we limit the simulations to MAP to present the method and leave a further characterization for future studies. In all cases, 8 MAP peptides have been added to the inner water compartment, delimited by both inner leaflets, marking the starting point of the CompEL simulations. The inner leaflets represent the extracellular side of the membrane, that is, the side that peptides would first encounter in a cell, whereas the outer leaflets and the outer water compartment represent the intracellular membrane and intracellular cytosol, respectively.

In the simulations, we differentiate between three behaviours. i) Partitioning: the peptide transitions from aqueous phase to the water–bilayer interface, interacting with the inner leaflet, ii) insertion: the peptide penetrates deeper into the bilayer, reaching the hydrophobic core and establishing contacts with the lipid tails and, in some cases, with the polar heads of the outer leaflet,

and iii) translocation: the peptide crosses further through the bilayer, interacting predominantly with the polar heads of the outer leaflet.

3.3.3.1.POPC:POPG

In POPC:POPG CompEL ΔQ 16 simulations, the most common result among replicas (see Table 15 for complete description of replicas results) is the insertion of two MAP peptides (out of 8 peptides in total, Figure 34A).

Table 15. *Peptide results for each CompEL ΔQ 16 simulation.*

Replica	POPC:POPG	POPC:POPG:CHOL	POPC:POPS
1	8 partitioning	1 insertion, 7 partitioning	1 translocation, 1 insertion, 6 partitioning
2	2 insertions, 6 partitioning	1 insertion, 7 partitioning	1 insertion, 7 partitioning
3	2 insertions, 6 partitioning	1 insertion, 7 partitioning	1 translocation, 7 partitioning

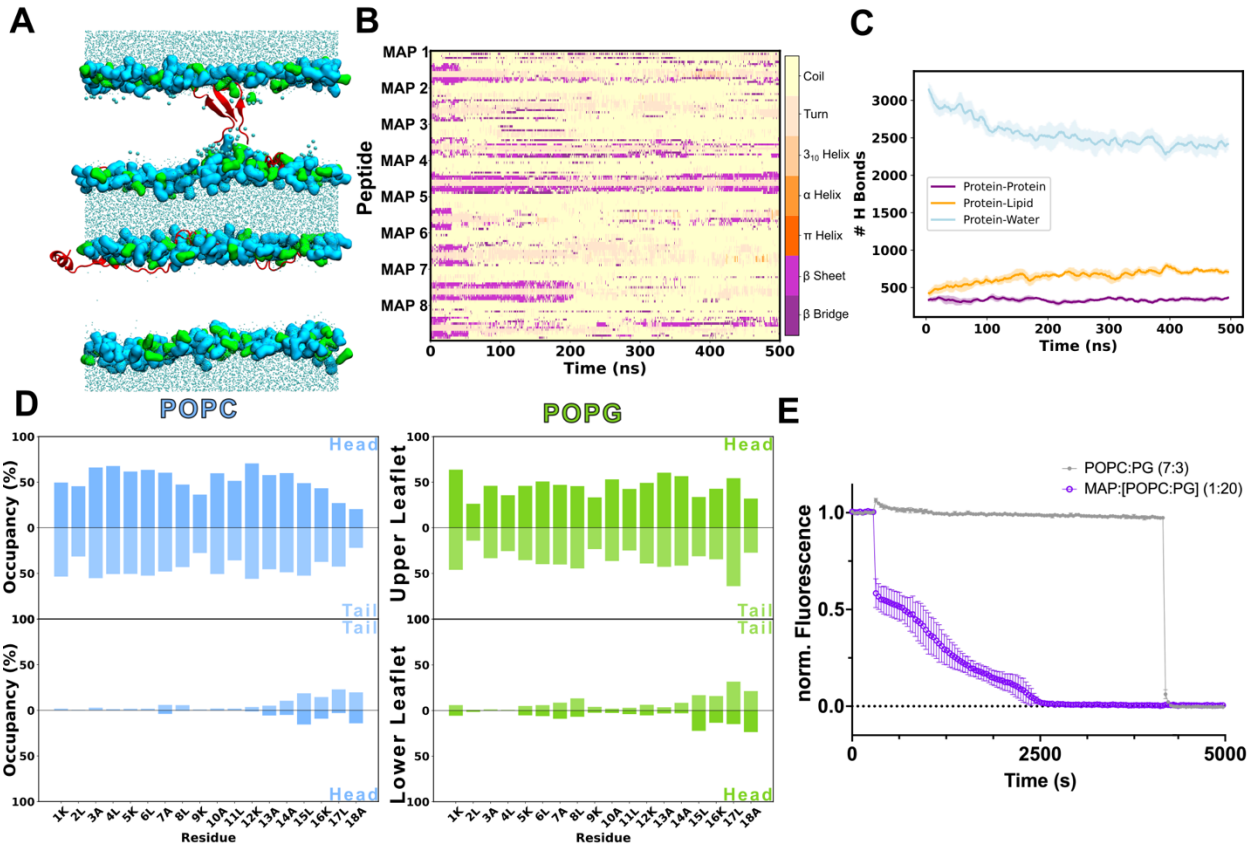

Figure 30. *POPC:POPG CompEL 16 ΔQ 500 ns simulation with 8 MAP peptides results. (A) Representative molecular configuration at the end of the 500 ns CompEL simulation. 2 peptides achieve insertion, whereas the other 6 peptides are partitioning with the inner leaflets. Lipid polar heads are represented in QuickSurf and coloured in light blue (POPC) or green (POPG). Peptides are represented as NewCartoon and coloured in red. Water molecules are shown as licorice and coloured in cyan, whereas larger water residues are used for the water molecules in the pore. Lipid tails are omitted for clarity. (B) Secondary structure evolution throughout the simulation. The average between the three replicas is shown. (C) Average number of hydrogen bonds formed during the simulation. (D) Average residue occupancy by POPC (left) or POPG (right). The occupancy is differentiated between upper and lower leaflets, and between lipid heads (darker blue) or tails (lighter blue).(E) Liposome leakage assays monitored by HPTS fluorescence quenching. Fluorescence traces are shown for liposomes in the absence of peptide (control, grey) and after addition of MAP (5 μM, purple).*

Peptide insertion is related to an increase in pore radius (Table 16) compared to the control simulations (without peptides, Table 17), showing that the pore is formed owing to the transmembrane potential through ion imbalance, but the pore can be transient and get rapidly closed, or get stabilized by peptide insertion, as seen for MAP in replicas 2 and 3 (Table 15).

Table 16. *Average pore radius (Å) for the 3 membranes, differentiating by replica, and indicating the standard deviation.*

Replica	POPC:POPG	POPC:POPG:CHOL	POPC:POPS
1	0.28 ± 0.02	2.02 ± 0.20	2.21 ± 0.23
2	3.10 ± 0.23	5.05 ± 0.48	1.80 ± 0.20
3	3.25 ± 0.27	3.80 ± 0.31	1.95 ± 0.21

Table 17. *Average pore radius in control simulations (without peptides).*

	POPC:POPG	POPC:POPG:CHOL	POPC:POPS
Average	0.20 ± 0.02	0.30 ± 0.05	0.18 ± 0.02

Regarding the secondary structure, all peptides start with β-sheet structure, but most of them lose it when interacting with the membrane. Nonetheless, peptide insertion seems to be associated with maintenance of secondary structure, in this case, by the stabilization of β-sheet (Figure 34B). Peptide insertion is in line with the increase in the number of protein-lipid hydrogen bonds formed, also linked to a decrease in the amount of H bonds between peptides and water molecules, indicating MAP peptides transitioning from water to water–bilayer interface (Figure 34C).

Residue occupancy by lipids (Figure 34D), that is, the percentage of simulation time that a residue has been in contact with a lipid, shows that most peptides are in contact with POPC or POPG lipids (both polar heads and lipid tails) in the inner leaflets, but some peptides reach and achieve interaction with the lower leaflet. Overall, occupancy levels for POPC and POPG lipids are similar, however, given the ratio 7:3 POPC:POPG, this implies that peptides preferentially interact with POPG lipids relative to POPC.

Liposome leakage experiments show that the addition of MAP at a concentration of 5 μM to POPC:POPG (7:3) liposomes results in a progressive rupture of the vesicles over time. These results indicate that MAP can directly interact with the lipid bilayer, disrupting membrane structure and ultimately leading to dye release and decreasing total fluorescence.

3.3.3.2.POPC:POPG:CHOL

In a more complex membrane, containing a 10 % of CHOL and a total POPC:POPG:CHOL 6:3:1 ratio, the same experiments have been performed. In CompEL ΔQ 16 simulations, one MAP molecule gets inserted, whereas the other seven peptides are partitioning in the water–bilayer interface. Besides, a pore is formed in a control membrane without peptides but is rapidly closed (Table 17), in contrast with the stable pores in simulations with MAP peptides.

In this membrane, loss of β-sheet structure is associated with peptide insertion, and instead MAP peptides gain α-helical structure upon insertion (Figure 35B). Besides, some peptides can also stabilize β-sheet structure when partitioning. As seen in the previous membrane, the total number of H bonds with waters is reduced, while increasing the peptide–lipid ones, indicating partitioning behaviour (Figure 35C). Peptide residue occupancy shows similar results to the previous membrane, with similar POPC/POPG and head/tail interaction (Figure 35D), but they do not show a prominent interaction with cholesterol (Figure 36), indicating the preference for the interaction with charged lipids.

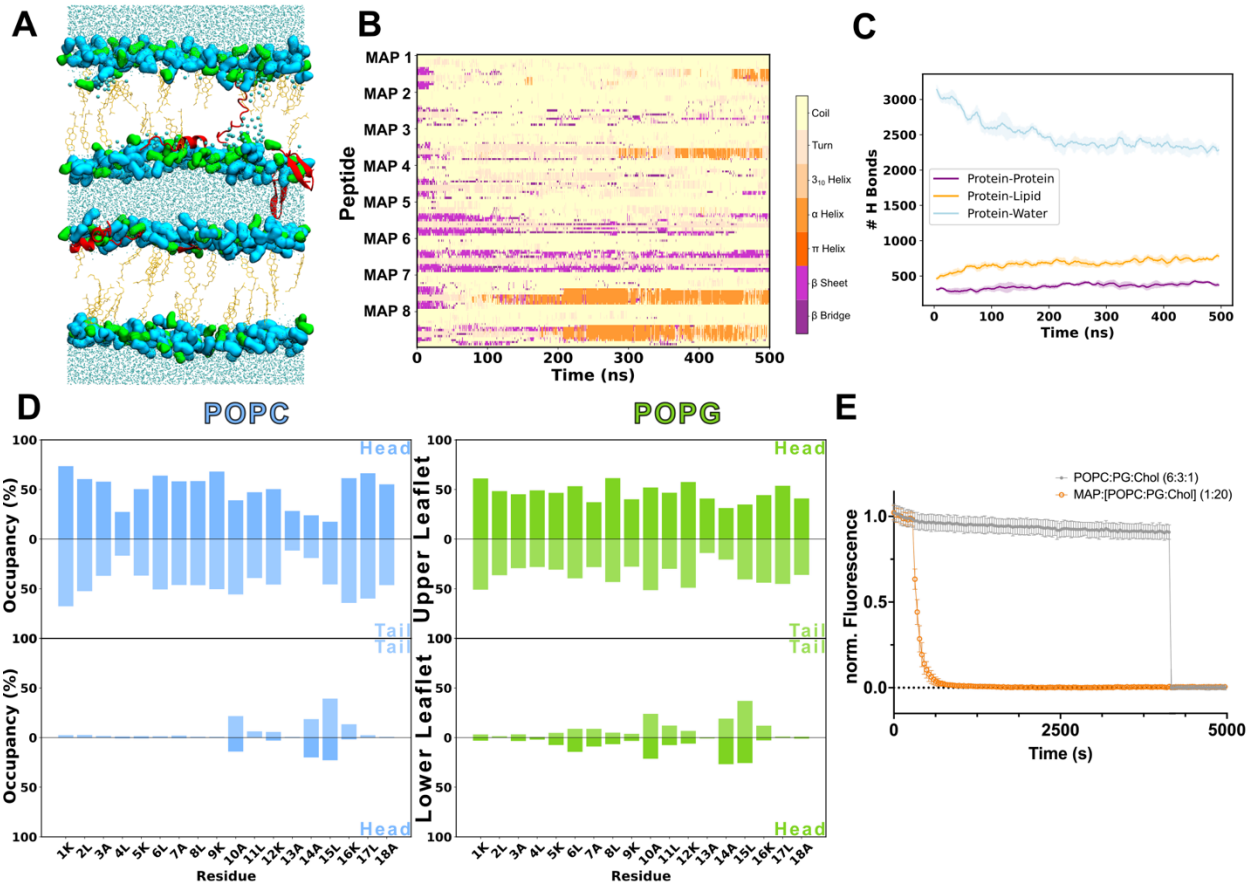

Figure 31. *POPC:POPG:CHOL MAP CompEL ΔQ 16 500 ns simulation results. (A) Representative molecular configuration of the CompEL system at the end of the simulation. One peptide is inserted, whereas the remaining 7 peptides are partitioning. The peptides are shown as cartoon and coloured in red, the polar heads in QuickSurf in light blue (POPC) or green (POPG), cholesterol lipids are shown as orange licorice, and water residues as licorice and coloured in cyan. Lipid tails are omitted for clarity. (B) Secondary structure of the 8 MAP peptides during the 500 ns of CompEL simulation. (C) Number of H bonds formed by peptides, lipids and waters throughout the simulation. (D) Occupancy of the peptide residues by POPC or POPG lipids. The occupancy is differentiated between upper and lower leaflets, and lipid head or tails. Cholesterol occupancy is shown in Figure S1. (E) Results of liposome leakage experiments. Fluorescence levels compare liposomes without peptide (control, grey), and with peptide addition (5 μM, orange).*

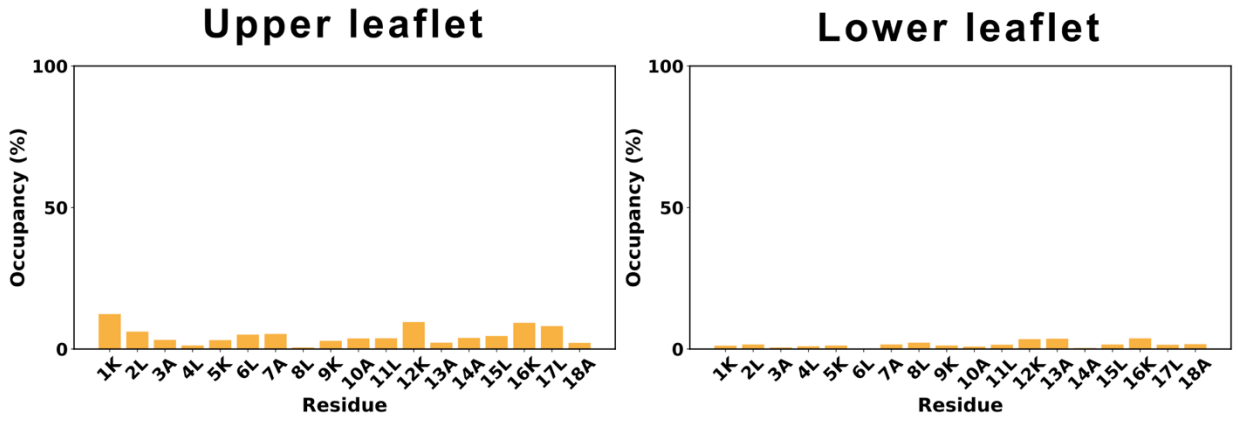

Figure 32. *Peptide residues occupancy by cholesterol. Occupancies are differentiated between upper and lower leaflets.*

Here, liposome leakage experiments performed with the same membrane composition show that MAP addition cause a fast disruption and rupture of vesicles, indicating the MAP potential for peptide-mediated membrane disruption.

3.3.3.3.POPC:POPS

After comparing CompEL symmetric membrane simulations with liposome leakage experiments, internalization experiments have been chosen to relate with CompEL asymmetric membrane simulations. In order to simulate a simplified model of the cell membrane, negatively charged lipids only in the negative leaflet and POPS instead of POPG due to its higher physiological relevance have been employed[276].

In this membrane, translocation of a MAP peptide has been observed in two replicas (see complete results in Table 15). As in previous membranes, a pore is generated due to the ion imbalance (Table 17), then the peptide is able to use this pore to get inserted and stabilize it. Furthermore, due to the

presence of negative lipids only in the outer leaflet, the peptide is attracted to the lower part of the membrane and is consequently able to achieve translocation (Figure 37A).

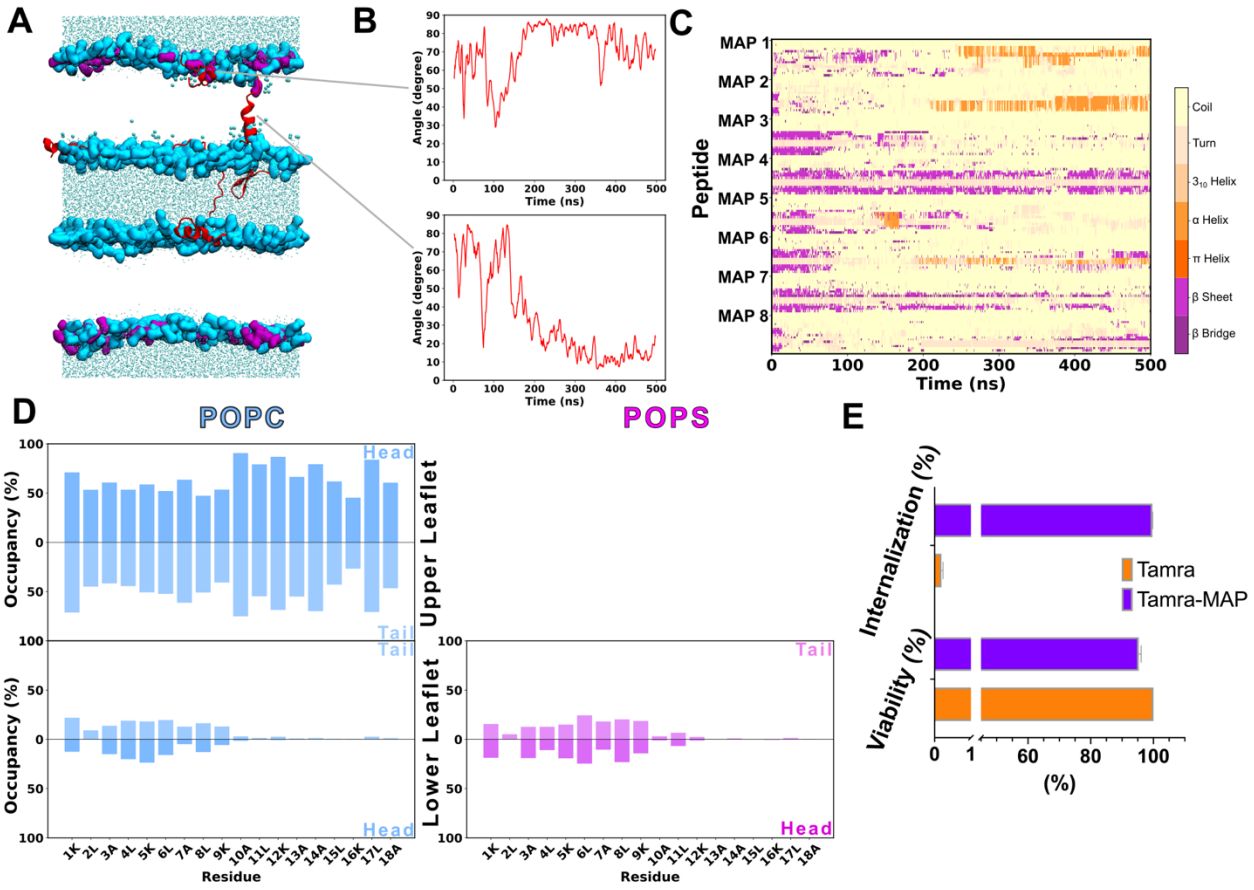

Figure 33. *POPC:POPS MAP CompEL ΔQ 16 500 ns simulation results. (A) Representative molecular configuration of the POPC:POPS CompEL system, with one insertion and one translocation. Polar heads are shown as QuickSurf in light blue (POPC) or purple (POPS). Peptide is shown as NewCartoon in red. Water molecules are shown as licorice in cyan. (B) Evolution of the peptide angle throughout the simulation. The peptide that translocates (upper plot) and the peptide that gets inserted (lower) are shown. (C) Secondary structure throughout the simulation. The average among the three replicas is shown. (D) Average residue occupancy by POPC and POPS lipids. (E) Results of internalization and viability assays. Data compare untreated controls with samples exposed to MAP. The complete internalization and viability results are in Figure 38.*

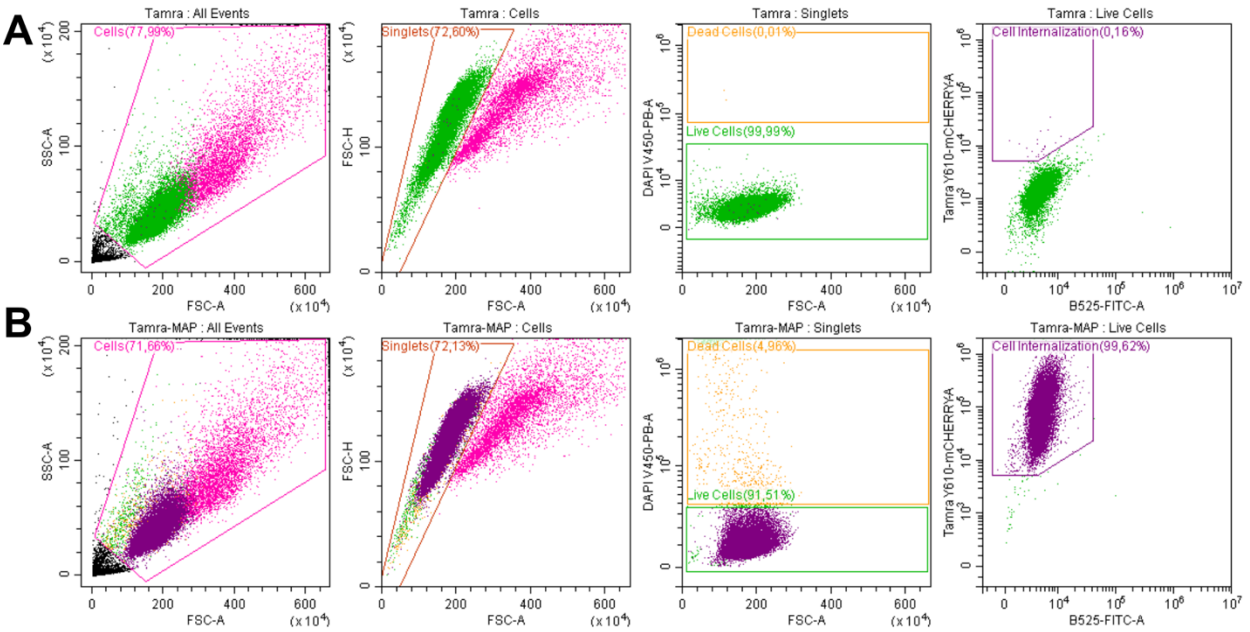

Figure 34. *(A) Internalization and viability experiments of the Carboxytetramethylrhodamine (TAMRA) fluorescent dye. (B) Internalization and viability results of MAP coupled with TAMRA dye.*

As seen in Figure 37B, the peptide changes its orientation along the membrane crossing. The script presented by Choe[233] has been applied, which calculates the orientation of the peptide with respect to the bilayer normal. Thus, values close to 0º indicate that the peptide is perpendicular to the membrane, and values close to 90º imply that it becomes parallel to it. First, when the peptide partitions, it is oriented parallel to the membrane in the inner leaflet, with values close to 90º. When the peptide gets inserted, it becomes perpendicular to the membrane axis with values close to 0º, as was described by Leontidaou and colleagues[301]. Last, when the peptide reaches translocation, it rotates again and is oriented parallel to the membrane in the outer leaflet, with values close to 90º again.

Regarding secondary structure (Figure 37C), we see similar results to the POPC:POPG:CHOL system, with peptides starting in β-structure conformation, which is maintained for some peptides that partition, whereas peptides that get inserted adopt an α-helical structure[286,288]. Similarly to previous bilayers, occupancy is shared between lipid polar heads and tails, but with higher values for the negatively charged lipid, in this case POPS, even though it has lower proportion in the membrane (Figure 37D).

Internalization and viability assays have been performed in HEK293 cells (Figure 37E). The results indicate that MAP can efficiently internalize into human kidney cells, with uptake values

approaching 100 %, while exerting minimal cytotoxic effects, as cell viability remained above 90 %.

3.3.3.4.Membrane analysis

Field and potential analyses can be seen in Figures S2A (POPC:POPG), S3A (POPC:POPG:CHOL), and S4A (POPC:POPS), indicating that both potential and field values are similar to those used in other biological studies[279–281]. Besides, there are no differences among bilayers in membrane thickness or lipid order parameters, indicating that there are no remarkable differences between membranes and they are correctly oriented in the system (Figures 39, 40, 41).

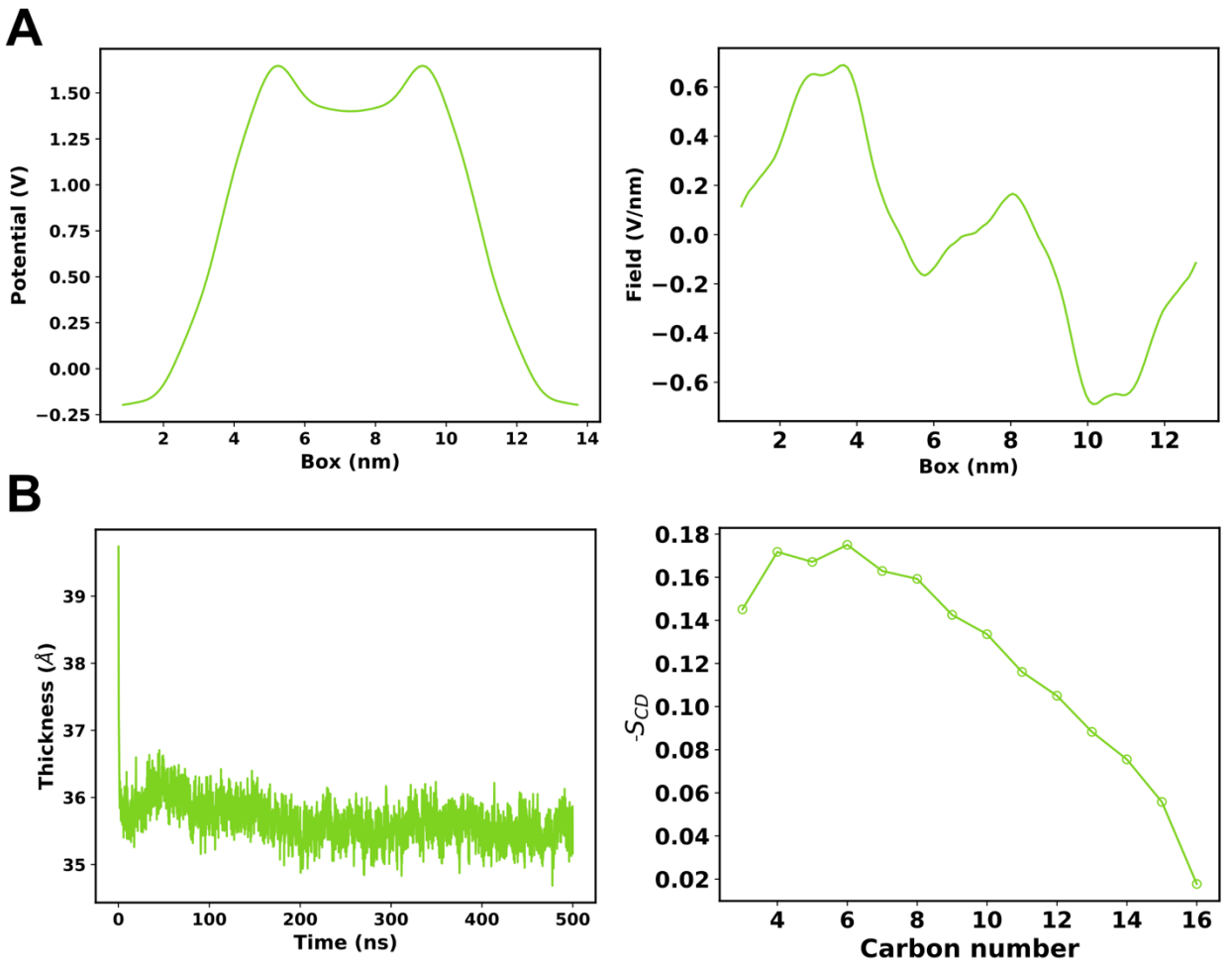

Figure 35. *(A) Internalization and viability experiments of the Carboxytetramethylrhodamine (TAMRA) fluorescent dye. (B) Internalization and viability results of MAP coupled with TAMRA dye.*

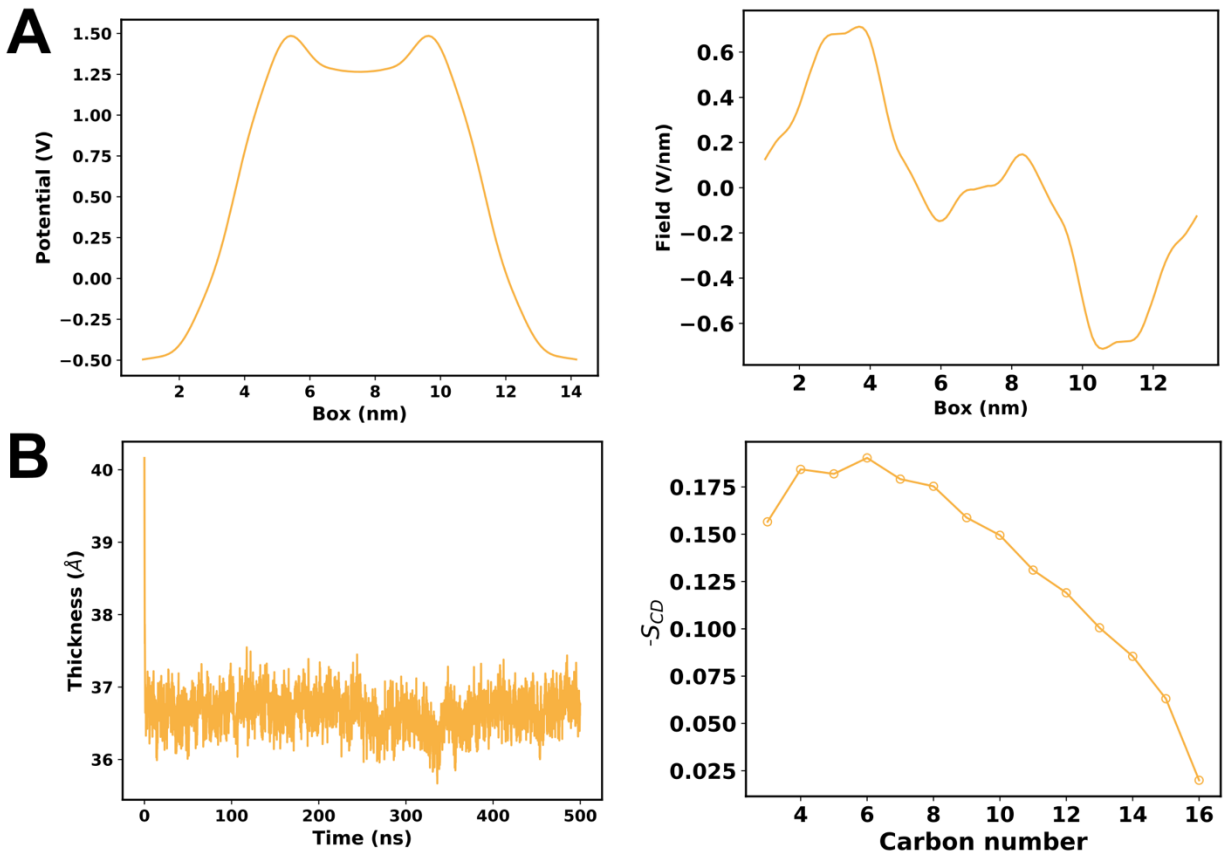

Figure 36. *(A) Potential (left) and field (right) in the system in the ΔQ 16 CompEL POPC:POPG simulation. (B) Membrane thickness (left) throughout the 500 ns of CompEL POPC:POPG simulation, and lipid order parameters (right) of the sn-1 (palmitoyl) segment of the POPC lipid. POPC has been chosen as representative lipid to indicate the membrane ordering since it is present in all three membrane compositions.*

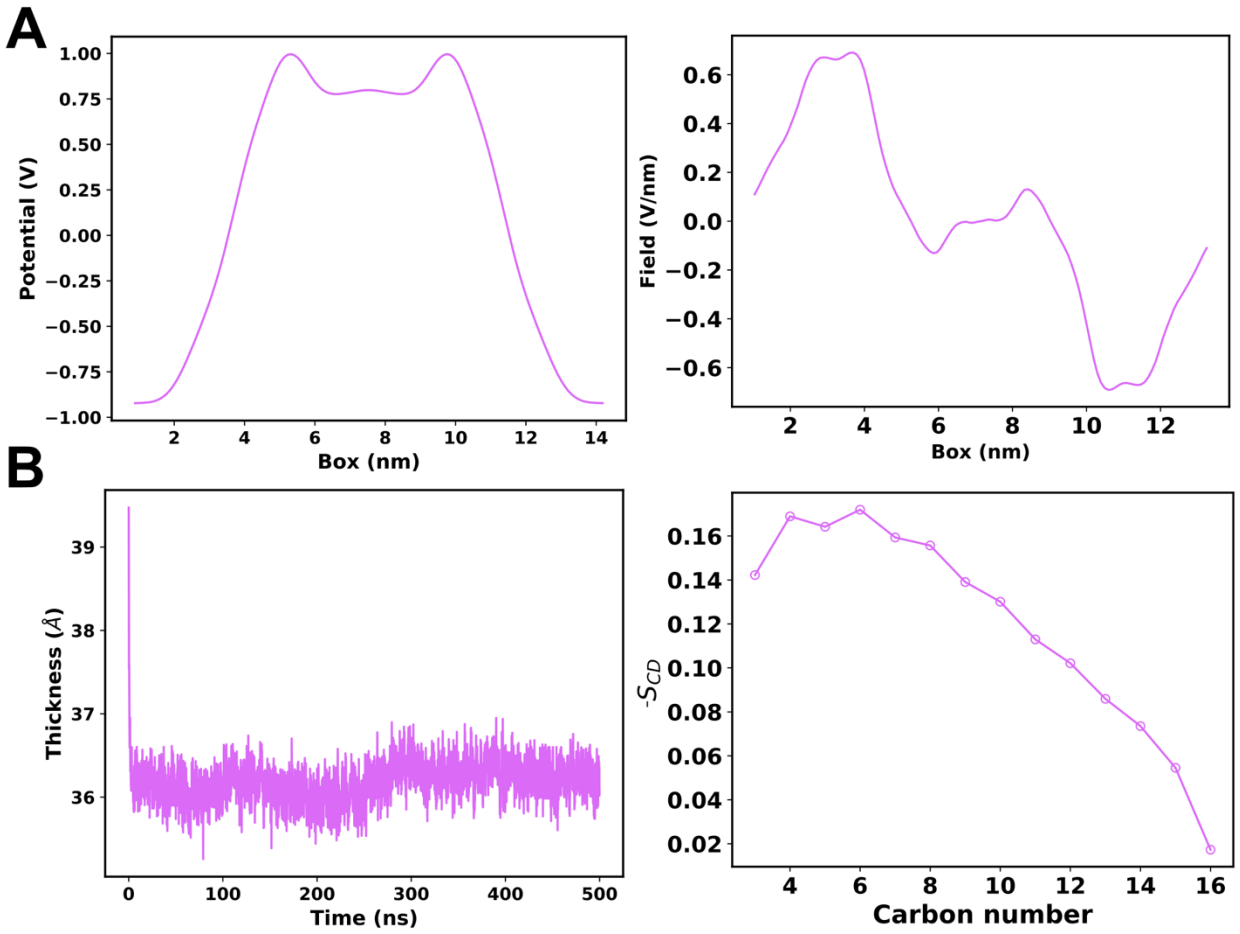

Figure 37. *(A) Potential (left) and field (right) in the system in the ΔQ 16 CompEL POPC:POPG:CHOL simulation. (B) Membrane thickness (left) throughout the 500 ns of CompEL POPC:POPG:CHOL simulation, and lipid order parameters (right) of the sn-1 (palmitoyl) segment of the POPC lipid.*

3.3.4. Discussion

Taken together the results from our previous study (MAP in POPC membrane) and the results obtained here, we can display the depth of MAP insertion/translocation across membranes (Figure 42).

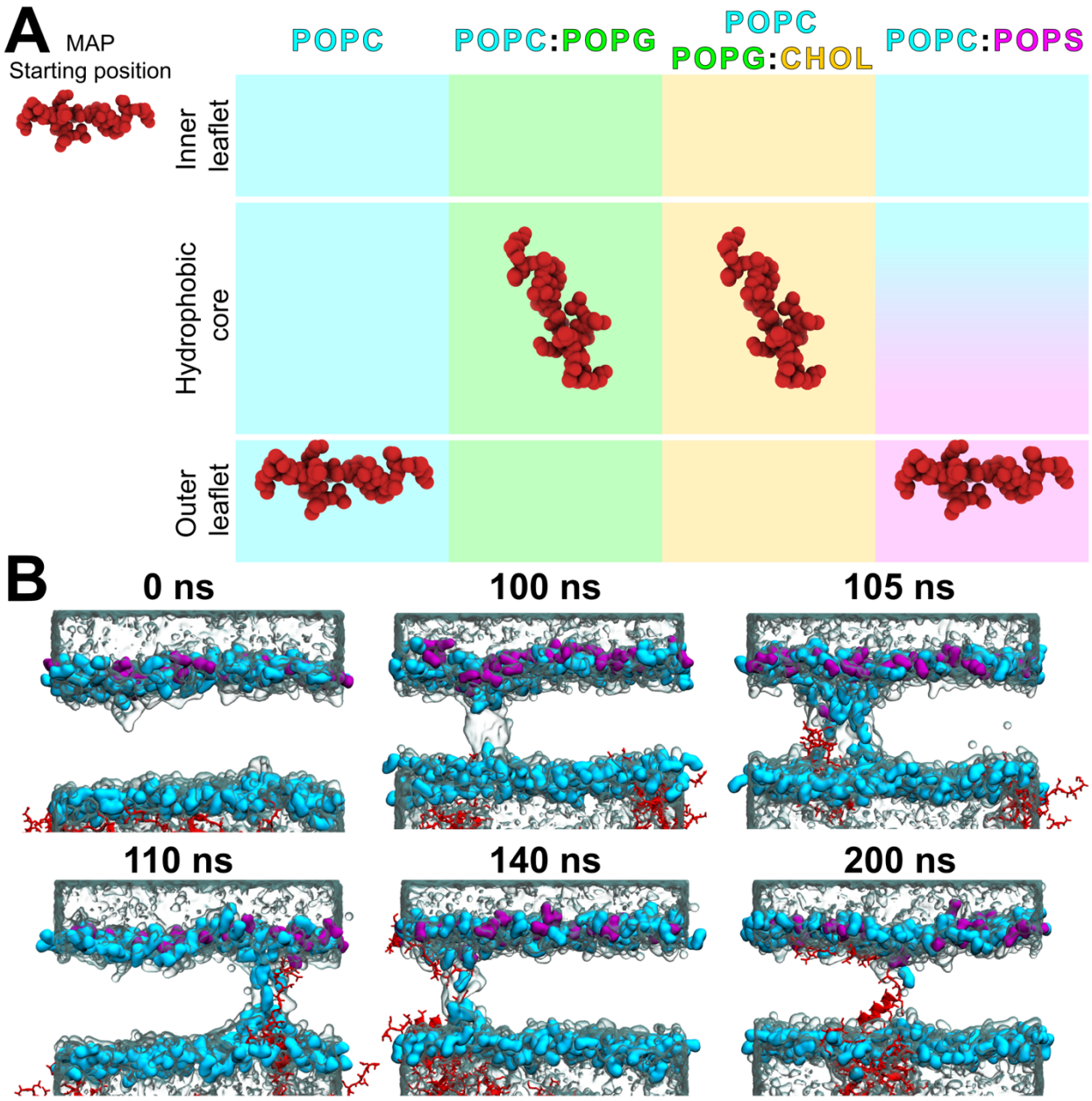

Figure 38. *Peptide insertion and translocation. (A) Process of pore formation, insertion, and translocation in POPC:POPS. The simulation start (0 ns), pore start (100 ns), start of insertion (105 ns), full insertion (110 ns), translocation start and insertion of another peptide (140 ns), and end of translocation (200 ns) steps are shown. Polar heads are represented as QuickSurf in light blue (POPC) or purple (POPG). The peptides are shown as NewCartoon, the side chain is shown as licorice and coloured in red. Waters are shown as transparent QuickSurf and coloured in cyan. (B) Comparison of MAP insertion extent across membranes. The results from four membranes are shown: POPC (from our previous study), POPC:POPG, POPC:POPG:CHOL, and POPC:POPS. The starting point is represented in the inner leaflet, with insertion in POPC:POPG, and POPC:POPG:CHOL, and translocation to the outer leaflet in POPC and POPC:POPS membranes.*

First, in POPC membrane one MAP peptide is able to translocate. In POPC:POPG and POPC:POPG:CHOL membranes, however, MAP peptides do not translocate, with two and one

peptides getting inserted, respectively. Thus, MAP loses its translocation capacity when increasing membrane complexity, suggesting that the presence of negatively charged lipids in the extracellular leaflet reduces translocation capacity[152,222]. Besides, the presence of CHOL further decreases the insertion capacity, implying reduced membrane disruption potential in CHOL containing bilayers, as discussed by Pae and collaborators [102]. Nonetheless, when an asymmetric membrane is used, translocation capacity is regained, suggesting that MAP peptides prefer the interaction with the negatively charged lipids in the outer leaflet (representing the intracellular leaflet). In all cases, only one or two peptides get inserted, whereas the other peptides are partitioning in the inner leaflet, as was previously described[301].

Interestingly, there exists a correlation between simulations and experimental results, suggesting that CompEL does indeed possess the capacity to observe timescales as the same order as some biological processes[259]. First, MAP does not induce large membrane leakage in POPC liposomes (Figure S6), suggesting that MAP can generate membrane disruption and pores are indeed formed. However, these pores are not stable due to MAP ability to translocate bilayers, leading to pore closure[31,304,321].

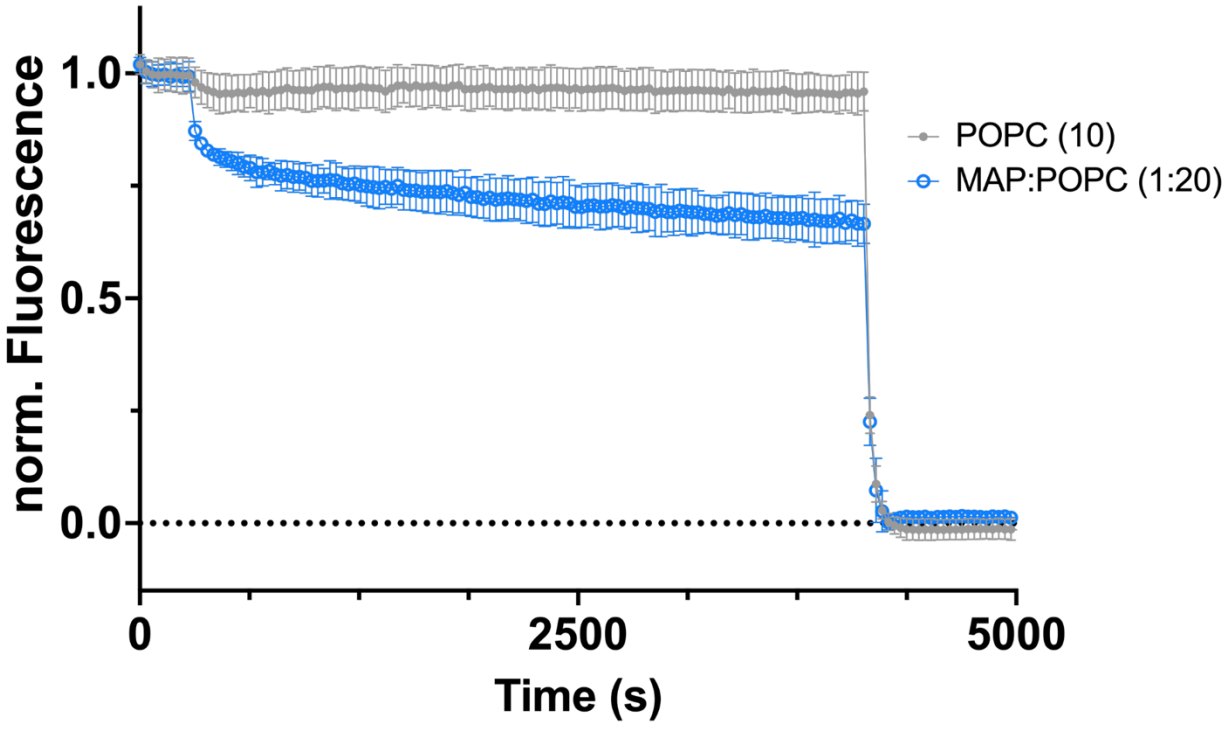

Figure 39. *Liposome leakage experiments. POPC liposomes in absence (grey) and presence of MAP (blue).*

In POPC:POPG membranes, MAP produces more liposome leakage, consistent with the simulations, where peptides are inserted and stabilize the pore, leading to increased leakage. Moreover, in POPC:POPG:CHOL, larger liposome leakage is observed, in line with the larger pores generated on average in simulations. Lastly, in an asymmetric membrane, a simplified model of the cell membrane, MAP has been observed to translocate, in agreement with the internalization observed in human cells. Nevertheless, a slight cytotoxicity is observed (below 10 %), which aligns with the cytotoxicity described for CPPs at higher concentrations[79]. Still, different strategies are being proposed to reduce such cytotoxicity and allow for a safer use of CPPs[113,114].

On another note, the RMSD (Figure 44) and trajectory visual inspection analyses show that the systems are stabilized during the first 250 ns. This stabilization implies that CompEL simulations do not need to be extended until 500 ns, and can instead be shortened to 250 ns, lowering computational requirements and simulation time.

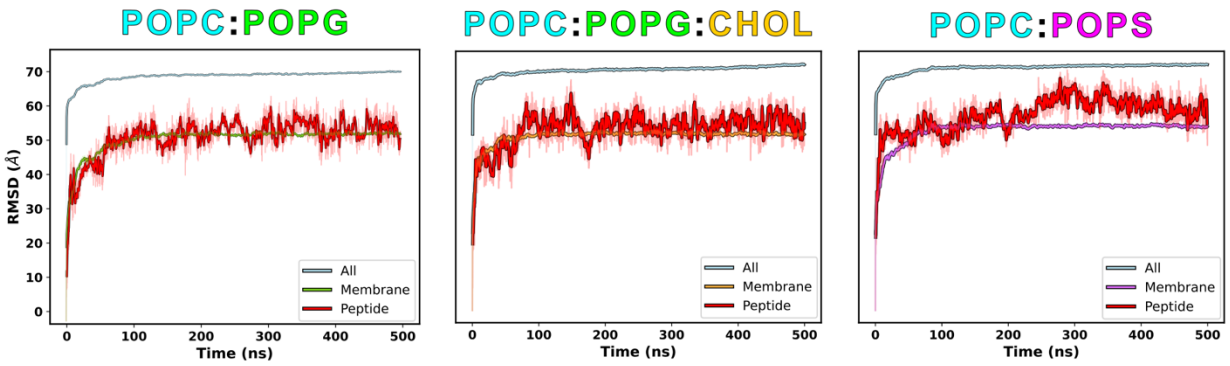

Figure 40. *Average RMSD analysis of the CompEL ΔQ 16 simulations.*

Regarding occupancy analysis, MAP peptides show higher interaction with POPG/POPS lipids compared to POPC, which can be related to the additional negative charge present in the polar headgroups[231]. Intriguingly, in POPC:POPG and POPC:POPG:CHOL membranes, MAP has higher occupancy in the lower leaflet with C-terminal residues, suggesting that MAP gets potentially inserted by the C-terminal residues, as seen for other amphipathic peptides[322]. Nonetheless, the N-terminal gain importance in the asymmetric membrane, implying the dependence on membrane compositions[287].

In contrast, less agreement in seen regarding the secondary structure. In POPC:POPG:CHOL and POPC:POPS bilayers, peptide insertion is linked to an increase in α-helical structure, as has been

described for MAP and amphiphilic CPPs[323]. In these simulations, β-sheet structure is limited to peptides that partition in the inner leaflet. In POPC:POPG membranes, however, insertion is related to β-sheet structure, suggesting that CPPs can present different secondary structures depending on the conditions[287].

Finally, the pore formation, insertion, and translocation processes are discussed using POPC:POPS simulations (Figure 42). First, the inherent CompEL ΔQ causes a pore formation (100 ns) that can be then used by the peptide and the polar heads to stabilize the pore (105 ns). Second, the peptide can reach full insertion (110 ns) and get perpendicularly oriented to the membrane plane. After, the peptide can start interacting with POPS lipids due to their negative charges, initiating the translocation mechanism (140 ns). Last, the peptide changes from perpendicular to parallel orientation and finalizes the translocation mechanism (200 ns). Water molecules solvate the insertion and translocation processes, suggesting the pore formation mechanism for MAP, as we discussed in a previous study, and as supported by the liposome leakage experiments.

3.3.5. Conclusion

In this study we have expanded the application of the CompEL technique to the CPPs and, in general, membrane active peptides, exploring their behaviour across different membrane compositions and benchmarking against experimental data. First, in POPC:POPG membranes, MAP loses its translocating capacity compared to pure POPC, instead inserting into the bilayer and stabilizing pores formed due to the transmembrane potential. These results agree with liposome leakage assays, where MAP induces strong membrane disruption and content release. Second, in POPC:POPG:CHOL membranes, CHOL reduces MAP inserting propensity, but enhances pore stabilization and leakage, again consistent with experimental observations. In contrast, in POPC:POPS membrane, a simplified model of the cell membrane, MAP is able to translocate, in line with the internalization capacity observed for MAP in human cells.

Secondary structure analysis reveals that MAP generally adopts an α-helical structure upon membrane insertion, although it also shows that secondary structure strongly depends on membrane and system conditions. Occupancy analysis further highlighted a clear preference of MAP for negatively charged lipids, consistent with its positive global charge.

Altogether, these results demonstrate that CompEL provides a powerful framework for connecting computational and experimental results, suggesting confidence on only using fast computational simulations in the future. Nonetheless, future work should extend this strategy to more complex and biologically relevant membranes, incorporating additional lipid species, such as phosphatidylethanolamine (PE), phosphatidylinositol (PI), more different asymmetric distributions, and even protein components to better capture the complexity of the cellular environment. We hope that this study can pose CompEL as an unbiased, entry-level technique useful for peptide–membrane interactions research.

3.4. Chapter IV: membrane disruption potential of endogenous opioid neuropeptide dynorphin A and related clinical variants

In this chapter, we make use of the aSMD in combination with cMD technique to computationally study and characterize DynA and its clinical variants interaction with different membrane compositions. Thus, we focus on general objectives 3,4 and specific objectives 2,3,5.

3.4.1. Introduction

Dynorphins are prohormones found in the brain and central nervous system, whose expression is altered in the brain of drug and alcohol abusers and in patients with some neurological disorders[123]. Physiologically, dynorphins are derived from prodynorphin (PDYN)[120] and constitute one of the most basic peptides in the human body[119]. Prodynorphin is cleaved at positively charged residue motifs yielding Big Dynorphin (BigDyn, 32 residues) and can be further processed into Dynorphin A (DynA, 17 residues) and Dynorphin B (DynB, 13 residues) by cleaving the K-R hinge region between them[121,122]. BigDyn and DynA have been previously described to possess internalization into neurons capacity, crossing the cell plasma membrane and leading to ion flow through membranes[124–128], consistent with the formation of membrane pores[324].

DynA interacts with opioid receptors, namely κ-opioid receptor (KOR) and μ-opioid receptor (MOR), and plays a role in pain, stress, and addiction. Besides its opioid effects, DynA has other non-opioid activities, such as anti-amyloidogenic properties[325] or inhibition of N-methyl-D-aspartate (NMDA) receptors[326]. Bakalkin *et al.* identified three different coding mutations within the DynA region in the PDYN gene in a form of the human neurodegenerative disorder spinocerebellar ataxia 23 (SCA23)[130]. The mutations correspond to positions L5, R6, and R9 of DynA, to S (L5S), W (R6W), and C (R9C), respectively. Analysis of DynA wild type (WT) and its clinical variants on striatal neurons concluded that DynA R6W and R9C cause a higher toxicity than DynA WT[130]. In a study -with both neutral and zwitterionic- large unilamellar vesicles (LUVs), DynA R6W and R9C showed the highest degree of leakage, whereas DynA L5S showed the least leakage[132]. Structural studies indicate DynA WT has some N-terminal helical structure upon DMPC binding, while R6W shows helical structure and strong bilayer association, unlike the less structured L5S[135]. In a more recent study, DynA L5S was shown to display increased degradation, whereas DynA R6W and R9C showed increased stability compared to DynA WT[131]. Besides, DynA WT and R6W were the most toxic peptides to primary cerebellar neurons. Nonetheless, the membrane disruption mechanism of DynA WT and its clinical variants remains elusive.

Molecular dynamics (MD) simulations have been used to study DynA interaction with membranes. Initially, DynA was found to get inserted with a tilt angle of ~35 º with respect to the membrane[327,328]. Then, DynA was found to stay in the outer surface of the membrane when

interacting with the κ-opioid receptor[329]. In a more recent study, DynA was found to be able to stabilize pores[330]. However, in order to analyse the membrane disrupting capacity, such as pore formation or membrane translocation, enhanced sampling techniques are needed[140,259].

DynA and the clinical variants show prototypical cell-penetrating peptides (CPP) features[54,86], such as amphiphilicity, positive net charge, α-helix structure propensity upon membrane interaction[133], and actual bilayer translocation in cell lines[124]. Thus, we decided to use a computational method that has been applied to CPP research. Umbrella Sampling (US)[146] has been used in previous studies[140,235], but US is primarily utilized to calculate the barrier of CPP translocation. Coarse-grained MD (CGMD) has also been used to study the translocation of nona-arginine (Arg9)[153], but the information provided by CGMD is limited due to lower resolution[331]. Therefore, we propose the use of adaptive steered molecular dynamics (aSMD), used by Gimenez-Dejoz and Numata[142], and combine it with conventional molecular dynamics (cMD). With this method, we are able to obtain a quantitative result with aSMD, such as the free energy of bilayer crossing, and, since aSMD generates a non-equilibrium state, we are able to characterize the bilayer resistance and the bilayer-peptide interactions with the unbiased cMD simulation, as we used in a previous study to describe the membrane disruption caused by CPPs. Thereafter, we combine aSMD and cMD to characterize the membrane disruption potential of DynA WT and its clinical variants (L5S, R6W, and R9C).

3.4.2. Computational methods

3.4.2.1.Systems preparation

The systems were prepared as described previously. Briefly, peptides were modelled in a Colabfold-Alphafold notebook and relaxed in an explicit solvent system at 310.15 K. AMBER program was used to run the simulations[183]. The AMBER ff14SB[184] force field and periodic boundary conditions were applied, and the SHAKE algorithm[185] was used to restrain the hydrogen atoms, allowing for a 2 fs timestep. 150 mM KCl ions and water TIP3P molecules were used to neutralize and solvate the system. A short minimization (5,000 cycles) and NVT equilibration (125 ps) were run with a restraint force of 4.184 $kJ \cdot mol^{-1} \cdot Å^{-2}$ (1 $kcal \cdot mol^{-1} \cdot Å^{-2}$) on the peptide, before the unrestrained cMD simulation of 100 ns. Then, clustering analysis was performed to obtain the most representative structure of the peptide, which was further used as initial structure.

Peptide-bilayer systems were built in CHARMM-GUI[186–192] for each relaxed peptide and membrane composition combination. One peptide was added to each system, using the cluster obtained from the peptide relaxation simulation analysis. The peptides were placed at approximately 10 Å from the centre of mass (COM) of the upper leaflet bilayer membrane. The N-terminus or C-terminus of the peptides were not modified at any extent.

Three membrane compositions of 150 lipid molecules -per leaflet- were defined. A neutral bilayer of Dioleoyl phosphatidylcholine (DOPC), namely (1) DOPC (150 lipid molecules), a simple membrane model. A ternary membrane with cholesterol and a different lipid tail was defined: 1,2-Dipalmitoyl phosphatidylcholine (DPPC), DOPC, and cholesterol (CHOL), namely (2) DPPC(50):DOPC(50):CHOL(50). A membrane model containing negatively charged lipids, and to keep a similar proportion as in the previous bilayer, we used: DPPC, DOPC, CHOL, and Dioleoyl phosphatidylserine (DOPS), namely (3) DPPC(38):DOPC(38):DOPS(38):CHOL(38). The same conditions as in the peptide relaxing simulations were used. For the membrane lipids, the Amber Lipid21[196] force field was selected.

Systems were minimized for 5,000 steps and equilibrated during 3.5 ns, starting in the NVT ensemble with positional restraints on the membrane atoms (restraint force of 10.46 $kJ \cdot mol^{-1} \cdot Å^{-2}$ or 2.5 $kcal \cdot mol^{-1} \cdot Å^{-2}$), and changing to the NPT ensemble after 500 ps. The system was relaxed for 100 ns of conventional molecular dynamics (cMD). During this step the peptide was kept restrained to avoid peptide-membrane interaction and allow for an unperturbed membrane relaxation (restraint force of 41.84 $kJ \cdot mol^{-1} \cdot Å^{-2}$ or 10 $kcal \cdot mol^{-1} \cdot Å^{-2}$). It is important to mention that the lipids are positioned randomly in a symmetric fashion an after such short relaxation, lipid lateral diffusion was not observed. Although our model is a polarity (charge) model and not a lipid phase model, at a given temperature of 310.15 K the bilayers are likely to be in liquid disordered phase, or in a mixed liquid ordered/disordered phase in the case of the complex membranes [332].

3.4.2.2.Adaptive steered molecular dynamics

The membrane length (ca. 40 Å) was divided in 8 stages of 5 Å, and 25 replicas were run for each step. The constant force used was 41.84 $kJ \cdot mol^{-1}$ or 10 $kcal \cdot mol^{-1}$, and a pulling speed of 1 Å/ns (5 ns per step), as discussed in our previous study. After each step, the Jarzynski average[141,202,203] across all replicas was calculated, and the last frame of the closest replica was used as input for

the following step. An aSMD step totalled 125 ns per step and 1,000 ns per aSMD simulation, totalling 12 μs for the aSMD part (4 peptides x 3 membrane compositions).

3.4.2.3.Conventional molecular dynamics

Starting from the last frame of the aSMD, a 100 ns cMD simulation was performed. The same simulating conditions were used as in the previous cases. A total of ~4 μs were run for the final relaxation part, accounting for 100 ns for each of the simulations (100 ns x 4 peptides x 3 membrane compositions x 3 replicas). Besides, 100 ns control simulations have been run for each membrane. We have run all simulations in a workstation with a GPU RTX3080Ti, where it ran at an average velocity of 80 ns per day.

3.4.2.4.PMF calculation

The Potential of the Mean Force (PMF) is computed by employing the Jarzynski equality[203], an equation that relates the non-equilibrium work during SMD simulations to the free energy difference between two states, as seen in Equation 1.

Afterwards, the replica with the closest work value to the Jarzynski average is selected as the starting point for the next simulation step. The Jarzynski equality employed in aSMD eliminates trajectories with minimal contributions to the overall PMF, significantly reducing the number of simulations needed for convergence[183].

3.4.2.5.Data analysis

Clustering and trajectory analysis was performed using MDAnalysis and PyLipID[208,210,211]. An in-house Python script was implemented to compute the radius pore size distribution, calculating the minimum pore size in the z axis of the membrane. This script calculates the maximum distance of the water residues per each membrane z-stack and outputs the minimum radius distance of all the z-stacks per each simulation frame. Matplotlib[216] and Seaborn[217] were used for graphics plotting. UCSF ChimeraX[218,219] and VMD[206] were used for molecular graphics.

3.4.3. Results

3.4.3.1.PMF barrier to membrane crossing

The aSMD process for DynA peptides is represented in Figure 45. Peptides (Figure 45A and Table 18) were steered across three types of membranes representing different sections of a cell bilayer (Figure 45B), which also correspond to energetic barriers to be overcome.

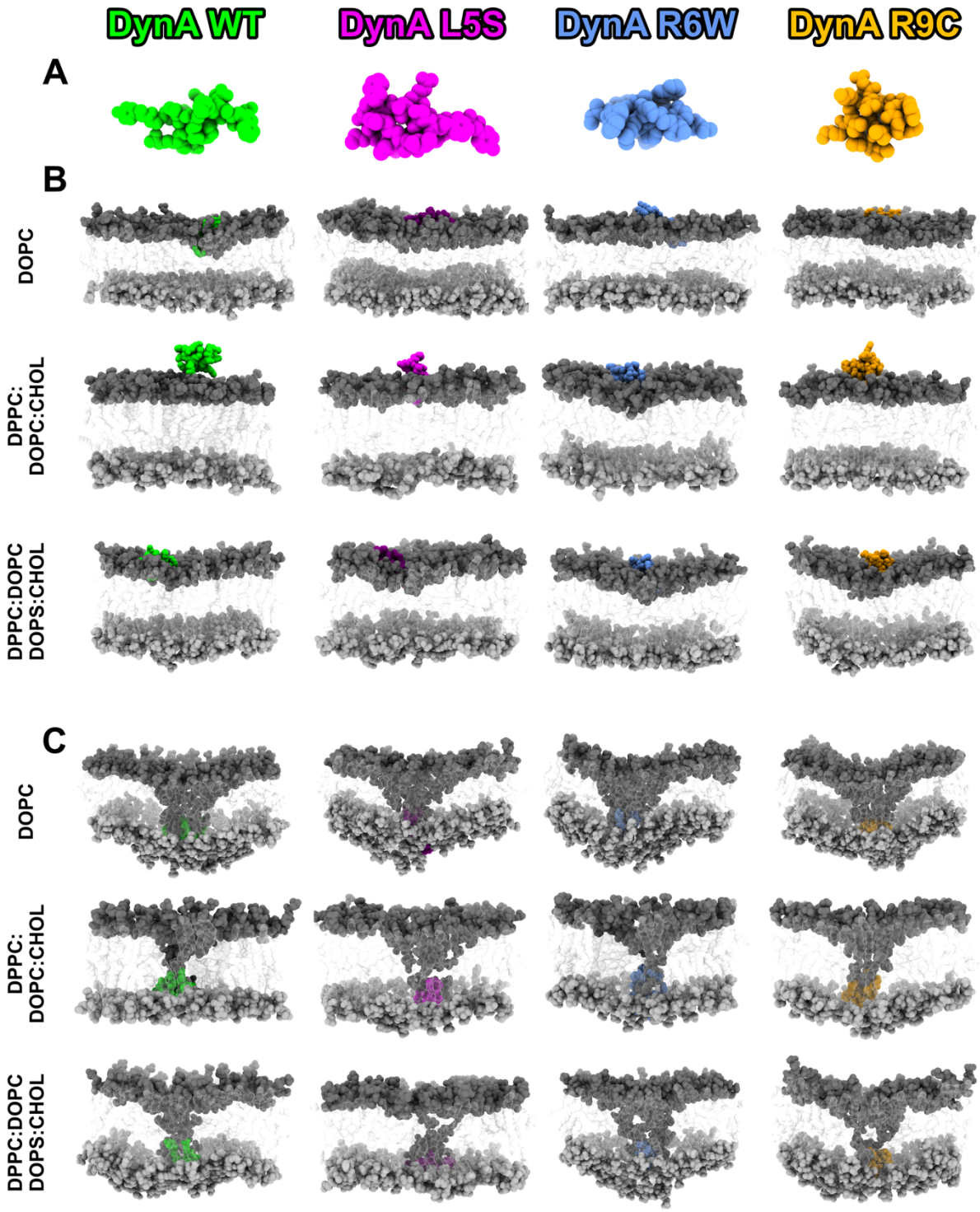

Figure 41. *Initial (A) and final (B) snapshots of the adaptive Steered Molecular Dynamics (aSMD) simulation of DynA WT and its three clinical variants: L5S, R6W, R9C. The timesteps in the three membrane compositions are shown. Peptides are coloured as: DynA WT in light green, L5S in purple, R6W in cornflower blue, and R9C in orange. The polar heads of phospholipids in both the upper and lower bilayers are illustrated in darker and lighter shades of grey, respectively. The lipid tails are portrayed in transparent white. Peptide colours are maintained in the following figures. Waters are omitted for clarity.*

Table 18. *Characteristics of the peptides used in this study.*

Peptide	Length	Sequence[a]	Type	Net charge	GRAVY score
DynA WT	17	YGGFLRRI RPKLKWD NQ	Amphipathic	+4	-1.26
DynA L5S	17	YGGF**S**RRI RPKLKWD NQ	Amphipathic	+4	-1.54
DynA R6W	17	YGGFL**W**RI RPKLKWD NQ	Amphipathic	+3	-1.05
DynA R9C	17	YGGFLRRI **C**PKLKWD NQ	Amphipathic	+3	-0.85

[a]Position for mutation in Dyn A WT are underlined, and the residue substitution is indicated in **bold** in the clinical variants.

In the process of DynA cell internalization, the peptide first encounters the outer side of the membrane, rich in neutral lipids. Then, it gets inserted into the hydrophobic core of the membrane, where it can find different lipid tails and cholesterol. Finally, DynA internalizes through interaction with the inner part of the bilayer, with negatively charged phospholipids. We have tried to model this process with three different membrane compositions: (1) the DOPC bilayer represents the transition from water to the neutral polar head feature of the extracellular/upper leaflet; (2) the DPPC:DOPC:CHOL bilayer represents the transition from the water-bilayer interface to the hydrophobic and rigid bilayer core; and (3) the DPPC:DOPC:DOPS:CHOL as a model for the transition from the hydrophobic core to the negatively charged inner/lower leaflet of the bilayer.

The final step of the aSMD simulation (Figure 45C) shows the peptide at the lower leaflet of each bilayer in a non-equilibrium state. Moreover, the membrane disturbance exerted is indicated by the polar heads from the upper leaflet dragged down together with the peptide, as a representation of the Defect-Assisted-by-Charge (DAC) phenomenon[221]. To quantify the membrane disruption potential of each peptide upon each bilayer, the PMF barrier was calculated (Figure 46 and Figure 47). The peptides have, in average, similar difficulty to traverse the DOPC and DPPC:DOPC:CHOL bilayers (average PMFs of 750 ± 50 and 750 ± 40 kJ·mol^{-1} (or 180 ± 10 and 180 ± 10 kcal·mol^{-1})) compared to DPPC:DOPC:DOPS:CHOL bilayer, with average PMF of 1000 ± 80 kJ·mol^{-1} (240 ± 20 kcal·mol^{-1}).

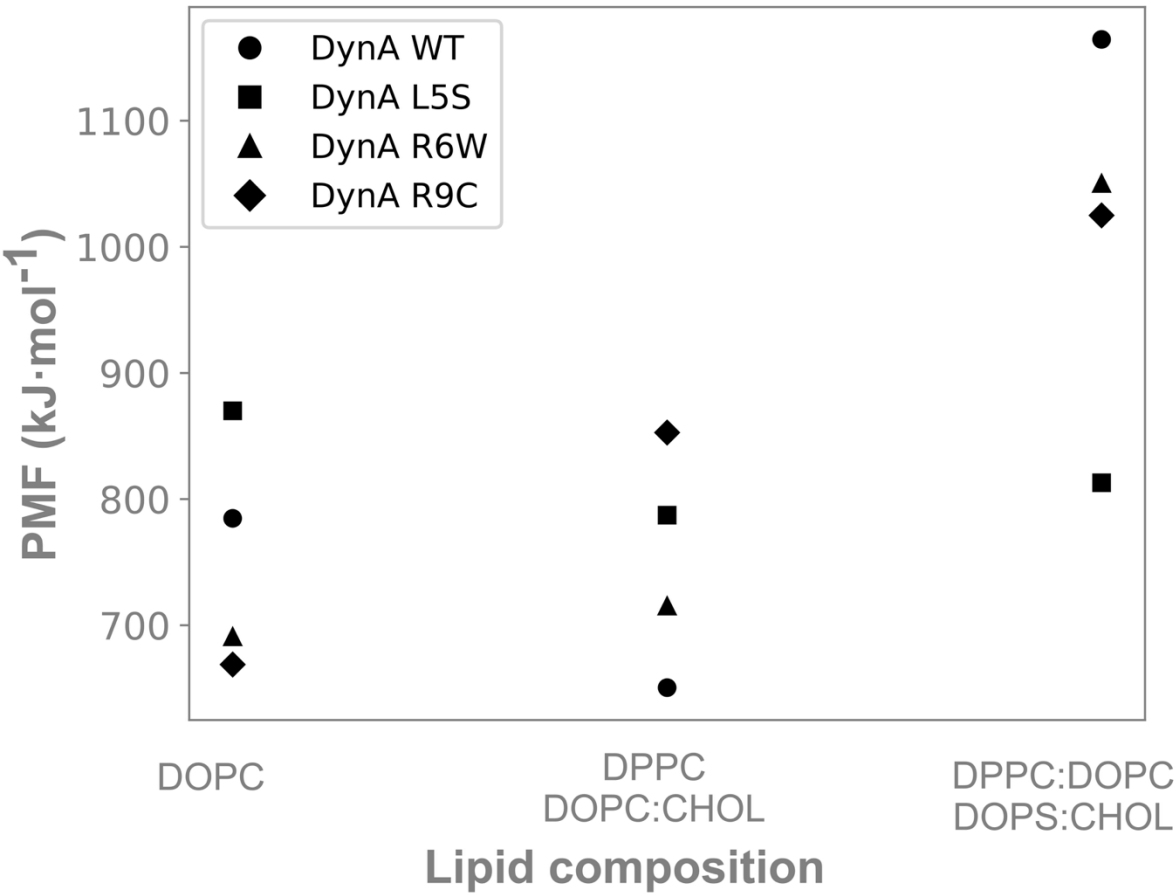

Figure 42. *Potential of Mean Force (PMF) of peptides with respect to the membrane composition. Size and colour indicate energy. The values indicated correspond to the last value (highest energy) of the PMF analysis. PMF profiles and the PMF of all the replicas are shown in Figure 47.*

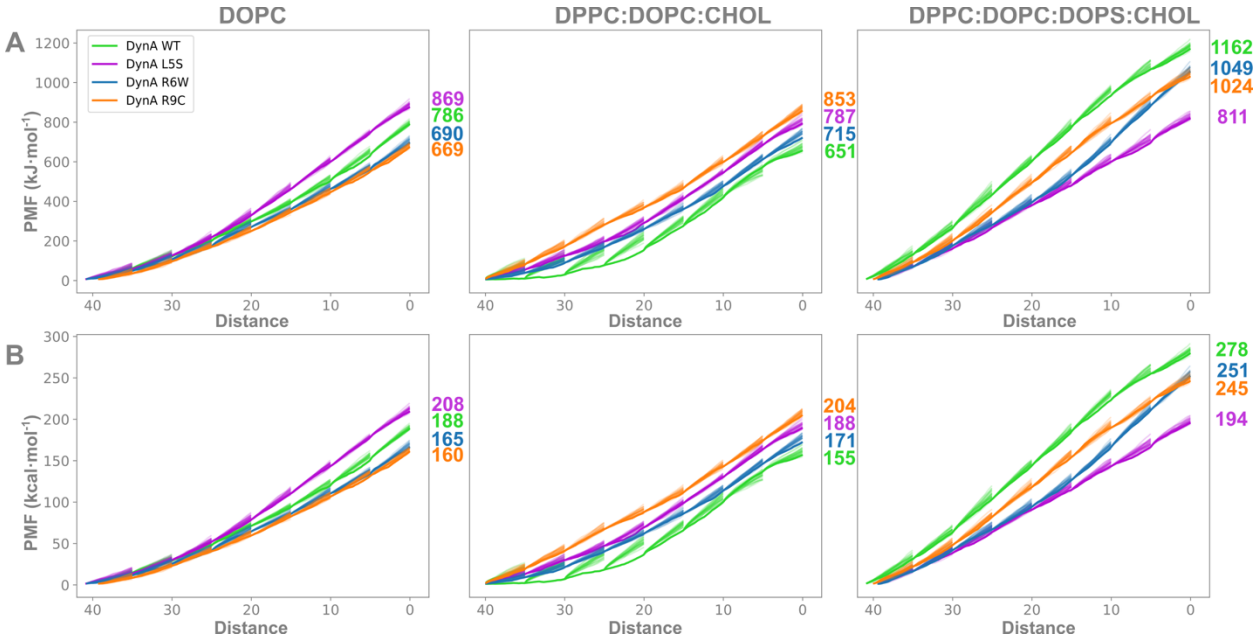

Figure 43. *PMF across all membranes of all replicas. The PMF of the replica chosen as start point for the next step has a thicker line width. Each peptide is depicted using the same colour as in main manuscript figures: DynA WT in green, L5S in purple, R6W in blue, R9C in orange. The PMF of all other replicas are shown in transparent. PMF values are shown in kJ·mol^{-1} (A) and kcal·mol^{-1} (B).*

DynA WT has a high PMF barrier for DOPC, whereas the steering through the DPPC:DOPC:CHOL bilayer is less restrictive, but the DPPC:DOPC:DOPS:CHOL bilayer opposes the strongest PMF barrier to DynA WT crossing (Figure 46, Figure 47 and Table 19).

Table 19. *PMF values and simulation results for DynA variants in three lipid membrane compositions.*

	Lipid membrane								
	DOPC			DPPC DOPC:CHOL			DPPC:DOPC DOPS:CHOL		
Peptide	**PMF (kJ·mol^{-1})**	**State**	**Pore Size (Å)[a]**	**PMF (kJ·mol^{-1})**	**State**	**Pore Size (Å)[a]**	**PMF (kJ·mol^{-1})**	**State**	**Pore Size (Å)[a]**
DynA WT	790 ± 10	Return (100%)	NA	650 ± 10	Pore (100%)	2.42 ± 0.08	1160 ± 10	Return (100%)	NA
DynA L5S	870 ± 10	Return (66%) Pore (33%)	1.38 ± 0.08 (66%) 5.45 ± 0.8 (33%)	790 ± 10	Pore (100%)	1.33 ± 0.07	810 ± 10	Pore (100%)	4.71 ± 0.08
DynA R6W	690 ± 10	Return (100%)	NA	720 ± 10	Return (100%)	NA	1050 ± 10	Return (100%)	NA
DynA R9C	670 ± 10	Return (100%)	NA	850 ± 10	Return (100%)	NA	1020 ± 10	Pore (66%) Return (33%)	0.87 ± 0.05 (66%) NA (33%)

These results indicate that DynA WT favours the interaction with different lipid tails and cholesterol. The L5S clinical variant shows higher PMF barriers for DOPC and DPPC:DOPC:CHOL compared to DynA WT, but significantly lower in the DPPC:DOPC:DOPS:CHOL membrane. In fact, in the latter, the PMF barrier for L5S is similar to DPPC:DOPC:CHOL bilayer and lower than the PMF in DOPC. In short, the main barrier for L5S is the partition in the upper leaflet of the bilayer, whereas the insertion to the hydrophobic core and the partitioning in the lower leaflet are energetically more favourable. The PMF barrier for WT is lower than L5S in the first two membranes and higher in the negatively charged membrane, indicating that the hydrophobic-to-polar substitution allows better stabilization in the lower leaflet, but encounters more difficulties in partitioning in the upper leaflet and inserting in the hydrophobic core. The R6W and R9C clinical variants have a lower PMF barrier in DOPC and DPPC:DOPC:DOPS:CHOL bilayers compared to DynA WT, due to the R substitution affecting water interactions and, thus, facilitates partition in the water-bilayer or bilayer-water interfaces,

respectively. In the DPPC:DOPC:CHOL, R6W and R9C show higher PMF barriers, indicating that the R-to-W and R-to-C substitutions hinder the insertion in the membrane's hydrophobic core. Thus, in terms of energy, DynA R6W and R9C show preference for the upper leaflet polar heads-hydrophobic bilayer interface, WT inserts at the hydrophobic core bilayer section, and L5S shows easier partitioning in the lower leaflet polar heads-water interface.

To compare DynA peptides values with previously studied CPPs using the same force field, we performed simulations of DynA in a DPPC membrane (Table 20).

Table 20. *PMF values and simulation results for DynA variants in two additional lipid membrane compositions.*

	DPPC			DPPC:DOPC DPPS:DOPS:CHOL		
Peptide	**PMF (kJ·mol^{-1})**	**State**	**Pore Size (Å)[a]**	**PMF (kJ·mol^{-1})**	**State**	**Pore Size (Å)[a]**
DynA WT	890 ± 10	Pore (100%)	16.60 ± 0.10	970 ± 10	Return (100%)	NA
DynA L5S	530 ± 10	Pore (100%)	18.80 ± 0.10	830 ± 10	Steady state (66%) Pore (33%)	NA (66%) 3.71 ± 0.05 (33%)
DynA R6W	640 ± 10	Pore (100%)	16.5 ± 0.1	960 ± 10	Return (100%)	NA
DynA R9C	840 ± 10	Return (100%)	NA	1150 ± 10	Return (100%)	NA

The calculated PMF values were comparable to those previously obtained for CPPs, suggesting that DynA peptides have similar energy requirements for translocation. Moreover, when extending the comparison to other forcefields, a wide range of PMF values is observed. For instance, in a study with DOPC membrane and GROMOS87 force field, the cyclic Arg9 was reported to require approximately 120 kJ·mol^{-1} to reach the bilayer centre in a path where the pore was forced and 200 kJ·mol^{-1} in a pore-free path[235]. In parallel, the TAT peptide required ~300 kJ·mol^{-1} to reach the bilayer centre in a DOPC membrane using the GROMOS96 53a6 force field[333]. Moreover, coarse grained studies(MARTINI 2.0 force field for Arg and waters and MARTINI 2.2 polarizable for lipids and ions, in a DPPC membrane) reported similar values for Arg9 and cyclic Arg9, ~330 kJ·mol^{-1} in a pore-free path and ~240 kJ·mol^{-1} in a pore-forming path in order to reach the bilayer

centre[153]. Thus, these force fields and methods can potentially yield PMF values in the same range as the ones described in this study when considering all the bilayer length. Besides, the OPLS-AA force field yielded a PMF value of ~60 kJ·mol^{-1} for the translocation of a single arginine[223], whereas the CHARMM36 force field resulted in a PMF of ~300 kJ·mol^{-1} for the complete translocation of an Arg9 in a DOPC/DOPG (4:1) membrane with the application of an electric field of 0.05 V/nm[233]. In conclusion, these results indicate that PMF values can be strongly influenced by the choice of force field, thus caution is needed when comparing simulations performed with different force fields[334], and comparisons should be limited to simulations using the same force field.

3.4.3.2. Peptide-induced membrane disruption

After the aSMD simulation, which ends in a non-equilibrium situation through the steering process, the molecular distribution is similar for all cases: the peptide has been steered into the lower part of the bilayer and is close to the polar heads of the lipids in the lower part of the bilayer, defining the starting point for the three 100 ns cMD replicas (Figure 45C). The polar heads in the upper leaflet have been dragged with the peptide in the aSMD, being able to enter in contact with the polar heads in the lower leaflet and creating a continuous flow of water between both compartments, defined as a water pore (of approximately 10 Å, see Figures 48 and 49A). Nonetheless, this water channel is transient and can be stabilized or rapidly closed in the cMD simulation (Figures 48 and 49B).

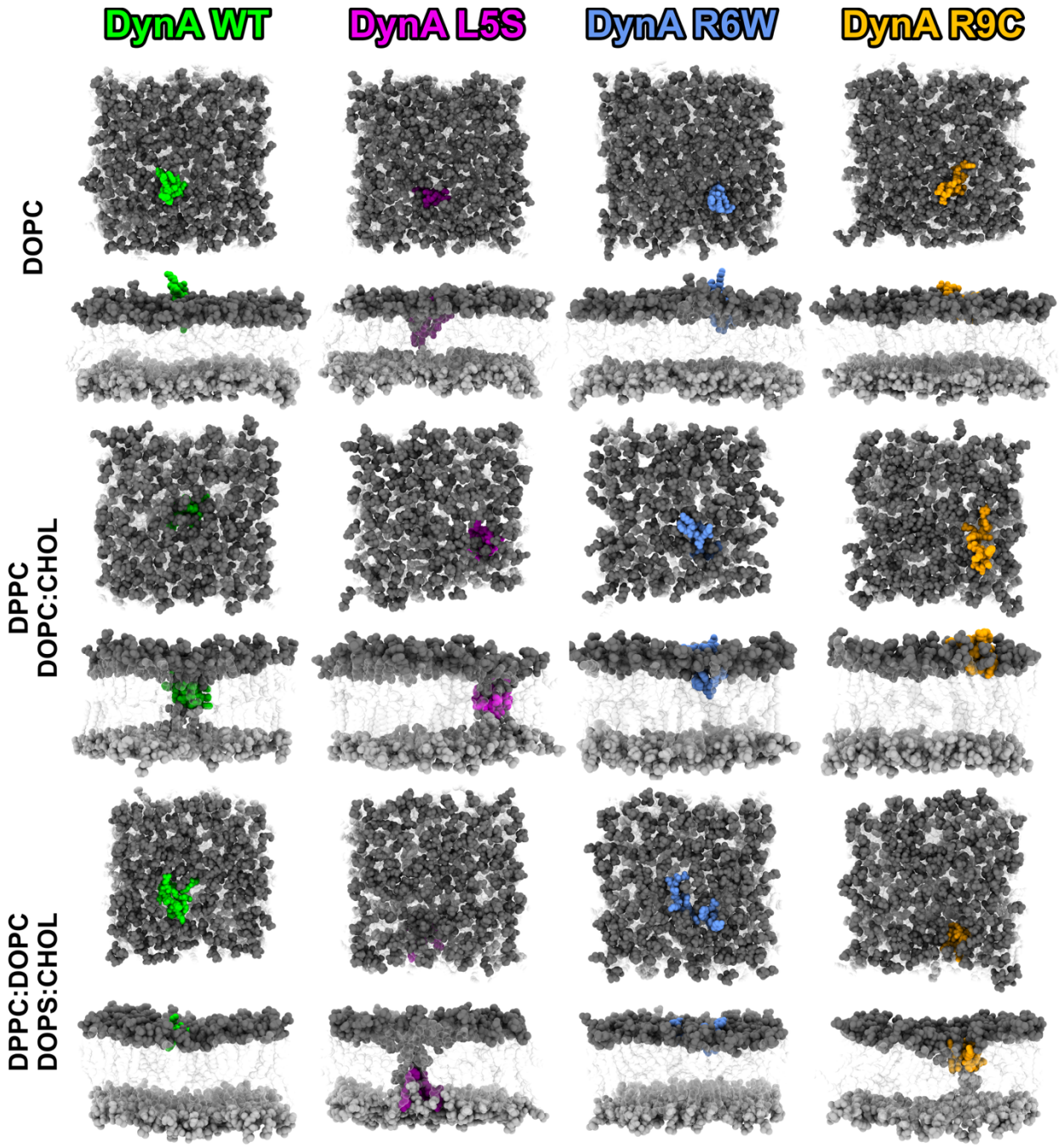

Figure 44. *Illustrative representation of the peptide location in the 3 membrane compositions after the 100 ns of conventional MD (relaxation). Top (top) and side (bottom) poses are shown for each case. The colour code is the following: DynA WT in light green, L5S in purple, R6W in cornflower blue, and R9C in orange. The polar heads of phospholipids in upper and lower bilayers are illustrated in darker and lighter shades of grey, respectively, while the lipid tails are portrayed in transparent white. Waters are omitted for clarity.*

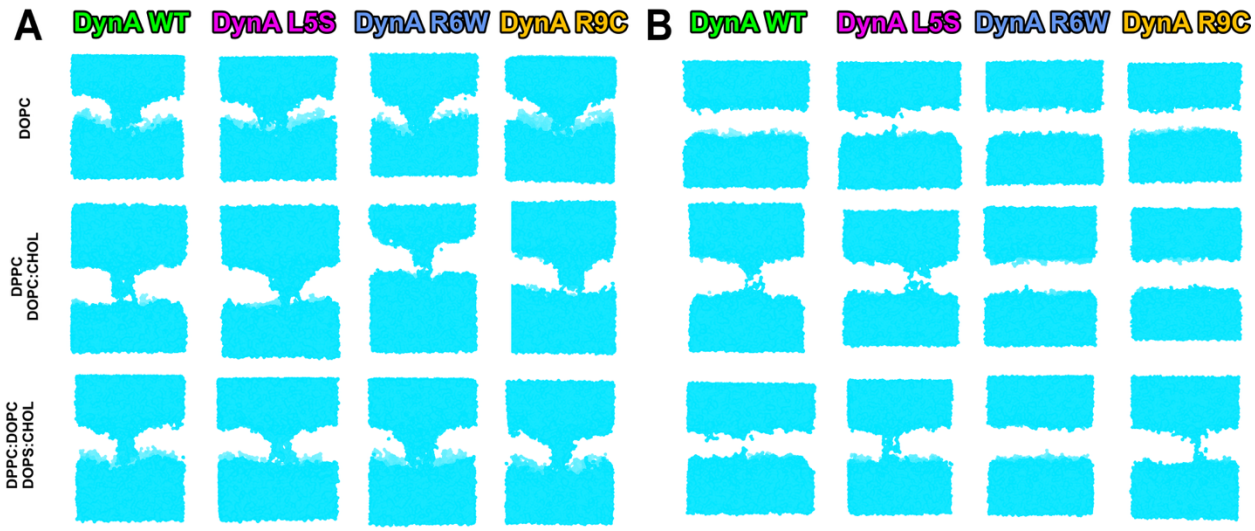

Figure 45. *Last snapshot of the water molecules in the (A) adaptive Steered Molecular Dynamics (aSMD) and (B) conventional Molecular Dynamics (cMD) simulations. The scale bar is shown for size clarity.*

The cMD simulation will explore whether the aSMD simulation has reached a close-to-equilibrium state. In Figure 48 the last step of the 100 ns cMD is shown, while the water distribution is shown in Figure 49B. All simulations that contain a pore channel, were extended until 500 ns (or until the channel closes) in order to analyse pore stability. DynA WT returns to the upper leaflet in DOPC and DPPC:DOPC:DOPS:CHOL, but WT is able to induce a strong membrane disturbance represented by a stable water-based pore channel (pore stable during the 500 ns simulations) in DPPC:DOPC:CHOL (Table 20, Figures 49B and 50). DynA L5S shows a stronger membrane disturbing behaviour compared to WT, as L5S induces a transient pore (duration of ca. 80 ns) in two out of the three replicas in DOPC, and a more stable pore channel (ca. 220 ns) in the third DOPC replica and in DPPC:DOPC:CHOL and DPPC:DOPC:DOPS:CHOL bilayers (stable over 500 ns) (Table 20, Figures 49B and 50). DynA R6W returns to the upper leaflet in all membrane compositions (Table 20). Last, DynA R9C returns to the upper leaflet in the first two membrane compositions but is able to form a pore in DPPC:DOPC:DOPS:CHOL (in two out of the three replicas of ca. 160 ns approximately), arguing for an easier interaction with the lower leaflet owing to the negative charge in the polar heads (Table 20).

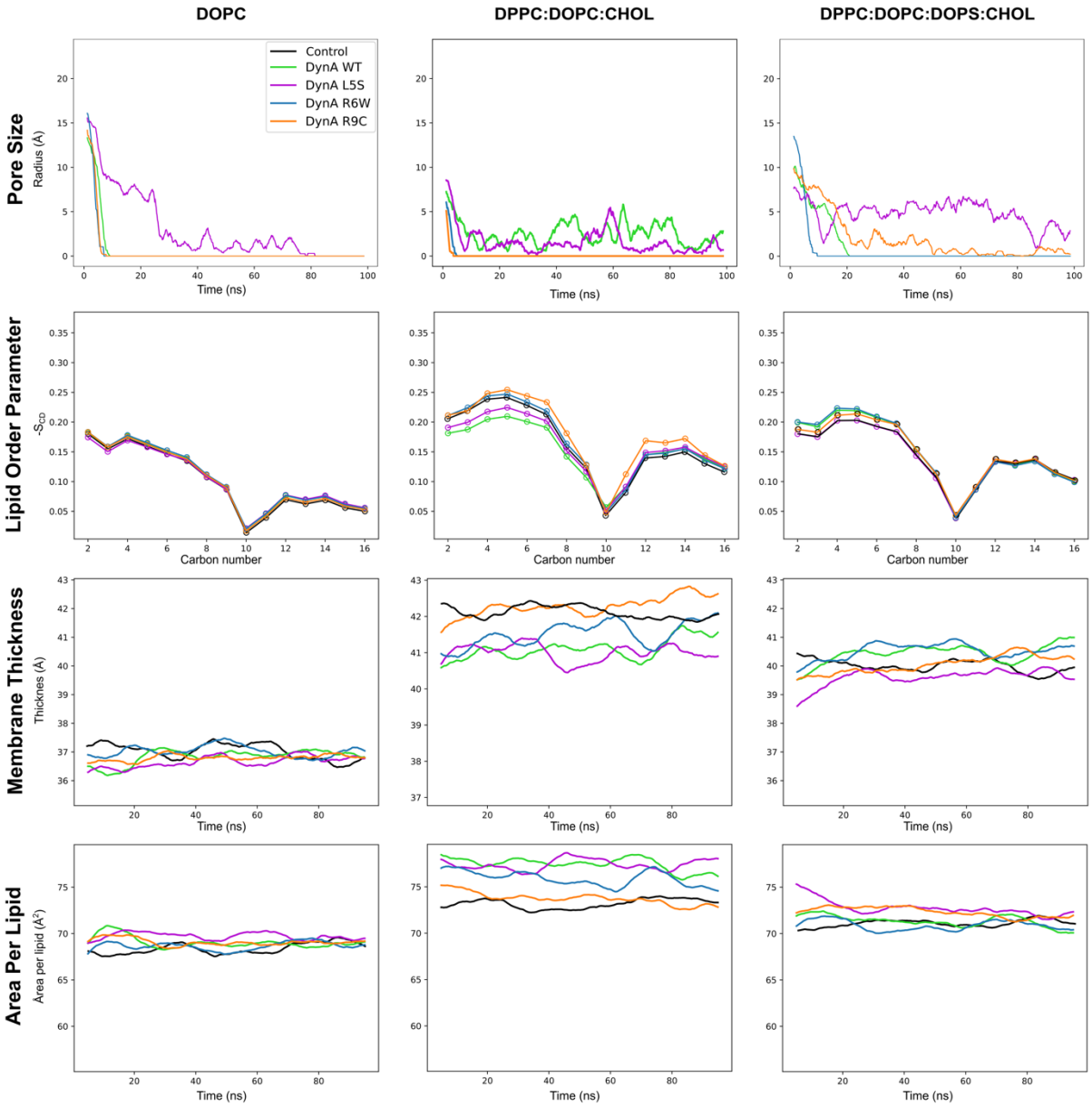

Figure 46. *Analysis of pore size, lipid order parameter, membrane thickness, and area per lipid in the cMD simulations for all membrane configurations. Peptide colours are kept the same as in previous figures.*

Overall, we observe two different results: return to the upper leaflet, and pore formation. In the first case, the peptide breaks the new interactions with the polar heads in the lower leaflet, again dragging the polar heads back to the upper leaflet. In the pore formation, the interaction between the polar heads of both leaflets opens a channel that allows water flow between the two water compartments.

In Figure 51, we show electron density of all the systems to observe the pore formation induced by peptide-bilayer interaction. We see how there is a higher density of water and polar heads in the middle of the bilayer for DynA L5S in DOPC, DynA WT and L5S in DPPC:DOPC:CHOL, and DynA L5S and R9C in DPPC:DOPC:DOPS:CHOL, demonstrating the pore formation. The importance of polar heads and peptides (Figures 50 and 51) in the pore formation leads to discuss that the kind of pores observed in this study are toroidal pores, where the peptide and polar heads in both leaflets interact, allowing water molecules to cross. Besides, peptides seem to have an important role in pore formation and stabilization, as seen in other studies[277,335].

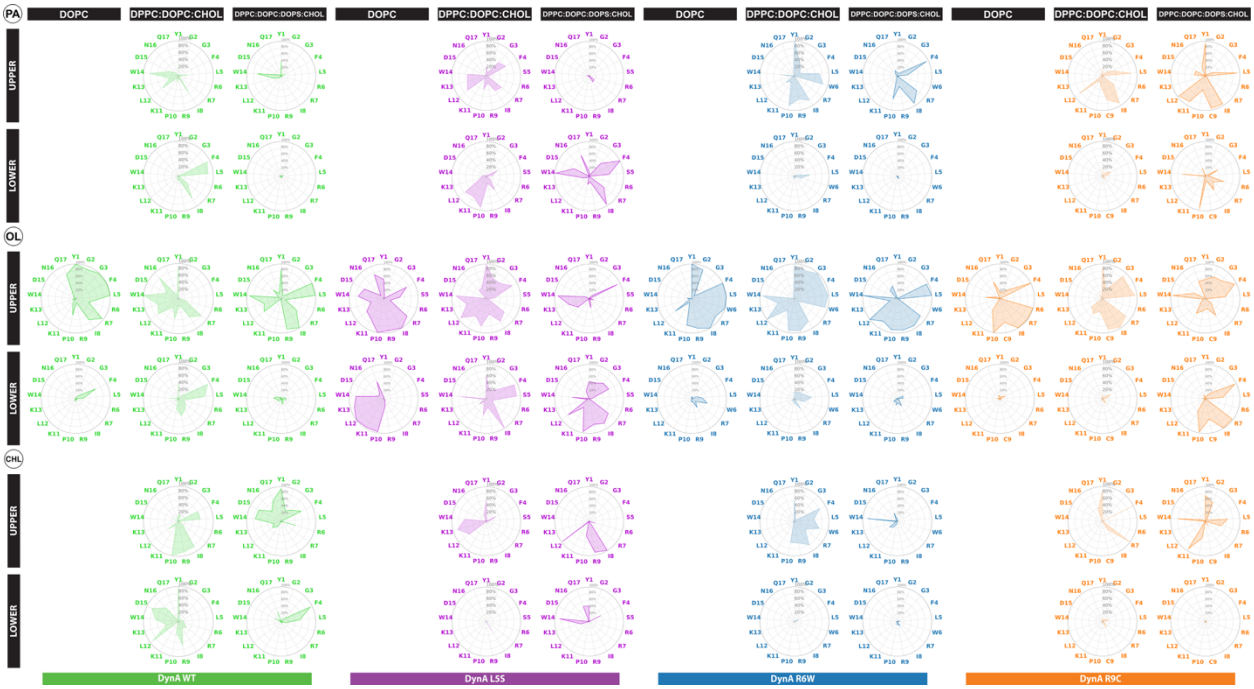

Figure 47. *Residue occupancy of the lipid tails and cholesterol in the three membrane compositions. PA refers to the lipid tail present in DPPC lipids, namely palmitic acid. OL refers to the lipid tail in DOPC/DOPS, namely oleic acid. CHL refers to cholesterol. These are the lipid names provided by the AMBERFF14SB and Amber Lipid21 forcefields.*

Pore formation requires that the peptide drags lipid polar heads from the upper leaflet along during the aSMD process. These polar heads remain hydrated by surrounding water molecules which protect them from the hydrophobic membrane environment. Peptide drag lipids from the upper leaflet lipids and contact the polar heads in the lower leaflet, leading to the interaction of waters from both compartments, ultimately opening a water channel[293]. These toroidal pores, as discussed before, are characterized by the presence of the peptide, lipid polar heads, and water, as illustrated in Figures 48, 49, 50.

3.4.3.3.Specific peptide-lipid interactions

To discuss the effect of lipid composition in the peptide-lipid interactions, lipid order parameter, membrane thickness, and area per lipid have been analysed (Figure 50). Lipid order parameter analysis measures the orientation of the lipid chains with respect to the bilayer normal[213]. Our results show that membranes are well organized, and no significant differences are observed between membranes regardless of the type of peptide-bilayer interaction or no peptide (control membranes). In parallel, membrane thickness and area per lipid results are related. DOPC membranes show the smallest membrane thickness (approximately 37 Å) and area per lipid (approximately 68 $Å^2$), indicating that DOPC is the most compact membrane. In DPPC:DOPC:CHOL membranes, the addition of a different lipid tail (DPPC) reduces the membrane compactness, increasing membrane thickness (~42Å) and area per lipid (~76 $Å^2$). In previous studies, the addition of cholesterol was linked to a decrease in area per lipid[228], but this effect seems to be counterbalanced by the addition of different lipid tails. Lastly, DPPC:DOPC:DOPS:CHOL membranes showcase a decrease in membrane thickness (~40 Å) and area per lipid (~67 $Å^2$), caused by the addition of negatively charged lipids (DPPS and DOPS), which tighten the membrane[222].

Membrane behaviour can also be related to the fluctuations in PMF values, indicative of the resistance offered by the bilayer to the peptide crossing. DOPC and DPPC:DOPC:CHOL showcase, on average, similar PMF values. Looking at membrane thickness and area per lipid, DPPC:DOPC:CHOL should have a lower PMF value since the membrane is less packed, leading to an easier penetration[100]. Cholesterol triggers a reduced efficiency in CPP translocation[102] and is able to counterbalance the effect of different lipid tails. In DPPC:DOPC:DOPS:CHOL, the membrane is more densely packed than DPPC:DOPC:CHOL (lower membrane thickness and area per lipid), and negative lipids increase peptide adsorption in the upper leaflet[222], ultimately requiring higher energy to break these interactions when internalising. Overall, these details cause the highest increase in PMF value of the study.

Analysis of peptide residue occupancy and the interactions with polar heads of the phospholipids in the upper and lower leaflets is shown in Figure 52. Occupancy, analysed with PyLipID[208], is defined as the percentage of simulation time during which the peptide residue is in contact with the polar head of the phospholipids. Thus, the values shown in Figure 52 represent the average

occupancy during the cMD simulation. DynA WT has five positively charged residues: R6, R7, R9, K11, and K13. In DOPC, R6, R7, and R9 interact with the polar heads, in DPPC:DOPC:CHOL these are R6, R7, K11, and K13, and in DPPC:DOPC:DOPS:CHOL, R7, R9, and K13 are key in the interaction with the polar heads. K/R neighbouring residues also show high occupancy. There is a high interaction zone in residue Y1 (extended to G2 in DOPC, to G3 in DPPC:DOPC:CHOL, and to F4 in DPPC:DOPC:DOPS:CHOL), which has been shown in NMR experiments by Lind *et al.*[134]. The only DynA residue with negative charge (D15) shows lower occupancy compared to surrounding residues.

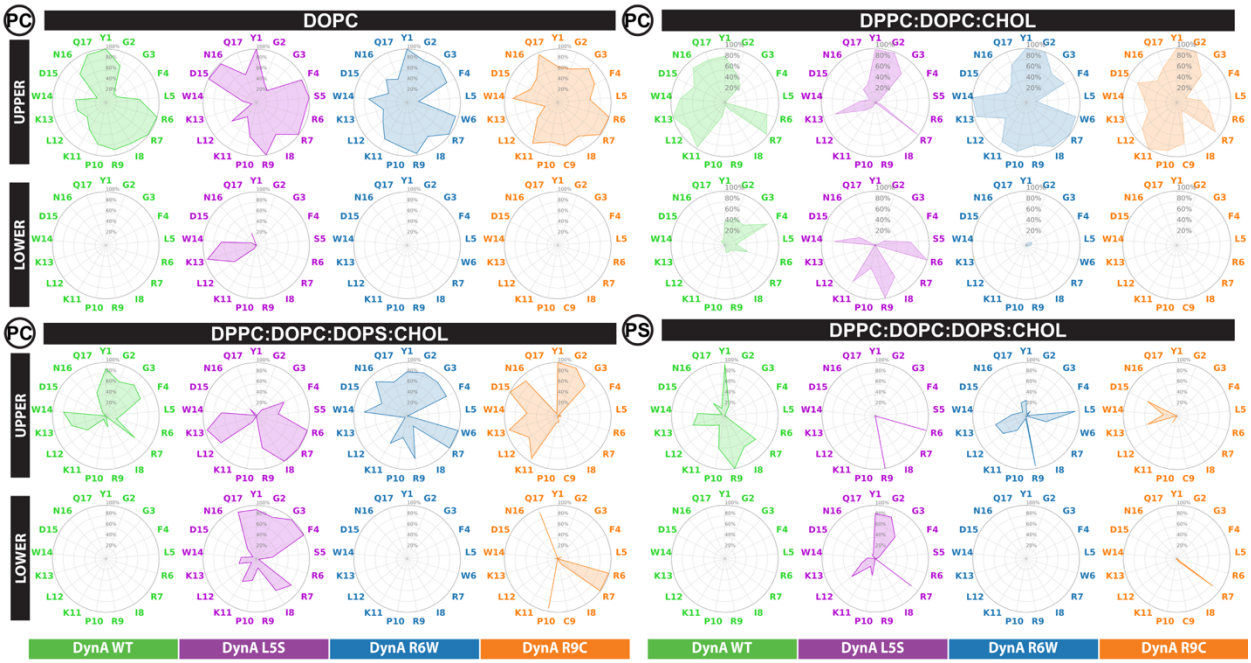

Figure 48. *Occupancy of the DynAs residues by the polar head of the lipid bilayer in upper and lower leaflets. Polar heads pertaining to PC lipids are shown for the three bilayers. PS interaction is also shown for DPPC:DOPC:DOPS:CHOL. The most representative replica analyses are shown for all simulations.*

The replacement of a hydrophobic residue by a polar residue in L5S facilitates interaction with the PC polar heads (S5 has higher occupancy than L5 in all cases) and the peptide global interactions with the polar heads in DOPC and DPPC:DOPC:DOPS:CHOL membranes. In the cases of DynA R6W and R9C, both mutations entail the loss of a positively charged residue (R). In general, interactions are maintained or shifted towards another part of the peptide. Nonetheless, the lack of R9 in R9C is easily spotted in DPPC:DOPC:DOPS:CHOL, since it is the peptide with the least interaction with PS polar heads.

DynA L5S in DOPC, DynA WT and L5S in DPPC:DOPC:CHOL, and DynA L5S and DynA R9C in DPPC:DOPC:DOPS:CHOL interact with both the upper and lower leaflets. This is the key to toroidal pore formation, since the peptide "complexes" with the phospholipids due to the interaction between positively charged residues and the negatively charged phosphate groups of polar heads[231]. Water molecules solvate positively charged residues (K, R) and their neighbours, leading to the connection of water molecules across both spaces and subsequent pore formation.

The presence of cholesterol in the DPPC:DOPC:CHOL bilayer system introduces a new variable that has not been previously proposed in the DynA clinical variants literature[131,132,135]. To assess the residue relevance in the hydrophobic core of the bilayer, we analyse the peptide residue occupancy at the cholesterol and lipid tails level (Figure S4). Hydrophobic (L and I), apolar (P and G), and aromatic (F, W and Y) residues mediate the interaction with the lipid tails. For DynA WT, the interaction with cholesterol happens in both leaflets of the DPPC:DOPC:CHOL and DPPC:DOPC:DOPS:CHOL bilayers, mediated by hydrophobic residues such as L5, I8, and L12, aromatic residues such as Y1, F4, and W14, apolar P10, and charged R9 and D15. In the DynA L5S, most cholesterol interactions are gone, shifted towards Y1, I8, R9, K13, and W14. For R6W, the lost R shifts cholesterol interaction towards the F4-I8 hydrophobic/aromatic patch, and W14 in DPPC:DOPC:DOPS:CHOL. The lost R in R9C restricts the cholesterol interaction to Y1, F4, L5, R7, K11, and W14 in the upper leaflet. In general terms, the presence of negatively charged lipids in the DPPC:DOPC:DOPS:CHOL bilayer, dampens the DynA:CHOL interaction.

3.4.3.4. Global bilayer effects

Cell penetrating peptides (CPPs) and antimicrobial peptides (AMPs) disrupt bilayers through specific mechanisms, with dynorphins—neuropeptides with CPP/AMP potential—proposed to induce cytotoxicity via plasma membrane poration. In a previous computational study, we characterized the membrane disruption potential of canonical CPPs. Here we extend that approach to neuropeptides, such as DynA, using symmetric bilayers to model: (1) peptide partitioning at the water-bilayer interface on the extracellular side (DOPC); (2) peptide transition through the hydrophobic core (DPPC:DOPC:CHOL); and (3) interactions with negatively charged lipids on the cytosolic side (DPPC:DOPC:DOPS:CHOL). Results show that DynA L5S induces strong membrane poration, WT and R9C moderate poration, and R6W no poration, by reaching different stages at the bilayer (Figure 53).

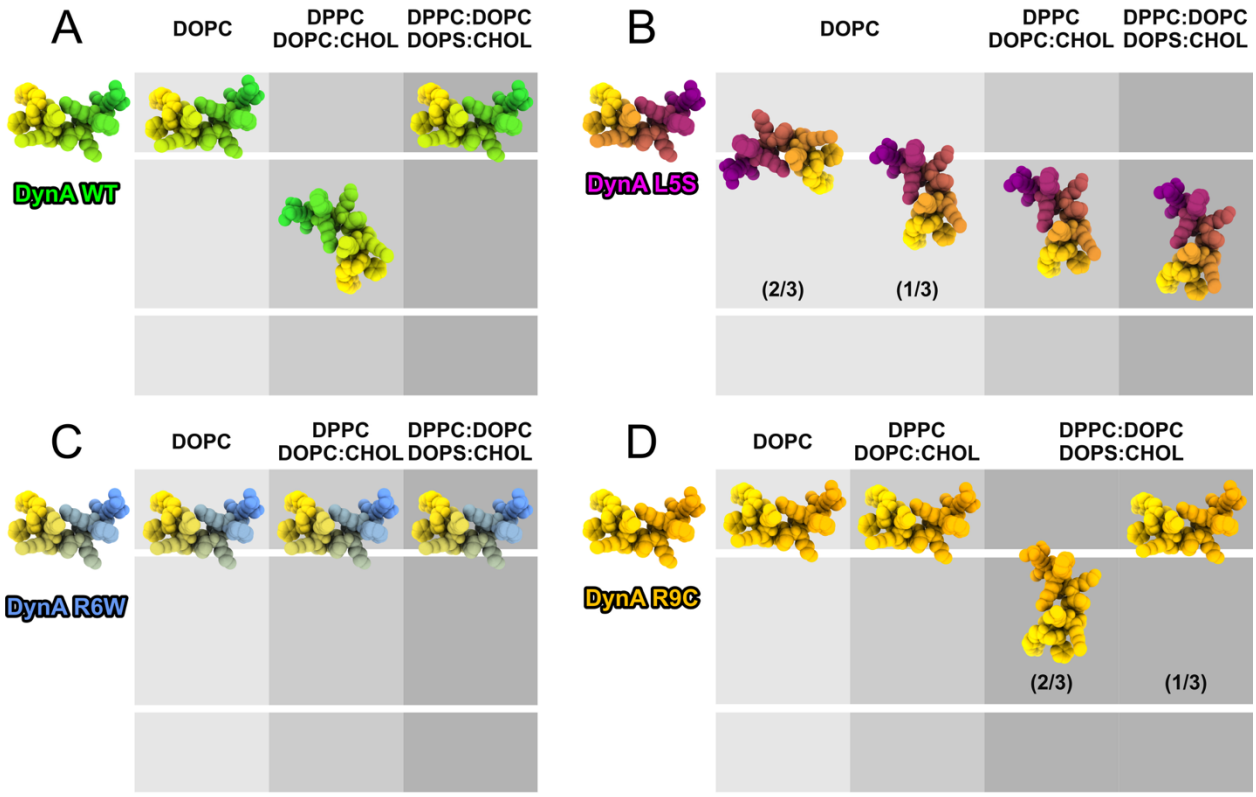

Figure 49. *Final position and orientation of the peptide in the different bilayer compositions. The peptides are coloured from N to C-terminal with a gradient from gold to its respective colour: (A) DynA WT in green, (B) DynA L5S in purple, (C) DynA R6W in cornflower blue, (D) DynA R9C in orange. The bilayer is represented in grey, and darker shades of grey represent higher bilayer complexity: DOPC in light grey, DPPC:DOPC:CHOL in grey, DPPC:DOPC:DOPS:CHOL in dark grey. The white lines differentiate between upper/outer part of the bilayer, hydrophobic core and lower/inner part of the bilayer. The ratios in DynA L5S DOPC and R9C DPPC:DOPC:DOPS:CHOL indicate the ratio of behaviours seen in replicas. If ratios are not shown, 100 % agreement between replicas is observed.*

Comparing the peptide penetration (Figure 53) and the PMF barrier (Figure 46, Table 20), we observe the following trend: DynA WT faces high PMF barrier to cross the DOPC membrane (PMF value of 790 kJ·mol^{-1}) and it is not able to get stabilized by forming a pore, contrary to what is observed in DPPC:DOPC:CHOL (PMF value of 650 kJ·mol^{-1}), where the peptide faces a lower PMF requirement and it is able to induce pore formation. In DPPC:DOPC:DOPS:CHOL, DynA WT finds the highest resistance to bilayer crossing (1160 kJ·mol^{-1}), resulting in rapid relocation in the upper leaflet. Overall, DynA WT seems to be able to get stabilized in the hydrophobic core of the membrane, but it encounters difficulty getting adsorbed in the upper leaflet or reaching the lower leaflet. For DynA L5S, the highest resistance to the bilayer crossing is in DOPC (870 kJ·mol^{-1}), which results in more or less stable (pore duration ranges between 80 to 220 ns) pore formation. Then, DynA L5S finds less resistance in the bilayer crossing in DPPC:DOPC:CHOL and

DPPC:DOPC:DOPS:CHOL bilayers (780 and 810 kJ·mol^{-1}, respectively) and, thus, L5S is able to porate the bilayer in both cases. In fact, DynA L5S is the only peptide that does not show a considerable increase in the barrier energy when comparing DPPC:DOPC:CHOL to DPPC:DOPC:DOPS:CHOL PMF values. This similarity can be related to the fact that it is the only peptide that is able to form a 500 ns-stable pore in the DPPC:DOPC:DOPS:CHOL bilayer, arguing that it does not encounter high energy barrier to diffuse from the hydrophobic core to the inner leaflet, as opposed to DynA WT. DynA R6W shows a similar barrier to cross the DOPC and DPPC:DOPC:CHOL membranes (640 and 720 kJ·mol^{-1}, respectively), but it is not able to induce poration in any of the cases. In the DPPC:DOPC:DOPS:CHOL bilayer, the PMF increases (1050 kJ·mol^{-1}, respectively) and does not seem to allow the R6W peptide for any membrane disturbance. In short, DynA R6W seems to be able to get adsorbed in the outer leaflet, but without being able to form a pore to access the hydrophobic core. Lastly, for DynA R9C the PMF barrier is low in DOPC, but high in DPPC:DOPC:CHOL and DPPC:DOPC:DOPS:CHOL (670 kJ·mol^{-1}, 850 kJ·mol^{-1}, and 1020 kJ·mol^{-1}, respectively) and only allows for a transient poration (of 160 ns) in DPPC:DOPC:DOPS:CHOL. However, DynA L5S in DOPC (highest PMF value) or DynA WT in DPPC:DOPC:CHOL (lowest PMF value) demonstrate that the PMF is not the sole determinant of membrane disruption, as these peptides show large PMF values, but are still able to induce pore formation. This behaviour indicates that there are more factors affecting the membrane disruption potential, such as peptide-lipid interactions, the disposition of positively charged residues (R, K), peptide orientation or secondary structure. In fact, peptide secondary structure was analysed to check for trends between any secondary structure, PMF fluctuation and/or membrane poration. Nonetheless, no relation was found between these behaviours (Figure 54), maybe because longer simulation timescales are required to observe meaningful changes in secondary structure, which will be tackled in a further study.

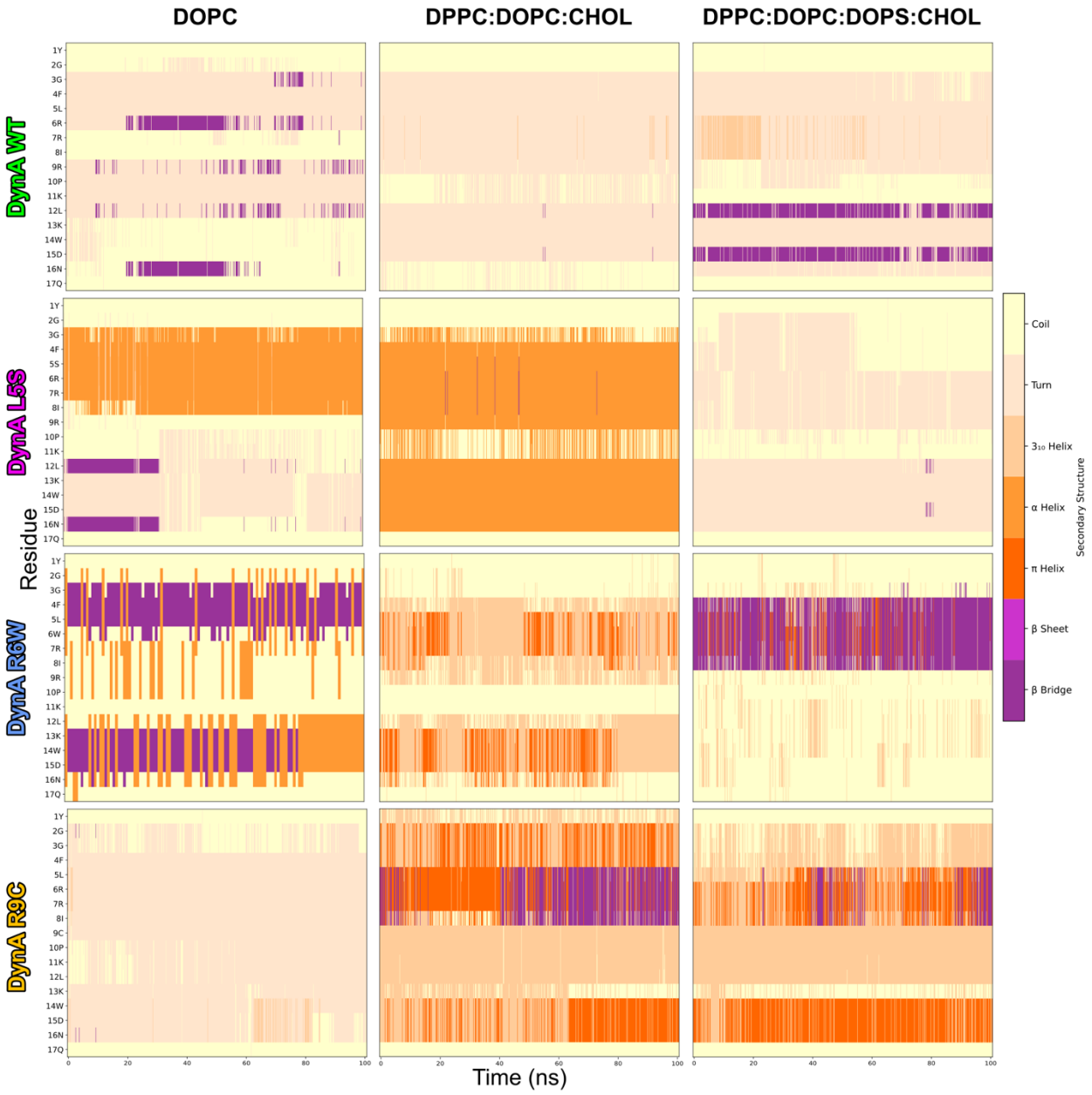

Figure 50. *Secondary structure of all peptides across all membranes.*

The N-terminus Y1 residue in DynA WT, L5S, and R9C orients towards the hydrophobic core as a prerequisite to poration (Figure 53), which agrees with experimental studies[134]. DynA peptides form toroidal pores with lipophilic residues facing lipid tails, and hydrophilic residues coordinated with the waters in the inner side of the pore (Figures 55 and 56).

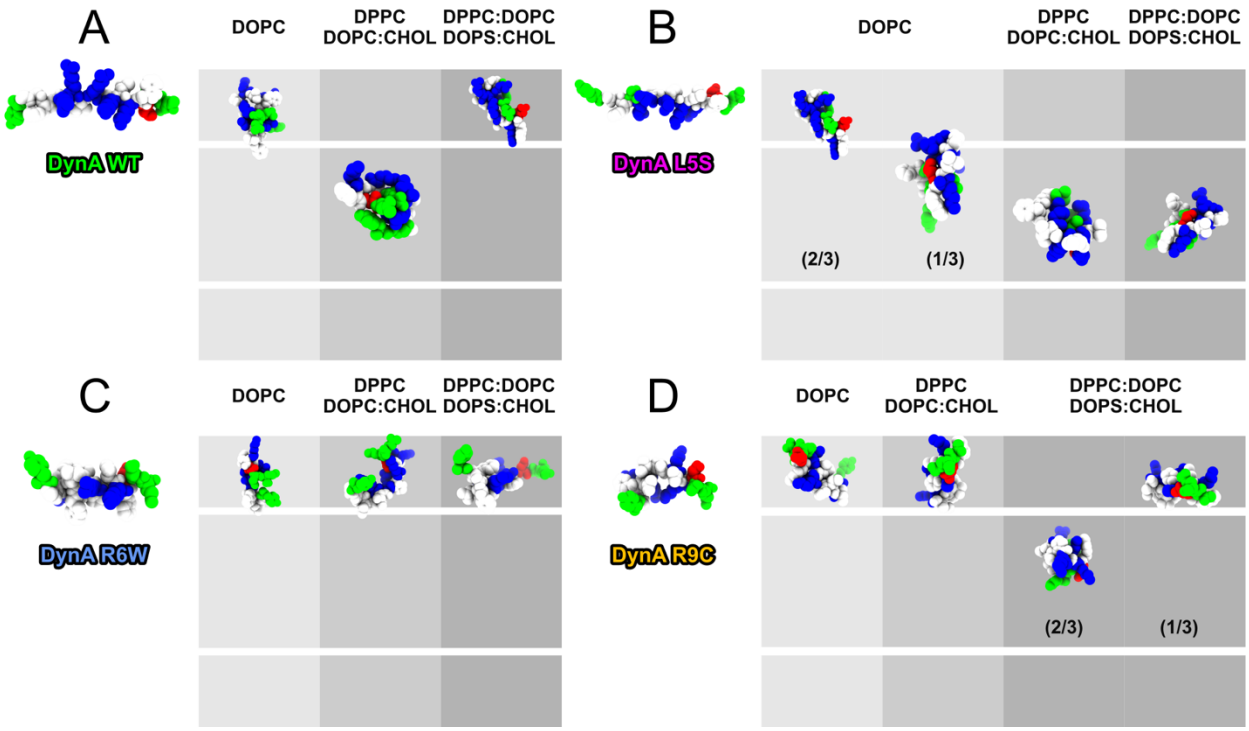

Figure 51. *Final position of the peptide in each membrane composition: (A) DynA WT, (B) DynA L5S, (C) DynA R6W, (D) DynA R9C.. The peptides are coloured based on the residue type, following VMD scale, differentiating between non-polar residues (white), basic residues (blue), acidic residues (red) and polar residues (green). The ratios in DynA L5S DOPC and DynA R9C DPPC:DOPC:DOPS:CHOL indicate the ratio of behaviours seen in replicas. If the ratios are not shown, 100 % agreement between replicas is observed. The initial pose corresponds to the pose after the initial peptide modelling.*

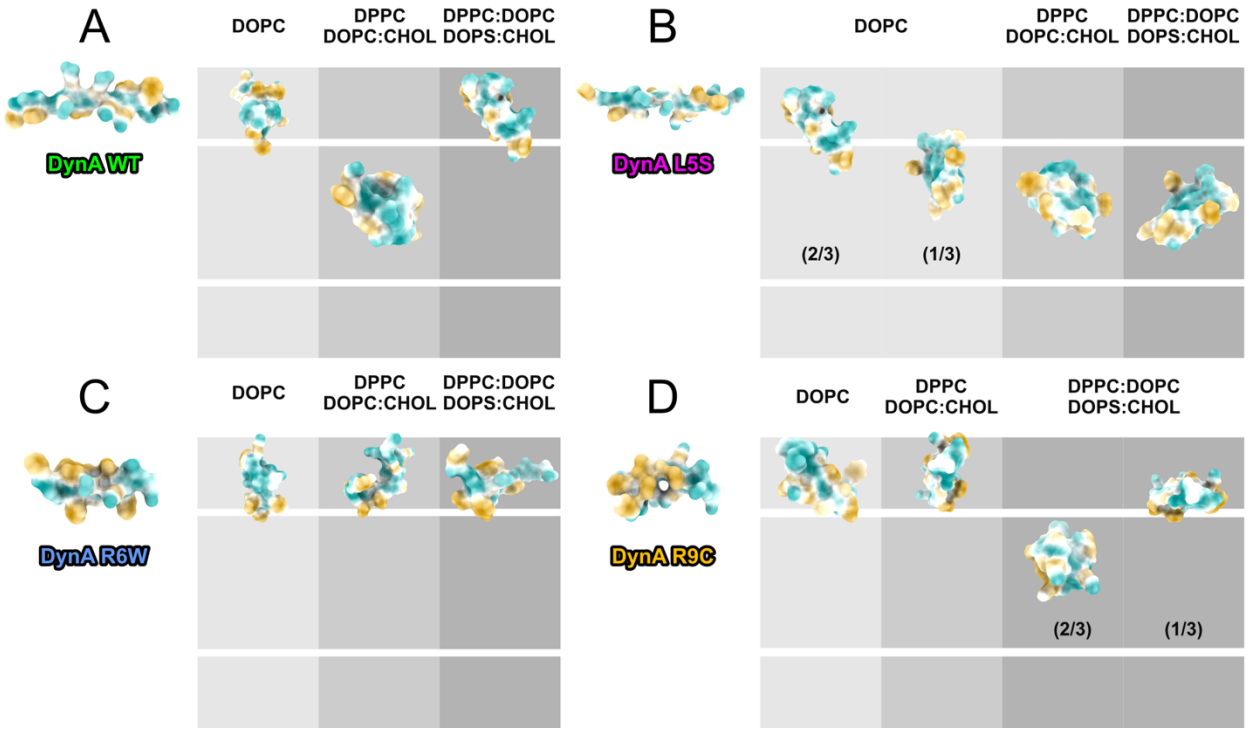

Figure 52. *Peptide's final position in each bilayer composition: (A) DynA WT, (B) DynA L5S, (C) DynA R6W, (D) DynA R9C. The peptides are coloured based on ChimeraX lipophilicity scale: which ranges from dark cyan (most hydrophilic) to white to dark goldenrod (most lipophilic). The ratios in DynA L5S DOPC and DynA R9C DPPC:DOPC:DOPS:CHOL indicate the ratio of behaviours seen in replicas. If the ratios are not shown, 100 % agreement between replicas is observed. The initial pose corresponds to the pose after the initial peptide modelling.*

Specific residues in DynA WT (L5, R6, R9) are crucial for membrane interaction of clinical variants at both polar head and hydrophobic core levels. WT, L5S, and R9C peptides can form water pores stable over 100 ns, agreeing with a pathological mechanism of DynA through plasma membrane poration[324,330], also observed in our simulations. L5S exhibits lower energy barriers and consistent pore formation across all bilayers, like what should be expected from CPPs. In fact, CPPs can decrease the potential of resting cells to low values, in which spontaneous pore formation is possible[308]. Our results may indicate difference to previous liposome leakage experiments, which, as discussed before, reveal that all DynA variants cause leakage, except L5S in large unilamellar vesicles[132]. Thus, DynA activity may be dependent on membrane compositions[131], whereas Madani *et al.* used a specific POPC/PG composition, here we use DPPC, DOPC/PS and cholesterol. Overall, DynA peptides, particularly L5S, WT, and R9C, demonstrate stronger water pore-formation potential compared to canonical CPPs. Thus, our method allows for the observation of pore formation and subsequent stabilization or pore closure due to upper or lower leaflet stabilization. DynA WT and the clinical variants show certain peptide aggregation/self-assembly, introducing a peptide concentration factor[131], thus further computational studies considering peptide self-assembly at or in the bilayer[330] should be pursued.

3.4.4. Conclusion

In this study, we employed a combination of adaptive steered molecular dynamics (aSMD) and conventional MD (cMD) simulations to investigate the membrane-disrupting potential of DynA WT and its clinical variants. Our results suggest that DynA peptides, particularly DynA L5S, exhibit comparable or lower potential of mean force (PMF) values than canonical CPPs, indicating potential CPP-like behaviour. cMD simulations further support this by showing that DynA L5S consistently induces stable pore formation across diverse membrane compositions, while other variants display distinct, bilayer-dependent behaviours.

We acknowledge that aSMD introduces artificial steering forces to accelerate rare events such as membrane translocation, which in biological systems are driven by a complex interplay of membrane potential, peptide cooperativity, lipid heterogeneity, and thermal fluctuations. While these factors are not explicitly modelled, aSMD enables exploration of translocation pathways within accessible timescales. Importantly, the timescales accessible to molecular dynamics simulations—typically in the range of nanoseconds to microseconds—remain orders of magnitude shorter than those of biological peptide translocation, which can occur over milliseconds to minutes. This discrepancy necessitates the use of enhanced sampling techniques to capture relevant events within computationally feasible timeframes.

The subsequent cMD simulations provide an unbiased view of membrane perturbation, offering complementary insights into the stability and consequences of these events. Although PMF values derived from aSMD are sensitive to the choice of force field and pulling protocol, relative PMF trends across membrane compositions remain informative. Future work should incorporate more biologically realistic membrane models—featuring lipid asymmetry, phase separation, and membrane potential—as well as varied peptide:lipid ratios and initial configurations to better capture physiological complexity.

Despite these limitations, our combined aSMD/cMD approach remains a valuable tool in computational biophysics. It enables mechanistic insights into peptide-membrane interactions that are difficult to access experimentally and complements in vitro and cellular studies by providing atomistic resolution. Our findings support the continued development and application of enhanced sampling techniques to advance our understanding of bioactive peptide function and membrane dynamics.

General discussion

4. DISCUSSION

4.1. Importance of each chapter

In the first chapter, we use the previously presented aSMD technique in combination with a cMD simulation. First, in the aSMD part, the peptide (we use diverse types of CPPs) is forced to pass through the bilayer until the lower leaflet, which allows for PMF calculation using replicas. Because the aSMD ends in a non-equilibrium step, we use the last frame of the aSMD part to perform a cMD simulation to permit system equilibration, enabling us to observe peptide equilibration and unbiased peptide–membrane interactions. The importance of this chapter lies in the presentation of a new technique, or a combination of two, in the field of protein–membrane interactions. We believe aSMD + cMD can overcome previous limitations, as it enables the calculation of PMF and provides a novel approach to studying peptide-mediated disruption.

In the second chapter, we repurpose the use of CompEL, a technique in which a transmembrane potential through ion imbalance (ΔQ) is used to induce membrane disruption. The peptide can make use of such disruption to get inserted and, in some cases, translocate to the lower leaflet. So, we use CompEL simulations with different peptides (CPPs and non-CPPs) and diverse peptide concentrations to study peptide–membrane interactions and peptide-translocating potential. We believe CompEL represents an advance in the study of protein–membrane interactions, as it enables the simultaneous use of multiple peptides, offers a faster alternative to existing methods, and serves as an accessible entry-level technique that helps to narrow the gap with biological conditions. A graphic summary of aSMD + cMD and CompEL techniques is in Figure 57.

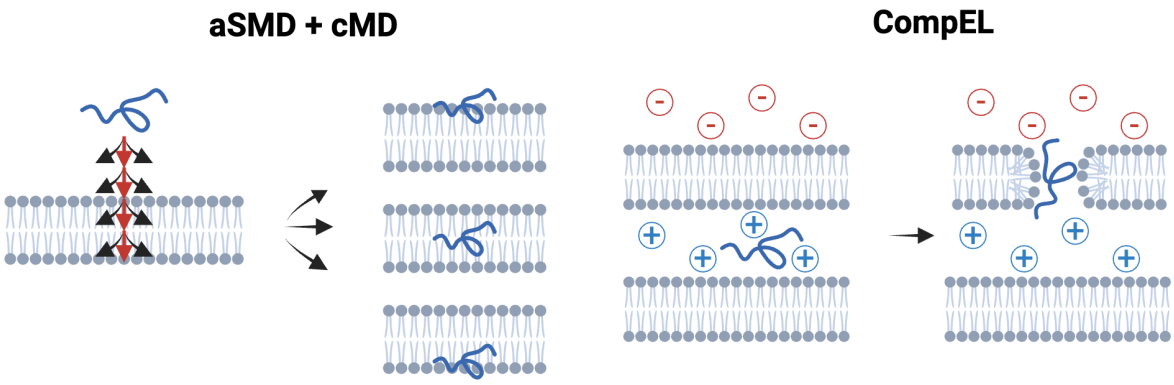

Figure 53. *Schematic representation of the procedure involved in aSMD + cMD and CompEL techniques.*

In the third chapter, we expand the use of CompEL to a broader variety of membrane compositions, including cholesterol-containing, negatively charged, and asymmetric membranes. Further, the computational results are compared with experimental studies of liposome leakage and peptide internalization, in order to try to correlate computational with experimental methods. Since this chapter is only intended to present the technique, only one CPP (MAP) is used in this part. This chapter importance is found in the use of more complex and biologically relevant membranes, which allow for easier comparison with experimental conditions and lend greater significance to the results obtained.

Finally, in the fourth chapter, we apply the technique presented in the first chapter, aSMD + cMD, to investigate membrane disruption of DynA WT and its clinical variants. Using a distinct set of neutral, cholesterol-containing and negatively charged membranes, we characterize how DynA interacts with different lipid environments. This chapter is key as it demonstrates the application of the new technique to biologically relevant systems, providing deeper insights into the mechanism of peptide-membrane interactions.

4.2. Peptide–membrane interactions

The aSMD + cMD technique allows for the observation of all the key processes in peptide translocation. The first step in the peptide–membrane interactions is the peptide interaction with the upper part of the bilayer leaflet (from this point onward referred to as the upper leaflet), step known as partitioning (Figure 11). Here, the positive residues in the peptide sequence (arginine, lysine, histidine) drive the peptide interaction with the negatively charged headgroups in the phospholipid bilayer. Consequently, electrostatic and hydrogen bonding interactions are key in the first step of peptide–membrane interactions.

Thereafter, the peptide crosses the headgroups in the membrane until it reaches the bilayer central core, process known as insertion. Hydrophobic interactions are key to allow the peptide insertion and contact with the lipid acyl chains, primarily attracted to the non-polar residues (such as valine, leucine, or isoleucine) in the peptide sequence. Nonetheless, even though peptide insertion occurs, the positive residues are still in contact with the polar heads, interactions that are not easily broken. Therefore, polar heads are dragged with the peptide as it gets inserted, thus leading to the start of peptide–mediated membrane disruption[336].

When the peptide crosses the hydrophobic core, if the peptide and the polar heads disturbance gets deep enough in the bilayer, they can reach the polar heads in the lower part of the bilayer leaflet (hereafter referred to as lower leaflet) and establish contact with them, hence uniting the headgroups of both leaflets (Figure 11). This process can lead to pore formation if waters permeate the disturbance (Figure 48)[284,304]. There are some peptides, such as Arg9, that need the pore formation to pass through the bilayer[284,302,337,338]. For Arg9, this fact can be explained due to the peptide nature: since all residues are positively charged, they do not favour interaction with the hydrophobic core and, consequently, Arg9 needs to always interact with either the polar heads or water residues (when a pore is formed).

Finally, the peptide deepens its insertion to the bilayer, which can lead to a rupture in the interactions with the lipid headgroups in both leaflets. Then, the polar heads pertaining to the upper leaflet returning to its starting position, in some cases also closing the membrane disturbance and the pore[304], with the peptide getting stabilized in the lower leaflet and achieving translocation.

Contrary to aSMD + cMD, CompEL technique does not enable the description of the whole translocation process, as the pore is created due to the ΔQ generated between both sides of the bilayer. Still, the peptide can make use of such disruption to interact with the bilayer, leading to peptide insertion. In addition, the peptide can reach the lipid headgroups in the lower leaflet, thus completing the translocation, which can lead to pore closure[31,321]. Precisely, this is the major difference in the effect between CPPs and AMPs, as the formers can reach the lower leaflet and lead to pore closure, thus forming highly labile pores, whereas the latter are more stable within the membrane, and can form stable pores which destabilize the membrane[339,340].

Both aSMD + cMD and CompEL techniques are useful to study the most important peptide–membrane interactions in the translocation process. First, positive residues are crucial for peptide partitioning, as they get attracted to the negative polar heads in the bilayer and stabilize the peptide–membrane interaction (Figures 16 and 51)[152,247,282,283]. Additionally, it has been seen that arginine residues provide stronger interactions with the negatively charged lipid headgroups, owing to the guanidium group present in arginine, not present in lysine[341–343]. Moreover, polar residues are also important for the interaction with the headgroups in the lower leaflet, crucial for the completion of the translocation process. Consequently, the importance of such residues explains the ubiquity of positive residues in CPPs and, in MAPs in general, as they are key for the interaction with polar headgroups in both leaflets[25,337].

On the other hand, hydrophobic residues are attracted to the membrane acyl tail core, while polar residues keep interacting with the polar heads of the upper leaflet, thus achieving peptide stability when it is inserted in the membrane core. Therefore, hydrophobic residues are also important for CPPs, as they can provide balance in the peptide sequence since they can interact within the hydrophobic core[247,283,342,344].

Thus, the presence of both charged and hydrophobic residues, and a correct balance between these, can be beneficial for CPPs and MAPs[285,345], which occur in some important CPPs, such as penetratin, TAT or MAP. Oligoarginines are an exception to this rule, as they are highly efficient translocating peptides without hydrophobic residues[152]. Nonetheless, the peptide sequence is not the only determinant for peptide translocation, and more variables need to be considered.

4.3. Peptide analysis: concentration, orientation, secondary structure

The systematic analysis of peptide variables is essential for exploring the molecular principles that govern their ability to interact with lipid membranes. In this sense, peptide concentration is an important factor involved in CPP translocation, but it is not often considered in computational studies, as most techniques do not allow for the use of more than one peptide molecule. In fact, from the techniques included in Figure 57 and Table 1, only cMD, HT-MD, MT-MD and CG-MD have been used with several peptide molecules[151,152,231].

On the one hand, aSMD + cMD does not allow for the study of multiple peptide molecules, so one peptide and 300 lipid molecules were used, leading to a 1:300 P:L ratio. On the other hand, CompEL does allow for the study of different P:L ratios. Even though CompEL initial simulations were performed with one peptide molecule and 256 lipid molecules (per bilayer, totalling a 1:256 P:L ratio), subsequent simulations were run with eight peptide molecules. It was previously demonstrated that a higher number of peptides does not increase PMF[223], and that a large number of peptide molecules induce higher membrane disruption, necessary for peptide insertion and translocation[31,152,231,233,301,302,346].

Hence, CompEL simulations were also run at a 1:32 P:L ratio, where it was observed that several peptide molecules allow for more peptide insertion and translocation events, even though only one or two peptide molecules get inserted[301]. Cooperativity helps create a stronger bilayer perturbation and, moreover, when one peptide gets inserted, it can help another peptide to enter within the membrane[305]. Furthermore, a higher P:L ratio more closely reflects the conditions employed in experimental studies, where larger peptide-to-lipid ratios are used[347,348]. It also provides a more physiologically relevant scenario, since local peptide concentrations at the membrane surface can be significantly higher than bulk concentrations due to peptide accumulation and electrostatic attraction[349]. Thus, using a higher P:L ratio not only improves the comparability between simulations and experimental data, but also enhances the biological relevance of the observed peptide–membrane interactions.

Peptide concentration has been identified as a key factor influencing CPP–membrane interactions in experimental studies. For instance, Binder and Lindblom [350] observed that peptide-to-lipid ratio must exceed approximately 1:20 to enable penetratin internalization. Below this threshold,

penetratin binds only to the outer surface of vesicles, whereas higher peptide concentrations facilitate translocation across the bilayer. Moreover, their study showed that accumulation of positively charged peptides on the membrane surface can generate an electric field across the bilayer, leading to membrane permeabilization and peptide translocation. Once internalized, the reduction of this electric field restores membrane stability. This behaviour is reminiscent of what we observe in our CompEL simulations, where an imposed transmembrane potential accelerates membrane permeabilization.

Similarly, the TAT peptide requires relatively high concentrations to disrupt membranes and induce the formation of transbilayer water channels[351]. in contrast, oligoarginines exhibit much higher translocation efficiencies, over 100-fold greater than TAT, as demonstrated in other experimental studies[352,353]. Nonetheless, other experiments have shown that penetratin can also internalize at low concentrations[354], suggesting that the translocation mechanism and degree of cooperativity vary among CPPs and depend strongly on peptide sequence and local concentration.

Peptide cooperativity also depends on the peptide and its characteristics. For instance, Arg9 peptides do not remarkably interact among them, as 80 % of hydrogen bonds formed are intrapeptide. On the other hand, Leu9 peptides showcase important interpeptide interactions, with 50 % of the hydrogen bonds formed being between different molecules.

A second important variable is the peptide orientation throughout the simulation. The peptide orientation varies as it crosses the bilayer (Figure 58), as a perpendicular orientation to the membrane allows for higher inserting capacity. To visualize this change in orientation, in Chapter III, we used an analysis script that measures the orientation with respect to the bilayer normal (Figure 37). This way, if the angle is close to 90 º, the peptide is parallel to the bilayer, whereas values closer to 0 º indicate that the peptide is parallel to the bilayer normal and is, thus, perpendicular to the bilayer. This analysis has been useful to determine the peptide orientation throughout the process, as it allows to find different orientations during the diverse phases in peptide translocation.

In the partitioning step, polar residues are interacting with the lipid polar heads or with water molecules, whereas hydrophobic residues are protected from polar surfaces and mainly interacting among them. Thus, MAP is parallel to the bilayer and perpendicular to the bilayer normal, with angle values close to 90 º. Once the peptide gets inserted in the bilayer, the hydrophobic residues

interact with the hydrophobic core of the membrane, but the interactions between positive residues and upper leaflet lipid polar heads are not broken. Moreover, the peptide starts interacting with the polar headgroups in the lower leaflet. Consequently, there are polar residues interacting in the upper and polar residues in the lower part of the bilayer, whereas the hydrophobic residues stay in the middle part, thus causing MAP to get stretched and perpendicular to the bilayer, changing its orientation to values closer to 0 º. For translocation to be achieved, the interactions with the upper leaflet and the hydrophobic core need to be interrupted, causing that hydrophobic residues need to protect again from polar molecules, thus orientating again parallel to the bilayer.

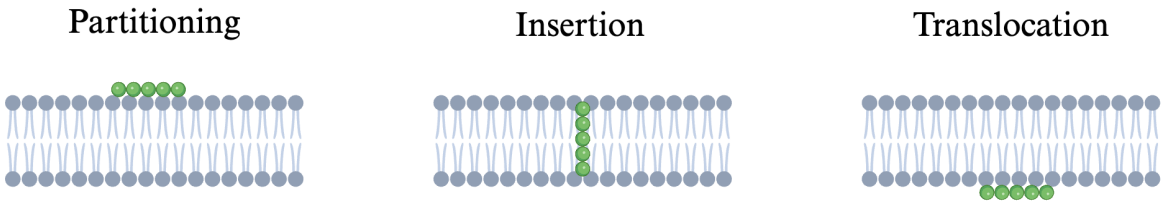

Figure 54. *Graphic representation of the peptide orientation through the lipid bilayer translocation process.*

A third variable that affects membrane disruption is the secondary structure of the peptide. This aspect has been studied in Chapter II using CompEL simulations with CPPs (Arg9, MAP, TP10, TP2) and nona-leucine (Leu9) as a negative control lacking translocation capacity (Figures 22, and 28), and in Chapter III through CompEL studies of MAP in different membrane compositions (Figures 34, 35, and 37). Previous work has shown that peptides capable of adopting an α-helical structure can transport transcellularly more efficiently[285,342]. However, peptide structure is not fixed, it seems to be affected by peptide composition and to depend on the interactions with the membrane[229].

In our CompEL study, we have seen how Arg9, which does not have hydrophobic residues, remains unstructured since it only favours interaction with polar parts and typically adopts coil or turn structures to engage with lipid polar heads. In contrast, Leu9 only seeks interaction with hydrophobic parts. Upon insertion into the pore, Leu9 orients as an α-helix, positioning hydrophobic sidechains outward while protecting backbone polar atoms inward, where they can interact with the water molecules in the pore. TP10 is the only peptide that possesses an α-helical structure in water simulations, which it retains during CompEL simulations. Further, TP10 gained additional helical structure in the simulations with eight peptides, showing a similar behaviour to

Leu9, with gain of helical structure upon membrane interaction and insertion. Likewise, TP2 shows α-helix structure in CompEL simulations with eight peptides, consistent with gain of helical structure after membrane interaction and insertion. In fact, the change of secondary structure upon insertion has been previously reported[336].

In parallel, MAP is the only peptide that has been studied using CompEL and different membrane compositions, where it has displayed structural variability. In Chapter II, some MAP peptides remained unstructured while others oriented in β-sheet structure, whereas in Chapter III, MAP exhibited α-helical in combination with β-sheet structure. Therefore, these changes in secondary structure highlight that peptide structure is not only peptide-dependent but is also strongly influenced by membrane composition[355].

4.4. Membrane analysis: composition, order, flip-flops

Peptide–membrane interactions do not only depend on the peptide but are also affected by the membrane characteristics. One of the main factors that influences membrane disruption is membrane composition. Hence, we have studied different membrane models. In aSMD + cMD, we focused on model membranes with model lipids: DOPC, DPPS, DOPS, alongside with CHOL. This way, Arg9, MAP, TP2 have been simulated in symmetric DPPC, DPPC:DOPC:CHOL, and DPPC:DOPC:DPPS:DOPS:CHOL (Chapter I), and DynA WT and its clinical variants (L5S, R6W, R9C) have been simulated in symmetric DOPC, DPPC:DOPC:CHOL, and DPPC:DOPC:DOPS:CHOL (Chapter IV). All lipid species in the membranes at a 1 to 1 ratio.

In CompEL we used more physiologically relevant lipids species[276]: POPC, POPE, POPG, POPS, together with CHOL. Here, Arg9, MAP, TP2, TP10, and Leu9 have been simulated in POPC (Chapter II), and only MAP in symmetric POPC:POPG (7:3 ratio) and POPC:POPG:CHOL (6:3:1), and asymmetric POPC:POPS (only POPC in the upper leaflet, and 7:3 ratio in the lower leaflet) membranes (Chapter III).

Importantly, in Chapter I, DPPC was selected to allow direct comparison with a previous study[142]. In Chapter IV, we maintained the same membrane composition to enable comparison with our previous study, but we focused on DOPC to study a different lipid tail composition. For Chapter II and Chapter III, we opted for more physiologically relevant lipid species, namely POPC, to better reflect native membrane environments.

First, the simple model membrane used, that is, DPPC in Chapter I, DOPC in Chapter IV with aSMD + cMD technique, and POPC in Chapter II using CompEL technique, allowed for the insertion of MAP and TP2 in DPPC, DynA L5S in DOPC, and MAP, TP10, TP2 and Leu9 in POPC. In addition, the translocation of Arg9 in DPPC and Arg9, MAP, TP10, and TP2 in POPC were also observed. Second, the CHOL-containing bilayer, DPPC:DOPC:CHOL in Chapter I and Chapter IV, and POPC:POPG:CHOL in Chapter III, did not allow for translocation events. Here, the insertion of Arg9, DynA WT, and DynA L5S in DPPC:DOPC:CHOL, and MAP in POPC:POPG were observed. Third, bilayers containing negatively charged lipids, DPPC:DOPC:DPPS:DOPS:CHOL in Chapter I, DPPC:DOPC:DOPS:CHOL in Chapter IV, and POPC:POPG and POPC:POPG:CHOL in Chapter III, allowed for the insertion of MAP, TP2 in

DPPC:DOPC:DPPS:DOPS:CHOL, DynA L5S and R9C in DPPC:DOPC:DOPS:CHOL, and MAP in POPC:POPG and POPC:POPG:CHOL. Fourth, asymmetric bilayers, only used in Chapter III, did show the translocation of MAP in POPC:POPS.

Hence, no significant differences were observed between the simple membrane models, as DPPC, DOPC and POPC bilayers allowed for insertion and translocation processes. However, in all cases, the addition of CHOL decreased the number of translocation/insertion events, as was observed in previous studies[102,338,356]. Likewise, the addition of negatively charged lipids (in the upper and lower leaflets) also decreased the number of membrane disruption events, especially the number of translocations, suggesting that peptides are more attracted to the negative residues in the upper leaflet and are less prone to further membrane disruption[152,222]. Moreover, even though the addition of CHOL and different lipid tails did not significantly increase PMF, the presence of negative lipid species in the upper leaflet did increase the required energy for bilayer translocation. In contrast, when negative lipids are added only to the lower leaflet (Figure 37), the number of translocation events are increased, indicating that peptides are more attracted to the lower leaflet and can, thus, complete the translocation procedure. These results confirm that the translocation of CPPs depend on lipid composition[249].

Another interesting phenomenon to study during peptide–membrane interactions are the changes in membrane thickness and S_{CD}. POPC:POPG, POPC:POPG:CHOL, POPC:POPS, DPPC, and DOPC membranes show similar thickness values (approximately 37-38 Å), whereas the addition of CHOL and a different lipid in DPPC:DOPC:CHOL increases membrane thickness (~42 Å), suggesting that the addition of a different lipid tail does not allow tight packing and induces increased membrane thickness. The addition of negatively charged lipid species in DPPC:DOPC:DOPS:CHOL and DPPC:DOPC:DPPS:DOPS:CHOL strengthens the interactions within the membrane, packing the bilayer and slightly decreasing membrane thickness (~40 Å). In any case, the presence or absence of peptide does not affect membrane thickness, as control simulations showcase similar values to those where the peptide is present.

On the other hand, S_{CD} analyses the orientation of the lipids relative to the bilayer normal, with values close to 0.5 indicating perfect alignment with the membrane, and values close to 0 denoting complete lipid disorder. In all cases, the bilayer seems to be correctly oriented, indicating that peptide insertion, pore formation or peptide translocation do not affect the general membrane

order. Nevertheless, the general order may be kept because even though S_{CD} is decreased for lipids around the peptide and pore area, it increases in those not in contact with that zone [301], counterbalancing the general membrane order.

After membrane disruption that can lead to pore formation, the membrane seeks to get stabilized again, in most cases, by closing the pore and returning to a position similar to the equilibrated starting position. Still, in some cases, lipids from the upper leaflet that have been dragged due to the peptide interaction can be stabilized in the lower leaflet, thus undergoing a lipid flip-flop procedure. In fact, Lai & Kaznessis concluded that lipid flip-flops occur when there is pore formation[341], and other studies showed that they occur simultaneously to peptide insertion and/or translocation[233,247,306,307]. As can be seen in Figure 25, lipid flip-flops occur from the upper to lower leaflet, confirming that flip-flops always occur from the peptide-enriched to the peptide-free leaflets[301].

4.5. Method comparison

In this thesis, two computational techniques have been presented (Figure 57): aSMD + cMD (Chapter I and Chapter IV) and CompEL (Chapter II and Chapter III). These methods are intended to provide a wide range of possibilities in the computational study of peptide–membrane interactions (Table 21), while being able to improve the characteristics of the already available techniques (Table 1).

In this regard, aSMD + cMD allows for PMF calculation and exploration of the peptide–membrane disruption after the peptide has been forced to cross the bilayer. Thus, this method allows to observe peptide translocation and provides atomic resolution. However, it has high computational requirements, as it comprises 8 steps, with 5 ns per step and needs 25 replicas, for the aSMD part, and 100 ns cMD with 3 replicas in the cMD part, accounting for 1300 ns per simulation. Besides, this method is not entry-level, as the reaction coordinate needs to be provided and the technique has a steep learning curve.

It is known that aSMD technique tends to yield higher PMF estimates compared to methods such as US, particularly due to the strong non-equilibrium nature of the pulling process and the limited sampling of rare low-work trajectories required for accurate application of Jarzynski's relation. As discussed in Chapter IV, section 3.4.3.1., part of this discrepancy also depends on the force field employed and on whether the PMF corresponds to crossing the entire bilayer thickness. In our case, the calculated barrier represents the full translocation process across the membrane, which partly explains the magnitude of the value obtained. Nevertheless, acknowledging the limitations of aSMD in providing fully converged free energy profiles for such complex systems, we subsequently turned to an alternative approach, such as CompEL simulations, in order to study peptide–membrane interactions and translocation under more physiologically realistic conditions.

Table 21. *Characteristics of aSMD + cMD and CompEL techniques.*

Technique	Resolution	PMF calculation	Peptide translocation	Entry-level	Computational requirements
aSMD + cMD	Atomic	Yes	Yes	No	Intensive
CompEL	Atomic	No	Yes	Yes	Moderate

On the other hand, CompEL has also atomic resolution, allows to observe peptide translocation, and even though the membrane disruption is induced, the peptide is not forced to cross the bilayer, allowing for peptide discrimination. Besides, in biological systems the transient pore is believed to be caused by an imbalance or asymmetry (such as mass, tension, or transmembrane potential)[31,321]. In this line, previous studies have suggested that a transmembrane potential is necessary for CPP translocation in live cell experiments and computational studies[308,357–362], even though others concluded that it is not strictly necessary, but it does favour translocation[337]. In fact, a transmembrane potential seems to trigger CPP translocation in live cells[361,362] by forming transient pores[231,234,308,357–359], as demonstrated in experimental and computational studies. Hence, CompEL allows to observe such disruption, which leads to CompEL attaining timescales of the same order as biological processes[259]. Moreover, CompEL is an entry-level technique, as the starting system can be rapidly prepared and no reaction coordinate needs to be chosen, and does also allow for simulation of several peptides, which permits the study of more realistic systems and to describe peptide cooperation. Besides, in more complex membrane systems containing POPC, POPG/POPS and CHOL, system stabilization occurs within 250 ns, so if three replicas are run, only 750 ns per system are required, implying that the computational requirements are not intensive as in other cases. In addition, CompEL allows for easier parallelization, as replicas can independently run in separate machines. Nonetheless, CompEL does not compute PMF, and should be combined with other technique if PMF calculation is sought.

It is worth noting that the distinction between insertion or translocation can, to some extent, arise from the limited timescales accessible to atomistic MD simulations, and different outcomes might emerge if the simulations were extended further. However, TP2 simulations were indeed extended

up to 1 μs and did not reveal any additional translocation events, suggesting that the system had reached a stable state. This interpretation is further supported by the RMSD analysis (Figure 27), which indicates that structural stabilization was achieved. Nevertheless, enhanced sampling methods such as US or metadynamics could be employed in future work to more precisely quantify the energetic barriers and refine the separation between bound and translocated states. Still, the current simulations already capture mechanistically distinct behaviours corresponding to stable pore binding versus crossing.

In summary, both techniques allow for possibilities that are not currently present in the peptide–mediated membrane disruption study. Whereas aSMD + cMD calculates the PMF and allows for peptide–membrane interactions, it is computationally intensive. In contrast, CompEL does not calculate PMF, but it requires less computational resources, can also observe translocation, and different peptide-to-lipid ratios can be used.

4.6. Biological implications at the cellular size and time scale

While MD simulations provide atomistic insights into the interactions between CPPs and lipid membranes, the simulations are limited in both spatial and temporal resolution. Therefore, it is important to consider how computational findings may translate to biological phenomena occurring at the cellular level. Here, several important considerations must be taken into account.

One key issue is the simplification inherent in the simulation models. MD studies employ model lipid bilayers that do not capture the full heterogeneity, asymmetry, and dynamic organization of real cellular membranes, with several different lipid species and diverse protein constituents[2–4]. At the scale of a single cell, CPP-mediated translocation involves the coordinated interplay of multiple processes, including peptide adsorption to the plasma membrane, transient disruption or reorganization of the lipid bilayer, and eventual uptake into the cytoplasm. In addition, the timescale of MD simulations (typically nanoseconds to microseconds) is orders of magnitude shorter than the processes observed in living systems and can generally capture the early stages of peptide–membrane interaction, such as partitioning, insertion or initial pore formation. However, events in living cells, like endocytosis or membrane repair, are embedded within much longer processes in the order of seconds to minutes[261,262].

Time and size scaling also highlight the importance of cooperative effects. In a cellular context, multiple CPP molecules often act in concert, forming transient aggregates that can destabilize the cell or stabilizing pores large enough to accommodate cargo[347,348]. Such collective phenomena are difficult to capture within the limits of standard MD simulations, yet they are central to understanding the efficiency and safety of CPP-mediated delivery. Another intrinsic limitation of MD approaches lies in the force fields employed. These are built on parameters derived from quantum mechanical calculations and experimental data. As a result, force fields provide generalized descriptions in which different atoms may share approximated parameter values, closely resembling, though never fully reproducing the full complexity of peptide-lipid and peptide-cargo interactions[363–365].

In summary, MD simulations provide a high-resolution picture of CPP–membrane interactions, however careful interpretation is required when extrapolating these findings to the complex and dynamic cellular environment. Considering the cellular size and time scale reveals a more complex

scenario, where atomistic mechanisms integrate with cooperative peptide action, membrane heterogeneity, and cellular processes operating at much longer timescales. This multi-level perspective, further combined with experimental validation, is crucial for translating computational findings into meaningful predictions about CPP function in biological systems.

4.7. Future perspectives and developments

This thesis presents new possibilities in the computational study of peptide–membrane interactions and demonstrates how MD simulations can yield valuable insights into the behaviour of CPPs. Computational biology is a rapidly developing field, and forthcoming advances, such as force fields specifically optimized for peptides and enhanced sampling trajectories tailored to their dynamics, will further expand its potential. Importantly, these innovations will complement the approaches explored in this work, enabling even more detailed and precise studies that can be seamlessly integrated with experimental validation. Together, these advances will support the design of novel peptides with improved uptake efficiency, specificity, and safety, ultimately strengthening their therapeutic applicability.

A natural next step would be to extend this work to a broader set of CPPs, particularly using CompEL with complex and asymmetric membranes, and to apply the same techniques to the computational study of AMPs. This would enable a more detailed comparison between CPPs and AMPs at the atomic level. The comparative analysis of these peptide families could further reveal both common principles and unique aspects of selectivity and activity. Expanding computational studies to include diverse peptides could broaden our understanding of sequence-function relationships and even shed light on how subtle sequence changes can shift a peptide's role. Additionally, future studies could also focus on the use of different peptide mixtures, potentially unveiling improved kinetics when diverse peptides are combined. Furthermore, simulations of CPPs coupled with cargo could be conducted to examine whether the cargo influences the translocation process.

Regarding DynA and its clinical variants, our research has so far been limited to aSMD + cMD technique. A further study and more profound peptide characterization could benefit from extending these studies to include CompEL simulations with more biologically relevant membrane compositions, combined with systematic comparison to experimental assays. Such an approach would allow a more thorough characterization of these peptides and provide deeper insight into their membrane–disrupting potential.

One major perspective is the integration of artificial intelligence (AI) into CPP research. While MD can capture atomic-level details of peptide–membrane interactions, AI-driven models can

allow the identification of patterns across much larger datasets. For example, screening vast peptide libraries to potentially unravel new CPPs, identifying novel sequences likely to show good penetration, and predict the peptide ability to cross biological membranes. Moreover, when combined with MD simulations, AI can help prioritize candidates for experimental testing or which mutations might enhance stability, accelerating the discovery of next-generation CPPs. Likewise, deep learning techniques could provide mechanistic insights into the key structural features that govern translocation efficiency. Furthermore, MD simulation data can be harnessed to train AI models, bridging atomistic detail with large-scale predictive insights enhancing their ability to capture complex biomolecular behaviours.

There is also considerable interest in the mutagenesis studies to improve current CPPs. Given the difference in arginine and lysine interactions, investigating the impact on some CPPs, such as MAP, of the lysine-to-arginine mutation could provide key insights into the role of guanidinium groups in peptide–membrane interactions and lead to better CPPs. Arginine-rich motifs are known to enhance electrostatic interactions and hydrogen bonding with lipid headgroups, and such mutational studies could help determine how these mutations allow for improved penetration without compromising peptide stability.

In addition, cyclic peptides are emerging as a particularly promising class of CPPs. Cyclization has been shown to enhance proteolytic stability, reduce conformational flexibility, and improve binding affinity to membranes, making them attractive candidates for therapeutic applications. Future studies could also tackle the modelling of cyclic CPPs to provide a more realistic picture of their potential advantages, as well as designing cyclic variants of known linear CPPs.

In conclusion, future progress in CPP research will possibly benefit from the convergence of advanced computational methods, AI-driven sequence design, systematic mutagenesis, and the exploration of novel peptide architectures such as cyclic peptides. These approaches may eventually lead to the development of highly efficient, stable, selective, and safe CPPs that are suitable for therapeutic delivery and broader biomedical applications.

Conclusions

5. CONCLUSIONS

The research conducted in this thesis can be summarized in the following topics and conclusions:

Techniques presented

- We have introduced two new techniques for the study of CPP–membrane interactions, and in general, peptide–membrane interactions. In aSMD + cMD, first aSMD is run to calculate PMF and force the peptide to cross the bilayer. Since aSMD ends in a non-equilibrium state, the cMD part is conducted to equilibrate and stabilize the system. In CompEL, a transmembrane potential is used to induce membrane disruption, which can be used by the peptide to get inserted and translocate.
- aSMD + cMD enables PMF calculation and subsequent unbiased peptide–membrane interactions but is limited to one peptide, is computationally intensive and reaction coordinates need to be defined. CompEL does not calculate PMF, but can be used to study unbiased translocation, to employ different peptide-to-lipid ratios, is an entry-level technique, and has lower computational requirements.

Peptide analysis

- Positive residues in the peptide sequence are key for the interaction with the negative charges in the lipid polar heads, primarily in peptide partitioning and translocation. Contrastingly, hydrophobic residues are important for the peptide insertion in the bilayer, as they are able to drive interaction with the lipid acyl chains in the hydrophobic core.
- Peptide translocation process starts with peptide partitioning to the upper leaflet, especially interacting with polar heads. Partitioning is followed by peptide insertion in the hydrophobic core, which in some cases includes pore formation, and finalizing with peptide reaching the polar heads in lower leaflet and breaking interactions with those in the upper leaflet.
- CPPs can induce membrane disruption to a lipid bilayer, but if they are able to translocate the bilayer, they can probably close the pore and membrane disruption, thus not affecting the viability of the bilayer. In contrast, AMPs do not translocate the membrane, instead they stabilize the pore and lead to larger membrane disruption and leakage.

- Arg9 is the only peptide that has shown translocation capacity in aSMD + cMD, whereas all CPPs have translocated with CompEL technique. Nonetheless, when more complex symmetric membranes are used, no peptide has been able to translocate, indicating the importance of using more realistic, asymmetric membranes, as has been done for MAP in CompEL POPC:POPS (Chapter III), where MAP has shown translocation capacity.
- DynA clinical variants show distinct behaviours. DynA WT is only able to disrupt the bilayer in DPPC:DOPC:CHOL, whereas DynA R9C only in DPPC:DOPC:DOPS:CHOL, showcasing DynA L5S, which has demonstrated disrupting behaviour in all membranes, as the most membrane–disrupting variant, potentially a CPP-like peptide. However, these results are not in line with experimental studies, and further investigation, such as DynA CompEL in complex membranes in combination with experimental studies, should be pursued.
- Peptide concentration and P:L ratio affect the membrane disruption capacity. A higher number of molecules does not significantly affect the cost of translocation and allows for higher membrane disruption and higher number of insertion and/or translocation events. Moreover, higher P:L ratios are closer to experimental and physiological ratios. Thus, new computational techniques should focus on simulations with higher number of peptides, as CompEL.
- Peptide orientation changes throughout the peptide translocation process. In the partitioning step, the peptide is parallel to the bilayer but gets stretched into a perpendicular orientation as it gets inserted in the bilayer. Finally, the peptide reorients and is parallel to the bilayer when it achieves translocation.
- Peptide secondary structure depends on peptide and membrane composition. Nonetheless, in general, peptides gain secondary structure upon membrane interaction and insertion.

Membrane analysis

- Higher membrane complexity is usually associated with reduced peptide translocation, especially if negative phospholipids are present in the outer leaflet. In aSMD + cMD technique, this can be observed in PMF calculation, whereas in CompEL this is seen in less translocation/insertion events.

- Membrane order is not generally modified due to the peptide insertion, pore formation or translocation, similar to membrane thickness. However, membrane thickness does change when other lipid species are added, such as CHOL or different tails, which can increase the thickness, or negatively charged lipids, that tightly pack the membrane and reduce thickness.
- Lipid flip-flops occur if there is pore formation and while the peptides are getting inserted or translocating. Flip-flops always occur from the peptide-enriched to the peptide-free leaflets.

Biological implications

- The limited spatial and temporal resolution of MD simulations restricts their direct applicability to living systems, as simplified bilayers models and nano-to-microsecond timescales cannot reproduce the heterogeneity, cooperative phenomena, and longer processes characteristics of cellular membranes.
- CPP translocation is an inherently multi-scale and cooperative process, involving peptide aggregation, membrane reorganization, and uptake mechanisms that extend well beyond the capabilities of standard MD approaches.

Future perspectives

- Future progress in CPP research will probably rely on the integration of advanced computational methods with experimental validation and consideration of cellular complexity, enabling deeper characterization of peptide-membrane interactions and more accurate translation of findings to biological contexts.
- The combination of molecular dynamics simulations with AI-driven sequence design and mutational studies offers a powerful strategy for accelerating CPP discovery, revealing structure-function relationships, identifying promising peptide variants, and improving stability, selectivity, and uptake efficiency.
- Exploring novel peptide architectures, such as cyclic peptides and diverse peptide mixtures, represents a promising direction for therapeutic development, as these approaches may enhance proteolytic stability, fine-tune membrane interactions, and broaden the biomedical applicability of CPPs.

Bibliography

6. BIBLIOGRAPHY

(1) Cooper, G. M. *The Cell: A Molecular Approach*, 2nd ed.; Sinauer Associates, 2000. https://doi.org/http://lib.ugent.be/catalog/ebk01:3450000000002155.

(2) Singer, S. J.; Nicolson, G. L. The Fluid Mosaic Model of the Structure of Cell Membranes. *Science (1979)* **1972**, *175* (4023), 720–731. https://doi.org/10.1126/SCIENCE.175.4023.720.

(3) Nicolson, G. L. Update of the 1972 Singer-Nicolson Fluid-Mosaic Model of Membrane Structure. *Discoveries* **2013**, *1* (1), e3. https://doi.org/10.15190/D.2013.3.

(4) Goñi, F. M. The Basic Structure and Dynamics of Cell Membranes: An Update of the Singer–Nicolson Model. *Biochimica et Biophysica Acta (BBA) - Biomembranes* **2014**, *1838* (6), 1467–1476. https://doi.org/10.1016/J.BBAMEM.2014.01.006.

(5) Jacobson, K.; Liu, P.; Lagerholm, B. C. The Lateral Organization and Mobility of Plasma Membrane Components. *Cell* **2019**, *177* (4), 806–819. https://doi.org/10.1016/J.CELL.2019.04.018.

(6) Sezgin, E.; Levental, I.; Mayor, S.; Eggeling, C. The Mystery of Membrane Organization: Composition, Regulation and Roles of Lipid Rafts. *Nature Reviews Molecular Cell Biology 2017 18:6* **2017**, *18* (6), 361–374. https://doi.org/10.1038/nrm.2017.16.

(7) Kusumi, A.; Fujiwara, T. K.; Chadda, R.; Xie, M.; Tsunoyama, T. A.; Kalay, Z.; Kasai, R. S.; Suzuki, K. G. N. Dynamic Organizing Principles of the Plasma Membrane That Regulate Signal Transduction: Commemorating the Fortieth Anniversary of Singer and Nicolson's Fluid-Mosaic Model. *Annu Rev Cell Dev Biol* **2012**, *28* (Volume 28, 2012), 215–250. https://doi.org/10.1146/ANNUREV-CELLBIO-100809-151736/CITE/REFWORKS.

(8) Ingólfsson, H. I.; Melo, M. N.; Van Eerden, F. J.; Arnarez, C.; Lopez, C. A.; Wassenaar, T. A.; Periole, X.; De Vries, A. H.; Tieleman, D. P.; Marrink, S. J. Lipid Organization of the Plasma Membrane. *J Am Chem Soc* **2014**, *136* (41), 14554–14559. https://doi.org/10.1021/JA507832E.

(9) Devaux, P. F. Static and Dynamic Lipid Asymmetry in Cell Membranes. *Biochemistry* **1991**, *30* (5), 1163–1173. https://doi.org/10.1021/BI00219A001.

(10) Van Meer, G.; Voelker, D. R.; Feigenson, G. W. Membrane Lipids: Where They Are and How They Behave. *Nat Rev Mol Cell Biol* **2008**, *9* (2), 112–124. https://doi.org/10.1038/NRM2330;KWRD.

(11) Lorent, J. H.; Levental, K. R.; Ganesan, L.; Rivera-Longsworth, G.; Sezgin, E.; Doktorova, M.; Lyman, E.; Levental, I. Plasma Membranes Are Asymmetric in Lipid Unsaturation, Packing and Protein Shape. *Nat Chem Biol* **2020**, *16* (6), 644–652. https://doi.org/10.1038/S41589-020-0529-6;SUBJMETA.

(12) Pei, D. How Do Biomolecules Cross the Cell Membrane? *Acc Chem Res* **2022**, *55* (3), 309. https://doi.org/10.1021/ACS.ACCOUNTS.1C00560.

(13) Cheng, X.; Smith, J. C. Biological Membrane Organization and Cellular Signaling. *Chem Rev* **2019**, *119* (9), 5849–5880. https://doi.org/10.1021/ACS.CHEMREV.8B00439.

(14) Israelachvili, J. N. *Intermolecular and Surface Forces*, Third.; Academic Press, 2011. https://doi.org/https://doi.org/10.1016/C2009-0-21560-1.

(15) Marsh, D. Protein Modulation of Lipids, and Vice-Versa, in Membranes. *Biochimica et Biophysica Acta (BBA) - Biomembranes* **2008**, *1778* (7–8), 1545–1575. https://doi.org/10.1016/J.BBAMEM.2008.01.015.

(16) Lemmon, M. A. Membrane Recognition by Phospholipid-Binding Domains. *Nature Reviews Molecular Cell Biology 2008 9:2* **2008**, *9* (2), 99–111. https://doi.org/10.1038/nrm2328.

(17) White, S. H.; Wimley, W. C. Membrane Protein Folding and Stability: Physical Principles. *Annu Rev Biophys Biomol Struct* **1999**, *28*, 319–365. https://doi.org/10.1146/ANNUREV.BIOPHYS.28.1.319.

(18) Bowie, J. U. Membrane Protein Folding: How Important Are Hydrogen Bonds? *Curr Opin Struct Biol* **2011**, *21* (1), 42–49. https://doi.org/10.1016/J.SBI.2010.10.003.

(19) Boggs, J. M. Lipid Intermolecular Hydrogen Bonding: Influence on Structural Organization and Membrane Function. *Biochimica et Biophysica Acta (BBA) - Reviews on Biomembranes* **1987**, *906* (3), 353–404. https://doi.org/10.1016/0304-4157(87)90017-7.

(20) Van Oss, C. J.; Good, R. J.; Chaudhury, M. K. The Role of van Der Waals Forces and Hydrogen Bonds in "Hydrophobic Interactions" between Biopolymers and Low Energy Surfaces. *J Colloid Interface Sci* **1986**, *111* (2), 378–390. https://doi.org/10.1016/0021-9797(86)90041-X.

(21) Shankaran, H.; Resat, H.; Wiley, H. S. Cell Surface Receptors for Signal Transduction and Ligand Transport: A Design Principles Study. *PLoS Comput Biol* **2007**, *3* (6), e101. https://doi.org/10.1371/JOURNAL.PCBI.0030101.

(22) Lombardo, D.; Calandra, P.; Barreca, D.; Magazù, S.; Kiselev, M. A. Soft Interaction in Liposome Nanocarriers for Therapeutic Drug Delivery. *Nanomaterials 2016, Vol. 6, Page 125* **2016**, *6* (7), 125. https://doi.org/10.3390/NANO6070125.

(23) Düzgüneş, N.; Nir, S. Mechanisms and Kinetics of Liposome–Cell Interactions. *Adv Drug Deliv Rev* **1999**, *40* (1–2), 3–18. https://doi.org/10.1016/S0169-409X(99)00037-X.

(24) McNeil, P. L.; Steinhardt, R. A. PLasma Membrane Disruption: Repair, Prevention, Adaptation. *Annu Rev Cell Dev Biol* **2003**, *19* (Volume 19, 2003), 697–731. https://doi.org/10.1146/ANNUREV.CELLBIO.19.111301.140101.

(25) Avci, F. G.; Akbulut, B. S.; Ozkirimli, E. Membrane Active Peptides and Their Biophysical Characterization. *Biomolecules 2018, Vol. 8, Page 77* **2018**, *8* (3), 77. https://doi.org/10.3390/BIOM8030077.

(26) Aluko, R. Bioactive Peptides. In *Functional Foods and Nutraceuticals*; Aluko, R. E., Ed.; Springer New York: New York, NY, 2012; pp 37–61. https://doi.org/10.1007/978-1-4614-3480-1_3.

(27) Kadam, S. U.; Tiwari, B. K.; Álvarez, C.; O'Donnell, C. P. Ultrasound Applications for the Extraction, Identification and Delivery of Food Proteins and Bioactive Peptides. *Trends Food Sci Technol* **2015**, *46* (1), 60–67. https://doi.org/10.1016/J.TIFS.2015.07.012.

(28) Sánchez, A.; Vázquez, A. Bioactive Peptides: A Review. *Food Quality and Safety* **2017**, *1* (1), 29–46. https://doi.org/10.1093/FQSAFE/FYX006.

(29) Izadpanah, A.; Gallo, R. L. Antimicrobial Peptides. *J Am Acad Dermatol* **2005**, *52* (3), 381–390. https://doi.org/10.1016/J.JAAD.2004.08.026.

(30) Lindgren, M.; Hällbrink, M.; Prochiantz, A.; Langel, Ü. Cell-Penetrating Peptides. *Trends Pharmacol Sci* **2000**, *21* (3), 99–103. https://doi.org/10.1016/s0165-6147(00)01447-4.

(31) Rice, A. I.; Zourou ID, A. C.; Cotten, M. L.; Pastor, R. W.; Levitt, M. A Unified Model of Transient Poration Induced by Antimicrobial Peptides. *Proceedings of the National Academy of Sciences* **2025**, *122* (35), e2510294122. https://doi.org/10.1073/PNAS.2510294122.

(32) Zhang, Y.; Wang, C.; Zhang, W.; Li, X. Bioactive Peptides for Anticancer Therapies. *Biomaterials Translational* **2023**, *4* (1), 5. https://doi.org/10.12336/BIOMATERTRANSL.2023.01.003.

(33) Xie, M.; Liu, D.; Yang, Y. Anti-Cancer Peptides: Classification, Mechanism of Action, Reconstruction and Modification. *Open Biol* **2020**, *10* (7). https://doi.org/10.1098/RSOB.200004/.

(34) Kurrikoff, K.; Aphkhazava, D.; Langel, Ü. The Future of Peptides in Cancer Treatment. *Curr Opin Pharmacol* **2019**, *47*, 27–32. https://doi.org/10.1016/J.COPH.2019.01.008.

(35) Gao, B.; Zhao, D.; Li, L.; Cheng, Z.; Guo, Y. Antiviral Peptides with in Vivo Activity: Development and Modes of Action. *Chempluschem* **2021**, *86* (12), 1547–1558. https://doi.org/10.1002/CPLU.202100351.

(36) Qureshi, A. A Review on Current Status of Antiviral Peptides. *Discover Viruses 2024 2:1* **2025**, *2* (1), 1–13. https://doi.org/10.1007/S44370-024-00006-5.

(37) Vilas Boas, L. C. P.; Campos, M. L.; Berlanda, R. L. A.; de Carvalho Neves, N.; Franco, O. L. Antiviral Peptides as Promising Therapeutic Drugs. *Cellular and Molecular Life Sciences 2019 76:18* **2019**, *76* (18), 3525–3542. https://doi.org/10.1007/S00018-019-03138-W.

(38) Ciociola, T.; Giovati, L.; Conti, S.; Magliani, W.; Santinoli, C.; Polonelli, L. Natural and Synthetic Peptides with Antifungal Activity. *Future Med Chem* **2016**, *8* (12), 1413–1433. https://doi.org/10.4155/FMC-2016-0035.

(39) Li, T.; Li, L.; Du, F.; Sun, L.; Shi, J.; Long, M.; Chen, Z. Activity and Mechanism of Action of Antifungal Peptides from Microorganisms: A Review. *Molecules 2021, Vol. 26, Page 3438* **2021**, *26* (11), 3438. https://doi.org/10.3390/MOLECULES26113438.

(40) Bondaryk, M.; Staniszewska, M.; Zielińska, P.; Urbańczyk-Lipkowska, Z. Natural Antimicrobial Peptides as Inspiration for Design of a New Generation Antifungal Compounds. *Journal of Fungi 2017, Vol. 3, Page 46* **2017**, *3* (3), 46. https://doi.org/10.3390/JOF3030046.

(41) Li, Y.; Li, Y.; Mengist, H. M.; Shi, C.; Zhang, C.; Wang, B.; Li, T.; Huang, Y.; Xu, Y.; Jin, T. Structural Basis of the Pore-Forming Toxin/Membrane Interaction. *Toxins 2021, Vol. 13, Page 128* **2021**, *13* (2), 128. https://doi.org/10.3390/TOXINS13020128.

(42) Lata, K.; Singh, M.; Chatterjee, S.; Chattopadhyay, K. Membrane Dynamics and Remodelling in Response to the Action of the Membrane-Damaging Pore-Forming Toxins. *The Journal of Membrane Biology 2022 255:2* **2022**, *255* (2), 161–173. https://doi.org/10.1007/S00232-022-00227-Z.

(43) Popoff, M. R. Overview of Bacterial Protein Toxins from Pathogenic Bacteria: Mode of Action and Insights into Evolution. *Toxins 2024, Vol. 16, Page 182* **2024**, *16* (4), 182. https://doi.org/10.3390/TOXINS16040182.

(44) Terwilliger, T. C.; Weissman, L.; Eisenberg, D. The Structure of Melittin in the Form I Crystals and Its Implication for Melittin's Lytic and Surface Activities. *Biophys J* **1982**, *37* (1), 353–361. https://doi.org/10.1016/S0006-3495(82)84683-3.

(45) Nagaraj, R.; Balaram, P. Alamethicin, a Transmembrane Channel. *Acc Chem Res* **1981**, *14*, 356–362.

(46) Zasloff, M.; Martin, B.; Chen, H. C. Antimicrobial Activity of Synthetic Magainin Peptides and Several Analogues. *Proc Natl Acad Sci U S A* **1988**, *85* (3), 910–913. https://doi.org/10.1073/PNAS.85.3.910;ISSUE:ISSUE:DOI.

(47) Green, M.; Loewenstein, P. M. Autonomous Functional Domains of Chemically Synthesized Human Lmmunodeficiency Virus Tat Trans-Activator Protein. *Cell* **1988**, *55* (6), 1179–1188. https://doi.org/10.1016/0092-8674(88)90262-0.

(48) Frankel, A. D.; Pabo, C. O. Cellular Uptake of the Tat Protein from Human Immunodeficiency Virus. *Cell* **1988**, *55* (6), 1189–1193. https://doi.org/10.1016/0092-8674(88)90263-2.

(49) Vivès, E.; Brodin, P.; Lebleu, B. A Truncated HIV-1 Tat Protein Basic Domain Rapidly Translocates through the Plasma Membrane and Accumulates in the Cell Nucleus. *Journal of Biological Chemistry* **1997**, *272* (25), 16010–16017. https://doi.org/10.1074/jbc.272.25.16010.

(50) Joliot, A. H.; Triller, A.; Volovitch, M.; Pernelle, C.; Prochiantz, A. Alpha-2,8-Polysialic Acid Is the Neuronal Surface Receptor of Antennapedia Homeobox Peptide. *New Biol* **1991**, *3* (11), 1121–1134.

(51) Derossit, D.; Joliott, M. H.; Chassaingl, G.; Prochiantztn, M. The Third Helix of the Antennapedia Homeodomain Translocates through Biological Membranes. *J Biol Chem* **1994**, *269* (14), 10444–10450. https://doi.org/10.1016/S0021-9258(17)34080-2.

(52) Bajiya, N.; Najrin, S.; Kumar, P.; Choudhury, S.; Tomer, R.; Raghava, G. P. S. CPPsite3: An Updated Large Repository of Experimentally Validated Cell-Penetrating Peptides. *Drug Discov Today* **2025**, 104421. https://doi.org/10.1016/J.DRUDIS.2025.104421.

(53) Futaki, S.; Suzuki, T.; Ohashi, W.; Yagami, T.; Tanaka, S.; Ueda, K.; Sugiura, Y. Arginine-Rich Peptides: An Abundant Source of Membrane-Permeable Peptides Having Potential as Carriers for Intracellular Protein Delivery. *Journal of Biological Chemistry* **2001**, *276* (8), 5836–5840. https://doi.org/10.1074/jbc.M007540200.

(54) Milletti, F. Cell-Penetrating Peptides: Classes, Origin, and Current Landscape. *Drug Discov Today* **2012**, *17* (15–16), 850–860. https://doi.org/10.1016/j.drudis.2012.03.002.

(55) Prochiantz, A. Getting Hydrophilic Compounds into Cells: Lessons from Homeopeptides. Commentary. *Curr Opin Neurobiol* **1996**, *6* (5), 629–634. https://doi.org/10.1016/S0959-4388(96)80095-X.

(56) Silva, S.; Kurrikoff, K.; Langel, Ü.; Almeida, A. J.; Vale, N. A Second Life for MAP, a Model Amphipathic Peptide. *Int J Mol Sci* **2022**, *23* (15), 8322. https://doi.org/10.3390/ijms23158322.

(57) Steiner, V.; Schzr, M.; B&men, K. O.; Mutter, M. *Retention Behaviour of a Template-Assembled Synthetic Protein and Its Amphiphilic Building Blocks on Reversed-Phase Columns*; 1991; Vol. 586, pp 43–50. https://doi.org/10.1016/0021-9673(91)80023-A.

(58) Yandek, L. E.; Pokorny, A.; Florén, A.; Knoelke, K.; Langel, Ü.; Almeida, P. F. F. Mechanism of the Cell-Penetrating Peptide Transportan 10 Permeation of Lipid Bilayers. *Biophys J* **2007**, *92* (7), 2434–2444. https://doi.org/10.1529/BIOPHYSJ.106.100198.

(59) Morris, M. C.; Depollier, J.; Mery, J.; Heitz, F.; Divita, G. A Peptide Carrier for the Delivery of Biologically Active Proteins into Mammalian Cells. *Nat Biotechnol* **2001**, *19* (12), 1173–1176. https://doi.org/10.1038/NBT1201-1173.

(60) Rádis-Baptista, G.; Campelo, I. S.; Morlighem, J. É. R. L.; Melo, L. M.; Freitas, V. J. F. Cell-Penetrating Peptides (CPPs): From Delivery of Nucleic Acids and Antigens to Transduction of Engineered Nucleases for Application in Transgenesis. *J Biotechnol* **2017**, *252*, 15–26. https://doi.org/10.1016/J.JBIOTEC.2017.05.002.

(61) Adzhubei, A. A.; Sternberg, M. J. E.; Makarov, A. A. Polyproline-II Helix in Proteins: Structure and Function. *J Mol Biol* **2013**, *425* (12), 2100–2132. https://doi.org/10.1016/J.JMB.2013.03.018.

(62) Hicks, J. M.; Hsu, V. L. The Extended Left-Handed Helix: A Simple Nucleic Acid-Binding Motif. *Proteins: Structure, Function and Genetics* **2004**, *55* (2), 330–338. https://doi.org/10.1002/PROT.10630.

(63) Mansiaux, Y.; Joseph, A. P.; Gelly, J. C.; de Brevern, A. G. Assignment of PolyProline II Conformation and Analysis of Sequence – Structure Relationship. *PLoS One* **2011**, *6* (3), e18401. https://doi.org/10.1371/JOURNAL.PONE.0018401.

(64) Cubellis, M. V.; Caillez, F.; Blundell, T. L.; Lovell, S. C. Properties of Polyproline II, a Secondary Structure Element Implicated in Protein-Protein Interactions. *Proteins:*

Structure, Function and Genetics **2005**, *58* (4), 880–892. https://doi.org/10.1002/PROT.20327.

(65) Lin, Y. Z.; Yao, S. Y.; Veach, R. A.; Torgerson, T. R.; Hawiger, J. Inhibition of Nuclear Translocation of Transcription Factor NF-Kappa B by a Synthetic Peptide Containing a Cell Membrane-Permeable Motif and Nuclear Localization Sequence. *J Biol Chem* **1995**, *270* (24), 14255–14258. https://doi.org/10.1074/jbc.270.24.14255.

(66) Marks, J. R.; Placone, J.; Hristova, K.; Wimley, W. C. Spontaneous Membrane-Translocating Peptides by Orthogonal High-Throughput Screening. *J Am Chem Soc* **2011**, *133* (23), 8995–9004. https://doi.org/10.1021/JA2017416.

(67) Hunt, J. F.; Rath, P.; Rothschild, K. J.; Engelman, D. M. Spontaneous, PH-Dependent Membrane Insertion of a Transbilayer α-Helix†. *Biochemistry* **1997**, *36* (49), 15177–15192. https://doi.org/10.1021/BI970147B.

(68) An, M.; Wijesinghe, D.; Andreev, O. A.; Reshetnyak, Y. K.; Engelman, D. M. PH-(Low)-Insertion-Peptide (PHLIP) Translocation of Membrane Impermeable Phalloidin Toxin Inhibits Cancer Cell Proliferation. *Proceedings of the National Academy of Sciences* **2010**, *107* (47), 20246–20250. https://doi.org/10.1073/PNAS.1014403107.

(69) Wolf, J.; Aisenbrey, C.; Harmouche, N.; Raya, J.; Bertani, P.; Voievoda, N.; Süss, R.; Bechinger, B. PH-Dependent Membrane Interactions of the Histidine-Rich Cell-Penetrating Peptide LAH4-L1. *Biophys J* **2017**, *113* (6), 1290–1300. https://doi.org/10.1016/j.bpj.2017.06.053.

(70) Lee, D. Y.; Noh, I.; Yoo, J.; Rejinold, N. S.; Kim, Y. C. PH-Controllable Cell-Penetrating Polypeptide That Exhibits Cancer Targeting. *Acta Biomater* **2017**, *57*, 187–196. https://doi.org/10.1016/J.ACTBIO.2017.05.040.

(71) Gori, A.; Lodigiani, G.; Colombarolli, S. G.; Bergamaschi, G.; Vitali, A. Cell Penetrating Peptides: Classification, Mechanisms, Methods of Study, and Applications. *ChemMedChem*. John Wiley and Sons Ltd September 1, 2023. https://doi.org/10.1002/cmdc.202300236.

(72) Qian, Z.; Martyna, A.; Hard, R. L.; Wang, J.; Appiah-Kubi, G.; Coss, C.; Phelps, M. A.; Rossman, J. S.; Pei, D. Discovery and Mechanism of Highly Efficient Cyclic Cell-Penetrating Peptides. *Biochemistry* **2016**, *55* (18), 2601. https://doi.org/10.1021/ACS.BIOCHEM.6B00226.

(73) Fang, D.; Wang, R.; Yu, X.; Tian, Y. Construction of Cyclic Cell-Penetrating Peptides for Enhanced Penetration of Biological Barriers. *J Vis Exp* **2022**, *2022* (187), e64293. https://doi.org/10.3791/64293.

(74) Dougherty, P. G.; Sahni, A.; Pei, D. Understanding Cell Penetration of Cyclic Peptides. *Chem Rev* **2019**, *119* (17), 10241–10287. https://doi.org/10.1021/ACS.CHEMREV.9B00008.

(75) Sajid, M. I.; Moazzam, M.; Stueber, R.; Park, S. E.; Cho, Y.; Malik, N. ul A.; Tiwari, R. K. Applications of Amphipathic and Cationic Cyclic Cell-Penetrating Peptides: Significant Therapeutic Delivery Tool. *Peptides (N.Y.)* **2021**, *141*. https://doi.org/10.1016/j.peptides.2021.170542.

(76) Qian, Z.; Liu, T.; Liu, Y. Y.; Briesewitz, R.; Barrios, A. M.; Jhiang, S. M.; Pei, D. Efficient Delivery of Cyclic Peptides into Mammalian Cells with Short Sequence Motifs. *ACS Chem Biol* **2012**, *8* (2), 423. https://doi.org/10.1021/CB3005275.

(77) Tian, Y.; Jiang, Y.; Li, J.; Wang, D.; Zhao, H.; Li, Z. Effect of Stapling Architecture on Physiochemical Properties and Cell Permeability of Stapled α-Helical Peptides: A Comparative Study. *ChemBioChem* **2017**, *18* (21), 2087–2093. https://doi.org/10.1002/CBIC.201700352.

(78) Breger, J. C.; Muttenthaler, M.; Delehanty, J. B.; Thompson, D. A.; Oh, E.; Susumu, K.; Deschamps, J. R.; Anderson, G. P.; Field, L. D.; Walper, S. A.; Dawson, P. E.; Medintz, I. L. Nanoparticle Cellular Uptake by Dendritic Wedge Peptides: Achieving Single Peptide Facilitated Delivery. *Nanoscale* **2017**, *9* (29), 10447–10464. https://doi.org/10.1039/C7NR03362A.

(79) Datta, N. A Review on the Cell-Penetrating Peptides. *Cell Therapy & Engineering Connect* **2025**, *1* (1), 1–10. https://doi.org/10.69709/CELLENGC.2025.145023.

(80) Ruseska, I.; Zimmer, A. Internalization Mechanisms of Cell-Penetrating Peptides. *Beilstein J. Nanotechnol* **2020**, *2020*, 101–123. https://doi.org/10.3762/bjnano.11.10.

(81) Alves, I. D.; Jiao, C. Y.; Aubry, S.; Aussedat, B.; Burlina, F.; Chassaing, G.; Sagan, S. Cell Biology Meets Biophysics to Unveil the Different Mechanisms of Penetratin Internalization in Cells. *Biochimica et Biophysica Acta (BBA) - Biomembranes* **2010**, *1798* (12), 2231–2239. https://doi.org/10.1016/J.BBAMEM.2010.02.009.

(82) Kawamoto, S.; Miyakawa, T.; Takasu, M.; Morikawa, R.; Oda, T.; Saito, H.; Futaki, S.; Nagao, H. Cell-Penetrating Peptide Induces Various Deformations of Lipid Bilayer Membrane: Inverted Micelle, Double Bilayer, and Transmembrane. In *International Journal of Quantum Chemistry*; 2012; Vol. 112, pp 178–183. https://doi.org/10.1002/qua.23177.

(83) Siegel, D. P. Inverted Micellar Intermediates and the Transitions between Lamellar, Cubic, and Inverted Hexagonal Lipid Phases. I. Mechanism of the L Alpha----HII Phase Transitions. *Biophys J* **1986**, *49* (6), 1155–1170. https://doi.org/10.1016/S0006-3495(86)83744-4.

(84) Kawamoto, S.; Takasu, M.; Miyakawa, T.; Morikawa, R.; Oda, T.; Futaki, S.; Nagao, H. Inverted Micelle Formation of Cell-Penetrating Peptide Studied by Coarse-Grained Simulation: Importance of Attractive Force between Cell-Penetrating Peptides and Lipid Head Group. *Journal of Chemical Physics* **2011**, *134* (9). https://doi.org/10.1063/1.3555531.

(85) Swiecicki, J. M.; Bartsch, A.; Tailhades, J.; Di Pisa, M.; Heller, B.; Chassaing, G.; Mansuy, C.; Burlina, F.; Lavielle, S. The Efficacies of Cell-Penetrating Peptides in Accumulating in Large Unilamellar Vesicles Depend on Their Ability to Form Inverted Micelles. *ChemBioChem* **2014**, *15* (6), 884–891. https://doi.org/10.1002/CBIC.201300742.

(86) Copolovici, D. M.; Langel, K.; Eriste, E.; Langel, Ü. Cell-Penetrating Peptides: Design, Synthesis, and Applications. *ACS Nano* **2014**, *8* (3), 1972–1994. https://doi.org/10.1021/nn4057269.

(87) Bechara, C.; Sagan, S. Cell-Penetrating Peptides: 20 Years Later, Where Do We Stand? *FEBS Lett* **2013**, *587* (12), 1693–1702. https://doi.org/10.1016/J.FEBSLET.2013.04.031.

(88) Islam, M. Z.; Sharmin, S.; Moniruzzaman, M.; Yamazaki, M. Elementary Processes for the Entry of Cell-Penetrating Peptides into Lipid Bilayer Vesicles and Bacterial Cells. *Applied Microbiology and Biotechnology*. Springer Verlag May 1, 2018, pp 3879–3892. https://doi.org/10.1007/s00253-018-8889-5.

(89) Mishra, A.; Lai, G. H.; Schmidt, N. W.; Sun, V. Z.; Rodriguez, A. R.; Tong, R.; Tang, L.; Cheng, J.; Deming, T. J.; Kamei, D. T.; Wong, G. C. L. Translocation of HIV TAT Peptide and Analogues Induced by Multiplexed Membrane and Cytoskeletal Interactions. *Proc Natl Acad Sci U S A* **2011**, *108* (41), 16883–16888. https://doi.org/10.1073/PNAS.1108795108.

(90) Mishra, A.; Gordon, V. D.; Yang, L.; Coridan, R.; L Wong, G. C.; Mishra, A.; Gordon, V. D.; Yang, L.; L Wong, G. C.; Gruner, S.; Cheng, J. J.; Garcia, A. HIV TAT Forms Pores in Membranes by Inducing Saddle-Splay Curvature: Potential Role of Bidentate Hydrogen Bonding. *Angewandte Chemie International Edition* **2008**, *47* (16), 2986–2989. https://doi.org/10.1002/ANIE.200704444.

(91) Islam, M. Z.; Ariyama, H.; Alam, J. M.; Yamazaki, M. Entry of Cell-Penetrating Peptide Transportan 10 into a Single Vesicle by Translocating across Lipid Membrane and Its Induced Pores. *Biochemistry* **2014**, *53* (2), 386–396. https://doi.org/10.1021/BI401406P.

(92) Pouny, Y.; Rapaport, D.; Mor, A.; Nicolas, P.; Shai, Y. Interaction of Antimicrobial Dermaseptin and Its Fluorescently Labeled Analogs with Phospholipid Membranes. *Biochemistry* **1992**, *31* (49), 12416–12423. https://doi.org/10.1021/bi00164a017.

(93) Conner, S. D.; Schmid, S. L. Regulated Portals of Entry into the Cell. *Nature* **2003**, *422* (6927), 37–44. https://doi.org/10.1038/NATURE01451.

(94) Xiang, S.; Tong, H.; Shi, Q.; Fernandes, J. C.; Jin, T.; Dai, K.; Zhang, X. Uptake Mechanisms of Non-Viral Gene Delivery. *Journal of Controlled Release* **2012**, *158* (3), 371–378. https://doi.org/10.1016/J.JCONREL.2011.09.093.

(95) Schmidt, N.; Mishra, A.; Lai, G. H.; Wong, G. C. L. Arginine-Rich Cell-Penetrating Peptides. *FEBS Lett* **2010**, *584* (9), 1806–1813. https://doi.org/10.1016/J.FEBSLET.2009.11.046.

(96) Fittipaldi, A.; Ferrari, A.; Zoppé, M.; Arcangeli, C.; Pellegrini, V.; Beltram, F.; Giacca, M. Cell Membrane Lipid Rafts Mediate Caveolar Endocytosis of HIV-1 Tat Fusion Proteins. *Journal of Biological Chemistry* **2003**, *278* (36), 34141–34149. https://doi.org/10.1074/jbc.M303045200.

(97) Kirkham, M.; Fujita, A.; Chadda, R.; Nixon, S. J.; Kurzchalia, T. V.; Sharma, D. K.; Pagano, R. E.; Hancock, J. F.; Mayor, S.; Parton, R. G. Ultrastructural Identification of Uncoated Caveolin-Independent Early Endocytic Vehicles. *Journal of Cell Biology* **2005**, *168* (3), 465–476. https://doi.org/10.1083/JCB.200407078.

(98) D'Souza-Schorey, C.; Chavrier, P. ARF Proteins: Roles in Membrane Traffic and Beyond. *Nature Reviews Molecular Cell Biology 2006 7:5* **2006**, *7* (5), 347–358. https://doi.org/10.1038/nrm1910.

(99) Glebov, O. O.; Bright, N. A.; Nichols, B. J. Flotillin-1 Defines a Clathrin-Independent Endocytic Pathway in Mammalian Cells. *Nat Cell Biol* **2006**, *8* (1), 46–54. https://doi.org/10.1038/NCB1342.

(100) Zakany, F.; Mándity, I. M.; Varga, Z.; Panyi, G.; Nagy, P.; Kovacs, T. Effect of the Lipid Landscape on the Efficacy of Cell-Penetrating Peptides. *Cells 2023, Vol. 12, Page 1700* **2023**, *12* (13), 1700. https://doi.org/10.3390/CELLS12131700.

(101) Palm-Apergi, C.; Lönn, P.; Dowdy, S. F. Do Cell-Penetrating Peptides Actually Penetrate Cellular Membranes? *Molecular Therapy* **2012**, *20* (4), 695–697. https://doi.org/10.1038/mt.2012.40.

(102) Pae, J.; Säälik, P.; Liivamägi, L.; Lubenets, D.; Arukuusk, P.; Langel, Ü.; Pooga, M. Translocation of Cell-Penetrating Peptides across the Plasma Membrane Is Controlled by Cholesterol and Microenvironment Created by Membranous Proteins. *Journal of Controlled Release* **2014**, *192*, 103–113. https://doi.org/10.1016/J.JCONREL.2014.07.002.

(103) Almeida, C.; Maniti, O.; Di Pisa, M.; Swiecicki, J. M.; Ayala-Sanmartin, J. Cholesterol Re-Organisation and Lipid de-Packing by Arginine-Rich Cell Penetrating Peptides: Role in Membrane Translocation. *PLoS One* **2019**, *14* (1), e0210985. https://doi.org/10.1371/JOURNAL.PONE.0210985.

(104) Takeuchi, T.; Futaki, S. Current Understanding of Direct Translocation of Arginine-Rich Cell-Penetrating Peptides and Its Internalization Mechanisms. *Chem Pharm Bull (Tokyo)* **2016**, *64* (10), 1431–1437. https://doi.org/10.1248/CPB.C16-00505.

(105) Futaki, S.; Nakase, I.; Tadokoro, A.; Takeuchi, T.; Jones, A. T. Arginine-Rich Peptides and Their Internalization Mechanisms. *Biochem Soc Trans* **2007**, *35* (4), 784–787. https://doi.org/10.1042/BST0350784.

(106) Åmand, H. L.; Rydberg, H. A.; Fornander, L. H.; Lincoln, P.; Nordén, B.; Esbjörner, E. K. Cell Surface Binding and Uptake of Arginine- and Lysine-Rich Penetratin Peptides in Absence and Presence of Proteoglycans. *Biochimica et Biophysica Acta (BBA) - Biomembranes* **2012**, *1818* (11), 2669–2678. https://doi.org/10.1016/J.BBAMEM.2012.06.006.

(107) Geng, J.; Xia, X.; Teng, L.; Wang, L.; Chen, L.; Guo, X.; Belingon, B.; Li, J.; Feng, X.; Li, X.; Shang, W.; Wan, Y.; Wang, H. Emerging Landscape of Cell-Penetrating Peptide-Mediated Nucleic Acid Delivery and Their Utility in Imaging, Gene-Editing, and RNA-Sequencing. *Journal of Controlled Release* **2022**, *341*, 166–183. https://doi.org/10.1016/j.jconrel.2021.11.032.

(108) Gagat, M.; Zielińska, W.; Grzanka, A. Cell-Penetrating Peptides and Their Utility in Genome Function Modifications (Review). *Int J Mol Med* **2017**, *40* (6), 1615. https://doi.org/10.3892/IJMM.2017.3172.

(109) Hoyer, J.; Neundorf, I. Peptide Vectors for the Nonviral Delivery of Nucleic Acids. *Acc Chem Res* **2012**, *45* (7), 1048–1056. https://doi.org/10.1021/AR2002304.

(110) Brooks, N. A.; Pouniotis, D. S.; Tang, C. K.; Apostolopoulos, V.; Pietersz, G. A. Cell-Penetrating Peptides: Application in Vaccine Delivery. *Biochimica et Biophysica Acta*

(BBA) - Reviews on Cancer **2010**, *1805* (1), 25–34. https://doi.org/10.1016/J.BBCAN.2009.09.004.

(111) Nguyen, Q. T.; Olson, E. S.; Aguilera, T. A.; Jiang, T.; Scadeng, M.; Ellies, L. G.; Tsien, R. Y. Surgery with Molecular Fluorescence Imaging Using Activatable Cell-Penetrating Peptides Decreases Residual Cancer and Improves Survival. *Proc Natl Acad Sci U S A* **2010**, *107* (9), 4317–4322. https://doi.org/10.1073/PNAS.0910261107.

(112) Yamada, T.; Das Gupta, T. K.; Beattie, C. W. P28, an Anionic Cell-Penetrating Peptide, Increases the Activity of Wild Type and Mutated P53 without Altering Its Conformation. *Mol Pharm* **2013**, *10* (9), 3375–3383. https://doi.org/10.1021/MP400221R.

(113) Jauset, T.; Beaulieu, M. E. Bioactive Cell Penetrating Peptides and Proteins in Cancer: A Bright Future Ahead. *Curr Opin Pharmacol* **2019**, *47*, 133–140. https://doi.org/10.1016/J.COPH.2019.03.014.

(114) Umezawa, N.; Arakawa, K.; Kato, M.; Hisamatsu, Y.; Yagi, H.; Miyajima, C.; Inoue, Y. Polyethylene Glycol Incorporation to Reduce the Cytotoxicity Associated with Cationic Cell-Penetrating-Peptide Conjugation. *RSC Med Chem* **2025**. https://doi.org/10.1039/D5MD00503E.

(115) Kristensen, M.; Birch, D.; Nielsen, H. M. Applications and Challenges for Use of Cell-Penetrating Peptides as Delivery Vectors for Peptide and Protein Cargos. *International Journal of Molecular Sciences 2016, Vol. 17, Page 185* **2016**, *17* (2), 185. https://doi.org/10.3390/IJMS17020185.

(116) Reissmann, S. Cell Penetration: Scope and Limitations by the Application of Cell-Penetrating Peptides. *Journal of Peptide Science* **2014**, *20* (10), 760–784. https://doi.org/10.1002/PSC.2672.

(117) Khakshur, A. A.; Khodaverdi, E.; Kamali, H.; Nokhodchi, A. An Insight into Cell-Penetrating Peptides: Perspectives on Design, Optimization, and Targeting in Drug Delivery Systems. *Pharm Dev Technol* **2025**. https://doi.org/10.1080/10837450.2025.2505000.

(118) Moreno-Vargas, L. M.; Prada-Gracia, D. Exploring the Chemical Features and Biomedical Relevance of Cell-Penetrating Peptides. *Int J Mol Sci* **2024**, *26* (1), 59. https://doi.org/10.3390/ijms26010059.

(119) Bakalkin, G. Y.; Rakhmaninova, A. B.; Akparov, V. K.; Volodin, A. A.; Ovchinnikov, V. V; Sarkisyan, R. A. Amino Acid Sequence Pattern in the Regulatory Peptides. *Int J Pept Protein Res* **1991**, *38* (6), 505–510. https://doi.org/10.1111/j.1399-3011.1991.tb01533.x.

(120) Yakovleva, T.; Marinova, Z.; Kuzmin, A.; Seidah, N. G.; Haroutunian, V.; Terenius, L.; Bakalkin, G. Dysregulation of Dynorphins in Alzheimer Disease. *Neurobiol Aging* **2007**, *28* (11), 1700–1708. https://doi.org/10.1016/j.neurobiolaging.2006.07.002.

(121) Fischli, W.; Goldstein, A.; Hunkapiller, M. W.; Hood, L. E. Two "Big" Dynorphins from Porcine Pituitary. *Life Sci* **1982**, *31* (16–17), 1769–1772. https://doi.org/10.1016/0024-3205(82)90206-5.

(122) Fischli, W.; Goldstein, A.; Hunkapillert, M. W.; Hoodt, L. E. Isolation and Amino Acid Sequence Analysis of a 4,000-Dalton Dynorphin from Porcine Pituitary. *Proc. NatL Acad. Sci. USA* **1982**, *79*, 5435–5437. https://doi.org/10.1073/pnas.79.17.5435.

(123) Ménard, C.; Herzog, H.; Schwarzer, C.; Quirion, R. Possible Role of Dynorphins in Alzheimer's Disease and Age-Related Cognitive Deficits. *Neurodegener Dis* **2014**, *13* (2–3), 82–85. https://doi.org/10.1159/000353848.

(124) Marinova, Z.; Vukojević, V.; Surcheva, S.; Yakovleva, T.; Cebers, G.; Pasikova, N.; Usynin, I.; Hugonin, L.; Fang, W.; Hallberg, M.; Hirschberg, D.; Bergman, T.; Langel, Ü.; Hauser, K. F.; Pramanik, A.; Aldrich, J. V; Gräslund, A.; Terenius, L.; Bakalkin, G. Translocation of Dynorphin Neuropeptides across the Plasma Membrane. *Journal of Biological Chemistry* **2005**, *280* (28), 26360–26370. https://doi.org/10.1074/jbc.M412494200.

(125) Hugonin, L.; Vukojević, V.; Bakalkin, G.; Gräslund, A. Calcium Influx into Phospholipid Vesicles Caused by Dynorphin Neuropeptides. *Biochimica et Biophysica Acta (BBA) - Biomembranes* **2008**, *1778* (5), 1267–1273. https://doi.org/10.1016/j.bbamem.2008.02.003.

(126) Hugonin, L.; Vukojević, V.; Bakalkin, G.; Gräslund, A. Membrane Leakage Induced by Dynorphins. *FEBS Lett* **2006**, *580* (13), 3201–3205. https://doi.org/10.1016/j.febslet.2006.04.078.

(127) Hauser, K. F.; Foldes, J. K.; Turbek, C. S. Dynorphin A (1-13) Neurotoxicity In Vitro: Opioid and Non-Opioid Mechanisms in Mouse Spinal Cord Neurons. *Exp Neurol* **1999**, *160* (2), 361–375. https://doi.org/10.1006/exnr.1999.7235.

(128) Alvero-Gonzalez, L. M.; Perini, D. A.; Queralt-Martín, M.; Perálvarez-Marín, A.; Viñas, C.; Alcaraz, A. Probing Electrophysiological Activity of Amphiphilic Dynorphin A in Planar Neutral Membranes Reveals Both Ion Channel-like Activity and Neuropeptide Translocation. **2023**. https://doi.org/10.1016/j.bioelechem.2023.108527.

(129) Wu, F.; Wang, X.; Li, X.; Teng, H.; Tian, T.; Bai, J. Spinocerebellar Ataxia Type 23 (SCA23): A Review. *Journal of Neurology*. Springer Science and Business Media Deutschland GmbH December 1, 2021, pp 4630–4645. https://doi.org/10.1007/s00415-020-10297-5.

(130) Bakalkin, G.; Watanabe, H.; Jezierska, J.; Depoorter, C.; Verschuuren-Bemelmans, C.; Bazov, I.; Artemenko, K. A.; Yakovleva, T.; Dooijes, D.; Van De Warrenburg, B. P. C.; Zubarev, R. A.; Kremer, B.; Knapp, P. E.; Hauser, K. F.; Wijmenga, C.; Nyberg, F.; Sinke, R. J.; Verbeek, D. S. Prodynorphin Mutations Cause the Neurodegenerative Disorder Spinocerebellar Ataxia Type 23. *The American Journal of Human Genetics* **2010**, *87* (5), 593–603. https://doi.org/10.1016/j.ajhg.2010.10.001.

(131) Smeets, C. J. L. M.; Zmorzyńska, J.; Melo, M. N.; Stargardt, A.; Dooley, C.; Bakalkin, G.; McLaughlin, J.; Sinke, R. J.; Marrink, S.-J.; Reits, E.; Verbeek, D. S. Altered Secondary Structure of Dynorphin A Associates with Loss of Opioid Signalling and NMDA-Mediated Excitotoxicity in SCA23. *Hum Mol Genet* **2016**, *25* (13), 2728–2737. https://doi.org/10.1093/hmg/ddw130.

(132) Madani, F.; Taqi, M. M.; Wärmländer, S. K. T. S.; Verbeek, D. S.; Bakalkin, G.; Gräslund, A. Perturbations of Model Membranes Induced by Pathogenic Dynorphin A Mutants Causing Neurodegeneration in Human Brain. *Biochem Biophys Res Commun* **2011**, *411* (1), 111–114. https://doi.org/10.1016/j.bbrc.2011.06.105.

(133) Hugonin, L.; Barth, A.; Gräslund, A.; Perálvarez-Marín, A. Secondary Structure Transitions and Aggregation Induced in Dynorphin Neuropeptides by the Detergent Sodium Dodecyl Sulfate. *Biochimica et Biophysica Acta (BBA) - Biomembranes* **2008**, *1778* (11), 2580–2587. https://doi.org/10.1016/j.bbamem.2008.07.011.

(134) Lind, J.; Gräslund, A.; Mäler, L. Membrane Interactions of Dynorphins. *Biochemistry* **2006**, *45* (51), 15931–15940. https://doi.org/10.1021/bi061199g.

(135) Björnerås, J.; Gräslund, A.; Mäler, L. Membrane Interaction of Disease-Related Dynorphin A Variants. *Biochemistry* **2013**, *52* (24), 4157–4167. https://doi.org/10.1021/bi4004205.

(136) Holm, T.; Johansson, H.; Lundberg, P.; Pooga, M.; Lindgren, M.; Langel, Ü. Studying the Uptake of Cell-Penetrating Peptides. *Nat Protoc* **2006**, *1* (2), 1001–1005. https://doi.org/10.1038/NPROT.2006.174.

(137) Zorko, M.; Langel, Ü. Studies of Cell-Penetrating Peptides by Biophysical Methods. *Q Rev Biophys* **2022**, *55*, e3. https://doi.org/10.1017/S0033583522000026.

(138) Rahman, A. Correlations in the Motion of Atoms in Liquid Argon. *Physical Review* **1964**, *136* (2A), A405. https://doi.org/10.1103/PhysRev.136.A405.

(139) Alder, B. J.; Wainwright, T. E. Phase Transition for a Hard Sphere System. *J Chem Phys* **1957**, *27* (5), 1208–1209. https://doi.org/10.1063/1.1743957.

(140) Yesylevskyy, S.; Marrink, S. J.; Mark, A. E. Alternative Mechanisms for the Interaction of the Cell-Penetrating Peptides Penetratin and the TAT Peptide with Lipid Bilayers. *Biophys J* **2009**, *97* (1), 40–49. https://doi.org/10.1016/j.bpj.2009.03.059.

(141) Park, S.; Schulten, K. Calculating Potentials of Mean Force from Steered Molecular Dynamics Simulations. *J Chem Phys* **2004**, *120* (13), 5946–5961. https://doi.org/10.1063/1.1651473.

(142) Gimenez-Dejoz, J.; Numata, K. Molecular Dynamics Study of the Internalization of Cell-Penetrating Peptides Containing Unnatural Amino Acids across Membranes. *Nanoscale Adv* **2022**, *4* (2), 397–407. https://doi.org/10.1039/d1na00674f.

(143) Ozer, G.; Valecv, E. F.; Quirt, S.; Hernandez, R. Adaptive Steered Molecular Dynamics of the Long-Distance Unfolding of Neuropeptide y. *J Chem Theory Comput* **2010**, *6* (10), 3026–3038. https://doi.org/10.1021/ct100320g.

(144) Barducci, A.; Bonomi, M.; Parrinello, M. Metadynamics. *Wiley Interdiscip Rev Comput Mol Sci* **2011**, *1* (5), 826–843. https://doi.org/10.1002/WCMS.31.

(145) Laio, A.; Parrinello, M. Escaping Free-Energy Minima. *Proc Natl Acad Sci U S A* **2002**, *99* (20), 12562–12566. https://doi.org/10.1073/PNAS.202427399.

(146) Torrie, G. M.; Valleau, J. P. Nonphysical Sampling Distributions in Monte Carlo Free-Energy Estimation: Umbrella Sampling. *J Comput Phys* **1977**, *23* (2), 187–199. https://doi.org/10.1016/0021-9991(77)90121-8.

(147) Sugita, Y.; Okamoto, Y. Replica-Exchange Molecular Dynamics Method for Protein Folding. *Chem Phys Lett* **1999**, *314* (1–2), 141–151. https://doi.org/10.1016/S0009-2614(99)01123-9.

(148) Kabelka, I.; Brožek, R.; Vácha, R. Selecting Collective Variables and Free-Energy Methods for Peptide Translocation across Membranes. *J Chem Inf Model* **2021**, *61* (2), 819–830. https://doi.org/10.1021/ACS.JCIM.0C01312.

(149) Zuckerman, D. M.; Chong, L. T. Weighted Ensemble Simulation: Review of Methodology, Applications, and Software. *Annu Rev Biophys* **2017**, *46* (1), 43–57. https://doi.org/10.1146/annurev-biophys-070816-033834.

(150) Choe, S. Free Energy Analyses of Cell-Penetrating Peptides Using the Weighted Ensemble Method. *Membranes (Basel)* **2021**, *11* (12), 974. https://doi.org/10.3390/membranes11120974.

(151) Wang, Y.; Chen, C. H.; Hu, D.; Ulmschneider, M. B.; Ulmschneider, J. P. Spontaneous Formation of Structurally Diverse Membrane Channel Architectures from a Single Antimicrobial Peptide. *Nature Communications 2016 7:1* **2016**, *7* (1), 1–9. https://doi.org/10.1038/ncomms13535.

(152) He, X.; Lin, M.; Sha, B.; Feng, S.; Shi, X.; Qu, Z.; Xu, F. Coarse-Grained Molecular Dynamics Studies of the Translocation Mechanism of Polyarginines across Asymmetric Membrane under Tension. *Sci Rep* **2015**, *5*. https://doi.org/10.1038/SREP12808.

(153) Hu, Y.; Liu, X.; Sinha, S. K.; Patel, S. Translocation Thermodynamics of Linear and Cyclic Nonaarginine into Model Dppc Bilayer via Coarse-Grained Molecular Dynamics Simulation: Implications of Pore Formation and Nonadditivity. *Journal of Physical Chemistry B* **2014**, *118* (10), 2670–2682. https://doi.org/10.1021/jp412600e.

(154) Marrink, S. J.; Monticelli, L.; Melo, M. N.; Alessandri, R.; Tieleman, D. P.; Souza, P. C. T. Two Decades of Martini: Better Beads, Broader Scope. *Wiley Interdiscip Rev Comput Mol Sci* **2023**, *13* (1), e1620. https://doi.org/10.1002/WCMS.1620.

(155) Sieradzan, A. K.; Jakubowski, R. Introduction of Steered Molecular Dynamics into UNRES Coarse-Grained Simulations Package. *J Comput Chem* **2017**, *38* (8), 553–562. https://doi.org/10.1002/JCC.24685.

(156) Suresh Patel, J.; Ytreberg, F. M. Fast Calculation of Protein-Protein Binding Free Energies Using Umbrella Sampling with a Coarse-Grained Model. *Biophys J* **2017**, *112* (3), 196a. https://doi.org/10.1016/j.bpj.2016.11.1087.

(157) Lazaridis, T.; Leveritt, J. M.; Pebenito, L. Implicit Membrane Treatment of Buried Charged Groups: Application to Peptide Translocation across Lipid Bilayers. *Biochim Biophys Acta Biomembr* **2014**, *1838* (9), 2149–2159. https://doi.org/10.1016/J.BBAMEM.2014.01.015.

(158) Schwarze, S. R.; Hruska, K. A.; Dowdy, S. F.; Schwarze, S. R.; Hruska, K. A.; Dowdy, S. F. Protein Transduction: Unrestricted Delivery into All Cells? *Trends Cell Biol* **2000**, *10* (7), 290–295. https://doi.org/10.1016/S0962-8924(00)01771-2.

(159) Tian, Y.; Zhou, S. Advances in Cell Penetrating Peptides and Their Functionalization of Polymeric Nanoplatforms for Drug Delivery. *Wiley Interdiscip Rev Nanomed Nanobiotechnol* **2021**, *13* (2), e1668. https://doi.org/10.1002/WNAN.1668.

(160) Tripathi, P. P.; Arami, H.; Banga, I.; Gupta, J.; Gandhi, S. Cell Penetrating Peptides in Preclinical and Clinical Cancer Diagnosis and Therapy. *Oncotarget* **2018**, *9* (98), 37252. https://doi.org/10.18632/ONCOTARGET.26442.

(161) Zhang, Y.; Guo, P.; Ma, Z.; Lu, P.; Kebebe, D.; Liu, Z. Combination of Cell-Penetrating Peptides with Nanomaterials for the Potential Therapeutics of Central Nervous System Disorders: A Review. *Journal of Nanobiotechnology 2021 19:1* **2021**, *19* (1), 1–22. https://doi.org/10.1186/S12951-021-01002-3.

(162) Li, T.; Bourgeois, J.-P.; Celli, S.; Glacial, F.; Le Sourd, A.-M.; Mecheri, S.; Weksler, B.; Romero, I.; Couraud, P.-O.; Rougeon, F.; Lafaye, P. Cell-Penetrating Anti-GFAP VHH and Corresponding Fluorescent Fusion Protein VHH-GFP Spontaneously Cross the Blood-Brain Barrier and Specifically Recognize Astrocytes: Application to Brain Imaging. *The FASEB Journal* **2012**, *26* (10), 3969–3979. https://doi.org/https://doi.org/10.1096/fj.11-201384.

(163) Li, Q.; Yang, J.; Chen, C.; Lin, X.; Zhou, M.; Zhou, Z.; Huang, Y. A Novel Mitochondrial Targeted Hybrid Peptide Modified HPMA Copolymers for Breast Cancer Metastasis Suppression. *Journal of Controlled Release* **2020**, *325*, 38–51. https://doi.org/https://doi.org/10.1016/j.jconrel.2020.06.010.

(164) Guo, F.; Fu, Q.; Zhou, K.; Jin, C.; Wu, W.; Ji, X.; Yan, Q.; Yang, Q.; Wu, D.; Li, A.; Yang, G. Matrix Metalloprotein-Triggered, Cell Penetrating Peptide-Modified Star-Shaped Nanoparticles for Tumor Targeting and Cancer Therapy. *J Nanobiotechnology* **2020**, *18* (1), 48. https://doi.org/10.1186/s12951-020-00595-5.

(165) Yang, Y.; Yang, Y.; Xie, X.; Cai, X.; Mei, X. Preparation and Characterization of Photo-Responsive Cell-Penetrating Peptide-Mediated Nanostructured Lipid Carrier. *J Drug Target* **2014**, *22* (10), 891–900. https://doi.org/10.3109/1061186X.2014.940589.

(166) Gestin, M.; Dowaidar, M.; Langel, Ü. Uptake Mechanism of Cell-Penetrating Peptides. In *Peptides and Peptide-based Biomaterials and their Biomedical Applications. Advances in Experimental Medicine and Biology*; Sunna, A., Care, A., Bergquist, P. L., Eds.; Advances in Experimental Medicine and Biology; Springer, Cham, 2017; Vol. 1030, pp 255–264. https://doi.org/10.1007/978-3-319-66095-0_11.

(167) Doherty, G. J.; McMahon, H. T. Mechanisms of Endocytosis. *Annu Rev Biochem* **2009**, *78* (Volume 78, 2009), 857–902. https://doi.org/https://doi.org/10.1146/annurev.biochem.78.081307.110540.

(168) Matsuzaki, K.; Yoneyama, S.; Murase, O.; Miyajima, K. Transbilayer Transport of Ions and Lipids Coupled with Mastoparan X Translocation. *Biochemistry* **1996**, *35* (25), 8450–8456. https://doi.org/10.1021/bi960342a.

(169) Lee, M.-T.; Hung, W.-C.; Chen, F.-Y.; Huang, H. W. Many-Body Effect of Antimicrobial Peptides: On the Correlation Between Lipid's Spontaneous Curvature and Pore Formation. *Biophys J* **2005**, *89* (6), 4006–4016. https://doi.org/10.1529/biophysj.105.068080.

(170) Derossi, D.; Calvet, S.; Trembleau, A.; Brunissen, A.; Chassaing, G.; Prochiantz, A. Cell Internalization of the Third Helix of the Antennapedia Homeodomain Is Receptor-Independent *. *Journal of Biological Chemistry* **1996**, *271* (30), 18188–18193. https://doi.org/10.1074/jbc.271.30.18188.

(171) Berlose, J.; Convert, O.; Derossi, D.; Brunissen, A.; Chassaing, G. Conformational and Associative Behaviours of the Third Helix of Antennapedia Homeodomain in Membrane-Mimetic Environments. *Eur J Biochem* **1996**, *242* (2), 372–386. https://doi.org/https://doi.org/10.1111/j.1432-1033.1996.0372r.x.

(172) De Oliveira, E. C. L.; Da Costa, K. S.; Taube, P. S.; Lima, A. H.; Junior, C. D. S. D. S. Biological Membrane-Penetrating Peptides: Computational Prediction and Applications. *Front Cell Infect Microbiol* **2022**, *12*, 838259. https://doi.org/10.3389/fcimb.2022.838259.

(173) Iwasaki, T.; Tokuda, Y.; Kotake, A.; Okada, H.; Takeda, S.; Kawano, T.; Nakayama, Y. Cellular Uptake and in Vivo Distribution of Polyhistidine Peptides. *Journal of Controlled Release* **2015**, *210*, 115–124. https://doi.org/https://doi.org/10.1016/j.jconrel.2015.05.268.

(174) Zaro, J. L.; Fei, L.; Shen, W.-C. Recombinant Peptide Constructs for Targeted Cell Penetrating Peptide-Mediated Delivery. *Journal of Controlled Release* **2012**, *158* (3), 357–361. https://doi.org/https://doi.org/10.1016/j.jconrel.2012.01.039.

(175) Pescina, S.; Ostacolo, C.; Gomez-Monterrey, I. M.; Sala, M.; Bertamino, A.; Sonvico, F.; Padula, C.; Santi, P.; Bianchera, A.; Nicoli, S. Cell Penetrating Peptides in Ocular Drug Delivery: State of the Art. *Journal of Controlled Release* **2018**, *284*, 84–102. https://doi.org/https://doi.org/10.1016/j.jconrel.2018.06.023.

(176) Pirhaghi, M.; Mamashli, F.; Moosavi-Movahedi, F.; Arghavani, P.; Amiri, A.; Davaeil, B.; Mohammad-Zaheri, M.; Mousavi-Jarrahi, Z.; Sharma, D.; Langel, Ü.; Otzen, D. E.; Saboury, A. A. Cell-Penetrating Peptides: Promising Therapeutics and Drug-Delivery Systems for Neurodegenerative Diseases. *Mol Pharm* **2024**, *21* (5), 2097–2117. https://doi.org/10.1021/acs.molpharmaceut.3c01167.

(177) Nakase, I.; Konishi, Y.; Ueda, M.; Saji, H.; Futaki, S. Accumulation of Arginine-Rich Cell-Penetrating Peptides in Tumors and the Potential for Anticancer Drug Delivery in Vivo. *Journal of Controlled Release* **2012**, *159* (2), 181–188. https://doi.org/https://doi.org/10.1016/j.jconrel.2012.01.016.

(178) Rothbard, J. B.; Garlington, S.; Lin, Q.; Kirschberg, T.; Kreider, E.; McGrane, P. L.; Wender, P. A.; Khavari, P. A. Conjugation of Arginine Oligomers to Cyclosporin A Facilitates Topical Delivery and Inhibition of Inflammation. *Nat Med* **2000**, *6* (11), 1253–1257. https://doi.org/10.1038/81359.

(179) Kim, G. C.; Cheon, D. H.; Lee, Y. Challenge to Overcome Current Limitations of Cell-Penetrating Peptides. *Biochimica et Biophysica Acta - Proteins and Proteomics*. Elsevier B.V. April 1, 2021. https://doi.org/10.1016/j.bbapap.2021.140604.

(180) Jiao, C.-Y.; Delaroche, D.; Burlina, F.; Alves, I. D.; Chassaing, G.; Sagan, S. Translocation and Endocytosis for Cell-Penetrating Peptide Internalization. *J Biol Chem* **2009**, *284* (49), 33957–33965. https://doi.org/10.1074/jbc.M109.056309.

(181) Mirdita, M.; Schütze, K.; Moriwaki, Y.; Heo, L.; Ovchinnikov, S.; Steinegger, M. ColabFold: Making Protein Folding Accessible to All. *Nat Methods* **2022**, *19* (6), 679–682. https://doi.org/10.1038/s41592-022-01488-1.

(182) Jumper, J.; Evans, R.; Pritzel, A.; Green, T.; Figurnov, M.; Ronneberger, O.; Tunyasuvunakool, K.; Bates, R.; Žídek, A.; Potapenko, A.; Bridgland, A.; Meyer, C.; Kohl, S. A. A.; Ballard, A. J.; Cowie, A.; Romera-Paredes, B.; Nikolov, S.; Jain, R.; Adler, J.; Back, T.; Petersen, S.; Reiman, D.; Clancy, E.; Zielinski, M.; Steinegger, M.; Pacholska, M.; Berghammer, T.; Bodenstein, S.; Silver, D.; Vinyals, O.; Senior, A. W.; Kavukcuoglu, K.; Kohli, P.; Hassabis, D. Highly Accurate Protein Structure Prediction with AlphaFold. *Nature* **2021**, *596* (7873), 583–589. https://doi.org/10.1038/s41586-021-03819-2.

(183) Case, D. A.; Belfon, K.; Ben-Shalom, I. Y.; Brozell, S. R.; Cerutti, D. S.; T. E. Cheatham, I. I. I.; Cruzeiro, V. W. D.; Darden, T. A.; Duke, R. E.; Giambasu, G.; Gilson, M. K.; Gohlke, H.; Goetz, A. W.; Harris, R.; Izadi, S.; Izmailov, S. A.; Kasavajhala, K.; Kovalenko, A.; Krasny, R.; Kurtzman, T.; Lee, T. S.; LeGrand, S.; Li, P.; Lin, C.; Liu, J.; Luchko, T.; Luo, R.; Man, V.; Merz, K. M.; Miao, Y.; Mikhailovskii, O.; Monard, G.; Nguyen, H.; Onufriev, A.; Pan, F.; Pantano, S.; Qi, R.; Roe, D. R.; Roitberg, A.; Sagui, C.; Schott-Verdugo, S.; Shen, J.; Simmerling, C. L.; Skrynnikov, N. R.; Smith, J.; Swails, J.; Walker, R. C.; Wang, J.; Wilson, L.; Wolf, R. M.; Wu, X.; Xiong, Y.; Xue, Y.; York, D. M.; Kollman, P. A. AMBER 2020. 2020.

(184) Maier, J. A.; Martinez, C.; Kasavajhala, K.; Wickstrom, L.; Hauser, K. E.; Simmerling, C. Ff14SB: Improving the Accuracy of Protein Side Chain and Backbone Parameters from Ff99SB. *J Chem Theory Comput* **2015**, *11* (8), 3696–3713. https://doi.org/10.1021/acs.jctc.5b00255.

(185) Kräutler, V.; van Gunsteren, W. F.; Hünenberger, P. H. A Fast SHAKE Algorithm to Solve Distance Constraint Equations for Small Molecules in Molecular Dynamics Simulations. *J Comput Chem* **2001**, *22* (5), 501–508. https://doi.org/10.1002/1096-987X(20010415)22:5<501::AID-JCC1021>3.0.CO;2-V.

(186) Brooks, B. R.; Brooks III, C. L.; Mackerell Jr., A. D.; Nilsson, L.; Petrella, R. J.; Roux, B.; Won, Y.; Archontis, G.; Bartels, C.; Boresch, S.; Caflisch, A.; Caves, L.; Cui, Q.; Dinner, A. R.; Feig, M.; Fischer, S.; Gao, J.; Hodoscek, M.; Im, W.; Kuczera, K.; Lazaridis, T.; Ma, J.; Ovchinnikov, V.; Paci, E.; Pastor, R. W.; Post, C. B.; Pu, J. Z.; Schaefer, M.; Tidor, B.; Venable, R. M.; Woodcock, H. L.; Wu, X.; Yang, W.; York, D. M.; Karplus, M. CHARMM: The Biomolecular Simulation Program. *J Comput Chem* **2009**, *30* (10), 1545–1614. https://doi.org/10.1002/jcc.21287.

(187) Lee, J.; Cheng, X.; Swails, J. M.; Yeom, M. S.; Eastman, P. K.; Lemkul, J. A.; Wei, S.; Buckner, J.; Jeong, J. C.; Qi, Y.; Jo, S.; Pande, V. S.; Case, D. A.; Brooks, C. L. I. I. I.; MacKerell, A. D. Jr.; Klauda, J. B.; Im, W. CHARMM-GUI Input Generator for NAMD, GROMACS, AMBER, OpenMM, and CHARMM/OpenMM Simulations Using the CHARMM36 Additive Force Field. *J Chem Theory Comput* **2016**, *12* (1), 405–413. https://doi.org/10.1021/acs.jctc.5b00935.

(188) Jo, S.; Kim, T.; Iyer, V. G.; Im, W. CHARMM-GUI: A Web-Based Graphical User Interface for CHARMM. *J Comput Chem* **2008**, *29* (11), 1859–1865. https://doi.org/10.1002/jcc.20945.

(189) Lee, J.; Patel, D. S.; Ståhle, J.; Park, S.-J.; Kern, N. R.; Kim, S.; Lee, J.; Cheng, X.; Valvano, M. A.; Holst, O.; Knirel, Y. A.; Qi, Y.; Jo, S.; Klauda, J. B.; Widmalm, G.; Im, W. CHARMM-GUI Membrane Builder for Complex Biological Membrane Simulations with Glycolipids and Lipoglycans. *J Chem Theory Comput* **2019**, *15* (1), 775–786. https://doi.org/10.1021/acs.jctc.8b01066.

(190) Jo, S.; Lim, J. B.; Klauda, J. B.; Im, W. CHARMM-GUI Membrane Builder for Mixed Bilayers and Its Application to Yeast Membranes. *Biophys J* **2009**, *97* (1), 50–58. https://doi.org/10.1016/j.bpj.2009.04.013.

(191) Lee, J.; Hitzenberger, M.; Rieger, M.; Kern, N. R.; Zacharias, M.; Im, W. CHARMM-GUI Supports the Amber Force Fields. *J Chem Phys* **2020**, *153* (3), 35103. https://doi.org/10.1063/5.0012280.

(192) Wu, E. L.; Cheng, X.; Jo, S.; Rui, H.; Song, K. C.; Dávila-Contreras, E. M.; Qi, Y.; Lee, J.; Monje-Galvan, V.; Venable, R. M.; Klauda, J. B.; Im, W. CHARMM-GUI Membrane Builder toward Realistic Biological Membrane Simulations. *J Comput Chem* **2014**, *35* (27), 1997–2004. https://doi.org/10.1002/jcc.23702.

(193) Hub, J. S. Joint Reaction Coordinate for Computing the Free-Energy Landscape of Pore Nucleation and Pore Expansion in Lipid Membranes. *J Chem Theory Comput* **2021**, *17* (2), 1229–1239. https://doi.org/10.1021/acs.jctc.0c01134.

(194) Awasthi, N.; Hub, J. S. Simulations of Pore Formation in Lipid Membranes: Reaction Coordinates, Convergence, Hysteresis, and Finite-Size Effects. *J Chem Theory Comput* **2016**, *12* (7), 3261–3269. https://doi.org/10.1021/acs.jctc.6b00369.

(195) Hub, J. S.; Awasthi, N. Probing a Continuous Polar Defect: A Reaction Coordinate for Pore Formation in Lipid Membranes. *J Chem Theory Comput* **2017**, *13* (5), 2352–2366. https://doi.org/10.1021/acs.jctc.7b00106.

(196) Dickson, C. J.; Walker, R. C.; Gould, I. R. Lipid21: Complex Lipid Membrane Simulations with AMBER. *J Chem Theory Comput* **2022**, *18* (3), 1726–1736. https://doi.org/10.1021/acs.jctc.1c01217.

(197) Case, D. A.; Cheatham, T. E.; Darden, T.; Gohlke, H.; Luo, R.; Merz, K. M.; Onufriev, A.; Simmerling, C.; Wang, B.; Woods, R. J. The Amber Biomolecular Simulation Programs. *J Comput Chem* **2005**, *26* (16), 1668–1688. https://doi.org/10.1002/jcc.20290.

(198) Ozer, G.; Quirk, S.; Hernandez, R. Adaptive Steered Molecular Dynamics: Validation of the Selection Criterion and Benchmarking Energetics in Vacuum. *Journal of Chemical Physics* **2012**, *136* (21). https://doi.org/10.1063/1.4725183.

(199) Zhuang, Y.; Bureau, H. R.; Quirk, S.; Hernandez, R. Adaptive Steered Molecular Dynamics of Biomolecules. *Mol Simul* **2021**, *47* (5), 408–419. https://doi.org/10.1080/08927022.2020.1807542.

(200) Liu, Z.; Xu, Y.; Tang, P. Steered Molecular Dynamics Simulations of Na + Permeation across the Gramicidin A Channel. **2006**. https://doi.org/10.1021/jp060688n.

(201) Hwang, H.; Schatz, G. C.; Ratner, M. A. Steered Molecular Dynamics Studies of the Potential of Mean Force of a Na + or K + Ion in a Cyclic Peptide Nanotube. **2006**. https://doi.org/10.1021/jp0657888.

(202) Hummer, G.; Szabo, A. Free Energy Reconstruction from Nonequilibrium Single-Molecule Pulling Experiments. *Proceedings of the National Academy of Sciences* **2001**, *98* (7), 3658–3661. https://doi.org/10.1073/pnas.071034098.

(203) Jarzynski, C. Nonequilibrium Equality for Free Energy Differences. *Phys Rev Lett* **1997**, *78* (14), 2690–2693. https://doi.org/10.1103/PhysRevLett.78.2690.

(204) Park, S.; Khalili-Araghi, F.; Tajkhorshid, E.; Schulten, K. Free Energy Calculation from Steered Molecular Dynamics Simulations Using Jarzynski's Equality. *Journal of Chemical Physics* **2003**, *119* (6), 3559–3566. https://doi.org/10.1063/1.1590311.

(205) Bureau, H. R.; Quirk, S.; Hernandez, R. The Relative Stability of Trpzip1 and Its Mutants Determined by Computation and Experiment. *RSC Adv* **2020**, *10* (11), 6520–6535. https://doi.org/10.1039/d0ra00920b.

(206) Humphrey, W.; Dalke, A.; Schulten, K. VMD: Visual Molecular Dynamics. *J Mol Graph* **1996**, *14* (1), 33–38. https://doi.org/10.1016/0263-7855(96)00018-5.

(207) Roe, D. R.; Cheatham, T. E. I. I. I. PTRAJ and CPPTRAJ: Software for Processing and Analysis of Molecular Dynamics Trajectory Data. *J Chem Theory Comput* **2013**, *9* (7), 3084–3095. https://doi.org/10.1021/ct400341p.

(208) Song, W.; Corey, R. A.; Ansell, T. B.; Cassidy, C. K.; Horrell, M. R.; Duncan, A. L.; Stansfeld, P. J.; Sansom, M. S. P. PyLipID: A Python Package for Analysis of Protein–Lipid Interactions from Molecular Dynamics Simulations. *J Chem Theory Comput* **2022**, *18* (2), 1188–1201. https://doi.org/10.1021/acs.jctc.1c00708.

(209) Smith, P.; Lorenz, C. D. LiPyphilic: A Python Toolkit for the Analysis of Lipid Membrane Simulations. *J Chem Theory Comput* **2021**. https://doi.org/10.1021/acs.jctc.1c00447.

(210) Gowers, R.; Linke, M.; Barnoud, J.; Reddy, T.; Melo, M.; Seyler, S.; Domański, J.; Dotson, D.; Buchoux, S.; Kenney, I.; Beckstein, O. MDAnalysis: A Python Package for the Rapid Analysis of Molecular Dynamics Simulations. In *Python in Science Conference*; 2016; pp 98–105. https://doi.org/10.25080/Majora-629e541a-00e.

(211) Michaud-Agrawal, N.; Denning, E. J.; Woolf, T. B.; Beckstein, O. MDAnalysis: A Toolkit for the Analysis of Molecular Dynamics Simulations. *J Comput Chem* **2011**, *32* (10), 2319–2327. https://doi.org/10.1002/JCC.21787.

(212) Ramasubramani, V.; Dice, B. D.; Harper, E. S.; Spellings, M. P.; Anderson, J. A.; Glotzer, S. C. Freud: A Software Suite for High Throughput Analysis of Particle Simulation Data. *Comput Phys Commun* **2020**, *254*, 107275. https://doi.org/10.1016/j.cpc.2020.107275.

(213) Repáková, J.; Holopainen, J. M.; Morrow, M. R.; McDonald, M. C.; Čapková, P.; Vattulainen, I. Influence of DPH on the Structure and Dynamics of a DPPC Bilayer. *Biophys J* **2005**, *88* (5), 3398–3410. https://doi.org/10.1529/biophysj.104.055533.

(214) Vermeer, L. S.; De Groot, B. L.; Réat, V.; Milon, A.; Czaplicki, J. Acyl Chain Order Parameter Profiles in Phospholipid Bilayers: Computation from Molecular Dynamics Simulations and Comparison with 2H NMR Experiments. *European Biophysics Journal*. November 2007, pp 919–931. https://doi.org/10.1007/s00249-007-0192-9.

(215) Piggot, T. J.; Allison, J. R.; Sessions, R. B.; Essex, J. W. On the Calculation of Acyl Chain Order Parameters from Lipid Simulations. *J Chem Theory Comput* **2017**, *13* (11), 5683–5696. https://doi.org/10.1021/acs.jctc.7b00643.

(216) Hunter, J. D. Matplotlib: A 2D Graphics Environment. *Comput Sci Eng* **2007**, *9* (3), 90–95. https://doi.org/10.1109/MCSE.2007.55.

(217) Waskom, M. L. Seaborn: Statistical Data Visualization. *J Open Source Softw* **2021**, *6* (60), 3021. https://doi.org/10.21105/JOSS.03021.

(218) Pettersen, E. F.; Goddard, T. D.; Huang, C. C.; Meng, E. C.; Couch, G. S.; Croll, T. I.; Morris, J. H.; Ferrin, T. E. UCSF ChimeraX: Structure Visualization for Researchers, Educators, and Developers. *Protein Sci* **2021**, *30* (1), 70–82. https://doi.org/10.1002/pro.3943.

(219) Goddard, T. D.; Huang, C. C.; Meng, E. C.; Pettersen, E. F.; Couch, G. S.; Morris, J. H.; Ferrin, T. E. UCSF ChimeraX: Meeting Modern Challenges in Visualization and Analysis. *Protein Sci* **2018**, *27* (1), 14–25. https://doi.org/10.1002/pro.3235.

(220) Kyte, J.; Doolittle, R. F. A Simple Method for Displaying the Hydropathic Character of a Protein. *J Mol Biol* **1982**, *157* (1), 105–132. https://doi.org/10.1016/0022-2836(82)90515-0.

(221) Elber, R. Defect Formation and Peptide Permeation across Phospholipid Membranes. *J Phys Chem B* **2023**, *127* (37), 7810–7818. https://doi.org/10.1021/ACS.JPCB.3C04895.

(222) Jain, M.; Matysiak, S. Dual Role of Anionic Lipids in Amyloid Aggregation. *Journal of Physical Chemistry B* **2024**, *128* (44), 10789–11038. https://doi.org/10.1021/acs.jpcb.4c05636.

(223) MacCallum, J. L.; Bennett, W. F. D.; Tieleman, D. P. Transfer of Arginine into Lipid Bilayers Is Nonadditive. *Biophys J* **2011**, *101* (1), 110–117. https://doi.org/10.1016/J.BPJ.2011.05.038.

(224) Ozer, G.; Quirk, S.; Hernandez, R. Thermodynamics of Decaalanine Stretching in Water Obtained by Adaptive Steered Molecular Dynamics Simulations. *J Chem Theory Comput* **2012**, *8* (11), 4837–4844. https://doi.org/10.1021/ct300709u.

(225) Kenien, R.; Shen, W. C.; Zaro, J. L. Vesicle-to-Cytosol Transport of Disulfide-Linked Cargo Mediated by an Amphipathic Cell-Penetrating Peptide. *J Drug Target* **2012**, *20* (9), 793–800. https://doi.org/10.3109/1061186X.2012.719899.

(226) Oehlke, J.; Lorenz, D.; Wiesner, B.; Bienert, M. Studies on the Cellular Uptake of Substance P and Lysine-Rich, KLA-Derived Model Peptides. *Journal of Molecular Recognition*. January 2005, pp 50–59. https://doi.org/10.1002/jmr.691.

(227) He, J.; Kauffman, W. B.; Fuselier, T.; Naveen, S. K.; Voss, T. G.; Hristova, K.; Wimley, W. C. Direct Cytosolic Delivery of Polar Cargo to Cells by Spontaneous Membrane-Translocating Peptides. *J Biol Chem* **2013**, *288* (41), 29974. https://doi.org/10.1074/JBC.M113.488312.

(228) Regen, S. L. Cholesterol's Condensing Effect: Unpacking a Century-Old Mystery. *JACS Au* **2022**, *2* (1), 84–91. https://doi.org/10.1021/jacsau.1c00493.

(229) Yue, T.; Sun, M.; Zhang, S.; Ren, H.; Ge, B.; Huang, F. How Transmembrane Peptides Insert and Orientate in Biomembranes: A Combined Experimental and Simulation Study. *Physical Chemistry Chemical Physics* **2016**, *18* (26), 17483–17494. https://doi.org/10.1039/c6cp01133k.

(230) Kabelka, I.; Vácha, R. Optimal Hydrophobicity and Reorientation of Amphiphilic Peptides Translocating through Membrane. *Biophys J* **2018**, *115*, 1045–1054. https://doi.org/10.1016/j.bpj.2018.08.012.

(231) Herce, H. D.; Garcia, A. E. Molecular Dynamics Simulations Suggest a Mechanism for Translocation of the HIV-1 TAT Peptide across Lipid Membranes. *Proceedings of the National Academy of Sciences* **2007**, *104* (52), 20805–20810. https://doi.org/10.1073/pnas.0706574105.

(232) Yi, D.; Guoming, L.; Gao, L.; Wei, L. Interaction of Arginine Oligomer with Model Membrane. *Biochem Biophys Res Commun* **2007**, *359* (4), 1024–1029. https://doi.org/https://doi.org/10.1016/j.bbrc.2007.06.015.

(233) Choe, S. Translocation of a Single Arg9 Peptide across a DOPC/DOPG(4:1) Model Membrane Using the Weighted Ensemble Method. *Scientific Reports 2023 13:1* **2023**, *13* (1), 1–9. https://doi.org/10.1038/s41598-023-28493-4.

(234) Herce, H. D.; Garcia, A. E.; Litt, J.; Kane, R. S.; Martin, P.; Enrique, N.; Rebolledo, A.; Milesi, V. Arginine-Rich Peptides Destabilize the Plasma Membrane, Consistent with a Pore Formation Translocation Mechanism of Cell-Penetrating Peptides. *Biophys J* **2009**, *97* (7), 1917–1925. https://doi.org/10.1016/j.bpj.2009.05.066.

(235) Huang, K.; García, A. E. Free Energy of Translocating an Arginine-Rich Cell-Penetrating Peptide across a Lipid Bilayer Suggests Pore Formation. *Biophys J* **2013**, *104* (2), 412–420. https://doi.org/10.1016/j.bpj.2012.10.027.

(236) Oba, M.; Nagano, Y.; Kato, T.; Tanaka, M. Secondary Structures and Cell-Penetrating Abilities of Arginine-Rich Peptide Foldamers. *Sci Rep* **2019**, *9* (1). https://doi.org/10.1038/s41598-018-38063-8.

(237) Bertrand, J.-R.; Malvy, C.; Auguste, T.; Tóth, G. K.; Kiss-Ivánkovits, O.; Illyés, E.; Hollósi, M.; Bottka, S.; Laczkó, I. Synthesis and Studies on Cell-Penetrating Peptides. *Bioconjug Chem* **2009**, *20* (7), 1307–1314. https://doi.org/10.1021/bc900005j.

(238) Säälik, P.; Elmquist, A.; Hansen, M.; Padari, K.; Saar, K.; Viht, K.; Langel, Ü.; Pooga, M. Protein Cargo Delivery Properties of Cell-Penetrating Peptides. A Comparative Study. *Bioconjug Chem* **2004**, *15* (6), 1246–1253. https://doi.org/10.1021/BC049938Y.

(239) Endoh, T.; Ohtsuki, T. Cellular SiRNA Delivery Using Cell-Penetrating Peptides Modified for Endosomal Escape. *Adv Drug Deliv Rev* **2009**, *61* (9), 704–709. https://doi.org/10.1016/J.ADDR.2009.04.005.

(240) Veldhoen, S.; Laufer, S. D.; Trampe, A.; Restle, T. Cellular Delivery of Small Interfering RNA by a Non-Covalently Attached Cell-Penetrating Peptide: Quantitative Analysis of Uptake and Biological Effect. *Nucleic Acids Res* **2006**, *34* (22), 6561–6573. https://doi.org/10.1093/NAR/GKL941.

(241) Silva, S.; Almeida, A. J.; Vale, N. Combination of Cell-Penetrating Peptides with Nanoparticles for Therapeutic Application: A Review. *Biomolecules*. 2019. https://doi.org/10.3390/biom9010022.

(242) Magzoub, M. Combating Proteins with Proteins: Engineering Cell-Penetrating Peptide Antagonists of Amyloid-β Aggregation and Associated Neurotoxicity. *DNA Cell Biol* **2020**, *39* (6), 920–925. https://doi.org/10.1089/dna.2020.5604.

(243) Fathi, N.; Hojaji, A.; Bolhassani, A.; Agi, E. Antitumor Effects of HPV E7 and L1-E7 Multiepitope DNA Constructs Delivered by Synthetic and Arginine-Rich Cell Penetrating Peptides. *International Journal of Peptide Research and Therapeutics 2024 31:2* **2025**, *31* (2), 1–10. https://doi.org/10.1007/S10989-024-10679-7.

(244) Lee, J.-H.; Yang, S.-B.; Park, S. J.; Kweon, S.; Ma, G.; Seo, M.; Kim, H. R.; Kang, T.-B.; Lim, J.-H.; Park, J. Cell-Penetrating Peptide Like Anti-Programmed Cell Death-Ligand 1 Peptide Conjugate-Based Self-Assembled Nanoparticles for Immunogenic Photodynamic Therapy. *ACS Nano* **2025**. https://doi.org/10.1021/ACSNANO.4C16128.

(245) Klimpel, A.; Lützenburg, T.; Neundorf, I. Recent Advances of Anti-Cancer Therapies Including the Use of Cell-Penetrating Peptides. *Curr Opin Pharmacol* **2019**, *47*, 8–13. https://doi.org/10.1016/J.COPH.2019.01.003.

(246) Wu, H.; Zhuang, Q.; Xu, J.; Xu, L.; Zhao, Y.; Wang, C.; Yang, Z.; Shen, F.; Liu, Z.; Peng, R. Cell-Penetrating Peptide Enhanced Antigen Presentation for Cancer Immunotherapy. *Bioconjug Chem* **2019**, *30* (8), 2115–2126. https://doi.org/10.1021/ACS.BIOCONJCHEM.9B00245.

(247) Muñoz-Gacitúa, D.; Guzman, F.; Weiss-López, B. Insights into the Equilibrium Structure and Translocation Mechanism of TP1, a Spontaneous Membrane-Translocating Peptide. *Scientific Reports 2022 12:1* **2022**, *12* (1), 1–10. https://doi.org/10.1038/s41598-022-23631-w.

(248) Thorén, P. E. G.; Persson, D.; Isakson, P.; Goksör, M.; Önfelt, A.; Nordén, B. Uptake of Analogs of Penetratin, Tat(48–60) and Oligoarginine in Live Cells. *Biochem Biophys Res Commun* **2003**, *307* (1), 100–107. https://doi.org/10.1016/S0006-291X(03)01135-5.

(249) Richard, J. P.; Melikov, K.; Brooks, H.; Prevot, P.; Lebleu, B.; Chernomordik, L. V. Cellular Uptake of Unconjugated TAT Peptide Involves Clathrin-Dependent Endocytosis and Heparan Sulfate Receptors. *Journal of Biological Chemistry* **2005**, *280* (15), 15300–15306. https://doi.org/10.1074/jbc.M401604200.

(250) Sahni, A.; Qian, Z.; Pei, D. Cell-Penetrating Peptides Escape the Endosome by Inducing Vesicle Budding and Collapse. *ACS Chem Biol* **2020**, *15* (9), 2485. https://doi.org/10.1021/ACSCHEMBIO.0C00478.

(251) Sahni, A.; Ritchey, J. L.; Qian, Z.; Pei, D. Cell-Penetrating Peptides Translocate across the Plasma Membrane by Inducing Vesicle Budding and Collapse. *J Am Chem Soc* **2024**, *16*, 56. https://doi.org/10.1021/JACS.4C10533.

(252) Langel, Ü. Cell-Translocation Mechanisms of CPPs. *CPP, Cell-Penetrating Peptides* **2019**, 359–394. https://doi.org/10.1007/978-981-13-8747-0_10.

(253) Magzoub, M.; Eriksson, L. E. G.; Gräslund, A. Conformational States of the Cell-Penetrating Peptide Penetratin When Interacting with Phospholipid Vesicles: Effects of Surface Charge and Peptide Concentration. *Biochimica et Biophysica Acta (BBA) - Biomembranes* **2002**, *1563* (1–2), 53–63. https://doi.org/10.1016/S0005-2736(02)00373-5.

(254) Lint, Y.-Z.; Yao, S.; Veach, R. A.; Torgerson, T. R.; Hawiger, J. Inhibition of Nuclear Translocation of Transcription Factor NF-KB by a Synthetic Peptide Containing a Cell Membrane-Permeable Motif and Nuclear Localization Sequence. *J Biol Chem* **1995**, *270* (24), 14255–14258. https://doi.org/10.1074/jbc.270.24.14255.

(255) Soomets, U.; Lindgren, M.; Gallet, X.; Hällbrink, M.; Elmquist, A.; Balaspiri, L.; Zorko, M.; Pooga, M.; Brasseur, R.; Langel, Ü. Deletion Analogues of Transportan. *Biochimica et Biophysica Acta (BBA) - Biomembranes* **2000**, *1467* (1), 165–176. https://doi.org/10.1016/S0005-2736(00)00216-9.

(256) Magzoub, M.; Kilk, K.; Eriksson, L. E. G.; Langel, Ü.; Gräslund, A. Interaction and Structure Induction of Cell-Penetrating Peptides in the Presence of Phospholipid Vesicles. *Biochimica et Biophysica Acta (BBA) - Biomembranes* **2001**, *1512* (1), 77–89. https://doi.org/10.1016/S0005-2736(01)00304-2.

(257) Thorén, P. E. G.; Persson, D.; Esbjörner, E. K.; Goksör, M.; Lincoln, P.; Nordén, B. Membrane Binding and Translocation of Cell-Penetrating Peptides†. *Biochemistry* **2004**, *43* (12), 3471–3489. https://doi.org/10.1021/BI0360049.

(258) Magzoub, M.; Pramanik, A.; Gräslund, A. Modeling the Endosomal Escape of Cell-Penetrating Peptides: Transmembrane PH Gradient Driven Translocation across Phospholipid Bilayers. *Biochemistry* **2005**, *44* (45), 14890–14897. https://doi.org/10.1021/BI051356W.

(259) Kutzner, C.; Grubmüller, H.; De Groot, B. L.; Zachariae, U. Computational Electrophysiology: The Molecular Dynamics of Ion Channel Permeation and Selectivity in Atomistic Detail. *Biophys J* **2011**, *101* (4), 809. https://doi.org/10.1016/J.BPJ.2011.06.010.

(260) Nymeyer, H.; Woolf, T. B.; Garcia, A. E. Folding Is Not Required for Bilayer Insertion: Replica Exchange Simulations of an α-Helical Peptide with an Explicit Lipid Bilayer. *Proteins: Structure, Function and Genetics* **2005**, *59* (4), 783–790. https://doi.org/10.1002/prot.20460.

(261) Reid, L. M.; Verma, C. S.; Essex, J. W. The Role of Molecular Simulations in Understanding the Mechanisms of Cell-Penetrating Peptides. *Drug Discov Today* **2019**, *24* (9), 1821–1835. https://doi.org/10.1016/j.drudis.2019.06.013.

(262) Ouyang, J.; Sheng, Y.; Wang, W. Recent Advances of Studies on Cell-Penetrating Peptides Based on Molecular Dynamics Simulations. *Cells* **2022**, *11* (24), 4016. https://doi.org/10.3390/cells11244016.

(263) Kutzner, C.; Köpfer, D. A.; Machtens, J. P.; De Groot, B. L.; Song, C.; Zachariae, U. Insights into the Function of Ion Channels by Computational Electrophysiology Simulations. *Biochimica et Biophysica Acta (BBA) - Biomembranes* **2016**, *1858* (7), 1741–1752. https://doi.org/10.1016/J.BBAMEM.2016.02.006.

(264) Wang, Y.; Gallagher, E.; Jorgensen, C.; Troendle, E. P.; Hu, D.; Searson, P. C.; Ulmschneider, M. B. An Experimentally Validated Approach to Calculate the Blood-Brain Barrier Permeability of Small Molecules. *Sci Rep* **2019**, *9*, 1–11. https://doi.org/10.1038/s41598-019-42272-0.

(265) Daggett, V.; Levitt, M. Molecular Dynamics Simulations of Helix Denaturation. *J Mol Biol* **1992**, *223* (4), 1121–1138. https://doi.org/10.1016/0022-2836(92)90264-K.

(266) Sani, M. A.; Separovic, F. How Membrane-Active Peptides Get into Lipid Membranes. *Acc Chem Res* **2016**, *49* (6), 1130–1138. https://doi.org/10.1021/acs.accounts.6b00074.

(267) Weng, J.; Wang, A.; Zhang, D.; Liao, C.; Li, G. A Double Bilayer to Study the Nonequilibrium Response of GIRK2 in Complex. *Phys. Chem. Chem. Phys* **2021**, *23*, 15784. https://doi.org/10.1039/d1cp01785c.

(268) Kluyver, T.; Ragan-Kelley, B.; Pérez, F.; Granger, B.; Bussonnier, M.; Frederic, J.; Kelley, K.; Hamrick, J.; Grout, J.; Corlay, S.; Ivanov, P.; Avila, D.; Abdalla, S.; Willing, C.; team, J. development; Kluyver, T.; Ragan-Kelley, B.; Pérez, F.; Granger, B.; Bussonnier, M.; Frederic, J.; Kelley, K.; Hamrick, J.; Grout, J.; Corlay, S.; Ivanov, P.; Avila, D.; Abdalla, S.; Willing, C.; team, J. development; Loizides, F.; Scmidt, B. Jupyter Notebooks – a Publishing Format for Reproducible Computational Workflows. In *20th International Conference on Electronic Publishing (01/01/16)*; Loizides, F., Scmidt, B., Eds.; IOS Press, 2016; pp 87–90. https://doi.org/10.3233/978-1-61499-649-1-87.

(269) Van Der Spoel, D.; Lindahl, E.; Hess, B.; Groenhof, G.; Mark, A. E.; Berendsen, H. J. C. GROMACS: Fast, Flexible, and Free. *J Comput Chem* **2005**, *26* (16), 1701–1718. https://doi.org/10.1002/JCC.20291.

(270) Lindahl, E.; Hess, B.; van der Spoel, D. GROMACS 3.0: A Package for Molecular Simulation and Trajectory Analysis. *J Mol Model* **2001**, *7* (8), 306–317. https://doi.org/10.1007/S008940100045.

(271) Hess, B.; Kutzner, C.; Van Der Spoel, D.; Lindahl, E. GROMACS 4: Algorithms for Highly Efficient, Load-Balanced, and Scalable Molecular Simulation. *J Chem Theory Comput* **2008**, *4* (3), 435–447. https://doi.org/10.1021/CT700301Q.

(272) Pronk, S.; Páll, S.; Schulz, R.; Larsson, P.; Bjelkmar, P.; Apostolov, R.; Shirts, M. R.; Smith, J. C.; Kasson, P. M.; Van Der Spoel, D.; Hess, B.; Lindahl, E. GROMACS 4.5: A High-Throughput and Highly Parallel Open Source Molecular Simulation Toolkit. *Bioinformatics* **2013**, *29* (7), 845–854. https://doi.org/10.1093/BIOINFORMATICS/BTT055.

(273) Frishman, D.; Argos, P. Knowledge-Based Protein Secondary Structure Assignment. *Proteins: Structure, Function, and Bioinformatics* **1995**, *23* (4), 566–579. https://doi.org/10.1002/PROT.340230412.

(274) Virtanen, P.; Gommers, R.; Oliphant, T. E.; Haberland, M.; Reddy, T.; Cournapeau, D.; Burovski, E.; Peterson, P.; Weckesser, W.; Bright, J.; van der Walt, S. J.; Brett, M.; Wilson, J.; Millman, K. J.; Mayorov, N.; Nelson, A. R. J.; Jones, E.; Kern, R.; Larson, E.; Carey, C. J.; Polat, İ.; Feng, Y.; Moore, E. W.; VanderPlas, J.; Laxalde, D.; Perktold, J.; Cimrman, R.; Henriksen, I.; Quintero, E. A.; Harris, C. R.; Archibald, A. M.; Ribeiro, A. H.; Pedregosa, F.; van Mulbregt, P.; Vijaykumar, A.; Bardelli, A. Pietro; Rothberg, A.; Hilboll, A.; Kloeckner, A.; Scopatz, A.; Lee, A.; Rokem, A.; Woods, C. N.; Fulton, C.; Masson, C.; Häggström, C.; Fitzgerald, C.; Nicholson, D. A.; Hagen, D. R.; Pasechnik, D. V.; Olivetti, E.; Martin, E.; Wieser, E.; Silva, F.; Lenders, F.; Wilhelm, F.; Young, G.; Price, G. A.; Ingold, G. L.; Allen, G. E.; Lee, G. R.; Audren, H.; Probst, I.; Dietrich, J. P.; Silterra, J.; Webber, J. T.; Slavič, J.; Nothman, J.; Buchner, J.; Kulick, J.; Schönberger, J. L.; de Miranda Cardoso, J. V.; Reimer, J.; Harrington, J.; Rodríguez, J. L. C.; Nunez-Iglesias, J.; Kuczynski, J.; Tritz, K.; Thoma, M.; Newville, M.; Kümmerer, M.; Bolingbroke, M.; Tartre, M.; Pak, M.; Smith, N. J.; Nowaczyk, N.; Shebanov, N.; Pavlyk, O.; Brodtkorb, P. A.; Lee, P.; McGibbon, R. T.; Feldbauer, R.; Lewis, S.; Tygier, S.; Sievert, S.; Vigna, S.; Peterson, S.; More, S.; Pudlik, T.; Oshima, T.; Pingel, T. J.; Robitaille, T. P.; Spura, T.; Jones, T. R.; Cera, T.; Leslie, T.; Zito, T.; Krauss, T.; Upadhyay, U.; Halchenko, Y. O.; Vázquez-Baeza, Y. SciPy 1.0: Fundamental Algorithms for Scientific Computing in Python. *Nature Methods 2020 17:3* **2020**, *17* (3), 261–272. https://doi.org/10.1038/s41592-019-0686-2.

(275) Ash, W. L.; Stockner, T.; MacCallum, J. L.; Tieleman, D. P. Computer Modeling of Polyleucine-Based Coiled Coil Dimers in a Realistic Membrane Environment: Insight into Helix-Helix Interactions in Membrane Proteins. *Biochemistry* **2004**, *43* (28), 9050–9060. https://doi.org/10.1021/BI0494572.

(276) Ingólfsson, H. I.; Carpenter, T. S.; Bhatia, H.; Bremer, P. T.; Marrink, S. J.; Lightstone, F. C. Computational Lipidomics of the Neuronal Plasma Membrane. *Biophys J* **2017**, *113* (10), 2271–2280. https://doi.org/10.1016/j.bpj.2017.10.017.

(277) Sengupta, D.; Leontiadou, H.; Mark, A. E.; Marrink, S. J. Toroidal Pores Formed by Antimicrobial Peptides Show Significant Disorder. *Biochimica et Biophysica Acta (BBA) - Biomembranes* **2008**, *1778* (10), 2308–2317. https://doi.org/10.1016/J.BBAMEM.2008.06.007.

(278) Yang, L.; Harroun, T. A.; Weiss, T. M.; Ding, L.; Huang, H. W. Barrel-Stave Model or Toroidal Model? A Case Study on Melittin Pores. *Biophys J* **2001**, *81* (3), 1475–1485. https://doi.org/10.1016/S0006-3495(01)75802-X.

(279) Tieleman, D. P. The Molecular Basis of Electroporation. *BMC Biochem* **2004**, *5* (1), 1–12. https://doi.org/10.1186/1471-2091-5-10.

(280) Gurtovenko, A. A.; Vattulainen, I. Pore Formation Coupled to Ion Transport through Lipid Membranes as Induced by Transmembrane Ionic Charge Imbalance: Atomistic Molecular Dynamics Study. *J Am Chem Soc* **2005**, *127* (50), 17570–17571. https://doi.org/10.1021/JA053129N.

(281) Tieleman, D. P.; Leontiadou, H.; Mark, A. E.; Marrink, S. J. Simulation of Pore Formation in Lipid Bilayers by Mechanical Stress and Electric Fields. *J Am Chem Soc* **2003**, *125* (21), 6382–6383. https://doi.org/10.1021/JA029504I.

(282) Alaybeyoglu, B.; Sariyar Akbulut, B.; Ozkirimli, E. Insights into Membrane Translocation of the Cell-Penetrating Peptide PVEC from Molecular Dynamics Calculations. *J Biomol Struct Dyn* **2016**, *34* (11), 2387–2398. https://doi.org/10.1080/07391102.2015.1117396.

(283) Lopez, C. F.; Nielsen, S. O.; Srinivas, G.; DeGrado, W. F.; Klein, M. L. Probing Membrane Insertion Activity of Antimicrobial Polymers via Coarse-Grain Molecular Dynamics. *J Chem Theory Comput* **2006**, *2* (3), 649–655. https://doi.org/10.1021/ct050298p.

(284) MacCallum, J. L.; Drew Bennett, W. F.; Peter Tieleman, D. Distribution of Amino Acids in a Lipid Bilayer from Computer Simulations. *Biophys J* **2008**, *94* (9), 3393. https://doi.org/10.1529/BIOPHYSJ.107.112805.

(285) Oba, M.; Nakajima, S.; Misao, K.; Yokoo, H.; Tanaka, M. Effect of Helicity and Hydrophobicity on Cell-Penetrating Ability of Arginine-Rich Peptides. *Bioorg Med Chem* **2023**, *91*, 117409. https://doi.org/10.1016/J.BMC.2023.117409.

(286) Whitley, P.; Grau, B.; Gumbart, J. C.; Martínez-Gil, L.; Mingarro, I. Folding and Insertion of Transmembrane Helices at the ER. *Int J Mol Sci* **2021**, *22* (23), 12778. https://doi.org/10.3390/IJMS222312778.

(287) Eiríksdóttir, E.; Konate, K.; Langel, Ü.; Divita, G.; Deshayes, S. Secondary Structure of Cell-Penetrating Peptides Controls Membrane Interaction and Insertion. *Biochimica et Biophysica Acta (BBA) - Biomembranes* **2010**, *1798* (6), 1119–1128. https://doi.org/10.1016/J.BBAMEM.2010.03.005.

(288) Fiedler, S.; Broecker, J.; Keller, S. Protein Folding in Membranes. *Cell Mol Life Sci* **2010**, *67* (11), 1779. https://doi.org/10.1007/S00018-010-0259-0.

(289) Fanghänel, S.; Wadhwani, P.; Strandberg, E.; Verdurmen, W. P. R.; Bürck, J.; Ehni, S.; Mykhailiuk, P. K.; Afonin, S.; Gerthsen, D.; Komarov, I. V.; Brock, R.; Ulrich, A. S. Structure Analysis and Conformational Transitions of the Cell Penetrating Peptide Transportan 10 in the Membrane-Bound State. *PLoS One* **2014**, *9* (6), e99653. https://doi.org/10.1371/JOURNAL.PONE.0099653.

(290) Almeida, P. F.; Ladokhin, A. S.; White, S. H. Hydrogen-Bond Energetics Drive Helix Formation in Membrane Interfaces. *Biochimica et Biophysica Acta (BBA) - Biomembranes* **2012**, *1818* (2), 178–182. https://doi.org/10.1016/J.BBAMEM.2011.07.019.

(291) Bennett, W. F. D.; Sapay, N.; Tieleman, D. P. Atomistic Simulations of Pore Formation and Closure in Lipid Bilayers. *Biophys J* **2014**, *106* (1), 210–219. https://doi.org/10.1016/J.BPJ.2013.11.4486.

(292) Lee, M. T.; Chen, F. Y.; Huang, H. W. Energetics of Pore Formation Induced by Membrane Active Peptides. *Biochemistry* **2004**, *43* (12), 3590–3599. https://doi.org/10.1021/bi036153r.

(293) Levine, Z. A.; Vernier, P. T. Life Cycle of an Electropore: Field-Dependent and Field-Independent Steps in Pore Creation and Annihilation. *Journal of Membrane Biology* **2010**, *236* (1), 27–36. https://doi.org/10.1007/s00232-010-9277-y.

(294) Tarek, M. Membrane Electroporation: A Molecular Dynamics Simulation. *Biophys J* **2005**, *88* (6), 4045–4053. https://doi.org/10.1529/BIOPHYSJ.104.050617.

(295) Park, S.; Kim, J.; Oh, S. S.; Choi, S. Q. Arginine-Rich Cell-Penetrating Peptides Induce Lipid Rearrangements for Their Active Translocation across Laterally Heterogeneous Membranes. *Advanced Science* **2024**. https://doi.org/10.1002/advs.202404563.

(296) Sun, D.; Forsman, J.; Woodward, C. E. Atomistic Molecular Simulations Suggest a Kinetic Model for Membrane Translocation by Arginine-Rich Peptides. *Journal of Physical Chemistry B* **2015**, *119* (45), 14413–14420. https://doi.org/10.1021/ACS.JPCB.5B08072.

(297) Thi Hong Nguyen, M. *Biologically Relevant Ions and Peptides in Aqueous Solutions and at Model*; 2024.

(298) Ferreira, T. M.; Coreta-Gomes, F.; Samuli Ollila, O. H.; Moreno, M. J.; Vaz, W. L. C.; Topgaard, D. Cholesterol and POPC Segmental Order Parameters in Lipid Membranes: Solid State 1H-13C NMR and MD Simulation Studies. *Physical Chemistry Chemical Physics* **2013**, *15* (6), 1976–1989. https://doi.org/10.1039/c2cp42738a.

(299) Duchardt, F.; Fotin-Mleczek, M.; Schwarz, H.; Fischer, R.; Brock, R. A Comprehensive Model for the Cellular Uptake of Cationic Cell-Penetrating Peptides. *Traffic* **2007**, *8* (7), 848–866. https://doi.org/10.1111/J.1600-0854.2007.00572.X.

(300) Hirose, H.; Takeuchi, T.; Osakada, H.; Pujals, S.; Katayama, S.; Nakase, I.; Kobayashi, S.; Haraguchi, T.; Futaki, S. Transient Focal Membrane Deformation Induced by Arginine-Rich Peptides Leads to Their Direct Penetration into Cells. *Molecular Therapy* **2012**, *20* (5), 984–993. https://doi.org/10.1038/MT.2011.313.

(301) Leontiadou, H.; Mark, A. E.; Marrink, S. J. Antimicrobial Peptides in Action. *J Am Chem Soc* **2006**, *128* (37), 12156–12161. https://doi.org/10.1021/ja062927q.

(302) Irudayam, S. J.; Berkowitz, M. L. Binding and Reorientation of Melittin in a POPC Bilayer: Computer Simulations. *Biochim Biophys Acta Biomembr* **2012**, *1818* (12), 2975–2981. https://doi.org/10.1016/j.bbamem.2012.07.026.

(303) Thi Hong Nguyen, M.; Vazdar, M. Molecular Dynamics Simulations Unveil the Aggregation Patterns and Salting out of Polyarginines at Zwitterionic POPC Bilayers in Solutions of Various Ionic Strengths. *Comput Struct Biotechnol J* **2024**, *23*, 3897–3905. https://doi.org/10.1016/j.csbj.2024.11.004.

(304) Sun, D.; Forsman, J.; Lund, M.; Woodward, C. E. Effect of Arginine-Rich Cell Penetrating Peptides on Membrane Pore Formation and Life-Times: A Molecular Simulation Study. *Physical Chemistry Chemical Physics* **2014**, *16* (38), 20785–20795. https://doi.org/10.1039/c4cp02211d.

(305) Illya, G.; Deserno, M. Coarse-Grained Simulation Studies of Peptide-Induced Pore Formation. *Biophys J* **2008**, *95* (9), 4163–4173. https://doi.org/10.1529/biophysj.108.131300.

(306) Vernier, P. T.; Ziegler, M. J.; Sun, Y.; Chang, W. V.; Gundersen, M. A.; Tieleman, D. P. Nanopore Formation and Phosphatidylserine Externalization in a Phospholipid Bilayer at High Transmembrane Potential. *J Am Chem Soc* **2006**, *128* (19), 6288–6289. https://doi.org/10.1021/ja0588306.

(307) Tieleman, D. P.; Marrink, S.-J. Lipids Out of Equilibrium: Energetics of Desorption and Pore Mediated Flip-Flop. **2006**. https://doi.org/10.1021/ja0624321.

(308) Trofimenko, E.; Grasso, G.; Heulot, M.; Chevalier, N.; Deriu, M. A.; Dubuis, G.; Arribat, Y.; Serulla, M.; Michel, S.; Vantomme, G.; Ory, F.; Dam, L. C.; Puyal, J.; Amati, F.; Lüthi, A.; Danani, A.; Widmann, C. Genetic, Cellular, and Structural Characterization of the Membrane Potential-Dependent Cell-Penetrating Peptide Translocation Pore. *Elife* **2021**, *10*. https://doi.org/10.7554/ELIFE.69832.

(309) Smith, A. P.; Lee, N. M. Pharmacology of Dynorphin. *Annu Rev Pharmacol Toxicol* **1988**, *28*, 123–140. https://doi.org/10.1146/annurev.pa.28.040188.001011.

(310) Morris, M. C.; Deshayes, S.; Heitz, F.; Divita, G. Cell-Penetrating Peptides: From Molecular Mechanisms to Therapeutics. *Biol Cell* **2008**, *100* (4), 201–217. https://doi.org/10.1042/BC20070116.

(311) Ciftci, I.; Sever, B.; Demirci, H.; Ivánczi, M.; Balogh, B.; Kis, L.; Mándity, I. Molecular Dynamics Simulations of Drug-Conjugated Cell-Penetrating Peptides. **2023**. https://doi.org/10.3390/ph16091251.

(312) Wolfe, J. M.; Fadzen, C. M.; Choo, Z. N.; Holden, R. L.; Yao, M.; Hanson, G. J.; Pentelute, B. L. Machine Learning to Predict Cell-Penetrating Peptides for Antisense Delivery. *ACS Cent Sci* **2018**, *4* (4), 512–520. https://doi.org/10.1021/acscentsci.8b00098.

(313) Pandey, P.; Patel, V.; George, N. V.; Mallajosyula, S. S. KELM-CPPpred: Kernel Extreme Learning Machine Based Prediction Model for Cell-Penetrating Peptides. *J Proteome Res* **2018**, *17* (9), 3214–3222. https://doi.org/10.1021/ACS.JPROTEOME.8B00322.

(314) Noh, S. Y.; Notman, R. Comparison of Umbrella Sampling and Steered Molecular Dynamics Methods for Computing Free Energy Profiles of Aromatic Substrates through Phospholipid Bilayers. *Journal of Chemical Physics* **2020**, *153* (3). https://doi.org/10.1063/5.0016114.

(315) Abramson, J.; Adler, J.; Dunger, J.; Evans, R.; Green, T.; Pritzel, A.; Ronneberger, O.; Willmore, L.; Ballard, A. J.; Bambrick, J.; Bodenstein, S. W.; Evans, D. A.; Hung, C. C.; O'Neill, M.; Reiman, D.; Tunyasuvunakool, K.; Wu, Z.; Žemgulytė, A.; Arvaniti, E.; Beattie, C.; Bertolli, O.; Bridgland, A.; Cherepanov, A.; Congreve, M.; Cowen-Rivers, A. I.; Cowie, A.; Figurnov, M.; Fuchs, F. B.; Gladman, H.; Jain, R.; Khan, Y. A.; Low, C. M. R.; Perlin, K.; Potapenko, A.; Savy, P.; Singh, S.; Stecula, A.; Thillaisundaram, A.; Tong, C.; Yakneen, S.; Zhong, E. D.; Zielinski, M.; Žídek, A.; Bapst, V.; Kohli, P.; Jaderberg, M.; Hassabis, D.; Jumper, J. M. Accurate Structure Prediction of Biomolecular Interactions with AlphaFold 3. *Nature 2024 630:8016* **2024**, *630* (8016), 493–500. https://doi.org/10.1038/s41586-024-07487-w.

(316) Bekker, H.; Berendsen, H.; Dijkstra, E.; Achterop, S.; VonDrumen, R.; VanDerSpoel, D.; Sijbers, A.; Keegstra, H.; Reitsma, B.; Renardus, M. Gromacs - a Parallel Computer for Molecular Dynamics Simulations. *PHYSICS COMPUTING '92* **1993**, 252–256.

(317) Berendsen, H. J. C.; van der Spoel, D.; van Drunen, R. GROMACS: A Message-Passing Parallel Molecular Dynamics Implementation. *Comput Phys Commun* **1995**, *91* (1–3), 43–56. https://doi.org/10.1016/0010-4655(95)00042-E.

(318) Páll, S.; Abraham, M. J.; Kutzner, C.; Hess, B.; Lindahl, E. Tackling Exascale Software Challenges in Molecular Dynamics Simulations with GROMACS. *Lecture Notes in*

Computer Science (including subseries Lecture Notes in Artificial Intelligence and Lecture Notes in Bioinformatics) **2015**, *8759*, 3–27. https://doi.org/10.1007/978-3-319-15976-8_1.

(319) Abraham, M. J.; Murtola, T.; Schulz, R.; Páll, S.; Smith, J. C.; Hess, B.; Lindah, E. GROMACS: High Performance Molecular Simulations through Multi-Level Parallelism from Laptops to Supercomputers. *SoftwareX* **2015**, *1–2*, 19–25. https://doi.org/10.1016/J.SOFTX.2015.06.001.

(320) Gomara, M. J.; Perez, Y.; Martinez, J. P.; Barnadas-Rodriguez, R.; Schultz, A.; von Briesen, H.; Peralvarez-Marin, A.; Meyerhans, A.; Haro, I. Peptide Assembly on the Membrane Determines the HIV-1 Inhibitory Activity of Dual-Targeting Fusion Inhibitor Peptides. *Scientific Reports 2019 9:1* **2019**, *9* (1), 1–13. https://doi.org/10.1038/s41598-019-40125-4.

(321) Matsuzaki, K.; Sugishita, K.-I.; Fujii, N.; Miyajima, K. Molecular Basis for Membrane Selectivity of an Antimicrobial Peptide, Magainin 2. *Biochemistry* **1995**, *34*, 3423–3429.

(322) Müller, A. T.; Posselt, G.; Gabernet, G.; Neuhaus, C.; Bachler, S.; Blatter, M.; Pfeiffer, B.; Hiss, J. A.; Dittrich, P. S.; Altmann, K. H.; Wessler, S.; Schneider, G. Morphing of Amphipathic Helices to Explore the Activity and Selectivity of Membranolytic Antimicrobial Peptides. *Biochemistry* **2020**, *59* (39), 3772–3781. https://doi.org/10.1021/ACS.BIOCHEM.0C00565.

(323) Xie, J.; Bi, Y.; Zhang, H.; Dong, S.; Teng, L.; Lee, R. J.; Yang, Z. Cell-Penetrating Peptides in Diagnosis and Treatment of Human Diseases: From Preclinical Research to Clinical Application. *Front Pharmacol* **2020**, *11*, 541971. https://doi.org/10.3389/FPHAR.2020.00697/XML.

(324) Maximyuk, O.; Khmyz, V.; Lindskog, C.-J.; Vukojević, V.; Ivanova, T.; Bazov, I.; Hauser, K. F.; Bakalkin, G.; Krishtal, O. Plasma Membrane Poration by Opioid Neuropeptides: A Possible Mechanism of Pathological Signal Transduction. *Cell Death Dis* **2015**, *6* (3), e1683–e1683. https://doi.org/10.1038/cddis.2015.39.

(325) Gallego-Villarejo, L.; Wallin, C.; Król, S.; Enrich-Bengoa, J.; Suades, A.; Aguilella-Arzo, M.; Gomara, M. J.; Haro, I.; Wärmlander, S.; Muñoz, F. J.; Gräslund, A.; Perálvarez-Marín,

A. Big Dynorphin Is a Neuroprotector Scaffold against Amyloid β-Peptide Aggregation and Cell Toxicity. *Comput Struct Biotechnol J* **2022**, *20*, 5672–5679. https://doi.org/10.1016/j.csbj.2022.10.014.

(326) Kanemitsu, Y.; Hosoi, M.; Zhu, P. J.; Weight, F. F.; Peoples, R. W.; McLaughlin, J. S.; Zhang, L. Dynorphin A Inhibits NMDA Receptors through a PH-Dependent Mechanism. *Molecular and Cellular Neuroscience* **2003**, *24* (3), 525–537. https://doi.org/10.1016/S1044-7431(03)00214-8.

(327) Sankararamakrishnan, R.; Weinstein, H. Molecular Dynamics Simulations Predict a Tilted Orientation for the Helical Region of Dynorphin A(1–17) in Dimyristoylphosphatidylcholine Bilayers. *Biophys J* **2000**, *79* (5), 2331–2344. https://doi.org/10.1016/S0006-3495(00)76479-4.

(328) Sankararamakrishnan, R.; Weinstein, H. Positioning and Stabilization of Dynorphin Peptides in Membrane Bilayers: The Mechanistic Role of Aromatic and Basic Residues Revealed from Comparative MD Simulations. **2002**. https://doi.org/10.1021/jp012174o.

(329) Kira, A.; Javkhlantugs, N.; Miyamori, T.; Sasaki, Y.; Eguchi, M.; Kawamura, I.; Ueda, K.; Naito, A. Interaction of Extracellular Loop II of κ-Opioid Receptor (196-228) with Opioid Peptide Dynorphin in Membrane Environments as Revealed by Solid State Nuclear Magnetic Resonance, Quartz Crystal Microbalance and Molecular Dynamics Simulation. *J Phys Chem B* **2014**, *118* (32), 9604–9612. https://doi.org/10.1021/JP505412J.

(330) Perini, D. A.; Aguilella-Arzo, M.; Alcaraz, A.; Perálvarez-Marín, A.; Queralt-Martín, M. Dynorphin A Induces Membrane Permeabilization by Formation of Proteolipidic Pores. Insights from Electrophysiology and Computational Simulations. *Comput Struct Biotechnol J* **2022**, *20*, 230–240. https://doi.org/10.1016/j.csbj.2021.12.021.

(331) Noid, W. G.; Chu, J. W.; Ayton, G. S.; Krishna, V.; Izvekov, S.; Voth, G. A.; Das, A.; Andersen, H. C. The Multiscale Coarse-Graining Method. I. A Rigorous Bridge between Atomistic and Coarse-Grained Models. *J Chem Phys* **2008**, *128* (24). https://doi.org/10.1063/1.2938860.

(332) Gu, R. X.; Baoukina, S.; Peter Tieleman, D. Phase Separation in Atomistic Simulations of Model Membranes. *J Am Chem Soc* **2020**, *142* (6), 2844–2856. https://doi.org/10.1021/JACS.9B11057.

(333) Her Choong, F.; Keat Yap, B. Cell-Penetrating Peptides: Correlation between Peptide-Lipid Interaction and Penetration Efficiency. *ChemPhysChem* **2021**, *22* (5), 493–498. https://doi.org/10.1002/CPHC.202000873.

(334) Bennett, W. F. D.; Hong, C. K.; Wang, Y.; Tieleman, D. P. Antimicrobial Peptide Simulations and the Influence of Force Field on the Free Energy for Pore Formation in Lipid Bilayers. *J Chem Theory Comput* **2016**, *12* (9), 4524–4533. https://doi.org/10.1021/ACS.JCTC.6B00265.

(335) Richardson, J. D.; Van Lehn, R. C. Free Energy Analysis of Peptide-Induced Pore Formation in Lipid Membranes by Bridging Atomistic and Coarse-Grained Simulations. *Journal of Physical Chemistry B* **2024**, *128*, 8737–8752. https://doi.org/10.1021/acs.jpcb.4c03276.

(336) Bennett, A. L.; Cranford, K. N.; Bates, A. L.; Sabatini, C. R.; Lee, H. S. A Molecular Dynamics Study of Cell-Penetrating Peptide Transportan-10 (TP10): Binding, Folding and Insertion to Transmembrane State in Zwitterionic Membrane. *Biochimica et Biophysica Acta (BBA) - Biomembranes* **2024**, *1866* (1), 184218. https://doi.org/10.1016/J.BBAMEM.2023.184218.

(337) Klug, J.; Berberián, M. V.; López Martí, J. M.; Mayorga, L. S.; Del Pópolo, M. G. Membrane Binding Strength vs Pore Formation Cost─What Drives the Membrane Permeation of Nanoparticles Coated with Cell-Penetrating Peptides? *J Phys Chem B* **2024**. https://doi.org/10.1021/ACS.JPCB.3C06461.

(338) Maia, R.; Ataka, K.; Heberle, J.; Baiz, C. R. Biophysics of PH-Driven Membrane Insertion: A Review of the PHLIP Peptide. *Journal of Physical Chemistry B* **2025**, *129*, 4123–4132. https://doi.org/10.1021/ACS.JPCB.5C00225.

(339) Alimohamadi, H.; de Anda, J.; Lee, M. W.; Schmidt, N. W.; Mandal, T.; Wong, G. C. L. How Cell-Penetrating Peptides Behave Differently from Pore-Forming Peptides: Structure

and Stability of Induced Transmembrane Pores. *J Am Chem Soc* **2023**. https://doi.org/10.1021/JACS.3C08014.

(340) Anahid, M.; Mahnam, K.; Saffar, B. Improving the Antimicrobial Activity of RP9 Peptide through Theoretical and Experimental Investigation. *Biochem Biophys Rep* **2025**, *41*, 101953. https://doi.org/10.1016/J.BBREP.2025.101953.

(341) Lai, P.-K.; Kaznessis, Y. N. Insights into Membrane Translocation of Protegrin Antimicrobial Peptides by Multistep Molecular Dynamics Simulations. *ACS Omega* **2018**, *3* (6), 6056–6065. https://doi.org/10.1021/acsomega.8b00483.

(342) Hao, M.; Zhang, L.; Chen, P. Membrane Internalization Mechanisms and Design Strategies of Arginine-Rich Cell-Penetrating Peptides. *Int J Mol Sci* **2022**, *23* (16). https://doi.org/10.3390/IJMS23169038.

(343) Tempra, C.; Brkljač, Z.; Vazdar, M. Why Do Polyarginines Adsorb at Neutral Phospholipid Bilayers and Polylysines Do Not? An Insight from Density Functional Theory Calculations and Molecular Dynamics Simulations †. **2023**. https://doi.org/10.1039/d3cp02411c.

(344) Fuselier, T.; Wimley, W. C. Spontaneous Membrane Translocating Peptides: The Role of Leucine-Arginine Consensus Motifs. *Biophys J* **2017**, *113* (4), 835–846. https://doi.org/10.1016/j.bpj.2017.06.070.

(345) Frøslev, P.; Franzyk, H.; Ozgür, B.; Brodin, B.; Kristensen, M. Highly Cationic Cell-Penetrating Peptides Affect the Barrier Integrity and facilitates Mannitol Permeation in a Human Stem Cell-Based Blood-Brain Model. *European Journal of Pharmaceutical Sciences* **2022**, *168*, 928–0987. https://doi.org/10.1016/j.ejps.2021.106054.

(346) Bartoš, L.; Kabelka, I.; Vácha, R. Enhanced Translocation of Amphiphilic Peptides across Membranes by Transmembrane Proteins. *Biophys J* **2021**, *120* (11), 2296–2305. https://doi.org/10.1016/j.bpj.2021.04.005.

(347) Walrant, A.; Matheron, L.; Cribier, S.; Chaignepain, S.; Jobin, M. L.; Sagan, S.; Alves, I. D. Direct Translocation of Cell-Penetrating Peptides in Liposomes: A Combined Mass Spectrometry Quantification and Fluorescence Detection Study. *Anal Biochem* **2013**, *438* (1), 1–10. https://doi.org/10.1016/J.AB.2013.03.009.

(348) Manzini, M. C.; Perez, K. R.; Riske, K. A.; Bozelli, J. C.; Santos, T. L.; Da Silva, M. A.; Saraiva, G. K. V; Politi, M. J.; Valente, A. P.; Almeida, F. C. L.; Chaimovich, H.; Rodrigues, M. A.; Bemquerer, M. P.; Schreier, S.; Cuccovia, I. M. Peptide:Lipid Ratio and Membrane Surface Charge Determine the Mechanism of Action of the Antimicrobial Peptide BP100. Conformational and Functional Studies. *BBA - Biomembranes* **2014**, *1838*, 1985–1999. https://doi.org/10.1016/j.bbamem.2014.04.004.

(349) Svirina, A.; Terterov, I. Electrostatic Effects in Saturation of Membrane Binding of Cationic Cell-Penetrating Peptide. *European Biophysics Journal* **2021**, *50* (1), 15–23. https://doi.org/10.1007/S00249-020-01476-3.

(350) Binder, H.; Lindblom, G. Charge-Dependent Translocation of the Trojan Peptide Penetratin across Lipid Membranes. *Biophys J* **2003**, *85* (2), 982–995. https://doi.org/10.1016/S0006-3495(03)74537-8.

(351) Chen, X.; Sa'Adedin, F.; Deme, B.; Rao, P.; Bradshaw, J. Insertion of TAT Peptide and Perturbation of Negatively Charged Model Phospholipid Bilayer Revealed by Neutron Diffraction. *Biochimica et Biophysica Acta (BBA) - Biomembranes* **2013**, *1828* (8), 1982–1988. https://doi.org/10.1016/J.BBAMEM.2013.04.022.

(352) Mitchell, D. J.; Steinman, L.; Kim, D. T.; Fathman, C. G.; Rothbard, J. B. Polyarginine Enters Cells More Efficiently than Other Polycationic Homopolymers. *Journal of Peptide Research* **2000**, *56* (5), 318–325. https://doi.org/10.1034/J.1399-3011.2000.00723.X;WGROUP:STRING:PUBLICATION.

(353) Wender, P. A.; Mitchell, D. J.; Pattabiraman, K.; Pelkey, E. T.; Steinman, L.; Rothbard, J. B. The Design, Synthesis, and Evaluation of Molecules That Enable or Enhance Cellular Uptake: Peptoid Molecular Transporters. *Proceedings of the National Academy of Sciences* **2000**, *97* (24), 13003–13008. https://doi.org/10.1073/PNAS.97.24.13003.

(354) Su, Y.; Mani, R.; Hong, M. Asymmetric Insertion of Membrane Proteins in Lipid Bilayers by Solid-State NMR Paramagnetic Relaxation Enhancement: A Cell-Penetrating Peptide Example. *J Am Chem Soc* **2008**, *130* (27), 8856–8864. https://doi.org/10.1021/JA802383T.

(355) Meher, G.; Chakraborty, H. Membrane Composition Modulates Fusion by Altering Membrane Properties and Fusion Peptide Structure. *Journal of Membrane Biology* **2019**, *252* (4–5), 261–272. https://doi.org/10.1007/S00232-019-00064-7.

(356) Sapay, N.; Bennett, W. F. D.; Tieleman, D. P. Thermodynamics of Flip-Flop and Desorption for a Systematic Series of Phosphatidylcholine Lipids. *Soft Matter* **2009**, *5* (17), 3295–3302. https://doi.org/10.1039/b902376c.

(357) Via, M. A.; Klug, J.; Wilke, N.; Mayorga, L. S.; Del Pópolo, M. G. The Interfacial Electrostatic Potential Modulates the Insertion of Cell-Penetrating Peptides into Lipid Bilayers. *Physical Chemistry Chemical Physics* **2018**, *20* (7), 5180–5189. https://doi.org/10.1039/C7CP07243K.

(358) Lin, J.; Alexander-Katz, A. Cell Membranes Open "Doors" for Cationic Nanoparticles/ Biomolecules: Insights into Uptake Kinetics. *ACS Nano* **2013**, *7* (12), 10799–10808. https://doi.org/10.1021/NN4040553/SUPPL_FILE/NN4040553_SI_003.PDF.

(359) Gao, X.; Hong, S.; Liu, Z.; Yue, T.; Dobnikar, J.; Zhang, X. Membrane Potential Drives Direct Translocation of Cell-Penetrating Peptides. *Nanoscale* **2019**, *11* (4), 1949–1958. https://doi.org/10.1039/C8NR10447F.

(360) Moghal, M. M. R.; Islam, M. Z.; Hossain, F.; Saha, S. K.; Yamazaki, M. Role of Membrane Potential on Entry of Cell-Penetrating Peptide Transportan 10 into Single Vesicles. *Biophys J* **2019**, *118* (1), 57. https://doi.org/10.1016/J.BPJ.2019.11.012.

(361) Zhang, X.; Jin, Y.; Plummer, M. R.; Pooyan, S.; Gunaseelan, S.; Sinko, P. J. Endocytosis and Membrane Potential Are Required for HeLa Cell Uptake of R.I.-CKTat9, a Retro-Inverso Tat Cell Penetrating Peptide. *Mol Pharm* **2009**, *6* (3), 836–848. https://doi.org/10.1021/MP800121F.

(362) Rothbard, J. B.; Jessop, T. C.; Lewis, R. S.; Murray, B. A.; Wender, P. A. Role of Membrane Potential and Hydrogen Bonding in the Mechanism of Translocation of Guanidinium-Rich Peptides into Cells. *J Am Chem Soc* **2004**, *126* (31), 9506–9507. https://doi.org/10.1021/JA0482536.

(363) Guvench, O.; MacKerell, A. D. Comparison of Protein Force Fields for Molecular Dynamics Simulations. *Methods in Molecular Biology* **2008**, *443*, 63–88. https://doi.org/10.1007/978-1-59745-177-2_4.

(364) Jing, Z.; Liu, C.; Cheng, S. Y.; Qi, R.; Walker, B. D.; Piquemal, J. P.; Ren, P. Polarizable Force Fields for Biomolecular Simulations: Recent Advances and Applications. *Annu Rev Biophys* **2019**, *48*, 371. https://doi.org/10.1146/ANNUREV-BIOPHYS-070317-033349.

(365) Marshall, G. R. Limiting Assumptions in Molecular Modeling: Electrostatics. *J Comput Aided Mol Des* **2013**, *27* (2), 107–114. https://doi.org/10.1007/S10822-013-9634-X.